NNT/NL : 2021AIXM0409/053ED352

THÈSE DE DOCTORAT

Soutenue à Aix-Marseille Université
en cotutelle avec l'Université de
Science et Technologie Chinoise
le 15 septembre 2021 par

Hanlin Xu

Search for doubly charged scalar bosons decaying to $W^{\pm}W^{\pm}$ at the LHC

Discipline
Physique et Sciences de la Matière

Spécialité
Physique des Particules et Astroparticules

École doctorale
ECOLE DOCTORALE 352

Laboratoire/Partenaires de recherche
School of Physics
Centre de Physique des Particules de Marseille

Composition du jury

Emmanuel MONNIER Centre de Physique des Particules de Marseille	Directeur de thèse
Yanwen Liu University of Science and Technology of China	Co-directeur de thèse
Bill Murray University of Warwick and RAL	Rapporteur
Lei Zhang Nanjing University	Rapporteur
Cristinel Diaconu Centre de Physique des Particules de Marseille	Président du Jury
Lailin Xu University of Science and Technology of China	Examinateur
Meng Xiao Zhejiang University	Examinateur

Je soussigné, Hanlin XU, déclare par la présente que le travail présenté dans ce manuscrit est mon propre travail, réalisé sous la direction scientifique de Emmanuel MONNIER et Yanwen LIU, dans le respect des principes d'honnêteté, d'intégrité et de responsabilité inhérents à la mission de recherche. Les travaux de recherche et la rédaction de ce manuscrit ont été réalisés dans le respect à la fois de la charte nationale de déontologie des métiers de la recherche et de la charte d'Aix-Marseille Université relative à la lutte contre le plagiat.

Ce travail n'a pas été précédemment soumis en France ou à l'étranger dans une version identique ou similaire à un organisme examinateur.

Fait à Marseille le 12/07/2021

Résumé

L'existence de neutrinos massifs est une preuve solide pour la physique au-delà du modèle standard. Le Modèle Standard du secteur de Higgs (SM), étendu par un triplet de jauge faible d'anciens scalaires avec une très petite valeur attendue dans le vide, est un cadre très prometteur pour expliquer les masses des neutrinos par le mécanisme dit de bascule de type II. Un tel modèle est appelé Double Triplet du Modèle de Higgs, incluant des bosons à charge simple et double qui peuvent être directement accessibles dans les expériences à l'échelle du TeV, ce qui donne lieu à une phénoménologie particulière au Grand collisionneur de hadrons.

Cette thèse présente une recherche de bosons de Higgs chargés se désintégrant en bosons WW ou WZ, impliquant des signatures expérimentales avec deux leptons de même charge, ou trois ou quatre leptons avec diverses combinaisons de charges électriques, de moments transversaux manquants et de jets de moment transversal erroné. Un échantillon de données correspondant à 139 fb^{-1} de luminosité intégrée, collectée par le détecteur ATLAS au LHC à une énergie centrale de masse de 13 TeV de 2015 à 2018 est utilisé.

Deux scénarios sont explorés, correspondant à la production de paires de bosons $H^{\pm\pm}$ doublement chargés ou à la production associée d'un boson $H^{\pm\pm}$ doublement chargé et d'un boson $H^{\pm}$ simplement chargé. Trois canaux sont désignés comme suit canal avec 2 leptons de même charge ($2\ell^{sc}$), canal avec trois leptons (3ℓ) et canal avec quatre-leptons (4ℓ) dépendant de la multiplicité de l'état final des leptons. Dans les canaux $2\ell^{sc}$ et 4ℓ les fonds irréductibles les plus dominants, WZ, est contraint par des données dans une région de contrôle dédiée afin d'éviter les erreurs dans une région de contrôle dédiée afin de supprimer l'incertitude de la normalisation.

Les fonds réductibles importants tels que les leptons non rapides et les flips d'électrons chargés sont estimés par des méthodes basées sur les données. Seuls quelques processus SM peuvent produire des états 4ℓ finaux; par conséquent, les leptons non rapides dans le canal 4ℓ sont estimés par une méthode basée sur les données en raison de la limite statistique. D'autres fonds provenant du SM sont estimés par la simulation de Monte-Carlo. Les régions de signal des trois canaux sont conçues séparément avec des coupes rectangulaires générées par l'algorithme recuit simulé (Simulated Annealing) avec plusieurs variables discriminantes. On n'observe pas de déviations significatives par rapport aux prédictions du modèle standard. La méthode CLs est utilisée pour dériver les limites supérieures de la section transversale de production du signal. Les bosons H sont exclus à 95% CL jusqu'à 350 GeV et 230 GeV GeV pour la paire et les modes de production associés.

Mots clés : Higgs à double charge, Higgs à charge unique, boson W, mécanisme de bascule de type II, LHC, ATLAS, Higgs, SM, BSM, Neutrino mass

Abstract

The existence of massive neutrinos is strong evidence for physics beyond the Standard Model. The Standard Model (SM) Higgs sector, extended by one weak gauge triplet of scalar fields with a very small vacuum expectation value, is a quite promising setting to account for neutrino masses through the so-called type-II seesaw mechanism. Such a model is called Doublet-Triplet-Higgs-Model including singly-charged and doubly-charged bosons, which can be directly accessible in TeV-scale experiments, leading to a distinctive phenomenology at the Large Hadron Collider.

This thesis presents a search for charged Higgs bosons decaying into $W^{\pm}W^{\pm}$ or $W^{\pm}Z$ bosons, involving experimental signatures with two leptons of the same charge, or three or four leptons with various electric charge combinations, missing transverse momentum, and jets. A data sample corresponding to 139 fb^{-1} integrated luminosity collected by the ATLAS detector at the LHC at a center-of-mass energy of 13 TeV from 2015 to 2018 is used.

Two scenarios are explored, corresponding to the pair production of doubly charged $H^{\pm\pm}$ bosons or the associated production of a doubly charged $H^{\pm\pm}$ boson and a singly charged $H^{\pm}$ boson. Three channels are defined as same-charge-two-lepton ($2\ell^{sc}$) channel, three-lepton (3ℓ) channel, and four-lepton (4ℓ) channel depending on the lepton multiplicity of final states. In $2\ell^{sc}$ and 3ℓ channels, the most dominant irreducible background, WZ, is constrained by data in a dedicated control region in order to suppress the uncertainty of the normalization. Important reducible backgrounds such as non-prompt leptons and charged flip electrons are estimated by data-driven methods. Only a few SM processes can produce 4ℓ final states; hence the non-prompt leptons in the 4ℓ channel are estimated by a semi-data-driven method due to the statistics limit. Other backgrounds from the SM are estimated by the Monte-Carlo simulation.

The signal regions of three channels are separately designed with rectangular cuts generated by Simulated Annealing (SA) algorithm with several discriminating variables. No significant deviations from the Standard Model predictions are observed. The CL$_s$ method is used to derive the upper limits on the signal production cross-section. $H^{\pm\pm}$ bosons are excluded at 95% CL up to 350 GeV and 230 GeV for the pair and associated production modes.

Keywords: Doubly charged Higgs, Singly charged Higgs, W boson, type II seesaw mechanism, LHC, ATLAS, Higgs, SM, BSM, Neutrino Mass

中国科学技术大学

博士学位论文

寻找大型强子对撞机实验中双电荷标量玻色子衰变至 W 玻色子事例

作者姓名：　许含霖

学科专业：　粒子物理与原子核物理

导师姓名：　刘衍文 教授　Emmanuel Monnier 教授

完成时间：　二〇二一年九月十四日

University of Science and Technology of China

A dissertation for doctor's degree

Search for doubly charged scalar bosons decaying to $W^{\pm}W^{\pm}$ at LHC

Author: Xu Hanlin

Speciality: Particle and Nuclear Physics

Supervisors: Prof. Liu Yanwen, Prof. Emmanuel Monnier

Finished time: September 14, 2021

中国科学技术大学学位论文原创性声明

本人声明所呈交的学位论文，是本人在导师指导下进行研究工作所取得的成果。除已特别加以标注和致谢的地方外，论文中不包含任何他人已经发表或撰写过的研究成果。与我一同工作的同志对本研究所做的贡献均已在论文中作了明确的说明。

作者签名：________________　　　　　签字日期：________________

中国科学技术大学学位论文授权使用声明

作为申请学位的条件之一，学位论文著作权拥有者授权中国科学技术大学拥有学位论文的部分使用权，即：学校有权按有关规定向国家有关部门或机构送交论文的复印件和电子版，允许论文被查阅和借阅，可以将学位论文编入《中国学位论文全文数据库》等有关数据库进行检索，可以采用影印、缩印或扫描等复制手段保存、汇编学位论文。本人提交的电子文档的内容和纸质论文的内容相一致。

保密的学位论文在解密后也遵守此规定。

☑公开　□保密（____年）

作者签名：________________　　　　　导师签名：________________

签字日期：________________　　　　　签字日期：________________

摘　要

中微子具有非零的静质量是在标准模型之外存在新物理的强力证据。双-三重态希格斯模型 (Doublet-Triplet-Higgs-Model) 通过第二型跷跷板机制, 在标准模型中的希格斯区域扩展一个真空期望值非常小的弱规范的三重标量场。该扩展模型是一个解释中微子质量问题的非常有前景的设置，它包含可以在 TeV 能区实验中直接访问的单电荷和双电荷玻色子，使得大型强子对撞机的现象学与众不同。

本论文探讨了一项对于带电希格斯玻色子衰变至 W 玻色子对或者 W 和 Z 玻色子的分析，涉及了二到四个不同电荷组合的轻子，丢失横向动量和喷注的信号。分析采用的数据样本对应于 LHC 的 ATLAS 探测器在 13 TeV 的对撞能量下收集的 139fb^{-1} 的积分亮度。带电希格斯玻色子的产生情形主要有两类，分别是双电荷希格斯玻色子的成对产生，以及双电荷希格斯玻色子和单电荷希格斯玻色子的协同产生。根据末态的轻子数，分析道分为同电荷二轻子道 ($2\ell^{sc}$)，三轻子道 (3ℓ) 和四轻子道 (4ℓ)。为了压低来自截面归一化的不确定性，在同电荷二轻子道和三轻子道中，WZ 过程作为最重要的不可约本底由特定区域中的数据所约束。非对撞直接产生的轻子和电荷错误识别电子作为重要的可约本底，是通过数据驱动的方法进行估算的。只有少量的标准模型过程可以产生四轻子末态，因此由于数据量的限制，在四轻子道中非对撞直接产生的轻子采用半数据驱动方法进行估计。分析中来自标准模型中的其他本底则由蒙特卡洛仿真来估计。

三个分析道进一步通过模拟退火算法生成的选择条件划分了信号区域。在信号区域的数据分析中没有观察到与标准模型预测的显着偏差。CL_s 方法则用以得出信号产生横截面的 95％置信水平上限。对于成对和协同的产生模式，双电荷希格斯玻色子在 95％置信度下分别排除了 350 GeV 和 230 GeV 的模型假设。

关键词： 双电荷标量玻色子，单电荷标量玻色子，W 玻色子，第二型跷跷板机制；大型强子对撞机；超环面仪器；标准模型；超越标准模型；希格斯玻色子；中微子质量

ABSTRACT

The existence of massive neutrinos is strong evidence for physics beyond the Standard Model. The Standard Model (SM) Higgs sector, extended by one weak gauge triplet of scalar fields with a very small vacuum expectation value, is a quite promising setting to account for neutrino masses through the so-called type-II seesaw mechanism. Such a model is called Doublet-Triplet-Higgs-Model including singly-charged and doubly-charged bosons，which can be directly accessible in TeV-scale experiments, leading to a distinctive phenomenology at the Large Hadron Collider.

This thesis presents a search for charged Higgs bosons decaying into $W^{\pm}W^{\pm}$ or $W^{\pm}Z$ bosons, involving experimental signatures with two leptons of the same charge, or three or four leptons with various electric charge combinations, missing transverse momentum, and jets. A data sample corresponding to 139 fb^{-1} integrated luminosity collected by the ATLAS detector at the LHC at a center-of-mass energy of 13 TeV from 2015 to 2018 is used.

Two scenarios are explored, corresponding to the pair production of doubly charged $H^{\pm\pm}$ bosons or the associated production of a doubly charged $H^{\pm\pm}$ boson and a singly charged $H^{\pm}$ boson. Three channels are defined as same-charge-two-lepton ($2\ell^{sc}$) channel, three-lepton (3ℓ) channel, and four-lepton (4ℓ) channel depending on the lepton multiplicity of final states. In $2\ell^{sc}$ and 3ℓ channels, the most dominant irreducible background, WZ, is constrained by data in a dedicated control region in order to suppress the uncertainty of the normalization. Important reducible backgrounds such as non-prompt leptons and charged flip electrons are estimated by data-driven methods. Only a few SM processes can produce 4ℓ final states; hence the non-prompt leptons in the 4ℓ channel are estimated by a semi-data-driven method due to the statistics limit. Other backgrounds from the SM are estimated by the Monte-Carlo simulation.

The signal regions of three channels are separately designed with rectangular cuts generated by Simulated Annealing (SA) algorithm with several discriminating variables. No significant deviations from the Standard Model predictions are observed. The $\mathrm{CL_s}$ method is used to derive the upper limits on the signal production cross-section. $H^{\pm\pm}$ bosons are excluded at 95% CL up to 350 GeV and 230 GeV for the pair and associated production modes.

Key Words: Doubly charged Higgs; Singly charged Higgs; W boson; type II seesaw mechanism; LHC; ATLAS; Higgs; SM; BSM; Neutrino mass

Synthèse en français

Introduction

Depuis la découverte du boson de Higgs [1, 2] en 2012, le Modèle Standard (SM) est devenu la théorie la plus aboutie de la physique des particules à nos jours. Cependant, de nombreux résultats expérimentaux, tels que l'existence de neutrinos massifs [3–5], ne peuvent pas être expliqués par le SM. La masse des neutrinos est une forte motivation pour la physique au-delà du SM. Étendre le SM en introduisant de nouvelles particules et forces est un moyen naturel d'aller au-delà du SM. Le secteur scalaire nouvellement découvert est le plus attrayant pour de telles extensions. Le mécanisme dit "de balancier de type II" [6–9] peut expliquer la masse non nulle des neutrinos et prédire de nouvelles particules scalaires en étendant le secteur de Higgs du SM avec un triplet scalaire. L'ajout d'un triplet scalaire peut prédire de nouvelles particules scalaires, dont certaines sont à l'échelle électrofaible et pourraient donc être détectées au LHC [10–13].

Dans cette thèse, une variante de cette extension est étudiée. Elle incorpore au modèle une hypercharge $Y = 2$ triplet scalaire, Δ qui compléte le doublet scalaire du Higgs SM. Le secteur scalaire doublet-triplet (DTHM) est controlé par cinq couplages, qui définissent les diverses interactions de chaque champ scalaire. La rupture de symétrie électrofaible est définie par deux valeurs d'espérance du vide, $\mathrm{v}_d \sim 246$ GeV et v_t[1], qui conduisent à une riche phénoménologie présentant sept scalaires: $H^{\pm\pm}$, $H^{\pm}$, A^0 (CP odd), H^0 (CP even), h^0 (CP even) [10, 11]. Le Higgs du SM est naturellement inclus dans ces sept scalaires et peut être H^0 ou h^0. L'analyse présentée dans cette thèse se focalise principalement sur la phénoménologie des bosons scalaires doublement chargés $H^{\pm\pm}$ dans l'espace des paramètres où le canal de décroissance dominant est $H^{\pm\pm} \to W^{\pm}W^{\pm}$ et le couplage aux leptons est défavorisé. Les bosons de Higgs doublement chargés peuvent être produits par paires et se désintégrer en quatre bosons W. Cette analyse explore également le scénario de production associée, un modèle "dégénéré", où tous les nouveaux bosons ont une masses très proches. Le mode de production dominant de cette production associée est $pp \to H^{\pm\pm}H^{\mp}$, et le canal de décroissance principal est $H^{\pm\pm} \to W^{\pm}W^{\pm}, H^{\pm} \to W^{\pm}Z$. Les états finaux étudiés dans cette analyse incluent les topologies multilepton pour lesquelles le fond hadronique est moins important et comprennent: les événements à deux leptons de même charge ($2\ell^{sc}$) avec E_T^{miss} et multi-jets; les événements à trois leptons (3ℓ) avec E_T^{miss} et multi-jets; les événements à quatre lepton (4ℓ) avec E_T^{miss}.

Des recherches approfondies sur les désintégrations leptoniques ont été effectuées dans diverses expériences [14–19], La collaboration CMS a publié des résultats pour le mode de désintégration $H^{\pm\pm} \to W^{\pm}W^{\pm}$ dans le contexte de la production unique de $H^{\pm\pm}$ par fusion vecteur-boson avec des valeurs $\mathrm{v_t}$ de quelques dizaines de GeV, pour un modèle à deux triplets de Higgs [20–22]. Une recherche directe de la production de paires $H^{\pm\pm}$ avec désintégration en $W^{\pm}W^{\pm}$ paires a été effectuée

[1] v_t est constraint par les mesures de precision à être d'un ordre de grandeur inferieur au GeV.

sur un jeu de données réduit de 36.1 fb^{-1} par la collaboration ATLAS [23], validant le principe d'une telle approche. Pour améliorer ces résultats publiés dans cette analyse, avec 36.1 fb^{-1} [23], d'une limite inférieure observée de 220 GeV sur la masse de Higgs doublement chargés décroissant à $W^{\pm}W^{\pm}$, la présente thèse étend l'analyse au 139.0 fb^{-1} de données accumulées durant tout le "Run2", entre 2015 et 2018, et affine et améliore l'approche de recherche. De plus, la production d'un boson $H^{\pm\pm}$ en association avec un boson $H^{\pm}$ est incluse, permettant de rechercher des bosons de Higgs à double et simple charge dans un espace de paramètres encore inexploré du modèle considéré.

Le modèle standard et le modèle Doublet-Triplet de Higgs (DTHM)

La présente thèse commence par une description de la théorie SM et du DTHM au Chapitre 2.

Bien qu'il existe encore de nombreux mystères non résolus en physique des particules, le modèle standard (SM) [24–27] est toujours la théorie la plus réussie décrivant les trois forces fondamentales entre les particules élémentaires dans notre univers. De nombreuses prédictions, confirmées plus tard par des expériences, telles que l'observation du quark top [28], du neutrino tau [29], et du boson de Higgs [1, 2], ont fait le succès du modèle standard.

Le SM est une théorie quantique des champs (QFT) [30, 31], qui fournit le cadre mathématique fondamental à la physique des particules moderne. Le développement de la théorie quantique des champs a commencé par l'étude des champs électromagnétiques dans l'electrodynamique quantique (QED), qui peut aider les physiciens à étudier les particules élémentaires à de très petites échelles (mécanique quantique) mais à de très grandes énergies (relativistes). La théorie des jauges s'avère essentielle pour expliquer la dynamique du QED qui est basé sur un groupe abélien U(1). La théorie de Yang-Mills [32] a étendu la théorie de jauge pour les groupes abéliens aux groupes non-abéliens pour expliquer les interactions fortes. Dans les années 1960, après avoir reconnu la rupture spontanée de la symétrie, les théoriciens ont combiné les interactions électromagnétiques et faibles [33] et ont adopté le mécanisme de Brout–Englert–Higgs (BEH) mechanism [34–36] pour briser la symétrie de jauge de l'interaction électrofaible. En 1973, la découverte de la liberté asymptotique a validé la chromodynamique quantique (QCD).

Jusqu'à présent, le modèle standard (SM) décrit bien les observations des expériences sur les accélérateurs. Cependant, ce n'est pas la théorie ultime de la physique des particules. Certaines caractéristiques du SM ont été ajoutées avec des hypothèses ad hoc. Cette approche permet au SM de fonctionner avec succès mais implique également un manque de compréhension de la physique fondamentale. Pour résumer brièvement certaines fonctionnalités ad hoc, le SM contient un grand nombre de paramètres et un réglage fin des paramètres.

De plus, il existe des phénomènes physiques fondamentaux dans la nature que le modèle standard n'explique pas suffisamment: i) Gravité: Le SM est incompatible avec la relativité générale [37]. ii) Matière noire et énergie noire: Le SM ne fournit pas d'explication fondamentale. iii) Asymétrie matière-antimatière: Le grand déséquilibre observé dans la quantité de matière et d'antimatière dans l'univers implique que la symétrie CP est violée au maximum, ce pour quoi le modèle standard ne peut pas fournir une explication. iv) Masses neutrinos: Les neutrinos sont des particules sans masse dans le SM puisqu'il n'y a pas de couplage de Yukawa pour les neutrinos avec le champ de Higgs. Cependant, des expériences d'oscillation de neutrinos ont montré que les neutrinos ont une masse. Il existe également d'autres problèmes et une incomplétude du SM. Dans cette thèse, nous étudierons une extension du SM qui aborde le problème des masses de neutrinos.

Le mécanisme de balancier est un modèle générique utilisé pour comprendre les tailles relatives des masses de neutrinos observées. Il n'y a qu'un seul opérateur de dimension cinq qui est pertinent pour le neutrino massif, $\kappa l_L l_L H H$, où l_L et H représentent respectivement le doublet leptonique et de Higgs $SU(2)_L$ [38]. La rupture de symétrie électrofaible (EWSB) conduit la masse du neutrino Majorana à être $m_\nu \sim \kappa v_0^2/\Lambda$, où v_0 est la valeur de l'espérance du vide (v.e.v) du Higgs, 246 GeV, κ est le couplage sans dimension et Λ est l'échelle de masse. De très petites masses de neutrinos peuvent ainsi être obtenues si Λ est beaucoup plus grand que v_0, qui est le concept de "balancier".

Cependant, l'opérateur de dimension cinq vient juste de la théorie des champs effectifs. Il est donc crucial de comprendre l'origine de l'opérateur de dimension cinq. Le modèle de Higgs de doublet-triplet (DTHM) [11] basé sur le mécanisme de balancier de type II [6–9] étend le SM en incluant un champ de triplet de $SU(2)_L$ Higgs Δ qui a une hypercharge $Y = 2$. Dans ce scénario, la masse neutrino devient alors $m_\nu \sim Y_\nu v_t$ où Y_ν est le couplage de yukawa et v_t est la v.e.v. du triplet Δ. L'EWSB conduit à une relation $v_t \sim \mu v_0^2/M_\Delta^2$ où μ est un paramètre dimensionnel pour le mélange de doublets et de triplets et M_Δ^2 est la masse du triplet Δ.

Cet EWSB provoque un mélange entre ces champs et aboutit à sept bosons scalaires: $H^{\pm\pm}$, $H^\pm$, A^0 (CP odd), H^0 (CP even), h^0 (CP even). La présente thèse étudiera deux scénarios qui sont les principaux canaux de production [10] au Grand Collisionneur de Hadrons (LHC - Large Hadron Colliser): la Production de Paire (PP): $pp \to \gamma^*, Z^* \to H^{\pm\pm}H^{\mp\mp}$ et la Production Associée (AP): $pp \to W^{*+} \to H^{\pm\pm}H^{\mp}$. Le mode de production unique $pp \to W^{\pm *}W^{\pm *} \to H^{\pm\pm}$ se fait par fusion boson-vecteur et est proportionnel à $\mathrm{v_t}$, donc négligeable en DTHM. La production associée ($pp \to W^{\pm *} \to H^{\pm\pm}W^{\mp *}$) avec W est également possible et est supprimée exactement pour la même raison.

L'expérience LHC et ATLAS

Un aperçu de l'expérience LHC et ATLAS est décrit au chapitre 3.

Le grand collisionneur de hadrons (LHC) [39] est la plus grande et la plus puissante machine au monde pour produire des collisions de protons et d'ions lourds, située au CERN (*Conseil Européen Pour la Recherche Nucléaire*) sous la frontière entre la France et de la Suisse. Il dispose de deux tubes à vide hebergeant des faisceaux de particules accélérées se déplaçant en sens opposé. Les faisceaux de protons entrent en collision dans les quatre expériences principales du LHC (ALICE, ATLAS, CMS et LHCb) situées autour du LHC. La chaîne d'injection de protons et les emplacements des quatre expériences sont illustrés à la Figure 3.1. Le détecteur ATLAS (A Toroidal LHC ApparatuS) [40] est l'un des deux détecteurs polyvalents du LHC. Comme le montre la Figure 3.2, le détecteur ATLAS est construit en couches de sous-détecteurs pour capturer toutes les particules détectables produites lors des collisions pp. En partant du tube faisceau du LHC, les sous-détecteurs sont le détecteur intérieur (ID), le calorimètre à argon liquide (LAr), le calorimètre à tuiles (Tile) et le spectromètre à muons (MS).

Reconstruction des objets physiques

Le chapitre 4 présente la configuration expérimentale de reconstruction des objets physiques.

Les particules produites lors de la collision de protons passent dans ATLAS à travers un ensemble de sous-détecteurs et génèrent des dépôts d'énergie par des interactions électromagnétiques et fortes avec la matière. La réponse de chaque sous-détecteur à ces dépôts d'énergie est lue et enregistrée. Des algorithmes de reconstruction dédiés sont ensuite appliqués pour reconstruire des objets physiques de ces dépots. Cette section décrit comment sont reconstruites les différentes particules, ou objet physique, dans ATLAS.

Analyse physique

La sélection des événements, l'identification des particules et les variables cinématiques utilisées dans la thèse sont décrites au chapitre 6.

La production par paire et la production associée sont les deux plus importantes pour des Higgs chargés. De plus, les bosons $W^{\pm}$ et Z des Higgs chargés se désintègrent davantage en leptons, neutrinos ou jets. Les rapports d'embranchement (BR) des différents états finaux contenant ou non des leptons légers (électrons et muons) sont présentés dans le tableau 6.1. Les canaux avec 0 ou 1 leptons ont les BR les plus élevés mais sont dominés par des processus multi-jets (QCD) produits en abondance au LHC. Afin de supprimer le bruit de fond multi-jets, des contraintes très strictes doivent être placées sur les variables cinématiques clés, ce qui n'est pas le cas pour les régions de signal multi-jets. Dans cette analyse, seuls les états finaux multileptoniques sont considérés. Malgré des BR inférieurs, ces canaux sont toujours cruciaux pour les recherches au-delà du SM (BSM) et nous permettent de sonder l'espace de phase BSM généralement non couvert par les recherches à 0 ou 1 leptons.

Estimation de fond

Les échantillons étudiés et l'estimation de fond sont présentés respectivement au chapitre 5 et au chapitre 7.

Cette analyse est réalisée avec les 139 fb^{-1} des données du "Run 2", collectées par le détecteur ATLAS à partir des collisions proton-proton produites à $\sqrt{s}$ =13 TeV d'énergie dans le centre de masse entre 2015 et 2018 (décrit au chapitre 3). L'ensemble de ces données a été collecté avec un espacement des paquets de 25 ns, et vérifie toutes les exigences de qualité des données qui doivent figurer dans la Good Run List recommandée [41].

Pour les deux processus, de production de paires $H^{\pm\pm}H^{\mp\mp}$ et de production associée $H^{\pm\pm}H^{\mp}$, les événements au niveau partonique sont générés avec le générateur MG5_aMC [42] (Matrix Element Leading Order, ME LO) en utilisant le PDF NNLOPDF30. Les événements sont ensuite developpés en utilisant PYTHIA8 [43] avec l'ajustement A14 [44], et sont ensuite passés à travers la simulation officielle du détecteur ATLAS (Algorithme AtlFast II, également désigné par AFII plus loin dans la thèse) et la reconstruction. Les échantillons sont numérisés en utilisant un espacement des paquets de 25 ns, les configurations générale MC16a (correspondant aux données collectées en 2015-2016), MC16d (correspondant aux données collectées en 2017) et MC16e (correspondant aux données collectées en 2018), et une distribution mise à jour du nombre moyen d'empilement d'interactions par croisement de paquets pour 2015-2018.

Ces échantillons signal ont été simulés avec $m_{H^{\pm\pm}}$ = 200, 300, 400, 500, 600 GeV pour les deux modes de production. $m_H^{\pm}$ a été choisi dans une petite gamme de masse (<5 GeV) pour maximiser la section efficace de la production associée. Un filtre qui sélectionne les événements avec au moins deux leptons légers (électrons ou muons, pas de veto tau appliqué) avec $p_T > 10$ GeV et $|\eta| < 10$ est appliqué au niveau de vérité pour la production de paires $H^{\pm\pm}H^{\mp\mp}$ et pour la production associée $H^{\pm\pm}H^{\mp}$. La section efficace de production (NLO) et l'efficacité des filtres sont indiquées dans les tableaux 5.1 et 5.2.

Les programmes de génération d'événement et les configurations utilisées pour la simulation des processus de bruit de fond sont indiqués dans le tableau 5.3. Des descriptions détaillées des configurations de générateur peuvent être trouvées dans les Réf. [45–48]. Dans tous les cas, une masse de boson SM Higgs de 125 GeV est supposée. Les événements générés passent par une simulation GEANT4 GEANT4 [49] complète du détecteur ATLAS.

Trois validations, les régions, $t\bar{t}$, Z + jets (Drell-Yan) et WZ, sont définies pour les trois processus de bruit de fond les plus importants. Les sélections pour les régions de validation sont répertoriées dans le tableau 7.1. Les distributions de la masse invariante du système di-lepton pour la région de validation des jets Z+jets sont illustrées à la figure 7.2. Les comparaisons montrent que les événements à deux leptons de signe opposé sont dominés par Drell-Yan et sont bien modélisés par la simulation de Monte-Carlo. Justifié par l'accord, nous utilisons le taux d'erreur d'identification de charge mesuré avec des données pour mettre à l'échelle les événements de signe opposé dans les échantillons Drell-Yan Monte-Carlo pour prédire la contribution Drell-Yan dans la région du signal $2\ell^{sc}$. Ceci est expliqué plus en détail dans la section 7.2.2.

Le processus WZ est le fond irréductible le plus important dans les canaux $2\ell^{sc}$ et 3ℓ. Cependant la distribution de multiplicité des jets dans la région de validation WZ (Figure 7.3) montre que les processus WZ ne sont pas bien modélisés dans les régions avec un nombre de jets> = 2. Cela a déjà été vu dans plusieurs analyses de la collaboration ATLAS. Aussi, une étude dédiée a été réalisée pour mesurer un facteur de correction (normalisation) pour mettre à l'échelle les processus WZ dans les régions avec un nombre de jets> = 2.

La figure 7.4 montre les résultats obtenus avec un ajustement avec une fonction constante pour obtenir le facteur de normalisation WZ (NF); et il est utilisé pour ajuster le rapport de multiplicité des jets entre les données avec soustraction du fond non-WZ (Monte-Carlo) et du fond WZ (Monte-Carlo). Le facteur de normalisation obtenu pour les processus WZ est de 0.83±0.02(stat)±0.07(syst).

Les sources de bruit de fond peuvent être divisées en deux catégories principales. Une catégorie est remplie par les événements SM qui ne contiennent que des leptons directs reconstruits. La deuxième catégorie contient des leptons non-direct, des électrons de charge inversée et des photons convertis. Les candidats lepton reconstruits à partir de ces différentes sources partagent les propriétés d'être moins isolés, d'avoir des paramètres d'impact plus importants par rapport au vertex primaire et d'être moins susceptibles de satisfaire aux critères d'identification des leptons.

Les processus de bruit de fond SM avec des leptons directs sont estimés avec des simulations Monte-Carlo, à l'exception du bruit de fond de la production WZ pour lequel la normalisation est corrigée à l'aide de données dans une région de contrôle dédiée (Section 7.1.1). Le bruit de fond de leptons non directs et d'électrons de charge inversée est estimé à l'aide de méthodes basées sur les données. Le bruit de fond de production $V\gamma$ peut contribuer aux SR si le photon se convertit en une paire électron-positon, et est estimé à l'aide de simulations de Monte-Carlo.

Dans le canal $2\ell^{sc}$, avec des estimations basées sur les données des contributions de faux leptons et de leptons de charge inversée, le bruit de fond total est comparé au nombre d'événements observés dans les données dans le tableau 7.14. Le bruit de fond de faux leptons est implémenté en utilisant les événements de la région "*signal+CandNotSig* di-lepton", pondérés par les facteurs de corrections des faux. Comme mentionné, les bruit de fond WZ, ZZ, même signe WW, etc. sont estimés à partir de la simulation de Monte-Carlo. Le très bon accord entre les données et la prédiction valide les méthodes d'estimation de fond basées sur les données décrites ci-dessus. D'autres distributions de validations des bruits de fond sont présentées dans les figures 7.15-7.17. Généralement, un accord entre les données et le bruit de fond est observé, validant les méthodes basées sur les données utilisées pour le fond d'électrons de charge inversée et l'estimation de fond de lepton non-direct.

Dans le canal 3ℓ, les distributions de validations des bruits de fond sont présentées dans les figures 7.24, 7.25, 7.26, au niveau de la présélection. En général, on observe une bonne concordance entre les données et l'estimation de fond, validant les méthodes basées sur les données utilisées pour l'estimation de fond de lepton non direct.

Dans le canal 4ℓ, la concordance entre les données et le bruit de fond au niveau de la présélection, en utilisant la méthode semi-guidée par les données décrite dans cette section pour l'estimation de fond de faux lepton, est représentée sur les figures Figure 7.28 et 7.29. La concordance entre les données et le Monte-Carlo est généralement bonne.

Définition de la région du signal

Les optimisations finales de la région du signal sont présentées au chapitre 8.

La méthode des coupures rectangulaires (entraînées avec l'algorithme de recuit simulé) implémentée dans le kit d'outils TMVA [50] est adoptée pour optimiser les définitions basées sur les coupes des régions de signal. Les coupes sont optimisées indépendamment pour chaque point de masse et pour chacun des canaux leptoniques. Pour tous les canaux d'analyse, l'optimisation des coupes est réalisée par TMVA. La méthode d'optimisation des coupes TMVA maximise le rejet du bruit de fond à une efficacité de signal donnée6 et analyse sur toute la plage d'efficacité du signal (de 1% à 100taille de pas de 1%). Un groupe de coupes avec une signification maximale sera dérivé après l'analyse d'optimisation de coupe. Dans chaque canal d'analyse, des vérifications supplémentaires seront effectuées pour avoir un ensemble de coupes stables.

Pour une efficacité de signal donnée, l'algorithme de recuit simulé est utilisé pour réaliser un ensemble de coupure avec le meilleur rejet du bruit de fond. L'algorithme de recuit simulé vise à résoudre un problème de minimisation globale, inspiré du processus de recuit en physique de la matière condensée. Le recuit simulé peut être utilisé pour approximer le minimum global pour une fonction avec de nombreuses variables. Dans cette analyse, l'algorithme de recuit simulé fonctionne avec l'option d'approche adaptative croissante (IncAdaptive): l'algorithme recherche les minima locaux et explore leur voisinage, tout en modifiant la température ambiante en fonction du nombre d'erreures dans les étapes précédentes. Les performances peuvent être améliorées en augmentant le nombre d'étapes d'itération (MaxCalls) ou en ajustant la température minimale (MinTemp). Des ajustements manuels de la vitesse d'augmentation de la température (TempScale et AdaptiveSpeed) pour des ensembles de données individuels peuvent également améliorer les performances.

Les régions de signal définies pour les canaux $2\ell^{sc}$, 3ℓ and 4ℓ, pour chaque point de masse, sont illustrées dans le tableau 8.8. Les variables utilisées dans ce tableau sont détaillées dans la section 6.3.

Pour mieux rendre compte de la distribution du bruit de fond dans le canal 3ℓ, chaque SR 3ℓ est divisé en deux, en fonction du nombre de paires de charges opposées de même saveur. Un SR 3ℓ est défini lorsque zéro de ces paires (SFOC 0) existe dans l'événement et un autre lorsque une ou deux de ces paires (SFOC 1, 2) existent, respectivement. Cette approche s'est avérée augmenter la sensibilité du canal 3ℓ lors de l'exécution de l'interprétation statistique (et en plaçant des limites sur la masse de boson de Higgs chargé). Pour la même raison, le canal $2\ell^{sc}$ est divisé en trois sous-canaux.

Incertitudes systématiques

Les incertitudes expérimentales et théoriques sont présentées au chapitre 9.

L'ensemble des incertitudes théoriques et expérimentales est considéré dans cette analyse. Le processus signal et le bruits de fond avec des leptons directs sont tirés des simulations de Monte-Carlo. Les incertitudes liées aux normalisations et aux acceptances proviennent pour la plupart de la précision finie sur les prédictions des sections efficaces et des cinématiques différentielles, et sont de nature théorique. Les incertitudes expérimentales découlent de la précision finie de la simulation du détecteur et des incertitudes associées aux méthodes basées sur les données qui sont utilisées pour estimer les bruits de fond instrumentaux.

Résultats

Les résultats, y compris la combinaison statistique des canaux d'analyse et les contraintes sur l'espace des paramètres de l'analyse, sont présentés au chapitre 10, suivis des conclusions finales au chapitre 11.

Les rendements d'événements attendus et observés dans toutes les régions de signal définies ($2\ell^{sc}$, 3ℓ, et 4ℓ, telles que définies dans la section 8.5) pour des valeurs de masse de 200 à 500 GeV pour le signal sont représentés sur la Figure 10.1 - 10.4. On peut observer une performance uniforme dans tous les canaux. Le rapport entre le signal et le bruit de fond (S/B) ainsi que la significance du signal ($S/\sqrt{B}$) dans les differents canaux pour $m_{H^{\pm\pm}}$ = 200 GeV sont indiqués sur la figure 10.5. Un diagramme de distribution combiné pour les processus de bruit de fond se trouve dans la figure 10.6. Les détails de rendement se trouvent dans le tableau 10.2. Aucun excès significatif n'a été observé. Les données sont utilisées pour contraindre le modèle de signal.

L'analyse statistique des résultats se fait avec TrHFitter. La procédure est basée sur le test du rapport de vraisemblance. Le paramètre d'intérêt (POI) est la force du signal, définie comme la section efficace de la contribution hypothétique due à la physique au-delà du SM en unité de section efficace du modèle de référence. Les tests d'hypothèse sont effectués en utilisant une case par région de signal, et il n'y a pas de région de contrôle impliquée. Les fonctions de vraisemblance sont construites par des statistiques de Poisson d'expériences de comptage dans les 6 régions de signal: les 3 sous-canaux (ee, $e\mu$ et $\mu\mu$) pour le canal $2\ell^{sc}$, les deux sous-canaux de même saveur-charge opposée (SFOC0, SFOC12) pour le 3ℓ, et la région de signal pour 4ℓ. Les incertitudes systématiques sont traitées comme des paramètres de nuisance implémentés dans les fonctions de vraisemblance. La méthode CL_s [51] est utilisée pour dériver les limites supérieures du niveau de confiance à 95% sur la section efficace de production du signal.

Les limites supérieures de la force du signal de la production de paires et de la production associée sont indiquées dans le tableau 10.1. Les limites attendues et observées obtenues après la combinaison des canaux $2\ell^{sc}$, 3ℓ and 4ℓ sont illustrées à la figure 10.8 (par rapport à la masse $H^{\pm\pm}$) pour la production de paires et pour la production associée, avec toutes les incertitudes incluses ou uniquement avec l'incertitude statistique incluse. En combinant tous les canaux, le modèle de référence devrait être exclu à $m_{H^{\pm\pm}} < 352$ GeV (358 GeV pour les résultats attendus) pour la production de paires de Higgs chargées et $m_{H^{\pm\pm}} < 228$ GeV (225 GeV pour les résultats attendus) pour les Production associée de Higgs. Avec une approche conservatrice, la limite finale, $m_{H^{\pm\pm}} > 350$ GeV, est défini pour la production de paires, et $m_{H^{\pm\pm}} > 220$ GeV est défini pour la production associée. Pour valider l'interpolation, ces deux points de masse ont été simulés et testés avec les régions de signal du 300 GeV et 200 points de masse GeV. Deux autres points de masse, les 450 et 550 GeV, ont également été simulés pour vérifier l'interpolation à la gamme supérieure pour la production associée.

Contents

Part I

Theoretical Information and Experiment Setup

1 Introduction

After the discovery of the Higgs boson [1, 2], the SM becomes the most successful theory of particle physics nowadays. However, many experimental results, such as the existence of massive neutrinos [3–5], can not be explained by the SM. The mass of the neutrinos is one strong motivation for physics beyond the SM. Extending the SM by introducing new particles and forces is a natural way to go beyond the SM. The newly discovered scalar sector is the most appealing for such extensions.

Type II seesaw mechanism [6–9] can explain the non-zero mass of neutrinos and predict new scalar particles by extending the Higgs sector of the SM with a scalar triplet. The addition of a scalar triplet can predict new scalar particles, some of which are at the electroweak scale, so they can be detected at the LHC [10–13].

In this thesis, a variant of this extension, named Doublet Triplet Higgs Model (DTHM), is studied: A hypercharge $Y = 2$ scalar triplet, Δ, supplementing the SM scalar doublet H. The doublet-triplet scalar sector is driven by five couplings, which define various interactions of each scalar field. The electroweak symmetry breaking is defined by two vacuum expectation values, $\mathrm{v_d} \sim 246$ GeV and $\mathrm{v_t}$[1], and leads to a rich phenomenology, including seven scalars: $H^{\pm\pm}$, $H^{\pm}$, A^0 (CP odd), H^0 (CP even), h^0 (CP even) [10, 11]. The SM Higgs is naturally included in those seven scalars and can be H^0 or h^0.

The analysis in the present thesis is mainly focusing on the phenomenology of the doubly-charged scalar bosons $H^{\pm\pm}$ in the parameter space where the dominant decay channel is $H^{\pm\pm} \rightarrow W^{\pm}W^{\pm}$ and the coupling to leptons is disfavored. The doubly charged Higgs bosons can be produced in pairs and decay to four W bosons as depicted in Figure 1.1. This analysis also explores the associate production scenario, with all new bosons having very close masses. The dominant production mode of this associate production is $pp \rightarrow H^{\pm\pm}H^{\mp}$, and the main decay channel is $H^{\pm\pm} \rightarrow W^{\pm}W^{\pm}$, $H^{\pm} \rightarrow W^{\pm}Z$.

Extensive searches for leptonic decays have been performed at various experiments [14–19], excluding doubly charged $H^{\pm\pm}$ bosons with masses up to about 870 GeV. The CMS Collaboration published results for the $H^{\pm\pm} \rightarrow W^{\pm}W^{\pm}$ decay mode in the context of single $H^{\pm\pm}$ production through vector-boson fusion with $\mathrm{v_t}$ values of a few tens of GeV, for a model with two Higgs triplets [20–22].

A direct search for $H^{\pm\pm}$ pair production with decays to $W^{\pm}W^{\pm}$ pairs has been performed on a smaller data set with 36.1 fb^{-1} by the ATLAS Collaboration [23], validating the principle of such an approach. To improve the results published with the 36.1 fb^{-1} analysis [23] with the 220 GeV observed lower limit on the mass of doubly charged Higgs decaying to $W^{\pm}W^{\pm}$, the present thesis extends the dataset to 139.0 fb^{-1} and refines the search approach. In addition, the production of a $H^{\pm\pm}$ boson in association with a $H^{\pm}$ boson is included, allowing to search for doubly- and singly-charged Higgs bosons in a yet unexplored parameter space of the considered model.

[1] $\mathrm{v_t}$ is constrained by electroweak precision measurements to be restricted to lower than 1.6 GeV. In the GM model [52], the v.e.v is not constrained by the same reason.

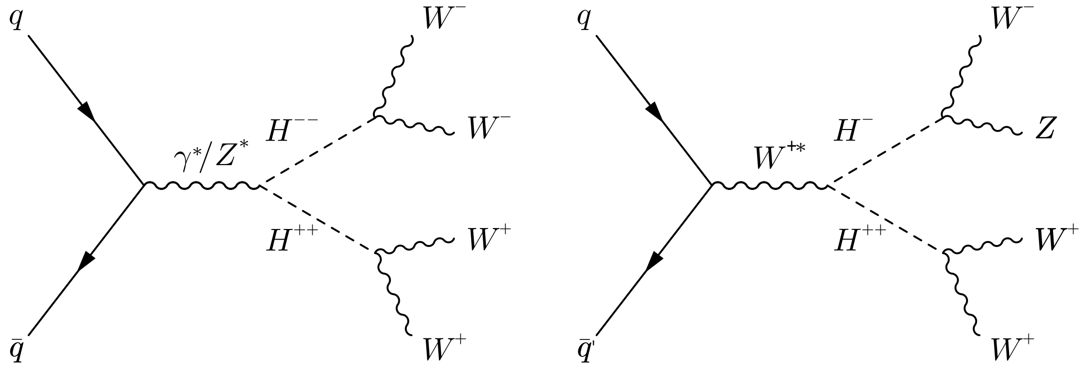

(a) pair-production (b) associate-production

Figure 1.1: The dominant production modes of doubly charged Higgs bosons in the DTHM: pair-production (left) and associate-production (right). The decays to bosons, dominating the width in the present model, are illustrated.

The present thesis starts with a description of the SM theory and the DTHM in Chapter 2. An overview of the LHC and ATLAS experiment is described in Chapter 3. Chapter 4 introduces the experimental setup of physics object. The event selection, particle identification and kinematic variables used in the thesis are described in Chapter 6. The samples, background estimation and final signal region optimizations are presented in Chapter 5, Chapter 7 and Chapter 8 , respectively. The experimental and theoretical uncertainties are presented in Chapter 9. The results, including the statistical combination of the analysis channels and the constraints to the parameter space of the analysis, are shown in Chapter 10, followed by final conclusions in Chapter 11.

2 Theory

Contents

2.1 The Standard Model

Although there are still many unsolved mysteries in particle physics, the Standard Model (SM) [24–27] is still the most successful theory describing three fundamental forces of elementary particles in our universe. Many predictions that are later confirmed by experiments, such as the observation of the top quark[28], tau neutrino[29], and the Higgs boson[1, 2] have made the Standard Model successful.

The SM is a Quantum field theory (QFT) [30, 31], which provides the fundamental mathematical framework to modern particle physics. Quantum field theory development began with the study of electromagnetic fields in QED, which can help physicists study the elementary particles at very small scales (quantum-mechanical) but very large energies (relativistic). Gauge theory is found essential in explaining the dynamics in QED which is based on an abelian group U(1). Yang-Mills theory [32] extended the gauge theory for abelian groups to nonabelian groups to explain strong interactions. In the 1960s, after recognizing spontaneous symmetry breaking, theorists combined the electromagnetic and weak interactions[33] and adopted the Brout–Englert–Higgs (BEH) mechanism [34–36] to break the gauge symmetry of the electroweak interaction. In 1973, the discovery of asymptotic freedom validated the Quantum chromodynamics (QCD).

The Standard Model not only incorporated all that was known about subatomic particles but also predicted the existence of additional particles. The discovery of W and Z bosons [53] in 1983 and the discovery of the Higgs boson [1, 2] in 2012 demonstrated huge success of the Standard Model.

Lagrangian and mathematics

In QFT, the Lagrangian formalism is used to model the behavior of a system. The essential components are quantum fields. Elementary particles are treated as the excitation of quantum fields, while interactions between particles are described by their corresponding quantum fields' interaction terms in the Lagrangian. With the principle of least action, the Euler–Lagrange Eq. (2.1) can be derived to describe the motion of a system[1].

$$\partial_\mu \left(\frac{\partial \mathcal{L}}{\partial \left(\partial_\mu \phi \right)} \right) - \frac{\partial \mathcal{L}}{\partial \phi} = 0 \tag{2.1}$$

With the statements from Noether's theorem that if a system is under a differentiable symmetry, there must be a corresponding conservation law. As a typical example for QFT, Lorentz invariance requires the Lagrangian to be consistent due to space-time symmetry (relativistic), denoted SO(1,3) in group-language. The SM includes three fundamental forces and can be represented as a gauge group $\mathrm{SU}(3)_C \otimes \mathrm{SU}(2)_L \otimes \mathrm{U}(1)_Y$. This gauge group includes strong interactions ($\mathrm{SU}(3)_C$) and electroweak interactions ($\mathrm{SU}(2)_L \otimes \mathrm{U}(1)_Y$). Here C stands for color charge, L refers to left-handed fields, and Y refers to the weak hypercharge.

2.1.1 Elementary particles

Elementary particles are subatomic particles with no substructure. In the SM, the elementary particles are classified into fermions and bosons, according to their spins.

Fermions carry half-integer spin and obey the Fermi–Dirac statistics. They can be split into two categories: leptons and quarks. Leptons category contains massive -1 charged leptons (electron, muon, tau) and massless neutral leptons (electron neutrino, muon neutrino, tau neutrino). Leptons are colorless and can interact with other fermions via electromagnetic (only massive leptons) and weak forces. Quarks category contains six colored fermions, can be further separated into 2/3 charged quarks (up, charm, top) and -1/3 charged quarks (down, strange, bottom). Besides electromagnetic and weak forces, quarks can also interact with other particles via strong forces. All fermions have their corresponding anti-fermions. Anti-fermion has the exact same properties as its corresponding fermion but only the opposite charge. The SM groups those four types of fermions (massive leptons, neutrinos, 2/3 charged quarks, -1/3 charged quarks) into three generations [54, 55].

Bosons carry integer spin and obey the Bose-Einstein statistics, which can also be further split into two categories: gauge bosons and scalar bosons. Gauge bosons are also called force carriers with spin = 1. The gauge bosons category includes photon for electromagnetic interaction, $W^\pm$ and Z for weak interaction, and gluon for the strong interaction. The scalar boson is a boson whose spin equals zero. There is only one elementary scalar boson in the SM: the Higgs boson. Unlike gauge bosons, the Higgs boson does not carry any charges but gives all other elementary particles mass from the Higgs mechanism.

The basic properties of the elementary particles are summarized in Figure 2.1.

[1] This is valid for both classical and quantum systems.

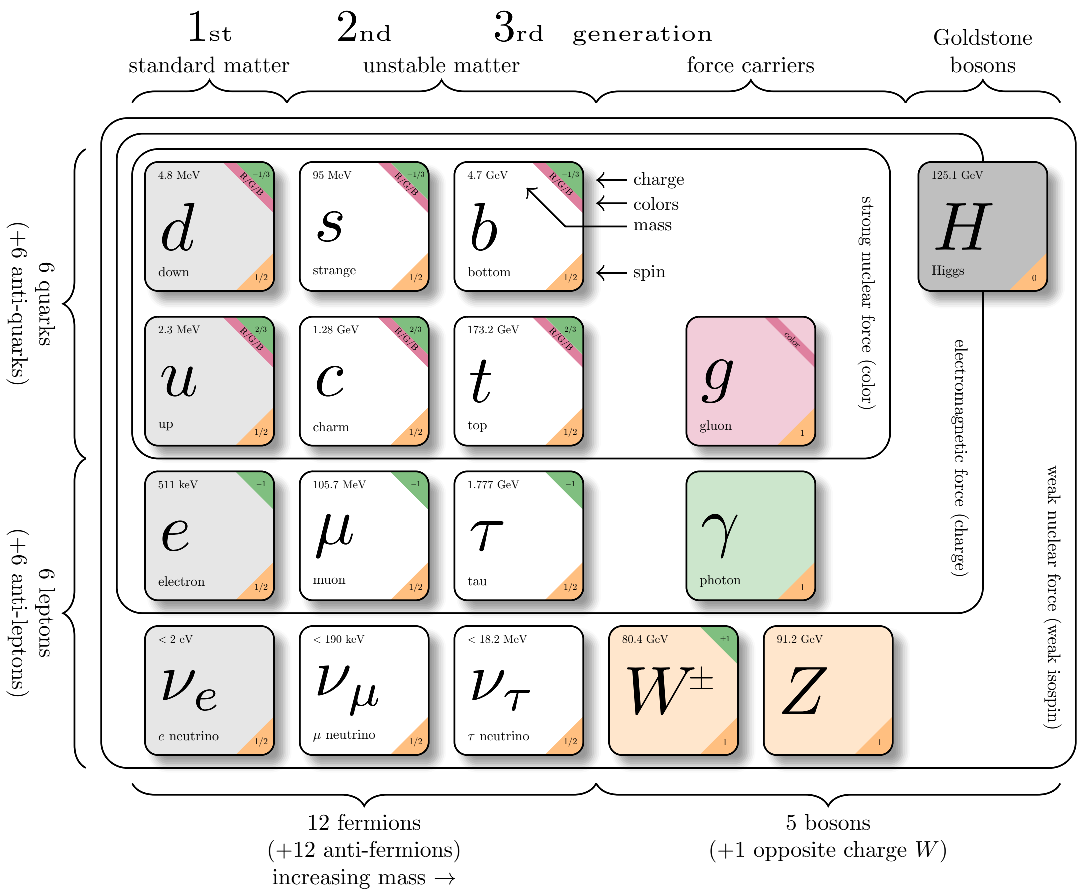

Figure 2.1: SM Properties summary of elementary particles, divided into fermions, gauge bosons, and the Higgs boson. The mass, charge, spin, and name of the particles are given in brackets around each particle. The three fundamental forces, along with the involved particles and three generations of fermions, are pointed out. The force in the larger rectangle also affects the fermions in the smaller rectangle. Taken from Ref. [56]

2.1.2 Quantum electrodynamics

The theory of Quantum electrodynamics (QED) [30, 57–59] describes electromagnetic interaction between charged fermions and photons. In the present thesis, the natural unit are applied to all equations.

$$\begin{aligned}\mathcal{L}_{\text{QED}} &= \mathcal{L}_{\text{Dirac}} + \mathcal{L}_{\text{Maxwell}} + \mathcal{L}_{\text{Int}} \\ &= \bar{\psi}[i\gamma^{\mu}\partial_{\mu} - m]\psi - \frac{1}{4}F^{\mu\nu}F_{\mu\nu} - e\bar{\psi}\gamma^{\mu}A_{\mu}\psi.\end{aligned} \tag{2.2}$$

The Lagrangian of quantum electrodynamics (QED) is constructed from three terms:
i) Dirac Lagrangian (Eq. (2.3) [2]) describes the motion of free fermions with mass m,

$$\begin{aligned}\mathcal{L}_{Dirac} &= \bar{\psi}\left(i\gamma^{\mu}\partial_{\mu} - m\right)\psi \\ &\rightarrow (i\gamma^{\mu}\partial_{\mu} - m)\psi = 0 \quad \text{(Dirac equation).}\end{aligned} \tag{2.3}$$

where ψ is the fermion field, ∂_{μ} is the partial derivative in four dimensions, and γ^{μ} are gamma matrices [60] that describe the behavior of the spin of the fermion field.

ii) The Lagrangian of electromagnetic fields (Eq. (2.4)) describes the kinematics of the electromagnetic field,

$$\begin{aligned}\mathcal{L}_{Maxwell} &= -\frac{1}{4}F_{\mu\nu}F^{\mu\nu} = -\frac{1}{4}(\partial_{\mu}A_{\nu} - \partial_{\nu}A_{\mu})^2 \\ &\rightarrow \partial^{\mu}F_{\mu\nu} = \partial_{\mu}^{2}A_{\nu} - \partial_{\nu}\partial_{\mu}A_{\mu} = 0 \qquad \text{(Maxwell equations).}\end{aligned} \tag{2.4}$$

Here $F^{\mu\nu} = \partial_{\mu}A_{\nu} - \partial_{\nu}A_{\mu}$ is the field strength tensor, while A_{μ} is a gauge vector boson field(the photon field).

Before introducing the final term, it is necessary to consider the U(1) gauge symmetry from the fact that the Lagrangian of QED need to be constructed under the rotation of electromagnetic phase (Eq. (2.5)),

$$\psi \xrightarrow{U(1)} \psi^{'} = \exp(i\alpha(x))\psi,\ \partial_{\mu}\psi \xrightarrow{U(1)} \partial_{\mu}\psi^{'} = \exp(i\alpha(x))(\partial_{\mu} + i\partial_{\mu}\alpha(x))\psi. \tag{2.5}$$

However, the second term breaks the U(1) gauge symmetry due to the derivative operator, which does not transform covariantly under a local gauge transformation. In order to satisfy the U(1) gauge symmetry, it is necessary to replace the derivative operator ∂_{μ} with a covariant derivative operator D_{μ}, as follows (Eq. (2.6)):

$$D_{\mu} = \partial_{\mu} - ieA_{\mu}(x)\ ,\ A_{\mu} \xrightarrow{U(1)} A_{\mu}^{'} \rightarrow A_{\mu} - \frac{1}{e}\partial_{\mu}\alpha(x) \tag{2.6}$$

[2] This equation is not in its final form with the covariant derivative.

The $\mathcal{L}_{Maxwell}$ keeps unchanged under this transformation. Thus, a gauge-invariant Lagrangian for charged fermions and photon can be written as Eq. (2.7),

$$\mathcal{L}_{\text{QED}} = \bar{\psi}(i\gamma^{\mu}D_{\mu} - m)\psi - \frac{1}{4}F_{\mu\nu}F^{\mu\nu}. \tag{2.7}$$

iii) The interaction term Eq. (2.8) can be simply derived by putting Eq. (2.6) into Eq. (2.7),

$$\mathcal{L}_{\text{Int}} = -e\bar{\psi}\gamma^{\mu}A_{\mu}\psi. \tag{2.8}$$

This term describes the coupling of electromagnetic interaction, which also can be illustrated in Feynman diagram (Vertex E in Figure 2.2).

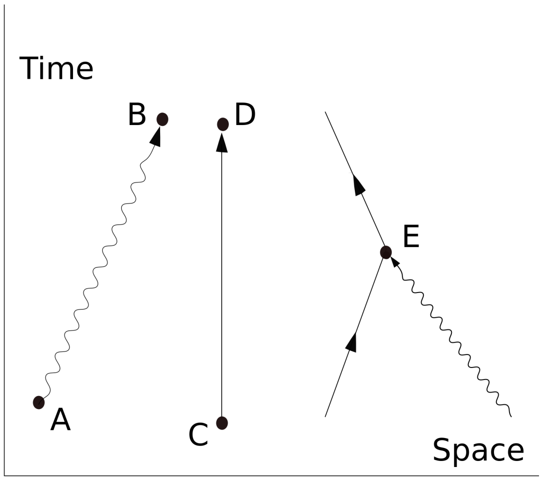

Figure 2.2: The key components of Feynman's presentation of QED (From left to right): i) A photon goes from one place and time to another place and time. ii) An electron goes from one place and time to another place and time. iii) An electron emits or absorbs a photon at a certain place and time. Taken from Ref. [61].

2.1.3 The Yang-Mills Theory

Quantum electrodynamics (QED) defined in Section 2.1.2 illustrates a simple correspondence between gauge invariance and interaction. In fact, all interactions in the SM are described by gauge theories [32, 62]. This section will discuss the SU(2) symmetry which is critical for electroweak interaction and SU(3) symmetry which is the base of the in strong interaction in the SM.

SU(2) Symmetry

Starting with a doublet of Dirac field (Eq. (2.9)) and its transformation under SU(2) symmetry,

$$\psi = \begin{pmatrix} \psi_1 \\ \psi_2 \end{pmatrix}, \ \psi \to \psi' = \exp(i\alpha^i \frac{\sigma^i}{2})\psi. \tag{2.9}$$

Here σ^i are Pauli matrices[63]. And the corresponding Lagrangian is written as

$$\mathcal{L}_{Dirac} = \bar{\psi}(i\gamma^\mu \partial_\mu)\psi, \tag{2.10}$$

where ψ is the fermion field, ∂_μ is the partial derivative in four dimensions, and γ^μ are gamma matrices [60] that describe the behavior of the spin of the fermion field.

The mass term is neglected here because it breaks the gauge invariance. Similar to what happened in Eq. (2.5), the Lagrangian (Eq. (2.10)) can not satisfy the gauge-invariant requirement. In order to fix this, the Yang-Mills Theory introduced the covariant derivative (Eq. (2.11)),

$$D_\mu = \partial_\mu - igA^i_\mu \frac{\sigma^i}{2}. \tag{2.11}$$

with three vector boson fields A^i and a coupling constant g (which is analogous to the electron charge in the QED case).

Thus the Lagrangian can be re-written as Eq. (2.12), which is the famous Yang-Mills Lagrangian,

$$\begin{aligned} \mathcal{L}_{Yang-Mills} &= \bar{\psi}(i\gamma^\mu D_\mu)\psi - \frac{1}{4}F^i_{\mu\nu}F^{\mu\nu}_i \\ &= \bar{\psi}[i\gamma^\mu(\partial_\mu - igA^i_\mu \frac{\sigma^i}{2})]\psi - \frac{1}{4}F^i_{\mu\nu}F^{\mu\nu}_i, \end{aligned} \tag{2.12}$$

where the field strength tensor is defined as $F^i_{\mu\nu} = \partial_\mu A^i_\nu - \partial_\nu A^i_\mu + g\epsilon^{ijk}A^j_\mu A^k_\mu$ and ϵ^{ijk} the Levi-Civita symbol to describe the relations between different vector boson fields.

SU(3) Symmetry

Similar to the discussion for SU(2) symmetry above, for SU(3) symmetry,

$$\mathcal{L}_{Yang-Mills} = \bar{\psi}\left(i\gamma^\mu D_\mu - m\right)\psi - \frac{1}{4}G^{\mu\nu}_a G^a_{\mu\nu}, \tag{2.13}$$

where $G^a_{\mu\nu}$ is the field strength tensor of the fields G^a_μ ($a = 1, \ldots, 8$),

$$G^a_{\mu\nu} = \partial_\mu G^a_\nu - \partial_\nu G^a_\mu + g_S f^{abc} G^b_\mu G^c_\nu. \tag{2.14}$$

In Eq. (2.14) g_S is the coupling constant, and f^{abc} are the structure constants of the SU(3) group. The covariant derivative D_μ is defined as

$$D_\mu = \partial_\mu - ig_S \frac{\lambda_a}{2} G^a_\mu, \tag{2.15}$$

where λ_a denotes the a^{th} Gell-Mann matrix [64].

2.1.4 The electroweak interaction

Electroweak interaction is the unification of electromagnetic interaction and weak interaction under the $SU(2)_L \otimes U(1)_Y$ symmetry group.

The weak interaction is carried by three vector bosons: two charged $W^{\pm}$ bosons and one neutral boson Z. There are two types of weak interactions: i) *charged current*: the exchange of a $W^{\pm}$ boson, which modifies both the fermions' flavor and electric charge. ii) *neutral current*: the exchange of a Z boson, which leaves the flavor unchanged. The behavior of particles in weak interactions is described with an additional quantum number called weak isospin, denote as I. One characteristic of the weak interaction is that $W^{\pm}$ bosons only interact with left-handed[3] fermions (right-handed anti-fermions), due to the observed parity violation [65].

Left-handed (Right-handed anti-fermions) fermions have weak isospin of $I = 1/2$, and the third component of the weak isospin I_3 can be $\pm 1/2$. As a supplement to elementary particles classification described in section 2.1.1, fermions can be separated into two types: $I_3 = -1/2$, down-type: Charged leptons (e^-, μ^-, τ^-) and -1/3 charged quarks (down, strange, bottom); $I_3 = +1/2$, up-type: Neutrinos: (ν_e, ν_μ, ν_τ) and 2/3 charged quarks (up, charm, top). Right-handed anti-fermions have opposite weak isospin. The right-handed (left-handed anti-fermions) have zero weak isospin and do not participate in the weak interaction.

Because in the SM SU(2) bosons only couple to left-handed fermions, the SU(2) symmetry group is denoted as $SU(2)_L$. The hypercharge Y corresponding to the gauge symmetry U(1) is defined in Eq. (2.16) [66, 67], where Q is the electric charge, and I_3 is the third component of the weak isospin,

$$Y = 2(Q - I_3). \tag{2.16}$$

With the Yang-Mills theory discussed in section 2.1.3, the electroweak Lagrangian under $SU(2)_L \otimes U(1)_Y$ is formed in Eq. (2.17),

$$\mathcal{L}_{\rm EW} = \bar{\psi}_{\rm L} i\gamma^\mu D^{\rm L}_\mu \psi_{\rm L} + \bar{\psi}_{\rm R} i\gamma^\mu D^{\rm R}_\mu \psi_{\rm R} - \frac{1}{4} W^{\mu\nu}_a W^a_{\mu\nu} - \frac{1}{4} B^{\mu\nu} B_{\mu\nu}. \tag{2.17}$$

The terms about fermions field are defined for left-hand and right-hand fermions separately. The left-handed fermion field is a doublet, e.g. $\psi_L = (\nu_{eL}, e^-_L)^T$ for first-generation lepton and $\psi_L = (u_L, d_L)^T$ for first-generation quark. The right-handed fermion field contains two singlets for up and down-type fermions, e.g. $\psi^{up}_R = 0$[4], $\psi^{down}_R = e_R$ or $\psi^{up}_R = u_R, \psi^{down}_R = d_R$. The covariant derivatives are defined in Eq. (2.18a) and Eq. (2.18b),

$$D^{\rm L}_\mu = \partial_\mu - i\frac{g}{2}\tau_a W^a_\mu - i\frac{g'}{2} Y B_\mu, \tag{2.18a}$$

$$D^{\rm R}_\mu = \partial_\mu - i\frac{g'}{2} Y B_\mu,. \tag{2.18b}$$

[3] Left-handed/right-handed is is classified by particles' chirality [63].
[4] There is no right-hand neutrino in the Standard Model.

where W_μ^a $(a = 1, 2, 3)$ are three massless vector gauge fields for $SU(2)_L$ transformation and B_μ is the other one gauge field for the $U(1)_Y$ transformations. The field strength tensors are defined as $W_{\mu\nu}^a = \partial_\mu W_\nu^a - \partial_\nu W_\mu^a - g\epsilon^{abc} W_\mu^b W_\nu^c$ and $B_{\mu\nu} = \partial_\mu B_\nu - \partial_\nu B_\mu$, respectively. g and $g^{'}$ are two coupling constants of W_μ^a and B_μ fields. τ_a are Pauli matrices, and Y is the weak-hypercharge.

However, the W_μ^a $(a = 1, 2, 3)$ and B_μ gauge fields do not directly correspond to the observed gauge bosons: $W^\pm$, Z, and the photon A_μ. The weak mixing angle θ_w [25] is defined to describe the mixing between W_μ^3 and B_μ field to produce Z and photon field.

$$\cos\theta_w = \frac{g}{\sqrt{g^2 + g'^2}}. \tag{2.19}$$

The relation between W_μ^3, B_μ boson fields and the photon field A_μ, the Z boson field Z_μ is described in Eq. (2.20):

$$\begin{pmatrix} Z_\mu \\ A_\mu \end{pmatrix} = \begin{pmatrix} \cos\theta_w & -\sin\theta_w \\ \sin\theta_w & \cos\theta_w \end{pmatrix} \begin{pmatrix} W_\mu^3 \\ B_\mu \end{pmatrix} \tag{2.20}$$

The charged vector bosons $W^\pm$ are the charge eigenstates that can be rewritten with the W_μ^1 and W_μ^2 fields:

$$W_\mu^\pm = \frac{1}{\sqrt{2}} \left(W_\mu^1 \mp i W_\mu^2 \right). \tag{2.21}$$

The electroweak theory introduced in this section assumes that all particles are massless because the Lagrangian Eq. (2.17) can not satisfy the local gauge invariance if any mass terms are included. This is untrue since the $W^\pm$ and Z bosons are found to be massive with high precision in various HEP experiments [53, 68–76]. The BEH mechanism resolves this conflict between theory and experimental observation, which will be discussed in section 2.1.5.

CKM matrix and flavor changing decay

In the SM, there is a mismatch between the quantum states of quarks when they propagate freely and when they take part in the weak interactions. This can be represented in the SM that weak eigenstates (d') of the down-type quarks to up-type quarks are not the same as their mass eigenstates, which causes the mixing among quarks and can be described in Cabibbo–Kobayashi–Maskawa (CKM) matrix [77]:

$$\begin{bmatrix} d' \\ s' \\ b' \end{bmatrix} = \begin{bmatrix} V_{ud} & V_{us} & V_{ub} \\ V_{cd} & V_{cs} & V_{cb} \\ V_{td} & V_{ts} & V_{tb} \end{bmatrix} \begin{bmatrix} d \\ s \\ b \end{bmatrix}, \tag{2.22}$$

$$\begin{bmatrix} V_{ud} & V_{us} & V_{ub} \\ V_{cd} & V_{cs} & V_{cb} \\ V_{td} & V_{ts} & V_{tb} \end{bmatrix} = \begin{bmatrix} 0.97427 \pm 0.00015 & 0.22534 \pm 0.00065 & 0.00351^{+0.00015}_{-0.00014} \\ 0.22520 \pm 0.00065 & 0.97344 \pm 0.00016 & 0.0412^{+0.0011}_{-0.0005} \\ 0.00867^{+0.00029}_{-0.00031} & 0.0404^{+0.0011}_{-0.0005} & 0.999146^{+0.000021}_{-0.000046} \end{bmatrix} \tag{2.23}$$

where $|V_{ij}|^2$ is the probability that a quark of flavor i is observed in flavor j.

Among all quarks, B-quark plays an important role in particle physics. Firstly, almost all top quarks will decay into b quarks and virtual W boson (this W boson will further decay into lepton-neutrino pair or quarks.) in a very short time ($< 10^{-24}$s). Secondly, B-hadron has a mean lifetime $\sim 10^{-12}$s [77], which means it can move a few hundred micrometers from the position it was produced. Leptons and neutrinos category has a similar structure [78] as quark category. However, because neutrinos are massless in the SM, lepton only can decay into neutrino within the same generation and virtual W boson.

Lifetime for W boson and Top quark is quite small ($< 10^{-24}$s), which is not enough for them to decay outside of a proton's diameter (0.84087±0.00039 femtometer). Decay that happened in a short distance or short time is called prompt decay. In contrast, decay like b-hadron is named non-prompt decay. The concept of prompt/non-prompt is useful in physics analysis. More discussion in section 4.3.

2.1.5 The Brout–Englert–Higgs mechanism

The BEH mechanism is a fundamental component of SM that explains the mechanism for masses of gauge bosons. At certain very high temperatures (e.g. the beginning of the universe), the electroweak symmetry is unbroken, and all elementary particles are massless. However, symmetry breaks spontaneously at the critical temperature, and the $W^\pm$ and Z bosons gained the masses.

Firstly, the *Higgs field* is a left-handed doublet with weak isospin $I = \frac{1}{2}$, $I^3 = -\frac{1}{2}$ and weak hypercharge $Y = 1$:

$$\phi = \begin{pmatrix} \phi^+ \\ \phi^0 \end{pmatrix} = \frac{1}{\sqrt{2}} \begin{pmatrix} \phi_1 + i\phi_2 \\ \phi_3 + i\phi_4 \end{pmatrix} \tag{2.24}$$

The corresponding Lagrangian is

$$\mathcal{L} = (\partial_\mu \phi)(\partial^\mu \phi)^\dagger - V(\phi). \tag{2.25}$$

To satisfy the SU(2)$_L$ symmetry, the covariant derivatives from Eq. (2.18a) are applied,

$$\mathcal{L} = (D_\mu \phi)^\dagger (D^\mu \phi) - \mu^2 \phi^\dagger \phi - \lambda(\phi^\dagger \phi)^2 - \frac{1}{4} W_a^{\mu\nu} W_{\mu\nu}^a - \frac{1}{4} B^{\mu\nu} B_{\mu\nu}, \tag{2.26}$$

where the Higgs potential $V(\phi)$ is given by

$$V(\phi) = \mu^2 \phi^\dagger \phi + \lambda(\phi^\dagger \phi)^2 \quad \lambda > 0,\ \mu^2 < 0. \tag{2.27}$$

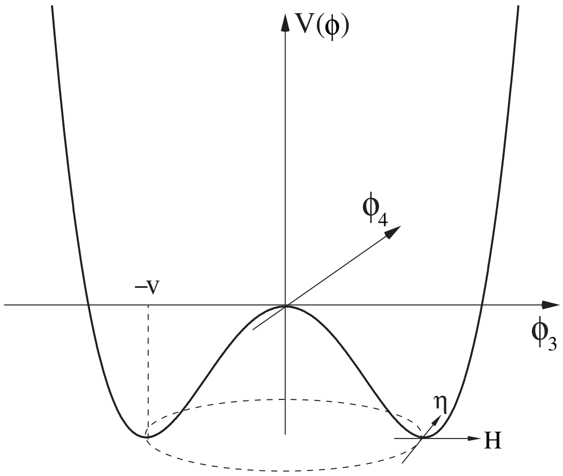

Figure 2.3: The Higgs potential from Eq. (2.27) projected in two dimensions, ϕ_3 and ϕ_4. The round line represents the circle of vacua. The Higgs field can be expanded around a chosen vacuum value with the new axes, H, and η. Taken from Ref. [79].

The Higgs potential plotted as a function of ϕ_3 and ϕ_4 is shown in Figure 2.3. The spontaneous symmetry breaking happens when the Higgs field assumes one specific vacuum state. One can pick a vacuum which has $\phi_1 = \phi_2 = \phi_4 = 0$ and $\phi_3 = \mathrm{v}$,

$$\phi_0 = \frac{1}{\sqrt{2}}\begin{pmatrix} 0 \\ \mathrm{v} + H \end{pmatrix} \tag{2.28}$$

This choice of vacuum breaks $SU(2)_L \otimes U(1)_Y$ symmetry. With the choice of $I = \frac{1}{2}$, $I^3 = -\frac{1}{2}$, $Y = 1$ and the Gell-Mann-Nishijima formula (Eq. (2.16)), the electric charge $Q = 0$, hence the $U(1)_{EM}$ symmetry is still valid, leaving the photon massless. By replacing the Higgs field in Eq. (2.26), the Lagrangian expanded around the vacuum is:

$$\begin{aligned} \mathcal{L}_{\text{Higgs}} =& \frac{1}{2}(\partial_\mu H)(\partial^\mu H) - \lambda \mathrm{v}^2 H^2 - \lambda \mathrm{v} H^3 - \frac{\lambda}{4} H^4 \\ &+ (\mathrm{v} + H)^2 \left(\frac{g^2}{4} W_\mu^+ W^{-\mu} + \frac{g^2}{8\cos^2\theta_W} Z_\mu Z^\mu \right). \end{aligned} \tag{2.29}$$

The masses of $W^\pm$ and Z gauge bosons, also the Higgs boson, can be obtained by expanding the Eq. (2.27).

$$m(W^\pm) = \frac{1}{2}\mathrm{v}g, \; m(Z) = \frac{\mathrm{v}g}{2\cos\theta_W} = \frac{m(W^\pm)}{\cos\theta_W}; \; m(H) = \sqrt{2\lambda}\mathrm{v}. \tag{2.30}$$

The vacuum expectation value (v.e.v.) of the Higgs field v is the only free dimensional parameter of the SM. The current best estimation is $\mathrm{v} \simeq 246\,\mathrm{GeV}$ [77]. However, λ is a free parameter hence the mass of the Higgs is not predicted by the SM. The ATLAS and CMS combined measurement [80] determines that the Higgs boson mass is $m(H) = 125.09 \pm 0.21(\text{stat}) \pm 0.11(\text{sys})$ GeV.

Yukawa couplings and masses of charged fermions

The BEH mechanism discussed above describes the way to generate masses of the gauge bosons. However, charged fermions are also observed to be massive. These mass terms of fermions are like $-m\bar{\psi}\psi = -m[\bar{\psi}_L\psi_R + \bar{\psi}_R\psi_L]$, which can not satisfy the symmetry of the SM, e.g., the $SU(2)_L$. The Higgs boson can also solve this problem through the so-called *Yukawa coupling*,

$$\mathcal{L}_{\text{Yukawa}} = -\lambda_f\,[\bar{\psi}_L\phi\psi_R + \bar{\psi}_R\bar{\phi}\psi_L], \tag{2.31}$$

where λ_f is the coupling constant. Taking electron as an example: $\psi_L = (\nu, e)^T_L$, $\psi_R = e_R$ together with Eq. (2.28), the Eq. (2.31) can be written as:

$$\begin{aligned}
\mathcal{L}_{\text{electron-yukawa}} &= -\lambda_e\frac{1}{\sqrt{2}}[(\bar{\nu},\bar{e})_L\begin{pmatrix}0\\ \text{v}+H\end{pmatrix}e_R + \bar{e}_R(0,\text{v}+H)\begin{pmatrix}\nu\\ e\end{pmatrix}_L] \\
&= -\lambda_e\frac{\text{v}+H}{\sqrt{2}}[\bar{e}_Le_R + \bar{e}_Re_L] \\
&= -\lambda_e\frac{\text{v}+H}{\sqrt{2}}\bar{e}e \\
&= -\frac{\lambda_e\text{v}}{\sqrt{2}}\bar{e}e - \frac{\lambda_eH}{\sqrt{2}}\bar{e}e
\end{aligned} \tag{2.32}$$

The first term is for electron mass, while the second term is for electron-Higgs interaction. For each fermion that interacts with the Higgs field, an individual Yukawa term is added to the SM Lagrangian.

2.1.6 Quantum chromodynamics

Similar to the QED, which describes the interactions between charged fermions through exchanging photons, the Quantum Chromodynamics (QCD) [64, 67, 81–83] describes the interactions between quarks through exchanging gluons. Color charges are properties of quarks and gluons in the QCD. There are three different color charges, defined as red, green and blue. Gluons carry a superposition of colored and anti-colored charges, resulting in eight different states. In addition, since gluons are charged, they affect each other, unlike the photon that lacks an electric charge.

The minimal symmetry group sufficient for the QCD formula for all observed phenomena is SU(3). The Lagrangian of the QCD is defined in Eq. (2.13) as discussed in section 2.1.3.

QCD has two main properties:

- Color confinement: The strength of the strong interaction increases drastically with distance. Therefore, the color-charged particles (such as quarks and gluons) cannot be isolated. Quarks and gluons must be together to form colorless hadrons.

- Asymptotic freedom [84, 85]: In contrast to color confinement, the strength of the strong interaction decreases rapidly as the distance decreases. Hence at very short distances (or large energy scales) the running coupling of the strong interaction becomes small. In this situation, the perturbation theory is valid.

Parton Shower

Hadrons are composed of many point-like constituents called "partons". Partons were referred to as quarks and gluons with the development of the quark model and asymptotic freedom in QCD. The accelerated colored partons will emit gluons. The gluons themselves carry color charges and can therefore emit further radiation, leading to parton showers [86]. Parton shower is extensively simulated in the Monte Carlo event generator [87] to describe the process in the collider experiment.

Simulations in the Monte Carlo event generator need parton distribution function (PDF) [88], which is defined as the probability for finding a particle with a certain longitudinal momentum fraction x at resolution scale Q^2. Due to color confinement, parton densities cannot be calculated using perturbative QCD. Parton distribution functions are obtained by fitting observables from experimental data, or in lattice QCD.

2.2 Beyond the Standard Model

So far, the Standard Model (SM) describes well the observations of accelerator experiments. However, it is not the ultimate theory of particle physics.

Some features of the SM were added with ad hoc hypotheses. This approach makes the SM work successfully but also implies a lack of understanding of fundamental physics. As a brief summary of some ad hoc features, the SM contains a large number of parameters and parameter fine-tuning.

Furthermore, there are fundamental physical phenomena in nature that the Standard Model does not adequately explain: i) Gravity: The SM is incompatible with general relativity [37]. ii) Dark matter and dark energy: The SM does not provide a fundamental explanation. iii) Matter–antimatter asymmetry: The observed large imbalance in the amount of matter and anti-matter. In particular, there are only left-handed neutrinos and right-handed antineutrinos existed in the universe implies the CP symmetry is maximally violated, for which the Standard Model can not provide an explanation. iv) Neutrinos masses: Neutrinos are massless particles in the SM since no Yukawa coupling for neutrinos with the Higgs field. However, neutrino oscillation experiments have shown that neutrinos do have mass. There are also other problems and incompleteness of the SM. In this thesis, we will study an extension of the SM that address the problem of neutrino masses.

2.2.1 Massive neutrinos

The oscillation between electron neutrinos and muon neutrinos were first observed by Super-Kamiokande [89] and Sudbury Neutrino Observatories [90] experiments from the sun and high-energy cosmic rays interacting with earth's atmosphere. This oscillation is only possible when there is a mass difference between the neutrino mass eigenstates. Hence the neutrino has a non-zero mass. The SM did not provide any terms to explain neutrino masses. One possible way is to implement the 'Dirac' mass terms like what has been done for charged fermion (e.g. electron in Eq. (2.32)). However, this will require the right-handed neutrinos, which were not observed and only play the roles of giving neutrino mass.

Another way which can discard right-handed neutrinos was first hypothesised by Ettore Majorana in 1937 [91], is that neutrinos are their antiparticles. The Majorana neutrino can be defined as $\nu = \nu_L + \nu_L^C$, where $\nu_L^C = C\bar{\nu}_L^T$ denotes the charge conjugation. The mass term for Majorana neutrinos is then

$$\mathcal{L}_{\text{Majorana}} = \frac{1}{2} m_L (\bar{\nu}_L^C \nu_L + \bar{\nu}_L \nu_L^C), \tag{2.33}$$

An extension is required to have a new particle to couple to the neutrino. The Doublet Triplet Higgs Model (DTHM), which integrates the mechanism of neutrino mass generation, will be presented in more detail in the following and will be used as the benchmark model to interpret the experimental measurements reported in this thesis.

2.2.2 The Type-II see-saw mechanism

The seesaw mechanism is a generic model used to understand the relative sizes of observed neutrino masses. There is only one dimension-five operator which is relevant for neutrino masses, $\kappa l_L l_L H H$, where l_L and H stand for the $SU(2)_L$ leptonic and Higgs doublet, respectively [38]. The electroweak symmetry breaking (EWSB) leads the neutrino Majorana mass to $m_\nu \sim \kappa \mathrm{v}_0^2/\Lambda$, where v_0 is the vacuum expectation value (v.e.v) of Higgs about 246 GeV, κ is the dimensionless coupling and Λ is the mass scale. Tiny neutrino masses can be understood if Λ is much greater than v_0, which is the concept of "seesaw".

However, the dimension-five operator is just coming from the effective field theory. Thus it is crucial to understand the origin of the dimension-five operator. The Doublet Triplet Higgs Model (DTHM) [11] based on the Type-II seesaw mechanism [6–9] extends the SM by including an $SU(2)_L$ Higgs triplet field Δ which has hypercharge $Y = 2$. In this scenario, the neutrino mass is then become $m_\nu \sim Y_\nu v_t$ where Y_ν is the yukawa coupling and v_t is the v.e.v of the triplet Δ. The EWSB leads to a relation $\mathrm{v_t} \sim \mu \mathrm{v}_0^2/M_\Delta^2$ where μ is a dimensional parameter for doublet and triplet mixing and M_Δ^2 is the mass of triplet Δ. Tiny neutrino masses can be understood if M_Δ is much greater than v_0, which is the concept of "seesaw"

2.2.3 Doublet Triplet Higgs Model

The Lagrangian of the standard Higgs doublet and $SU(2)_L$ Higgs triplet Δ of DTHM is Eq. (2.34):

$$\mathcal{L} = (D_\mu H)^\dagger (D^\mu H) + Tr(D_\mu \Delta)^\dagger (D^\mu \Delta) - V(H, \Delta) + \mathcal{L}_{Yukawa} \tag{2.34}$$

where $H \sim (1,2,1)$, $\Delta \sim (1,3,2)$ under the SM gauge group, $SU(3) \times SU(2) \times U(1)$, and $V(H,\Delta)$ is given by Eq. (2.37):

$$V(H,\Delta) = -m_H^2 H^\dagger H + \frac{\lambda}{4}(H^\dagger H)^2 + m_\Delta^2 Tr(\Delta^\dagger \Delta) \tag{2.35}$$

$$+ [\mu(H^T i\sigma^2 \Delta^\dagger H) + h.c.] + \lambda_1 (H^\dagger H) Tr(\Delta^\dagger \Delta) + \lambda_2 (Tr \Delta^\dagger \Delta)^2 + \lambda_3 Tr \left(\Delta^\dagger \Delta\right)^2 \tag{2.36}$$

$$+ \lambda_4 H^\dagger \Delta \Delta^\dagger H. \tag{2.37}$$

The potential depends on five independent coupling parameters λ and λ_{1-4} and three mass parameters m_H^2, M_Δ^2, μ. The parameters μ and λ_{1-4} define the scalar sector couplings and therefore determine the Higgs bosons phenomenology after the electroweak symmetry breaking.

The Yukawa term to generate neutrino masses is given by

$$\mathcal{L}_{Yukawa} \supset -Y_\nu L^T C \otimes i\sigma^2 \Delta L \tag{2.38}$$

where L denotes the SU(2)$_L$ lepton doublets and Y_ν denotes the neutrino Yukawa couplings, C denotes the charge conjugation operator, and σ^2 denotes the second Pauli matrix.

Electroweak Symmetry Breaking (EWSB) can be achieved if the neutral components of H and Δ acquire vacuum expectation values of $\mathrm{v_d}$ and $\mathrm{v_t}$, respectively, at the minimum of the potential. The mass of doublet and triplet can be read as Eq. (2.40):

$$m_H = \frac{\lambda \mathrm{v_d}^2}{4} - \sqrt{2}\mu \mathrm{v_t} + \frac{\lambda_1 + \lambda_4}{2}\mathrm{v_t^2} \tag{2.39}$$

$$M_\Delta = \frac{2\mu \mathrm{v_d}^2 - \sqrt{2}(\lambda_1 + \lambda_4)\mathrm{v_d}^2 \mathrm{v_t} - 2\sqrt{2}(\lambda_2 + \lambda_3)\mathrm{v_t^3}}{2\sqrt{2}\mathrm{v_t}} \tag{2.40}$$

This EWSB also causes mixing between these fields and results in seven scalar bosons: $H^{\pm\pm}$, $H^\pm$, A^0 (CP odd), H^0 (CP even), h^0 (CP even). The masses of the charged Higgses are given by,

$$m_{H^{\pm\pm}} = \frac{\sqrt{2}\mu \mathrm{v_d}^2 - \lambda_4 \mathrm{v_d}^2 \mathrm{v_t} - 2\lambda_3 \mathrm{v_t}^3}{2\mathrm{v_t}} \tag{2.41}$$

$$m_{H^\pm} = \frac{(\mathrm{v_d}^2 + \mathrm{v_t}^2)[2\sqrt{2}\mu - \lambda_4 \mathrm{v_t}]}{4\mathrm{v_t}} \tag{2.42}$$

The mass matrices for the neutral scalar and pseudo-scalar Higgses are given by,

$$\mathcal{M}^2_{\mathrm{CP_{even}}} = \begin{pmatrix} \frac{\lambda \mathrm{v_d}^2}{2} & \mathrm{v_d}(-\sqrt{2}\mu + (\lambda_1 + \lambda_4)\mathrm{v_t} \\ \mathrm{v_d}(-\sqrt{2}\mu + (\lambda_1 + \lambda_4)\mathrm{v_t} & \frac{\sqrt{2}\mu \mathrm{v_d}^2 + 4(\lambda_2 + \lambda_3)\mathrm{v_t}^3)}{2\mathrm{v_t}} \end{pmatrix} \tag{2.43}$$

$$\mathcal{M}^2_{\mathrm{CP_{odd}}} = \begin{pmatrix} 2\mathrm{v_t} & -\mathrm{v_d} \\ -\mathrm{v_d} & \mathrm{v_d}^2/2\mathrm{v_t} \end{pmatrix} \tag{2.44}$$

Diagonalizing these matrices gives the mass eigenstates. The mass eigenstates for the CP_{even} mass states is found to be,

$$\begin{pmatrix} h^0 \\ H^0 \end{pmatrix} = \begin{pmatrix} \cos\alpha & \sin\alpha \\ -\sin\alpha & \cos\alpha \end{pmatrix} \begin{pmatrix} h \\ \xi^0 \end{pmatrix}; \quad \begin{pmatrix} A^0 \\ G^0 \end{pmatrix} = \begin{pmatrix} -\sin\beta & \cos\beta \\ \cos\beta & \sin\beta \end{pmatrix} \begin{pmatrix} Z_1 \\ Z_2 \end{pmatrix}; \tag{2.45}$$

where h and ξ^0 are the real part of doublet and triplet fields shifted by their v.e.v value while Z_1 and Z_2 are imaginary part, respectively. G^0 is the massless Goldstone boson, while A^0 is massive. α and β correspond to the mixing (rotation) angles for the CP_{even} and CP_{odd} matrices, respectively. If $\alpha \to 0$, the mixing between h^0 and H^0 is negligible. In such a case, h^0 can be assumed to be the SM Higgs.

Parameter constraint of Doublet Triplet Higgs Model

There are various constraints in this DTHM model (section 3 in Ref. [11]). One of them is the constraints from electroweak precision measurements, which can directly affect the decay branch ratio for this analysis. In the SM, there is an extra symmetry called custodial symmetry [92], which can be represented as the SM Higgs potential is only a function of $H^\dagger H$. This ensures that $\rho \equiv \frac{M_W^2}{M_Z^2 \cos^2\theta_W}$ should be equal to 1 at tree level, which is also verified experimentally with a very good precision: $\rho_0 = 1.0004 \pm 0.00048$ [93].

As discussed in section 2.1.5, $W^\pm$ and Z gain their masses from spontaneous symmetry breaking. In the present DTHM, after EWSB, $W^\pm$ and Z masses are:

$$m(W^\pm)^2 = \frac{1}{4} g^2 ({\rm v_d}^2 + 2{\rm v_t^2}), \; m(Z)^2 = \frac{1}{4}(g^2 + g'^2)({\rm v_d}^2 + 4{\rm v_t}^2) = \frac{g^2({\rm v_d}^2 + 4{\rm v_t}^2)}{4\cos\theta_W^2}. \tag{2.46}$$

Hence the modified ρ for the DTHM at tree level is given by,

$$\rho = \frac{{\rm v_d}^2 + 2{\rm v_t^2}}{{\rm v_d}^2 + 4{\rm v_t^2}},$$

With the relation $\sqrt{{\rm v_d}^2 + {\rm v_t^2}} = 246\,\text{GeV}$, the upper bound of $\rm v_t$ is 1.6 GeV at 2σ level dedicated by the measured ρ_0 value. The smallness of $\rm v_t$ is one of the main features of this model.

2.2.4 Searches at the LHC

The present thesis will investigate two scenarios which are leading production channels [10] at the Large Hadron Collider (LHC). The single production $pp \to W^{\pm *}W^{\pm *} \to H^{\pm\pm}$ mode proceeds via vector-boson fusion and is proportional to $\rm v_t$, hence negligible in DTHM. Associate-production ($pp \to W^{\pm *} \to H^{\pm\pm}W^{\mp *}$) with W is also possible and is suppressed for the exact same reason.

A Pair-production: $pp \to \gamma^*, Z^* \to H^{\pm\pm}H^{\mp\mp}$ (see Figure 1.1, left). The mass of the doubly-charged Higgs particles are assumed to be as the order of a few hundred GeV, so that they are accessible at the LHC. All other BSM Higgs are heavier than doubly charged Higgs by at least a few hundred GeV. The associate-production is suppressed; only the pair-production is considered in this scenario.

B Associate-production: $pp \to W^{*+} \to H^{\pm\pm}H^{\mp}$ (see Figure 1.1, right). The doubly and singly charged bosons are quasi-degenerate in mass: $m_{H^{\pm}} \approx m_{H^{\pm\pm}}$ Only the associate-production is considered in this scenario. Pair-production cross-section will not be suppressed in this mass-configuration. The decays $H^{\pm\pm} \to W^{\pm}W^{\pm}$ are still dominant. Only the bosonic decays of the single charged bosons are considered $H^{\pm} \to W^{\pm}Z$ (BR∼60%). The $H^{\pm} \to tb$ and $H^{\pm} \to WH$, though leading to striking signatures, are subdominant and not considered in the present analysis. The contribution has been estimated with truth information. Other decay modes are mainly suppressed by b-veto. In addition, the effect on the excluded charged Higgs mass is negligible.

The production cross-section of $pp \to W^{\pm *}W^{\pm *} \to H^{\pm\pm}$ via vector-boson fusion is proportional to v_t, hence negligible in DTHM. Associate-production ($pp \to W^{\pm *} \to H^{\pm\pm}W^{\mp *}$) with W is also possible and is suppressed for the exact same reason. The doubly charged Higgs bosons can decay in two channels: $H^{\pm\pm} \to \ell^{\pm}\ell^{\pm}$ and $H^{\pm\pm} \to W^{\pm}W^{\pm}$; the two modes' branching ratios depend on v_t. Leptonic final states have been analyzed at various experiments [14–19], excluding doubly charged $H^{\pm\pm}$ bosons with masses up to about 870 GeV, with $v_t \simeq 0$, e.g. 0.001 GeV [19]. The analysis presented in this thesis sets $v_t = 0.1$ GeV in DTHM, hence for any given mass of $H^{\pm\pm}$ the WW mode is favored while the $\ell^{\pm}\ell^{\pm}$ is negligible [10].

For the $H^{\pm\pm}$ pair-production mode, the mixing between the CP-even scalars is taken to be 10^{-4} and the remaining five couplings in the potential are adjusted to obtain a given $H^{\pm\pm}$ boson mass hypothesis while requiring h_0 to have a mass of 125 GeV. Results from previous analysis [23] on this mode has excluded the mass range $m_{H^{\pm\pm}} < 220$ GeV.

Similar settings are also used for the associate-production mode. The cross-section calculation for both the pair production of $H^{\pm\pm}$ bosons and the associated production of $H^{\pm\pm}$ and $H^{\pm}$ bosons are performed for on-shell W and Z bosons, and therefore only the region $m_{H^{\pm\pm}} > 200$ GeV is considered in the present analysis. More details about decay and experimental signatures will be discussed in section 6.

3 The LHC and the ATLAS Experiment

Contents

3.1 The Large Hadron Collider

The Large Hadron Collider (LHC) [39] is the world's largest and the highest-energy machine for protons and heavy ions collisions, which is located at CERN (*Conseil Européen Pour la Recherche Nucléaire*) beneath the boundary of France and Switzerland.

The LHC is located in a 27 km long tunnel, approximately 100 m under ground. The collider tunnel contains two adjacent parallel beam pipes contained in one large cryogenic cylinder. Protons are accelerated sequentially by the accelerator complex at CERN and injected into the LHC:
i) Linac2[1] which accelerates ionized hydrogen gas (protons) to 50 MeV,
ii) Proton Synchrotron Booster (PSB) which accelerates the protons to 1.4 GeV,
iii) Proton Synchrotron (PS) which accelerates the protons to 26 GeV,
iv) Super Proton Synchrotron Booster (SPS), which accelerates the protons to 450 GeV,
v) LHC for last acceleration to target energy (Table 3.1). Finally, the proton-beams collide at four main LHC experiments (ALICE, ATLAS, CMS, and LHCb) around the LHC. The injection chain of protons and locations of the four experiments are shown in Figure 3.1.

Besides the energy, luminosity is essential. During proton-proton (pp) collisions, there are 40 million bunches collisions per second, and each bunch contains about 10^{11} protons.

[1] Linac2 has been replaced by linac4 ready for runs in the future. It goes to 160 MeV making PSBs job easier.

Parameters	2015 - 2018	Design
Beam Energy [TeV]	6.5	7
Integrated Luminosity [fb^{-1}]	156	300 (The design goal with 7 years running.)
Max Peak Luminosity [$10^{34}\text{cm}^{-2}\,\text{s}^{-1}$]	2.14	1
Bunch Spacing [ns]	25/50	25

Table 3.1: Status of the LHC as of 2019 and its running parameters. Taken from Ref. [94]. In early 2015 the bunch spacing was set as 50 ns to re-establish operation at high stored energies [95].

Instantaneous luminosity [97] is the ratio of the number of events detected at a certain time (in a unit of 1 second) to the interaction cross-section (in a unit of 1 cm^2). In LHC, the luminosity depends on many parameters of the LHC and can be summarized as

$$\mathcal{L} = \frac{N_1 N_2 f N_b}{4\pi\sigma_x\sigma_y}, \tag{3.1}$$

where N_b is the number of colliding bunches in one beam, N_1 and N_2 are the number of protons of two colliding bunches, f is the revolution frequency, σ_x and σ_y are the bunch lengths perpendicular to the beam direction. The designed value of luminosity in the LHC is $10^{34}\text{cm}^{-2}\,\text{s}^{-1}$.

3.2 The ATLAS experiment

The ATLAS (A Toroidal LHC ApparatuS) [40] detector is one of the two[2] general-purpose detectors at the LHC. As shown in Figure 3.2, the ATLAS detector is built in layers of sub-detectors to capture all detectable particles produced in pp collisions. Starting from the LHC beam pipe, the sub-detectors are the Inner Detector (ID), the Liquid Argon (LAr) calorimeter, the Tile calorimeter, and the Muon Spectrometer (MS). The general performance goals of the ATLAS detector are given in Table 3.2.

Table 3.2: Resolution goals and pseudorapidity coverage of the sub-systems of the ATLAS detector. Numbers for energy and transverse momentum are in units of GeV. Taken from Table 1.1 in Ref. [40].

Sub-detector	required resolution	η-coverage measurement	η-coverage trigger
Inner Detector	$\sigma_{p_T}/p_T = 0.05\%\ p_T \oplus 1\%$	$\lvert\eta\rvert < 2.5$	
Electromagnetic LAr calorimeter	$\sigma_E/E = 10\%/\sqrt{E} \oplus 0.7\%$	$\lvert\eta\rvert < 3.2$	$\lvert\eta\rvert < 2.5$
Hadronic calorimeter			
Barrel and end-cap	$\sigma_E/E = 50\%/\sqrt{E} \oplus 3\%$		$\lvert\eta\rvert < 3.2$
Forward	$\sigma_E/E = 100\%/\sqrt{E} \oplus 10\%$		$3.1 < \lvert\eta\rvert < 4.9$
Muon Spectrometer	$\sigma_{p_T}/p_T = 10\%$ at $p_T = 1$ TeV	$\lvert\eta\rvert < 2.7$	$\lvert\eta\rvert < 2.4$

[2] The other is CMS.

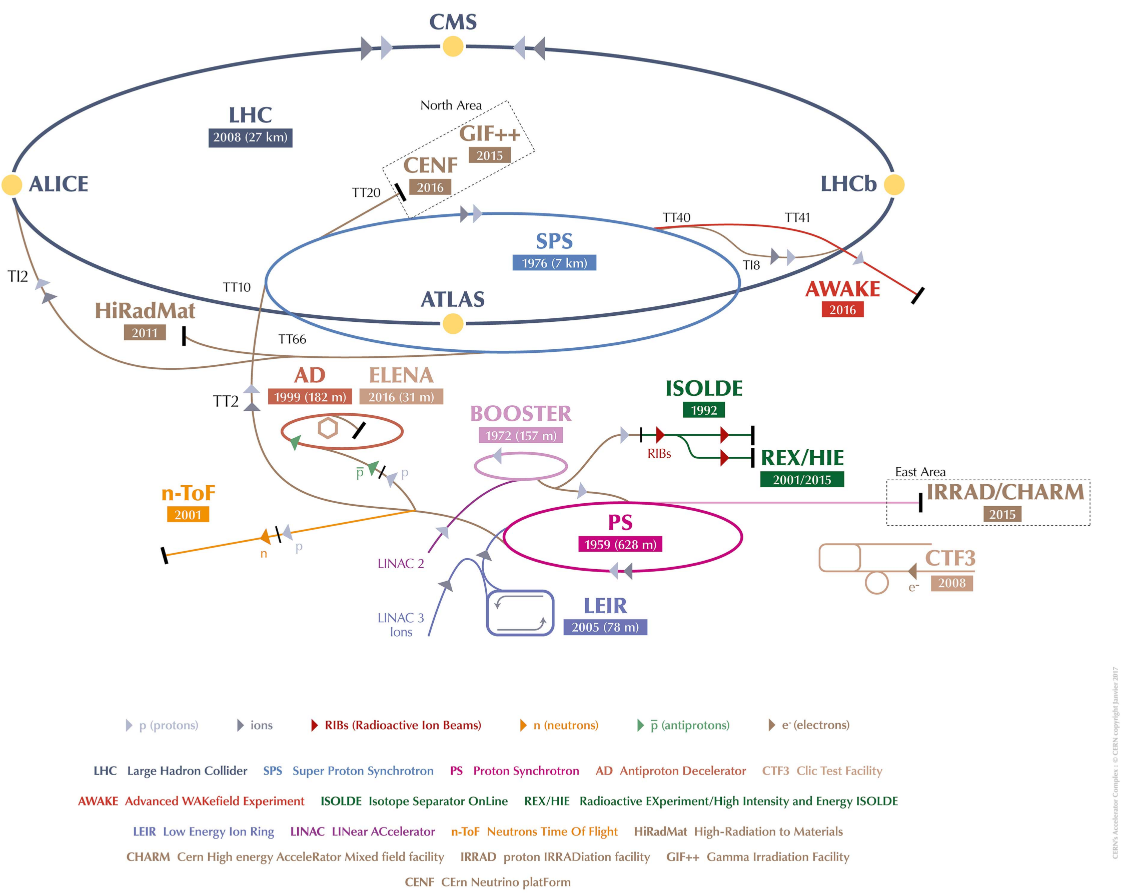

Figure 3.1: The LHC is the last ring (dark blue line) in a complex chain of particle accelerators. The four main experiments (ALICE, ATLAS, CMS, and LHCb) are indicated with yellow dots. The other smaller machines are used to help boost the particles to their final energies and provide beams to other experiments. Taken from Ref. [96].

The ATLAS magnet system

ATLAS has a superconducting magnets system [98], used to bend the trajectories of charged particles. As shown in Figure 3.3, the ATLAS magnet system consists of a central solenoid system producing a 2 T axial magnetic field in the ID. For the muon detectors, a barrel toroid and two end-cap toroids producing 0.5 T and 1 T magnetic fields, respectively.

The ATLAS coordinate system

The ATLAS coordinate system is a right-handed coordinate system originating from the pp interaction points (IP) with the z-axis along the tunnel. The x-axis points from the IP to the center of the LHC ring and the y-axis points upwards. Cylindrical coordinates are used in the transverse plane. The azimuthal angle ϕ is defined between $[0, 2\pi]$ with $\phi = 0$ corresponding to the x-axis.

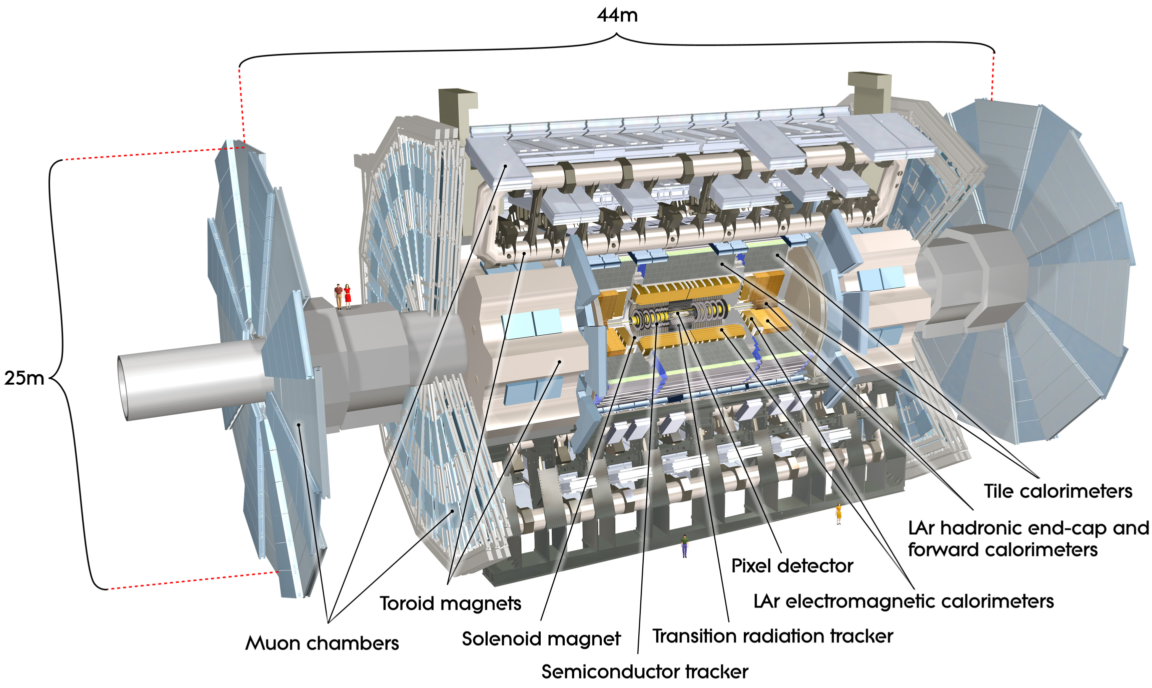

Figure 3.2: Cut-away view of the ATLAS detector. The dimensions of the detector are 25 m in height and width and 44 m in length. The overall weight of the detector is approximately 7000 tons. Taken from Figure 1.1 in Ref. [40].

The polar angle θ, defined in $[0, \pi]$, corresponds to the z-axis with $\theta = 0$ and the y-axis with $\theta = \pi/2$. However, θ is not usually used in ATLAS, because the angular distance $\Delta\theta$ between two objects is not Lorentz invariant along the z-axis. The pseudorapidity $\eta = -\ln\tan(\theta/2)$ is used instead of θ because η is a purely angular quantity and the angular distance $\Delta\eta$ is invariant under Lorentz boosts along z-axis. The total angular distance between objects is then defined as $\Delta R = \sqrt{\Delta\phi^2 + \Delta\eta^2}$. The $x - y$ plane, the transverse plane to the beam direction, is used to project the momenta of particles from the IP: $p_{\mathrm{T}} = p\sin\theta$. This projection is also applied to the mass of massive particles and missing momentum to build m_{T} and $E_{\mathrm{T}}^{\mathrm{miss}}$.

3.2.1 The Inner Detector

The Inner Detector [99] is to reconstruct tracks of charged particles arising from collisions and the collision vertices. The ID consists of three independent sub-detectors: the Pixel detector (including the Insertable B-Layer, IBL), the Semiconductor Tracker (SCT), and the Transition Radiation Tracker (TRT). A sketch of the ID is presented in Figure 3.4.

All sub-systems are separated into a barrel region and two end-cap regions. The planes of the detector surfaces in the end-cap region are approximately orthogonal to the beam pipe to ensure better coverage for tracks transversing the detector at high $|\eta|$.

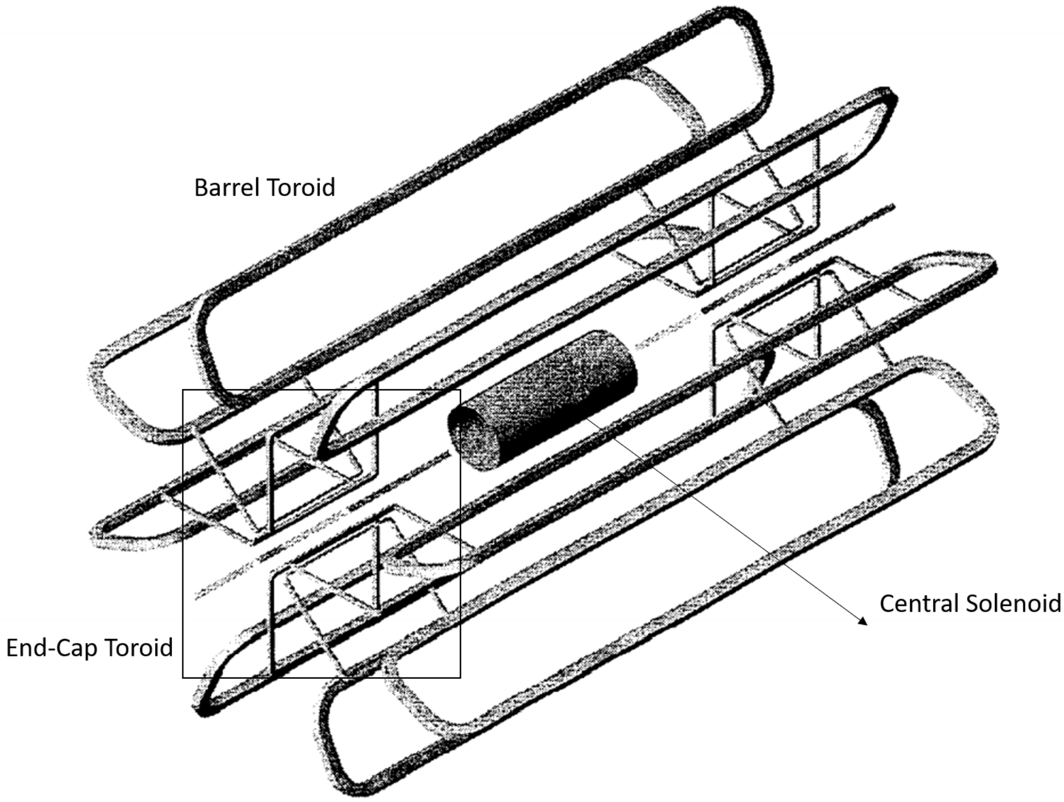

Figure 3.3: The ATLAS superconducting magnet system constructed by the Central Solenoid, the eight coils of the Barrel Toroid and the 2 x 8 coils of the End-Cap Toroids. Taken from Figure 2.1 in Ref. [98].

Pixel detector and the IBL

The Pixel detector is the innermost part of the ID and covers the region $|\eta| < 2.5$, composed of four cylindrical layers in the barrel region and three co-axial discs in the end-cap region.

The IBL [102] is the innermost layer, placed 33.5 mm away from the beam-line, formed by 14 sectors along the beam pipe with full coverage in ϕ. The other parts in the Pixel detector composed of three cylindrical layers in the barrel region, placed 50.5 mm, 88.5 mm, 122.5 mm away from the beam-line, and three co-axial discs in the end-cap region. The intrinsic measurement accuracy of all layers in $R - \phi$ direction is 10 μm. The accuracy[3] in z-axis direction is 72 μm for the IBL while 115 μm for other layers (for end-cap layers, the accuracy is for R-axis direction). An overview of the ATLAS Pixel detector is shown on the left-bottom part in Figure 3.4.

[3] All numbers were take from Table 4.1 in Ref. [40] (Table 7 in Ref. [102] for the IBL).

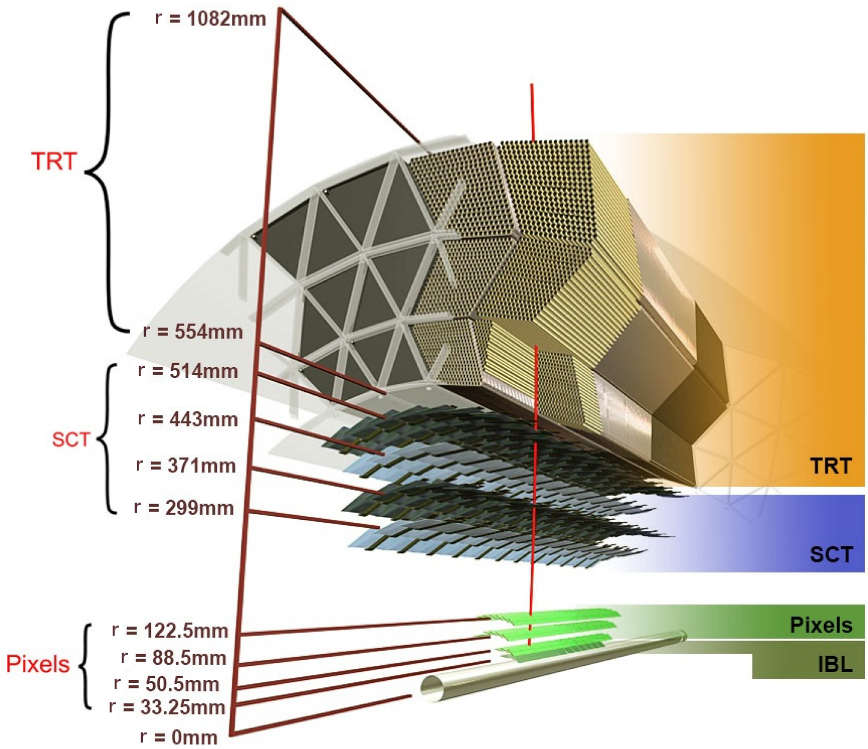

Figure 3.4: Sketch of the barrel region of the ATLAS Inner Detector traversed by a charged track of $p_{\mathrm{T}} = 10\,\mathrm{GeV}$. Taken from Figure 4.2 in Ref. [100].

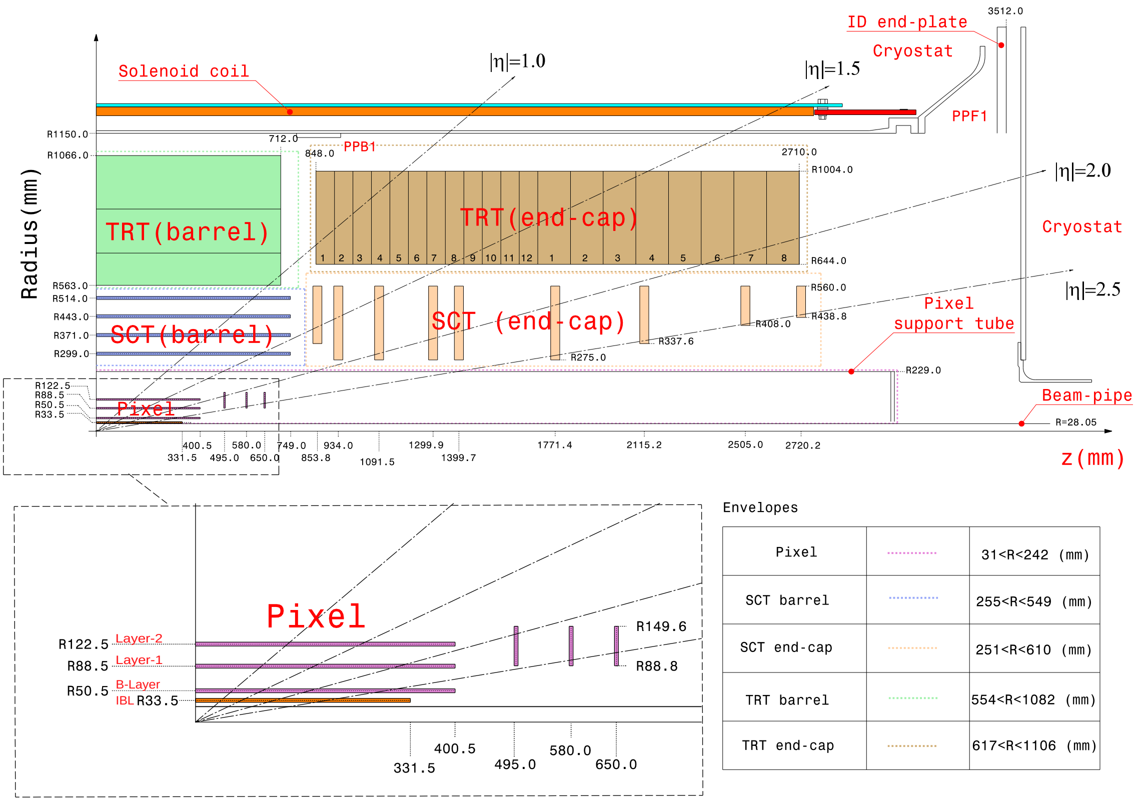

Figure 3.5: The $r-z$ cross-section view of the layout of a quadrant of the ATLAS Inner Detector. The top panel shows the whole Inner Detector, whereas the bottom-left panel shows a magnified view of the pixel detector region. Taken from Figure 1 in Ref. [101].

Semiconductor Tracker

The SCT uses the silicon micro-strip technology, positioned in four layers in the barrel region from 299.0 mm to 514.0 mm away from the beam-line and in nine discs in each of the end-caps, covers the region $|\eta| < 2.5$. The hit resolution of the SCT modules is 17 µm in the $R - \phi$ direction and 580 µm in z-axis (R-axis) direction for barrel (end-cap) layers. An overview of the ATLAS SCT detector is shown in the middle part of Figure 3.4.

Transition radiation tracker

When charged particles pass through a boundary between media with different dielectric properties, they emit photons in a process called transition radiation. Energy deposition of charged particles due to transition radiation is inversely proportional [103] to their masses. The TRT detector is designed to differentiate electrons from other particles. It is a straw tracker and located in the outermost part of the ID, covers the phase-space up to $|\eta| < 2.0$. Similar to Pixel and SCT, TRT also has the barrel and end-cap sections. The barrel section has 73 layers of straws aligned with the direction of the beam axis. The two end-caps are respectively composed of 18 wheels of straws, aligned perpendicular to the beam axis, pointing radially outward. The straws are made of polypropylene/polyethylene fibers for the barrel region and polypropylene foils for the end-cap region, with xenon gas fulfilled. The hit resolution of the TRT is 130 µm. An overview of the ATLAS TRT detector is shown on the top part in Figure 3.4.

3.2.2 Calorimeters

The calorimeter system is designed for measuring particles energy and absorbing outgoing particles except muons and neutrinos. In ATLAS, the calorimeter system involves electromagnetic EM calorimeters and hadronic calorimeters, covers the full ϕ range and $|\eta| < 4.9$. Two types of technologies were used for the ATLAS calorimeter system: i) The Liquid Argon (LAr) calorimeter [104] is used for both EM and hadronic measurements, while ii) The tile calorimeter [105] is used only for hadronic measurements. An overview of the ATLAS calorimetry is presented in Figure 3.6.

Liquid Argon calorimeters

The LAr electromagnetic calorimeter is a lead-liquid argon sampling detector. Lead is used for energy absorption because of its large electromagnetic interaction cross-section, which causes a cascade of secondary particles, and the energy is eventually deposited. For high $|\eta|$ range, copper/copper-tungsten is chosen for better radiation tolerances, and higher absorption length to allow the showers to develop.

Liquid argon is chosen as active material due to its intrinsic linear behavior, the stability of response, and intrinsic radiation-hardness. The LAr calorimeters include two parts with four types calorimeters of for different functionalities and $|\eta|$ range,

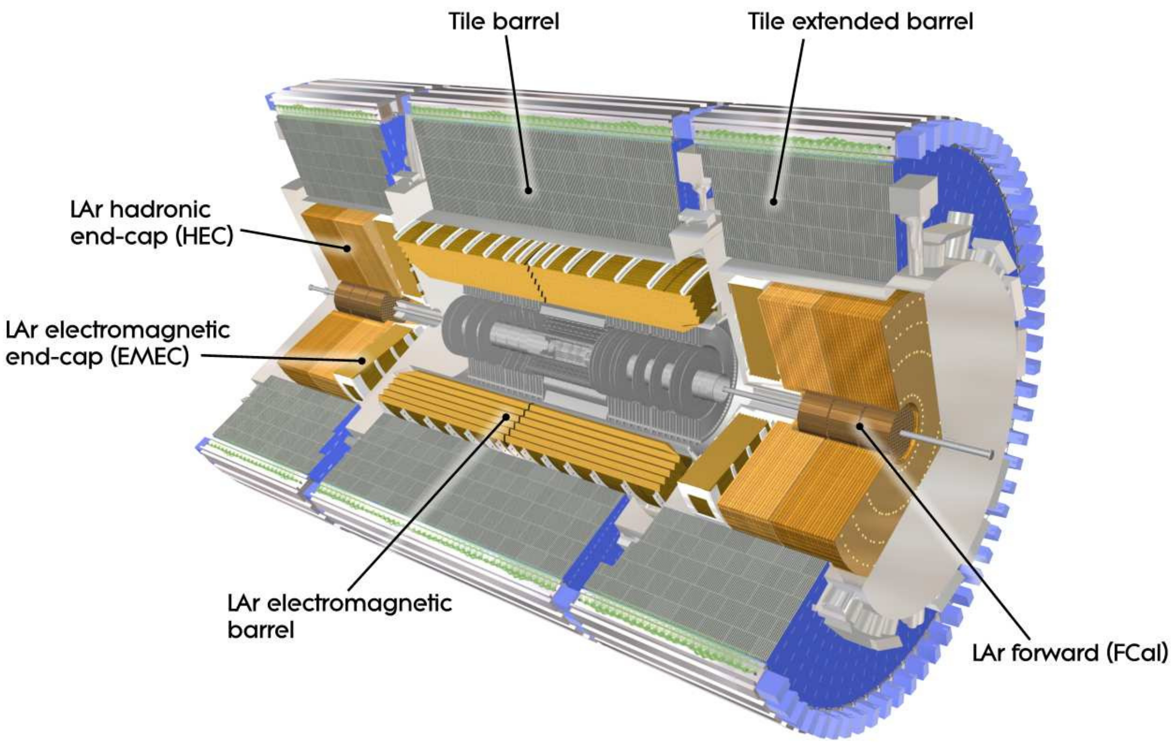

Figure 3.6: Cut-away overview of the ATLAS electromagnetic and hadronic calorimeters. Taken from Figure 1.3 in Ref. [40].

i) The LAr electromagnetic barrel calorimeter covers $|\eta| < 1.475$ and full ϕ range with "accordion-shape" (Figure 3.7). The modules of LAr electromagnetic barrel calorimeter are assembled into three layers, as shown in Figure 3.7. The first layer, also called the strip layer, has a very fine segmentation to provide precise energy measurement of electrons and photons. The granularity of the first layer is $\Delta\eta \times \Delta\phi = 0.003 \times 0.1$. The second layer absorbs most of the electromagnetic cascades and has a granularity of $\Delta\eta \times \Delta\phi = 0.025 \times 0.025$. The third layer is designed to collect the tail of the electromagnetic cascades and to determine the amount of energy lost beyond the EM calorimeter, has broader structures of $\Delta\eta \times \Delta\phi = 0.005 \times 0.025$.

ii) The LAr electromagnetic end-cap (EMEC) calorimeter, covers $1.375 < |\eta| < 3.2$, has a similar shape and structure as the barrel: accordion geometry with three longitudinal layers with similar thickness. The EMEC has two parts for positive and negative η range, each part consists of two co-axial wheels, with a 3 mm boundary between them located at $|\eta| < 2.5$, which is corresponding to the acceptance of the ATLAS ID.

The resolution[4] of both barrel and end-cap calorimeters is $\sigma_E/E = 10\%/\sqrt{E\,[\text{GeV}]} \oplus 0.7\%$ for electrons. In addition, the transition region between the barrel and end-cap EM calorimeter within

[4] All resolution numbers in the calorimeters section are taken from Ref. [104, 105].

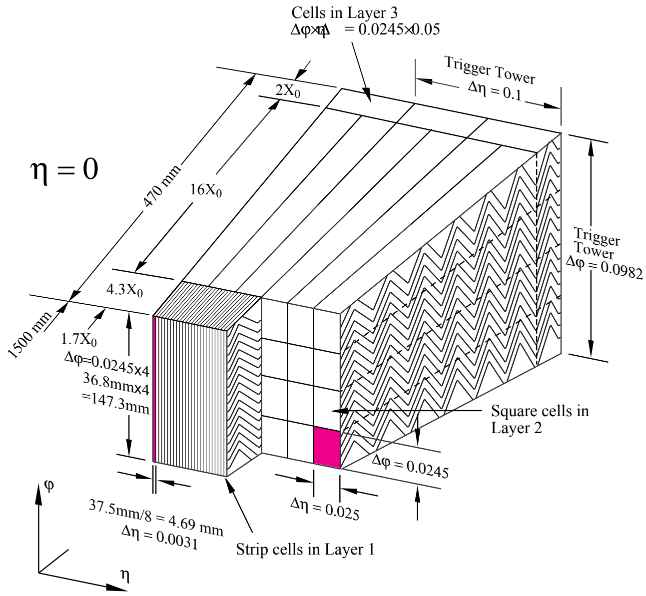

Figure 3.7: Sketch of a barrel LAr module where the different layers are clearly visible with the ganging of electrodes in ϕ. The granularity in η and ϕ of the cells of each of the three layers and of the trigger towers is also shown. Taken from Figure 5.4 in Ref. [40].

$1.37 < |\eta| < 1.52$ is usually excluded from ATLAS analyses due to a worse reconstruction efficiency of electrons and photons, caused by the amount of dead material in the transition region.

iii) The LAr hadronic end-cap calorimeter (HEC) is a copper/LAr calorimeter, covers $1.5 < |\eta| < 3.2$. It is located directly behind the EMEC, also has two parts similar to EMEC. The resolution is $\sigma_E/E = 21\%/\sqrt{E\ [\text{GeV}]} \oplus 0\%$ for electrons, $\sigma_E/E = 70\%/\sqrt{E\ [\text{GeV}]} \oplus 6\%$ for pions.

iv) The LAr forward calorimeter (FCal) is a copper-tungsten/LAr calorimeter, covers $3.1 < |\eta| < 4.9$. The FCal is composed of two end-caps that each have three modules. The first module in each end-cap uses copper as the absorber for precise electromagnetic energy deposit measurements. The outer two modules are optimized for a high absorption length by using tungsten instead of copper. A schematic diagram of the three FCal modules is shown in Figure 3.8. The resolution of FCal is $\sigma_E/E = 25\%/\sqrt{E\ [\text{GeV}]} \oplus 4\%$ for electrons, $\sigma_E/E = 100\%/\sqrt{E\ [\text{GeV}]} \oplus 10\%$ for pions.

Tile calorimeter

The tile calorimeter is located in the central region of the hadronic calorimeter, covers the range $|\eta| < 1.7$. It is composed of steel tiles as passive absorber material and plastic scintillators as active materials. It is further separated into the 'long barrel' in the range $|\eta| < 1.0$ and two 'extended barrels' in the range $0.8 < |\eta| < 1.7$. A tile calorimeter module is sketched in Figure 3.9. Similar to the EM calorimeter structure, the tile calorimeter has three layers as well. The signal from the scintillator is read out through the wavelength-shifting fiber and directed to the photomultiplier tube. The resolution of the tile calorimeter is $\sigma_E/E = 50\%/\sqrt{E\ [\text{GeV}]} \oplus 3\%$ for pions.

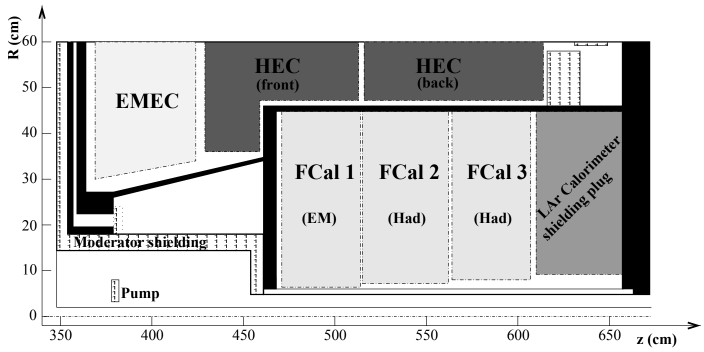

Figure 3.8: Schematic diagram showing the three FCal modules. The material in front of the FCal and the shielding plug behind it are also shown. The EM calorimeter end-cap (EMEC) and the HEC are also clearly visible. Taken from Figure 5.19 in Ref. [40].

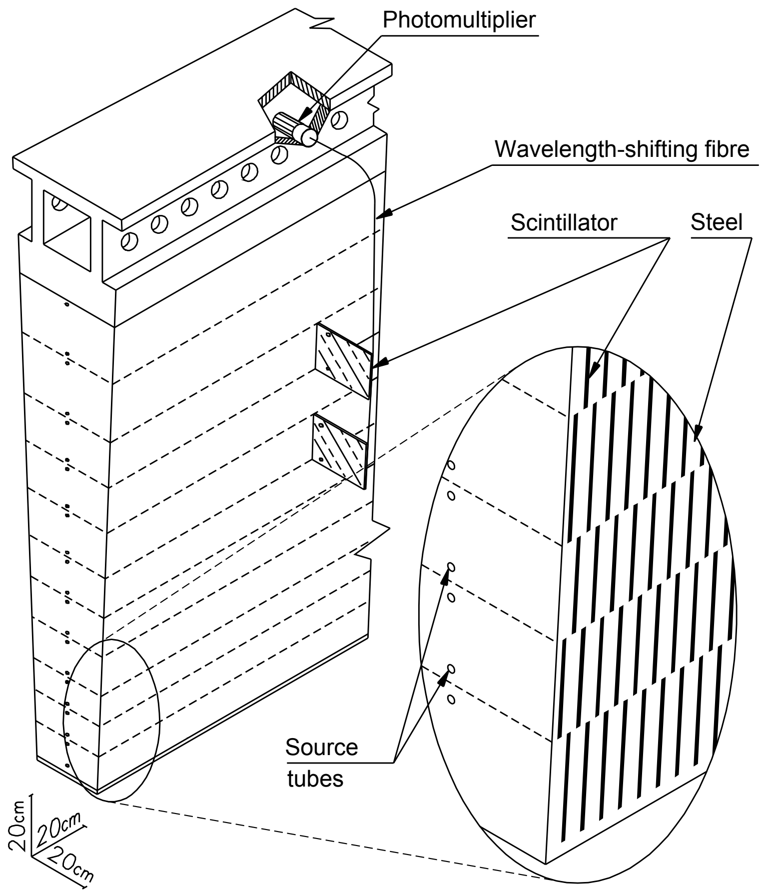

Figure 3.9: Sketch of the tile calorimeter shows how the mechanical assembly and the optical readout are integrated together. The various components of the optical readout, the fibers, and the photomultipliers are shown. Taken from Figure 5.9 in Ref. [40].

3.2.3 Muon Spectrometers

The ATLAS Muon Spectrometer (MS) [106] is the outermost part of the ATLAS detector, covers the range $|\eta| < 2.7$ for the measurement of the muon tracks. A trigger system is also designed to trigger on muons in the range $|\eta| < 2.4$. There are four sub-detectors: Monitored Drift-Tube (MDT) chambers, Cathode Strip Chambers (CSC), Resistive Plate Chambers (RPC), and Thin Gap Chambers (TGC). Barrel and end-cap toroidal magnets provide a magnetic field for muon tracks measurement. The system is shown schematically in Figure 3.10.

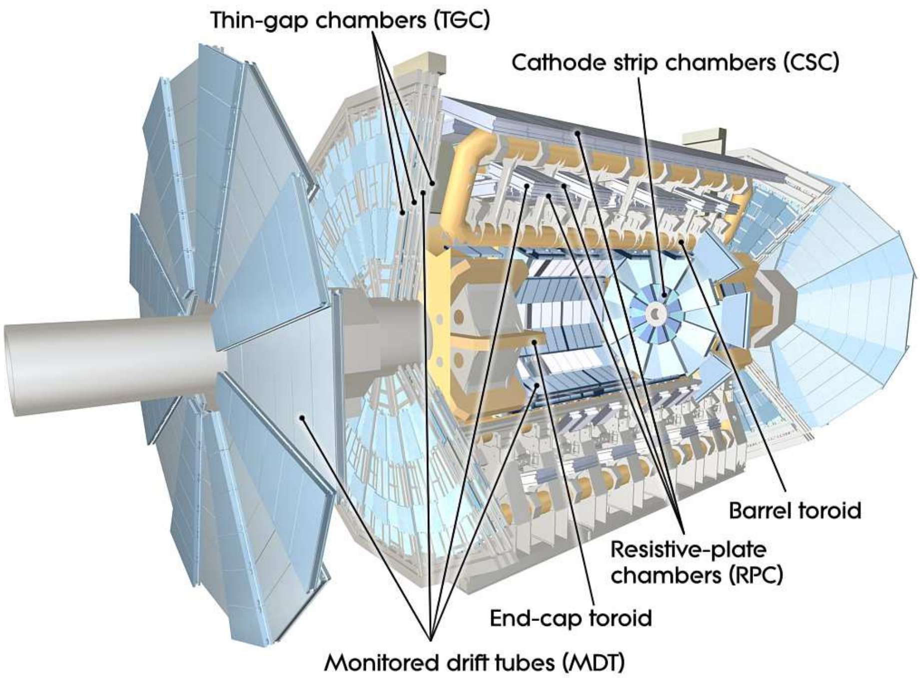

Figure 3.10: Cut away schematic view of the ATLAS Muon Spectrometer. Taken from Ref. [40].

Precision-measurement tracking chambers: MDT and CSC

MDTs perform the precision momentum measurement of muons. They cover the range up to $|\eta| < 2.7$ in all layers except the innermost layer which is limited to $|\eta| < 2.0$. MDTs are wire proportional chambers based on drift tubes filled with argon and carbon dioxide mixture (97/3), and with a tungsten-rhenium anode producing a radial electric field. For MDTs, the hit spatial resolution[5] is 35 µm in z-axis direction. Additionally, the innermost layer of MS is equipped with CSCs in the range $2.0 < |\eta| < 2.7$. CSCs are multiwire proportional chambers with finer granularity, higher acceptance rate, and time resolution compared to MDT. For CSCs, the hit spatial resolution is 40 µm in the radius axis and 5 mm in the ϕ direction, the timing resolution is 7 ns.

[5] All resolution numbers in the muon spectrometer section are taken from Ref. [106].

Trigger chambers: RPC and TGC

The response time of MDT is approximately 500 ns, which is too slow for triggering. RPCs and TGCs are designed for a muon triggering system and additional tracking information, especially the ϕ coordinate of the tracks.

RPCs are gaseous parallel electrode-plate detector, cover the range of $|\eta| < 1.05$. RPCs have three layers and are built by two resistive plates. The two resistive plates are separated by two insulating spacers that form a gap filled with a gas mixture of $C_2H_2F_4$/iso-C_4H_{10}/SF_6 (94.7/5/0.3). For RPCs, the hit spatial resolution is 10 μm in z-axis direction and 10 mm in the ϕ direction, and the timing resolution is 1.5 ns.

The TGCs are multi-wire proportional chambers, cover the range $1.05 < |\eta| < 2.4$, with a reduced cathode-anode distance in order to give very fast timing information, sufficient for triggering every 25 ns. For TGCs, the hit spatial resolution is 2-6 mm in radius direction and 3-7 mm in the ϕ direction, and the timing resolution is 4 ns.

3.2.4 The ATLAS trigger and data acquisition system

The ATLAS trigger system is an essential component of the experiment since it is responsible for deciding whether or not to keep a collision event for offline data analysis. When the LHC is operated under nominal conditions, pp collisions occur at a rate of 40 MHz, with a combined data volume of more than 60 million megabytes per second. The main goal of the trigger and the data acquisition system (called 'TDAQ') is to perform an online event selection of pp collisions to reduce the flow of data to manageable levels, and to record the selected events.

ATLAS trigger system [107] is a two-level online event selection system: i) Hardware 'Level-1' (L1) trigger, reduces the event rate down to about 100 kHz. ii) Software 'high-level trigger' (HLT) further reduces the event rate to about 1.0 kHz. The ATLAS trigger system is sketched in Figure 3.11.

The L1 trigger is designed for fast object identification and selection. It uses information from the RPCs and TGCs for high-p_T muons for Level-1 Muon input; And all calorimeters for high energy electrons, photons, jets, hadronic taus, and E_T^{miss} for Level-1 Calo input. The Level-1 Muon and Calo input are further transferred to the L1 Central Trigger: Muon-to-CTP interface (MUCPTI) combines barrel and end-cap information from Level-1 Muon input; Level-1 Topological Trigger (L1Topo) perform selections based on the geometric or kinematic association between trigger objects received from the Level-1 Calo systems and MUCTPI; Central Trigger Processor (CTP) receives inputs from Level-1 Calo, Level-1 Muon, L1Topo, MUCTPI as well as some other sub-systems such as the Minimum Bias Trigger Scintillators (MBTS), the LUCID Cherenkov counter and the Zero-Degree Calorimeter (ZDC), provides L1 trigger decision to the Read-Out System (ROS) and Region-of-Interest (RoI) to HLT.

Events passing the L1 trigger are buffered in the ROS and further processed by the HLT. More information such as finer-granularity calorimeter information, precision measurements from the MS, and tracking information from the ID are used in HLT. The HLT decision can either be executed within RoI identified at L1 or for the full detector. After the events are accepted by the HLT, they

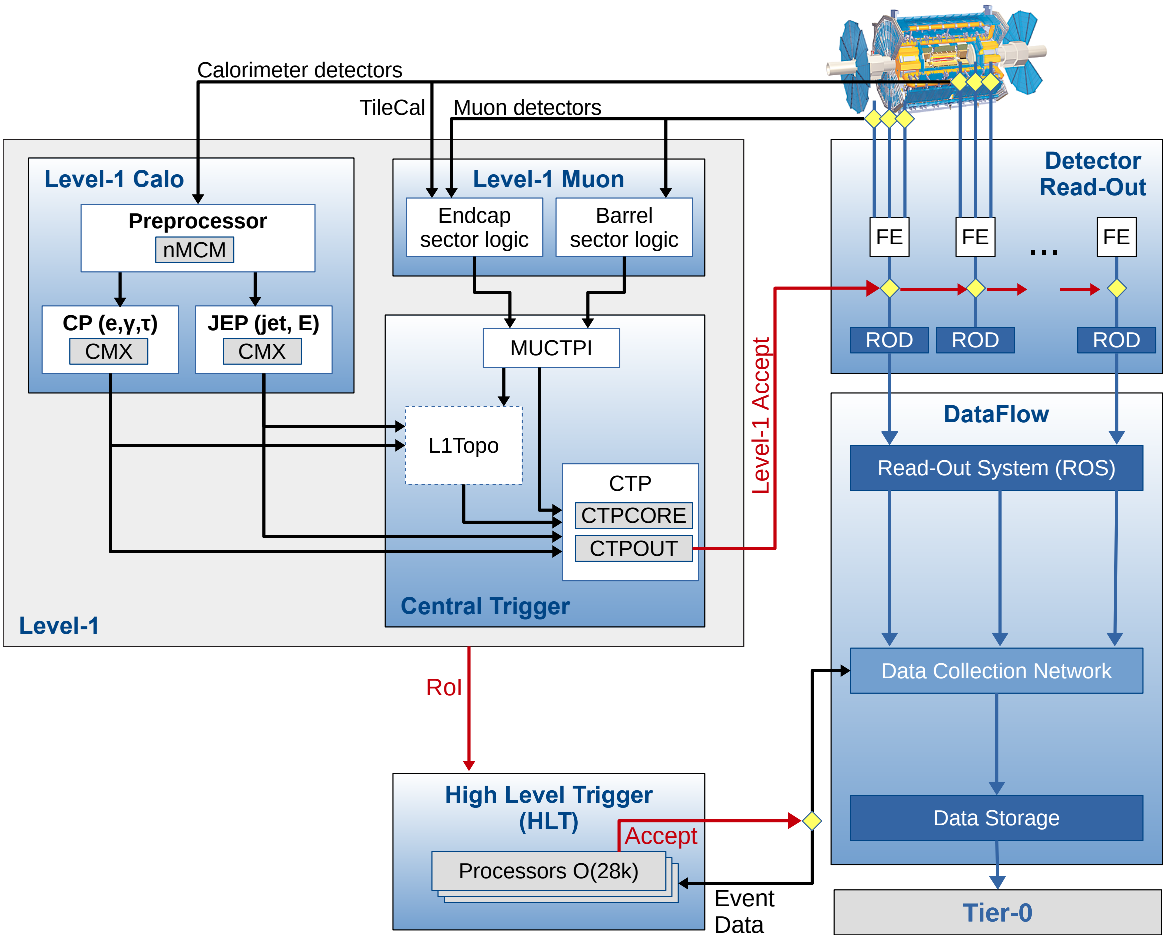

Figure 3.11: The ATLAS TDAQ system with emphasis on the components relevant for triggering. Taken from Figure 1 in Ref. [107].

are transferred to local storage at the experimental site and exported to the Tier-0 facility at CERN's computing center for offline reconstruction.

In conclusion, the L1 + HLT system provides a selection of pp collision events for new physical search, precise SM measurement and performance research with the maximum possible bandwidth allowed by the ATLAS data acquisition infrastructure.

3.2.5 Luminosity measurement

High precision (< 5%) measurement of luminosity is important to perform a reliable measurement. The luminosity is measured for each bunch interaction by the forward sub-detectors, mainly the luminosity measurement using Cerenkov Integrating Detector (LUCID) [108]. LUCID is a Cherenkov detector located at a distance of approximately ±17 m the interaction point, covering $5.5 < |\eta| < 5.9$. The measured luminosity form 2015-2018 is shown in Figure 3.12.

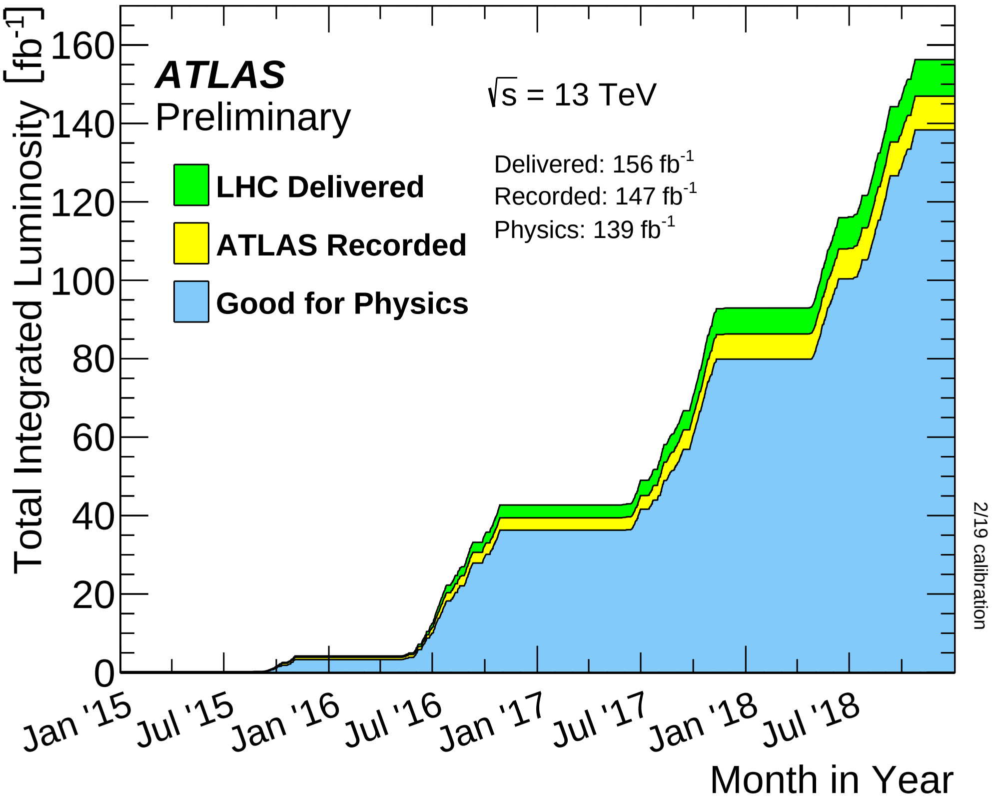

Figure 3.12: Integrated luminosity versus time delivered to ATLAS (green), recorded by ATLAS (yellow), and certified to be good quality data (blue) during stable beams for pp collisions at 13 TeV center-of-mass energy in 2015-2018. The All Good Data Quality criteria require all reconstructed physics objects to be of good data quality. Taken from https://twiki.cern.ch/twiki/bin/view/AtlasPublic/LuminosityPublicResultsRun2.

4 Physics Object Reconstruction

Contents

The particles produced in the proton collision will further pass through the ATLAS sub-detector systems and generate energy deposition by electromagnetic interaction and strong interaction. The detector response for energy deposition from all sub-detector systems readout and recorded. Dedicated reconstruction algorithms are applied to reconstruct physics objects. This section describes how to reconstruct different particles in ATLAS.

4.1 Track

Track, which is the trajectory of a charged particle reconstructed in ID or MS. Tracks can be described by five parameters (**q**):

$$\mathbf{q} = (d_0, z_0, \phi_0, \theta, q/p), \tag{4.1}$$

An illustration of the five defined track parameters is shown in Figure 4.1. Here d_0 and z_0 are the impact parameters in the transverse and longitudinal direction, respectively. The transverse impact parameter d_0 is defined as the nearest distance between track projection in xy plane and the IP. The longitudinal impact parameter, z_0, is defined as the distance in z-axis between the IP and the point on the track used to evaluate d_0. At perigee view, ϕ_0 and θ are defined as the azimuthal and the polar angle. q/p is the ratio between the charged and reconstructed momentum of the track.

The track is identified in the inner detector using the ATLAS New Tracking (NEWT) algorithm [110] that proceeds in several steps [111]. The first step is clusterization, through assembling hits on pixel or SCT with deposited energy above a certain threshold into clusters. *Space-points*, as three-dimensional measurements, are created referred to as these clusters. Track seeds, which consist of three hits in different layers of the pixels or SCT, are formed for next step. Secondly, a combinatorial Kalman

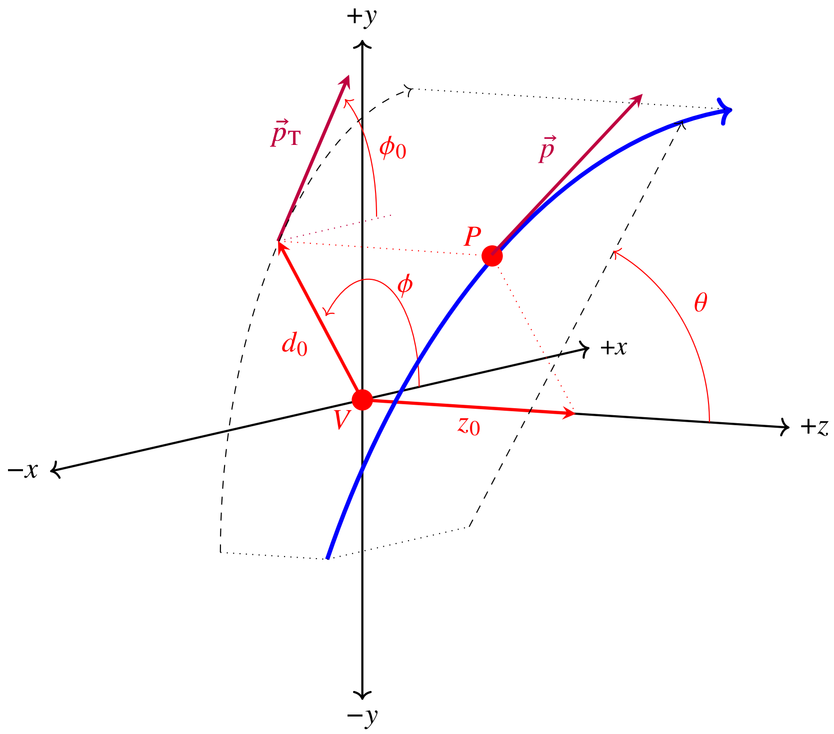

Figure 4.1: Illustration of the five defined track parameters at the perigee. Taken from Ref. [109].

filter [112] is used to recognize patterns of track candidates[1], followed by a stringent ambiguity-solver [111] that compares and evaluates individual tracks by assigning relative track scores. Lastly, the track candidates passing requirements of the ambiguity-solver are refitted with a high-resolution fit determined with Artificial Neural Networks [113]. The pattern recognition and track fit are both based on the pion hypothesis that the energy loss due to ionization in the detector material is evaluated assuming all particles are pions [114].

4.2 Vertex

Since there are a large number of pp collisions at each bunch crossing, multiple interaction vertices are usually reconstructed in one event. The points in space where the pp collision occurred are defined as Primary Vertices. PV candidates are reconstructed with an adaptive vertex fitting algorithm [115], by using the reconstructed tracks with p_T>500 MeV introduced in previous Section 4.1.

A beam-spot[2] constraint is applied to all primary vertices candidates to improve the resolution on the vertex position in 3-dimensional space. The number of reconstructed primary vertices is used as a measure of the in-time pile-up.

[1] The filter creates multiple track candidates per seed if more than one compatible space-point extension exists on the same layer
[2] The beam spot [115] indicates the luminous region of pp collision in ATLAS detector.

After the beam spot constraint applied, primary vertices candidates will be further separated into three categories:

1) Primary Vertex: The vertex with the highest sum of the track p_T squared corresponding to the hardest pp interaction in an event.
2) Pile up vertices: The rest of the primary vertices candidates satisfied the beam spot constraint.
3) Secondary vertices: The rest of the primary vertices candidates failed the beam spot constraint.

4.3 Truth classification and matching

Truth classification

As discussed in section 2.1.4, leptons decayed from W or Z bosons are produced promptly, which is not the case for leptons decayed from b- and lighter hadrons. Leptons decayed from b-hadron or c-hadron through W^* boson are named heavy-flavor decay (HF) leptons. For lighter quarks, those leptons that decay from hadrons are named light-flavor decay (LF) leptons. Leptons from the decays of hadrons are referred to as non-prompt leptons. In contrast, prompt leptons are defined as leptons produced intermediately at the IP, such as Higgs ($H \to 4\ell$), Z bosons ($Z \to \ell\ell$), and W bosons ($W \to \ell\nu$). Top quark also has a very short lifetime; hence leptons decayed from Top quarks through W boson are also prompt leptons. Tau has a similar lifetime as $b-$hadron. However, when the decayed products do not include any hadrons, e.g. $\tau^- \to \nu_\tau \, \overline{\nu}_e \, e^-$, the leptons decayed from tau (from the IP) are also considered as prompt leptons. Because of the instability of tau, the category "lepton" only includes electron and muon in the latter part of this thesis.

Besides lifetime differences, there are also some other sources to create leptons away from the IP. Firstly, Photons from IP can interact with detector materials and produce lepton pairs (mostly electrons. very unlikely to produce muons). These leptons are named photon conversion leptons. This type of leptons tends to have fewer ID hits. Secondly, there may be more than one interactions that happened in one bunch crossing; leptons produced not at the Primary Vertex are named as pile-up leptons or underlying leptons. This type of leptons tends to have low momentum and large d_0/z_0. Lastly, the reconstruction algorithm may misidentify hadrons as leptons, which can create "unknown" leptons. These three types of leptons are usually included in the non-prompt (also named "fake") leptons category.

Truth match for leptons

In physics analysis, only the detector information can be used for final results. Truth particles are particles created in the Monte-Carlo generator, while reconstructed particles are objects formed by the ATLAS reconstruction algorithm based on the detector response generated by the simulation of truth particles. In order to understand the reconstruction performance in the Monte-Carlo simulations, the truth match [116] technique is widely used in ATLAS, mainly based on the angular distance ΔR between truth particles and reconstructed objects (typical discriminant is $\Delta R < 0.2$). The most similar reconstructed object is labelled with the corresponding truth particle.

4.4 Electron

Electron[3] reconstruction [117, 118] starts from energy deposits in the EM calorimeter, together with the reconstructed tracks of charged particles in the ID. Several steps are described below in details and schematically summarized in Figure 4.2.

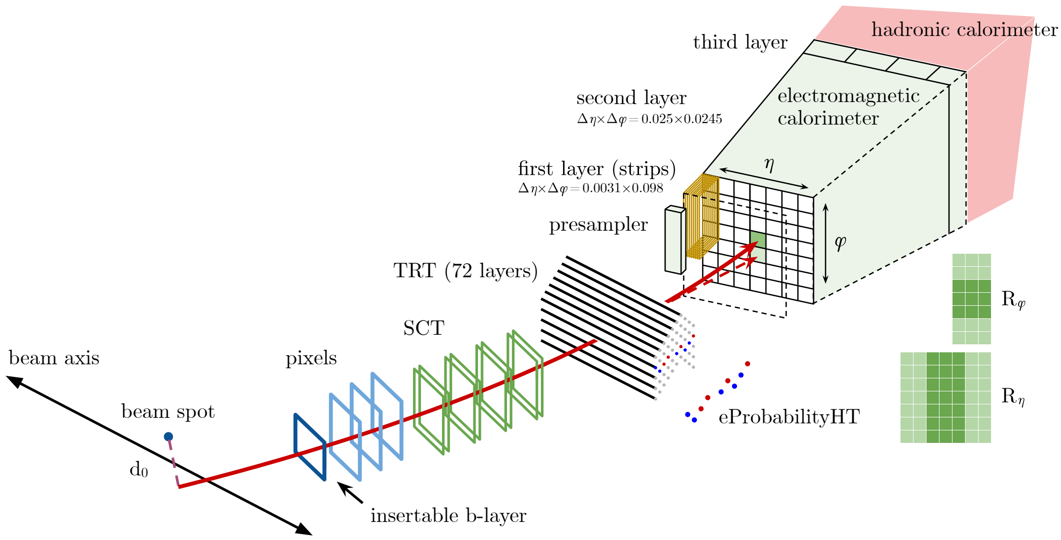

Figure 4.2: A schematic view of the electron reconstruction and identification quantities. The dimensions in this figure are not drawn to scale. Taken from Ref. [118].

Seed-cluster reconstruction

The energy deposits in the EM calorimeter are collected in all three layers (the strip/first, the middle/second, the back/third), and in the presampler[4]. The collected energy is summed in towers. These towers are local elements of size $\Delta\eta \times \Delta\phi = 0.025 \times 0.025$. The $\eta - \phi$ space of the EM calorimeter system can be divided into 200×256 towers, corresponding to the granularity of the second layer of the EM calorimeter. The energy of the cell across several towers is evenly distributed among the towers without considering any geometric weighting.

A dynamical, topological cell clustering-based approach named supercluster [119] is used to reconstruct the towers' seed clusters. Only clusters with EM energy[5] greater than 400 MeV are considered. For real electrons, the cluster reconstruction is expected to be very efficient. The EM fraction (f_{EM}) is the ratio of the EM energy to the total cluster energy. A pre-selection requirement of $f_{\mathrm{EM}} > 0.5$ was chosen for the seed clusters, as it rejects ~60% of pile-up clusters without affecting the efficiency for selecting real electron seed clusters [120].

[3] In the central region of the ATLAS detector ($|\eta| < 2.47$).
[4] Only in the $|\eta| < 1.8$ range, due to the acceptance.
[5] The energy from cells in the EM calorimeter

Electron-track reconstruction

Track reconstruction can be divided into two steps: pattern recognition and track fit, as described in Section 4.1. However, a track seed with a transverse momentum larger than 1 GeV may not be extended to a full track with at least seven silicon hits with the pion hypothesis. In this case, a new pattern recognition using the electron hypothesis is retried. This modified pattern recognition algorithm is based on a Kalman-filter-smoother formalism [112], which allows up to 30% energy loss at each material surface. This refitting procedure improves the performance of electron reconstruction and has the least impact on the main track reconstruction. In electron-track reconstruction, tracks are fitted with either the pion or the electron hypotheses using the ATLAS Global χ^2 Track Fitter [121]. After the Global χ^2 fit, tracks are considered as loosely matched to an EM calorimeter cluster. if they pass requirements defined in Ref. [119]. An optimized electron track fitter, the GaussianSum Filter (GSF) [122] which is a non-linear generalization of the Kalman filter algorithm takes the bremsstrahlung into account and improves the original determination of the defining track parameters. The GSF algorithm is applied for precisely re-estimating the track parameters of these candidates. TRT-only tracks (tracks which only have TRT detector hits.) and tracks that fail the GSF fit (about 0.01%) keep the defined track parameters from the Global χ^2 Track fit.

Electron-candidate reconstruction

An electron object is reconstructed if at least one track satisfied the track–cluster matching criteria, described in previous section 4.4 , with the GSF refitted tracks and tighter requirements: $\Delta\phi_{\text{track, cluster}} < 0.1$. More than one track can be associated with a cluster. The best-matched track is chosen as the primary track and used to define the kinematic properties of the electron. Information of the chosen track is also included in the multivariate electron identification.

All tracks matching to the seed cluster are kept for each electron and used for further studies. Choosing the primary track is a crucial stage in the electron reconstruction chain. Several priorities described below for the electron primary track selection:

1. Tracks with at least one pixel hit are preferred, then tracks with hits in the SCT but not in the pixel detector.

2. Within each category, tracks with smaller ΔR are preferred unless the differences between tracks are small (<0.1). Where the ΔR is the distance between the cluster barycenter and the extrapolated track in the second layer of the EM calorimeter

3. If more than one track satisfied requirements above, the track with the most and as inner as possible pixel hits is used to define the reconstructed electron properties.

The final clusters are formed by rebuilding EM calorimeter clusters which are satisfied the necessary selection criteria [119] and associated with any electron candidate around the seed cluster. After selecting all electron candidates, the energy of the final clusters is calibrated. The calibration is based on multivariate techniques and detailed in Ref. [123]. Typical results are shown in Figure 4.3,

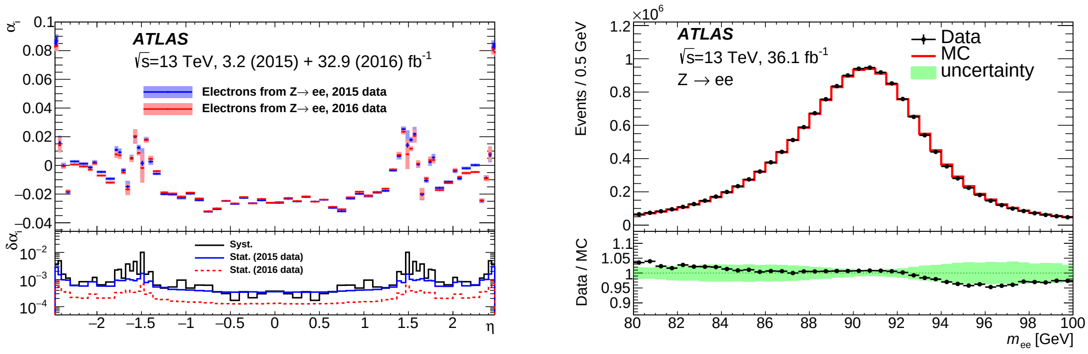

(a) (b)

Figure 4.3: (a) Results of the data-to-Monte-Carlo calibration from $Z \to ee$ events for the energy scale corrections α_i, defined by $E_{\text{data}}/E_{\text{Monte-Carlo}} - 1$ and (b) Comparison of the invariant mass distribution of the two electrons in the selected $Z \to ee$ candidates, after the calibration and resolution corrections are applied. The systematic and statistical uncertainties are shown separately in the bottom panels. Taken from Figure 7a and Figure 8 in Ref. [123].

Electron identification

Quality criteria called "electron identification" are applied to improve the purity of electrons. Prompt electrons are selected with a LH based identification, to suppress backgrounds from HF, LF, and photon conversion (γ) induced fakes. The electron identification variables in the tracking system and the calorimetry system are summarized in Table 4.1.

The LH identification is a multivariate method that simultaneously evaluates several properties of the electro candidates when making a selection decision. This method uses the chosen discriminating variables distribution of input signal and background to build corresponding PDFs. Based on these PDFs, the overall likelihood function is calculated for the candidate object. The likelihood identification is based on likelihood function for signal, L_{S}, and for background, L_{B}, which are products of the input PDFs. Correlations in the quantities selected for the LH are neglected.

For each electron candidate, a discriminant d_L is then formed,

$$d_L = \frac{L_{\text{S}}}{L_{\text{S}} + L_{\text{B}}}, \quad L_{\text{S(B)}}(\vec{x}) = \prod_{i=1}^{n} P_{\text{s(b)},i}(x_i), \tag{4.2}$$

where $\vec{x}$ is the vector of discriminating variable introduced in Table 4.1. $P_{\text{s(b)},i}(x_i)$ is the value of the PDF of the variable i evaluated at value x_i. The discriminant d_L is sharp at 1 for signal and zero for background. Hence additional transformation is needed and developed to smooth the distribution [123]. The signal and background PDFs are derived from the data using the tag-and-probe technique [120]. Tag and probe technique is based on two bodies decays of known resonances, e.g., $Z \to ee$. With a strong requirement on one of the electrons, named tag electron, and the mass window of two electrons, e.g., $|m_{ee} - m_Z| < 10\,\text{GeV}$, the other electron, named probe, can be selected with no direct quality requirement, hence the sample of the probe electrons can be used to derive an unbias measurement of the identification efficiency.

Several workings points are defined by choosing fixed values of the likelihood discriminant with different signal efficiency and background rejection to cover the requirements of various ATLAS analyses. The working points, chosen for the main analysis, are referred to as Loose, Medium, and Tight with 93%, 88%, and 80% efficiency at E_T at 40 GeV. Details of efficiencies in various p_T and η range are shown in Figure 4.4. The background rejection is higher than 99.2% for all working points [118].

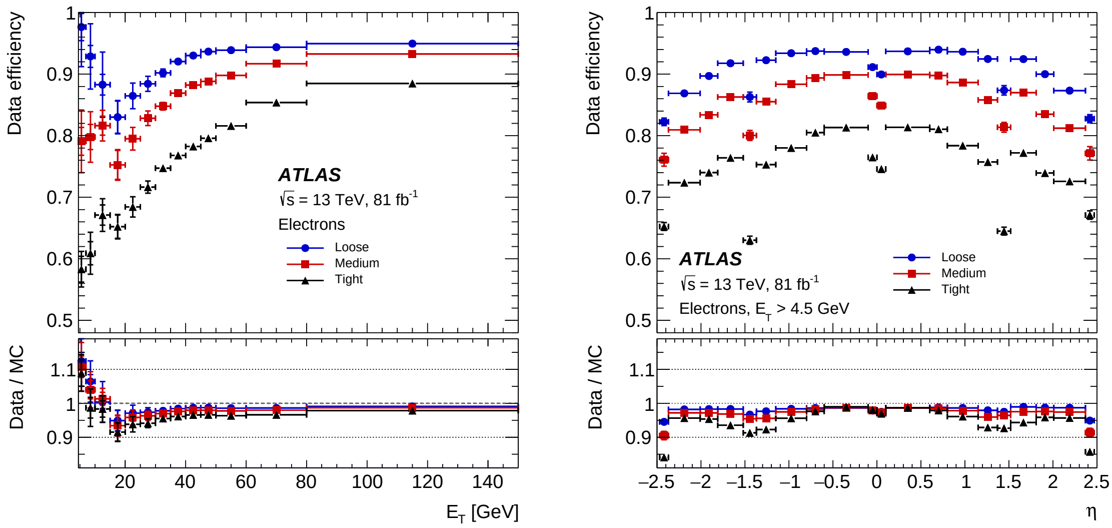

(a) (b)

Figure 4.4: The electron identification efficiency in $Z \to ee$ events in data as a function of E_T (left) and as a function of η (right). The inner uncertainties are statistical, and the total uncertainties are the statistical and systematic uncertainties added in quadrature. For both plots, the bottom panel shows the data-to-simulation ratios. Taken from Figure 17 in Ref. [120].

Electron charge identification (ECIDS)

Electron charge reconstruction is based on the curvature of related tracks reconstructed in ID. When electrons move through ID, their interaction with detector materials will further create secondary particles, e.g. photons and electron-positron pairs. Those secondary particles can cause deformation of the electron's primary track, e.g., by including additional hit information from secondary particles, or even chose the wrong primary track because of a too noisy environment. Hence the curvature of an electron may be wrongly reconstructed due to the secondary particles; It is possible to misidentify the charge of an electron. Electrons with wrongly reconstructed charge (charge-flip, charge misidentification) are suppressed using a boosted decision tree discriminant exploiting additional tracks in the vicinity of the electron and the track-to-cluster matching variables [125]. The efficiencies

Table 4.1: Definitions of electron discriminating variables and the types of backgrounds the variables help to discriminate against (indicated with a check-mark x). HF indicates non-prompt electrons originating from decays of hadrons containing heavy quarks (b, c), LF indicates fakes originating from light quarks (u d, or s) or gluons, γ indicates photon conversion induced fakes. Taken from Ref. [124].

Type	Description	Name	Rejects		
			HF	LF	γ
Hadronic leakage	Ratio of E_{T} in the first layer of the hadronic calorimeter to E_{T} of the EM cluster. (used over the range $\lvert\eta\rvert < 0.8$ or $\lvert\eta\rvert > 1.37$)	R_{had1}	x	x	
	Ratio of E_{T} in the hadronic calorimeter to E_{T} of the EM cluster. (used over the range $0.8 < \lvert\eta\rvert < 1.37$)	R_{had}	x	x	
Third layer of EM calorimeter	Ratio of the energy in the third layer to the total energy in the EM accordion calorimeter. This variable is only used for $p_{\mathrm{T}} < 80$ GeV due to known inefficiencies at high p_{T}, and is also removed from the LH for $\lvert\eta\rvert > 2.37$, where it is poorly modeled by the Monte-Carlo.	f_3		x	
Second layer of EM calorimeter	Lateral shower width, $\sqrt{(\Sigma E_i \eta_i^2)/(\Sigma E_i) - ((\Sigma E_i \eta_i)/(\Sigma E_i))^2}$, where E_i is the energy and η_i is the pseudorapidity of cell i and the sum is calculated within a window of 3×5 cells	$w_{\eta 2}$		x	x
	Ratio of the energy in 3×3 cells over the energy in 3×7 cells centered at the electron cluster position	R_{ϕ}	x	x	x
	Ratio of the energy in 3×7 cells over the energy in 7×7 cells centered at the electron cluster position	R_{η}	x	x	x
First layer of EM calorimeter	Ratio of the energy difference between the maximum energy deposit and the energy deposit in a secondary maximum in the cluster to the sum of these energies	E_{ratio}		x	x
	Ratio of the energy in the strip layer to the total energy in the EM accordian calorimeter	f_1		x	
Track conditions	Transverse impact parameter with respect to the beam-line	d_0	x		x
	Significance of transverse impact parameter defined as the ratio of d_0 and its uncertainty	$\lvert d_0/\sigma_{d_0}\rvert$	x		x
	Momentum lost by the track between the perigee and the last measurement point divided by the original momentum	$\Delta p/p$		x	
TRT	Likelihood probability based on transition radiation in the TRT	eProbabilityHT		x	
Track-cluster matching	$\Delta\eta$ between the cluster position in the strip layer and the extrapolated track	$\Delta\eta_1$		x	x
	$\Delta\phi$ between the cluster position in the second layer of the calorimeter and the momentum rescaled track, extrapolated from the perigee, times the charge q	$\Delta\phi_{\mathrm{res}}$		x	x

of the additional BDT requirement for electrons already identified with a Medium requirement are shown in Figure 4.5 for candidate electrons from $Z \to ee$ events.

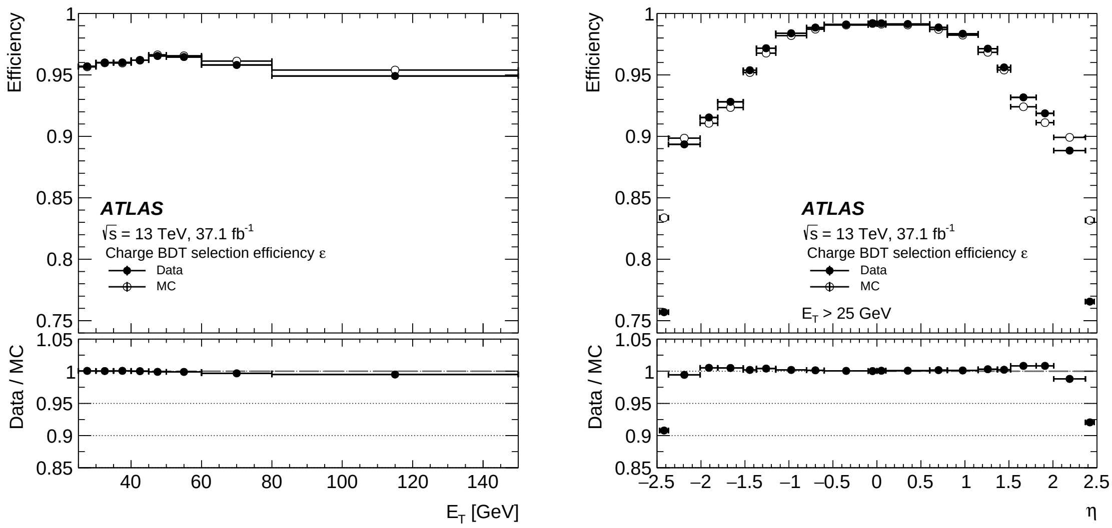

(a) (b)

Figure 4.5: Efficiency of applying the additional BDT selection criterion to choose Medium electrons reconstructed with the correct charge, as evaluated in $Z \to ee$ events. The criterion is based on a BDT discriminant optimized to select electrons with a correct charge assignment with an efficiency (compared to all electrons correct charge) of 97%. Left: vs. E_T; right: vs. η. Taken from Figure 14 in Ref. [125].

4.5 Muon

Muons are reconstructed independently in the ID and MS. The information from individual subdetectors is later combined to form muon tracks used in physics analyses. The muon tracks in the ID are reconstructed as described in Section 4.1. This section is focusing on the muon reconstruction in the MS.

In the MS, the muon tracks reconstruction starts with a search for hit patterns inside each muon chamber to form segments. In MDT chambers, a Hough transform Ref. [126] is used to search for hits aligned on a trajectory in the bending plane of the detector. The RPC or TGC hits measure the coordinate orthogonal to the bending plane. Segments in the CSC detectors are built using a separate combinatorial search in the $\eta - \phi$ detector planes. A detailed description of the muon reconstruction and identification is given in Ref. [127].

The combined ID–MS muon reconstruction is performed according to various algorithms based on the information provided by the ID, MS, and calorimeters. Four muon types are defined depending on which subdetectors are used in reconstruction:

- Combined (CB) muon: Track is refitted with the information from independent reconstruction in ID and MS. MS hits may be added to or removed from the track to improve the fit quality.
- Segment-tagged (ST) muons: Once a track in the ID extrapolated to the MS is is associated with at least one local track segment in the MDT or CSC chambers, it will be classified as a muon. ST muons are used when muons cross only one layer of MS chambers.
- Calorimeter-tagged (CT) muon: Matching an ID track to an energy deposit in the calorimeter defines the CT muon. Even the purity provided by this type of muons is low, they recover the acceptance in the region where the MS is only partially adapted ($|\eta| < 0.1$) and in the p_{T} range of 15 to 100 GeV.
- Extrapolated (ME) muon: Only use the MS tracking information that has passed the relaxed requirements (originating from IP) to perform the reconstruction. ME muons are generally used to recover ATLAS acceptance in the region $2.5 < |\eta| < 2.7$ not covered by the ID, where the CB muon reconstruction is not possible.

Before producing the muons used in physics analyses, overlaps between different muon types are resolved by giving preference to CB muons, then to ST, and finally to CT muons.

Muon identification

To improve the purity of muons, quality requirements called "muon identification" are applied to suppress background, mainly from pion and kaon decays, while keeping high efficiency and guaranteeing a robust momentum measurement for prompt muons selection. Several working points were defined to address the specific needs of different physics analyses, similar as the situdation in electron reconstruction (Section 4.4). The Medium working is chosen for the main analysis, which is also the default selection for muons in ATLAS. This selection uses only CB and ME tracks with the minimized systematic uncertainties associated with muons reconstruction and calibration. CB muons are required to have >= 3 hits in at least two MDT layers, except for tracks in the $|\eta| < 0.1$ region, where tracks with at least one MDT layer but no more than one MDT hole layer are allowed. ME muons are required to have >= 3 hits in MDT/CSC layers and are used only in the region $2.5 < |\eta| < 2.7$ to extend the acceptance outside the ID geometrical coverage. The q/p significance, defined as the absolute value of the difference between the ratio of the charge and momentum of the muons measured in the ID and MS divided by the sum in quadrature of the corresponding uncertainties, is required to be less than seven to suppress the contamination due to hadrons.

The reconstruction efficiency measured in $Z \to \mu\mu$ events as a function of η for muons with $p_{\mathrm{T}} > 10$ GeV is shown in Figure 4.6.

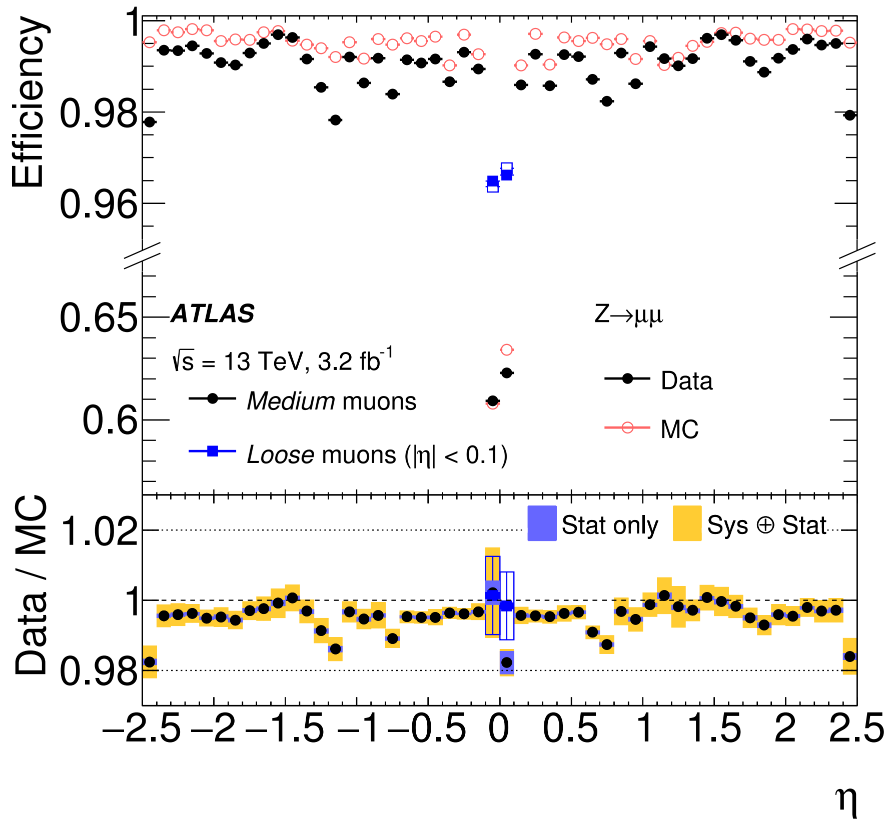

Figure 4.6: Muon reconstruction efficiency as a function of η measured in $Z \rightarrow \mu\mu$ events for muons with $p_{\mathrm{T}} > 10\,\mathrm{GeV}$ shown for the Medium muon selections. The error bars on the efficiencies indicate the statistical uncertainty.Panels at the bottom show the ratio of the measured to predicted efficiencies, with statistical and systematic uncertainties. In addition, the plot also shows the efficiency of the Loose identification (squares) in the region $|\eta| < 0.1$ where the Loose and Medium identification criteria differ significantly. Taken from Ref. [127].

4.6 Jet and b-tagging

Due to QCD confinement, quarks and gluons can not exist as free particles which should be colorless states at TeV energy scale. Hence the colored product from pp collision, namely quarks and gluons, will hadronize to form a spray of collimated hadrons refer to as *Hadronic Jets*.

Jet reconstruction and energy calibration

Hadronic jets are reconstructed using the anti-k_t algorithm with radius parameter $R = 0.4$ [128, 129]. The reconstruction is performed up to $|\eta| = 4.9$. The particle flow (*PFlow*) algorithm [130], which directly[6] combines measurements from both the tracker and the calorimeter to form the input signals for jet reconstruction.

The Jet Energy Scale (JES) calibration [132] restores the jet energy to that of jets reconstructed at the particle level. All stages correct the four-momentum, scaling the jet p_T, energy, and mass. The average jet energy response is shown in Figure 4.7 and defined as the mean of a Gaussian fit to the core of the $E^{\mathrm{reco}}/E^{\mathrm{truth}}$ distribution for jets[7].

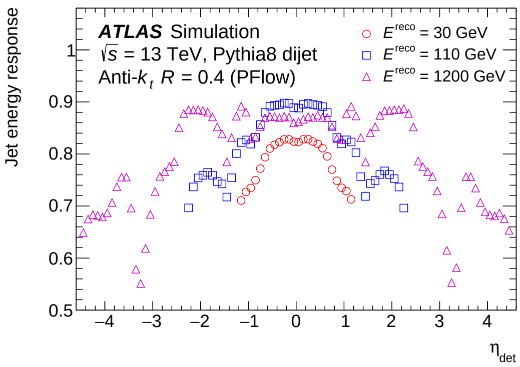

(a)

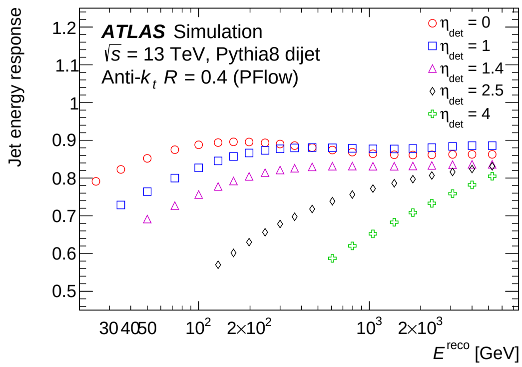

(b)

Figure 4.7: The average energy response as a function of the reconstructed jet (a) detector pseudorapidity, η_{det}, and (b) reconstruction energy. Each value is obtained from the corresponding parameterized function derived with the Pythia8 Monte-Carlo sample and only jets satisfying $p_T > 20$ GeV are shown. Taken from Figure 5 in Ref. [132].

Jet selection

Only jets with $p_{\mathrm{T}} > 20$ GeV and $|\eta| < 2.5$ (central jets), or $p_{\mathrm{T}} > 30$ GeV and $2.5 < |\eta| < 4.5$ (named forward jets) are considered as baseline jets in analysis. For jets with $p_{\mathrm{T}} < 60$ GeV and $|\eta| < 2.4$,

[6] For previous EM scale topo-clusters jets [131], an indirect method named correction factor, which includes information from tracks associated with the jet, was found to to improve the jet energy resolution greatly.

[7] E^{reco} is the reconstructed jet energy and E^{truth} is the energy of the truth particle jet

Jet Vertex Tagging (JVT) discriminant [133] is used to suppress jets originating from pile-up. All baseline jets will be used in missing transverse energy reconstruction described below (section 4.8).

b-jet identification

Hadronic jets initiated by b-quarks is an important experimental signature. B-hadron has a longer lifetime than light-flavor hadrons. As discussed in section 2.1.4, b-hadrons can travel small distances (~1 mm) before it decays. Hence the decay vertices of the b-hadron can be differentiated from the PV.

DL1r *b*-tagging algorithm based on a deep neural network [134, 135] is used to identify the jets which contain *b*-flavored hadrons in the region $|\eta| < 2.5$. It makes use of the impact parameters and truth category information of tracks associated with the jet, the position of reconstructed secondary vertices and their compatibility with the decay chains of such hadrons. Specially, a RNN [136] illustrated in Figure 4.8 is used to provide low level input of tracks associated with the jet to DL1r. Comparison in Figure 4.9 shows that with RNN input, the tagger has better performance in selecting *b*-jets.

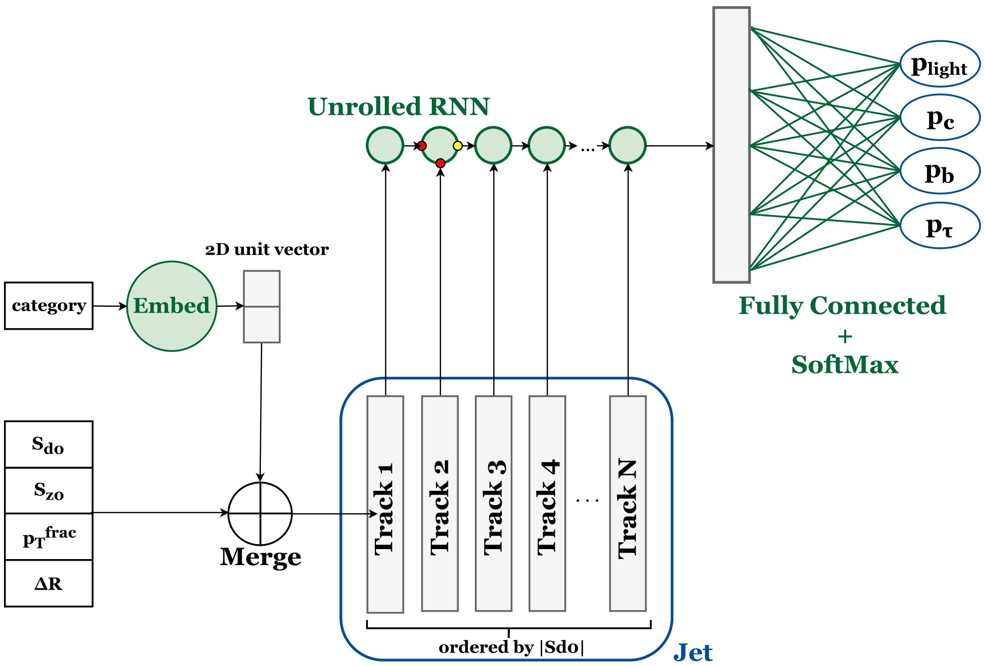

(a)

Figure 4.8: A schematic diagram of the RNN-based flavor-tagger, showing input features, network structure, and the 4-class output. In training, track sequences are truncated after a maximum of 15 tracks, while in application all tracks are considered. All tracks are feed into an unrolled RNN ordered by |Sdo| (d_0/σ_{d_0}). Taken from Ref. [136].

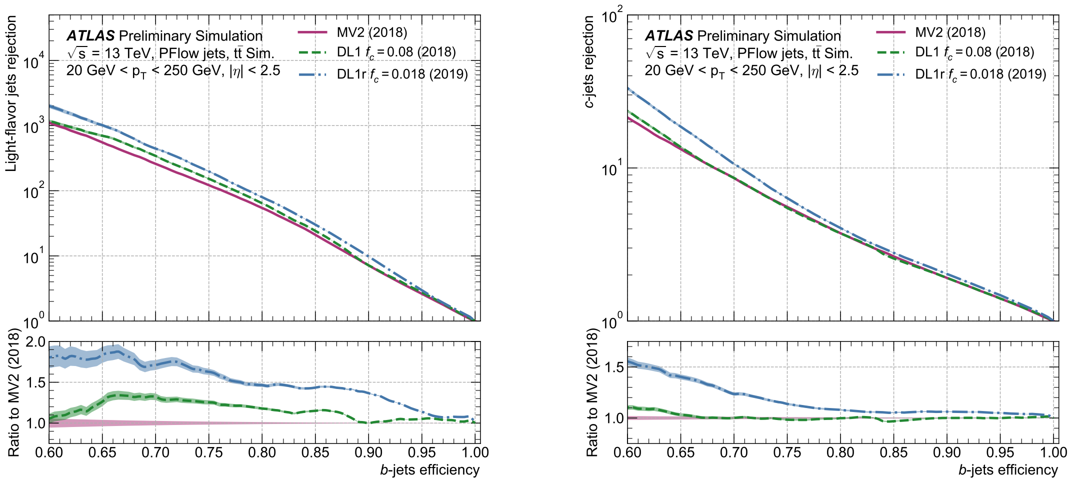

(a) (b)

Figure 4.9: Comparison of ROC curves for 2019 DL1r algorithm, and previous ATLAS used 2018 recommended versions of MV2(based on BDT) and DL1(based on DNN). The x-axis corresponds to the b-jet efficiency, while the y-axis corresponds to (a) light-flavor jets rejection ($1/\epsilon_u$) and (b) c-jets rejection ($1/\epsilon_c$). The performance is evaluated on anti-k_t $R = 0.4$ particle flow jets with $20 < p_T < 250$ GeV and $|\eta| < 2.5$, on a simulated dataset of $t\bar{t}$ events. The shaded bands represent the statistical uncertainty. Taken from Ref. [136]

For the analyses presented in this thesis, b-jet identification (b-tagging) is important to reduce the $t\bar{t}$ background by a b-jet veto. The chosen working point is with 70% b-tagging average efficiency[137], as measured in $t\bar{t}$ events.

4.7 Electron and Muon Isolation

Particles from colorless and colored final states have quite a different detector response in ATLAS. Colorless final states, such as $pp \to W \to \ell\nu$ and $pp \to Z \to \ell\ell$, will produce isolated particles. Isolated indicates no other particles in the vicinity. At the detector level, these particles deposit energies in very localized detector regions. On the contrary, colored final states, such as $pp \to b\bar{b}$, $pp \to$ jets, will produce many colored particles and form jets because of QCD confinement. Hence a hadron tends to have many other particles nearby, which means it is not isolated. Figure 4.10 shows the predictions of cross-section at proton-proton colliders. Such a large amount of hadronic final states indicates that it is necessary to develop tools to identify isolated leptons in analysis with leptonic final states.

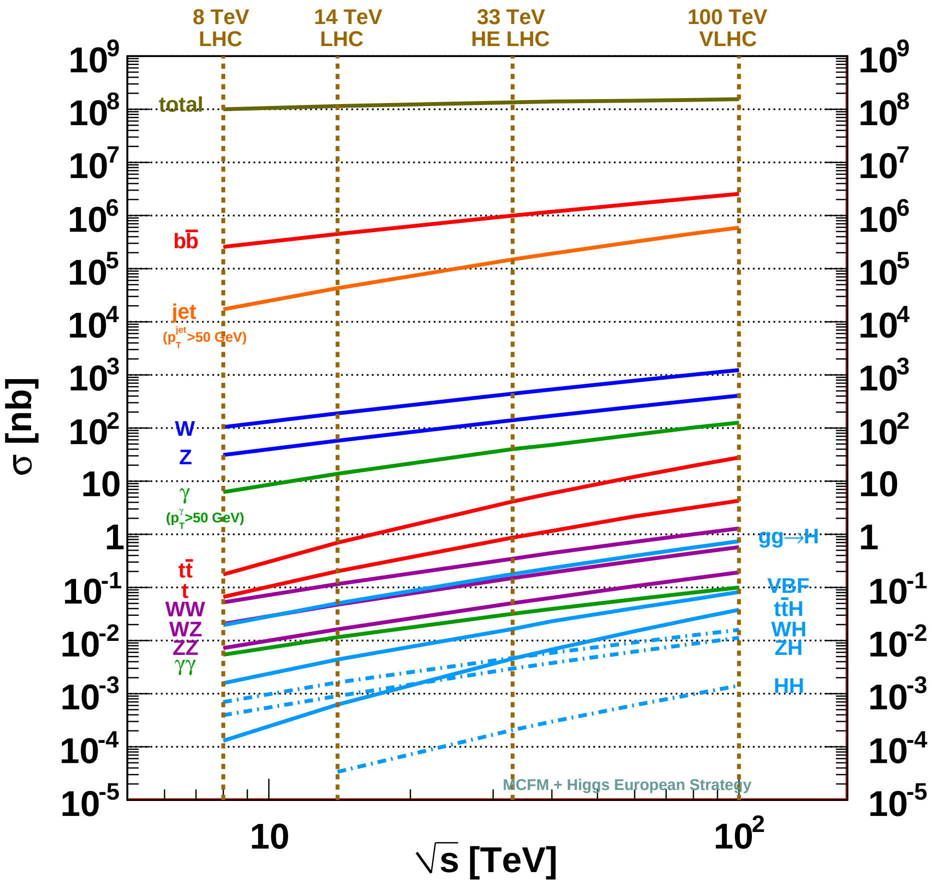

(a)

Figure 4.10: Cross section predictions at proton-proton colliders as a function of center-of-mass operating energy, $\sqrt{s}$. Taken from Ref. [138].

Lepton isolation variables and working points

In Section 4.4 and 4.5, electron and muon identification was introduced for selecting prompt electron/muon candidates. In order to complement the selection between leptons and jets, lepton *isolation* criteria, which describe the isolated situation near leptons, are chosen and tuned to select prompt leptons. Ref. [120, 139] discussed the isolation optimization study. The isolated leptons tend to have concentrated energy deposits in calorimeter or detector hits in ID. Hence two variables are used as input for the isolation criteria, constructed separately from the calorimeter and the ID information.

The calorimeter-based isolation variable is defined as the sum of the transverse energy of topological cell clusters in a cone around the lepton, excluding the transverse momentum of the electron of muon. The size of the cone is $\Delta R = 0.2$ for both leptons, thus the isolation variable is referred to as $E_{\mathrm{T}}^{\mathrm{cone20}}$. A correction for the pile-up and underlying-event contribution to the isolation cone is also estimated [140].

In order to estimate pileup event's contribution, the ATLAS jet calibration technique [133] is applied, but cause poor energy resolution to isolation variable.

The track-based isolation is defined as the scalar sum of the transverse momenta of the ID tracks associated with the primary vertex in a cone around the lepton. The lepton track itself is excluded. The size of cone is size $\Delta R = 0.2$, or $\Delta R = \min(10\mathrm{GeV}/p_{\mathrm{T}}^{\ell}, 0.3)$, thus the isolation variables are referred to as $p_{\mathrm{T}}^{\mathrm{cone20}}$ and $p_{\mathrm{T}}^{\mathrm{varcone30}}$, depending on the isolation selection criterion, for both leptons. Track-based isolation variables are more robust, because of the rejection of pile-up event's tracks.

The two isolation variables have their own advantages. Track-based isolation is better at energy resolution and pile-up tolerance, while calorimeter-based isolation can include neutral particles contribution which is not included by track-based isolation. Combining selections on track-based and calorimeter-based isolation is widely used in ATLAS and generally results in better performance than using only one of them. Furthermore, a multivariate discriminant, prompt lepton BDT [141], is developed including not only two isolation variables but more information, such as tracks kinematic information and multiplicity within a cone of size $\Delta R = = 0.4$ around the lepton, lepton kinematics and detector response, and the low level RNN algorithms[8] output used for b-tagging.

Working points used in the main analysis are presented in Table 4.2. Typical prompt electrons efficiencies [120, 139, 142] for Tight (Loose) working points are ~80% (~95%), while ~90% (~97%) in muons case. For heavy-flavor decay, the typical efficiencies are ~8% (~25%) for electrons and ~10% (~30%) for muons. For light-flavor decay, the typical efficiencies are ~12% (~25%) for electrons and ~15% (~30%) for muons. Prompt lepton BDT working points are defined with similar efficiency as Tight working points for both electrons and muons.

[8] Same algorithm as described in Section 4.6

Table 4.2: Definitions of the lepton isolation working points. The criteria used are listed in the second column, Non-BDT WPs exist in two variants: one with the cone ΔR parameter decreasing with p_T as min(10 GeV/pT, 0.3), referred to as $p_T^{\text{varcone30}}$; the other remaining constant at $\Delta R = 0.2$ for $p_T > 50$ GeV, referred to as p_T^{cone20}.

Lepton	Working point	Definition
Electron	Loose	$p_T^{\text{varcone30}}/p_T < 0.15$ and $E_T^{\text{cone20}} < 0.2$
Electron	Tight	$p_T^{\text{varcone30}}/p_T < 0.06$ and $E_T^{\text{cone20}} < 0.06$
Muon	Loose	$p_T^{\text{varcone30}}/p_T < 0.15$ and $E_T^{\text{cone20}} < 0.3$
Muon	Tight	$p_T^{\text{varcone30}}/p_T < 0.04$ and $E_T^{\text{cone20}} < 0.15$
Electron and Muon	prompt lepton BDT	$p_T^{\text{varcone30}}/p_T < \max(1.8, 0.15 p_T)$ BDT cut as a function with p_T [141]

4.8 Missing transverse energy

Neutrinos interact weakly with the ATLAS detector material. Detecting them with the ATLAS detector is challenging. However, indirect information on such particles' presence can still be detected by the momentum imbalance in the xy plane. For collision event in ATLAS, the transverse momentum of the initial state is zero, hence the final state should also have zero transverse momentum. The imbalance in the total measured momentum in the transverse plane is defined as the E_T^{miss}.

The E_T^{miss} reconstruction [143–145], in the main analysis, is calculated with the vector sum of the transverse momenta of all identified muon candidates, electron candidates and jets, and an additional soft term,

$$E_T^{\text{miss}} = E_{T,e}^{\text{miss}} + E_{T,\mu}^{\text{miss}} + E_{T,\text{jet}}^{\text{miss}} + E_{T,\text{SoftTerms}}^{\text{miss}}. \tag{4.3}$$

where the notation $E_{T,\text{obj}}^{\text{miss}}$ indicates a negative vector sum of momenta of a certain type of objects: $E_{T,\text{obj}}^{\text{miss}} = -\sum \vec{p}_T{}^{\text{obj}}$. The soft term $E_{T,\text{SoftTerms}}^{\text{miss}}$ is constructed from all tracks that are matched to the primary vertex but not associated with any reconstructed objects.

Figure 4.11 shows the performance of E_T^{miss} measurement performed in Ref. [145], where Loose E_T^{miss} working point includes the jet selection[9] described in section 4.6, the Medium identification and Loose isolation for electron, $p_T > 10$ GeV for CB and ST muons.

[9] Except the p_T requirement for jets in range $2.5 < |\eta| < 4.5$, which is >60 GeV in the measurement.

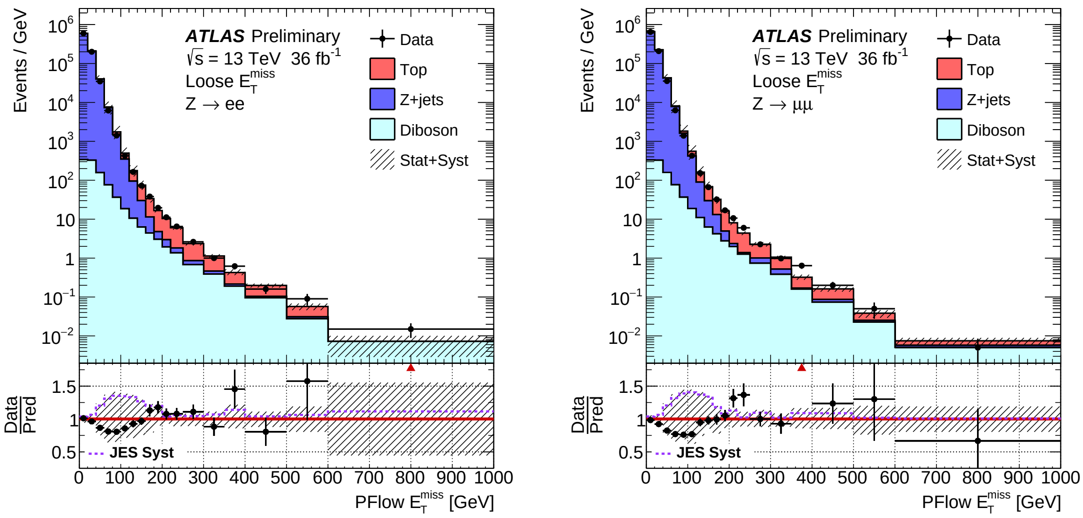

(a) (b)

Figure 4.11: Performance of $E_{\mathrm{T}}^{\mathrm{miss}}$ measurement based on the Loose $E_{\mathrm{T}}^{\mathrm{miss}}$ operating point are shown in data and Monte-Carlo simulation for events satisfying the (a) $Z \to ee$ and (b) $Z \to \mu\mu$ selections. The bottom panel shows the ratio of data to Monte-Carlo simulation, and the bands correspond to the full uncertainties. The largest contribution to the uncertainty band comes from the JES systematic uncertainties, and it is shown in a dotted line. Taken from Figure 8 in Ref. [145].

Part II

Search for doubly charged Higgs bosons decayed into same-sign W bosons

5 Data and Monte Carlo Samples

Contents

5.1 Data

This analysis is performed using 139 fb^{-1} of data collected from proton-proton collision recorded by the ATLAS detector at $\sqrt{s}$ =13 TeV center-of-mass energy, from 2015 to 2018 (Described in Chapter 3). The data set has been collected with a bunch spacing of 25 ns[1], and verifying data quality requirements which must be in the recommended Good Run List [41].

5.2 Signal samples

For both the pair-production of $H^{\pm\pm}H^{\mp\mp}$ and the associate-production of $H^{\pm\pm}H^{\mp}$ processes, the events at partonic level are generated with the MG5_aMC [42] generator (Matrix Element Leading Order, ME LO) using the PDF NNLOPDF30. The events are subsequently showered using PYTHIA8 [43] with A14 tune [44], and passed through the official ATLAS detector simulation (AtlFast II Algorithm, denoted also with AFII later in the thesis) and reconstruction. The samples were digitized using a 25 ns bunch spacing configuration, and the general MC16a (corresponding to data collected in 2015-2016), MC16d (corresponding to data collected in 2017) and MC16e (corresponding to data collected in 2018) configuration, and the updated distribution of the average number of pile-up interactions per bunch crossing for 2015-2018.

The signal samples have been simulated with $m_{H^{\pm\pm}}$ = 200, 300, 400, 500, 600 GeV. for both production modes. $m_{H^{\pm}}$ has been chosen[2] in a small mass range (<5 GeV) to maximize the cross-section of associate-production. One filter that selects events with at least two light leptons[3] (electron or

[1] In early 2015, the bunch spacing was set as 50 ns to re-establish operation at high stored energies [81].
[2] The value of other parameters (such as λ) were checked to have trivial values followed Eq. (eq:EWSB mhpp) and Eq. (eq:EWSB mh). To make sure valid λ parameters exist, $m_{H^{\pm}}$ is usually not equal to $m_{H^{\pm\pm}}$
[3] For pair-production, at least two same-sign leptons were required.

muons, no tau veto applied) with $p_T > 10$ GeV and $|\eta| < 10$ is applied at truth level for both the pair-production $H^{\pm\pm}H^{\mp\mp}$ and the associate-production $H^{\pm\pm}H^{\mp}$. The production cross sections (NLO) and the filter efficiencies are shown in Table 5.1 and 5.2, while the k-factor is taken from Ref. [146].

H^{++} mass (GeV)	200	300	400	500	600
cross section (fb)	81.04	16.48	4.883	1.766	0.726
filter efficiency	0.1089	0.1161	0.1198	0.1249	0.1237

Table 5.1: Cross sections (ME LO + PDF LO, k-factor = 1.25 is applied for NLO correction), filter efficiencies of the AFII signal samples (pair-production $pp \to H^{\pm\pm}H^{\mp\mp}$).

H^{++} mass (GeV)	200	300	400	500	600
H^{+} mass (GeV)	196	295	395	496	602
cross section (fb)	88.66	9.463	2.988	1.175	0.513
filter efficiency	0.2573	0.2814	0.2997	0.3178	0.3278

Table 5.2: Cross sections (ME LO + PDF LO, k-factor = 1.25 is applied for NLO correction), filter efficiencies of the AFII signal samples (associate-production $pp \to H^{\pm\pm}H^{\mp}$).

5.3 Background samples

Event generator programs and configurations used for simulating the background processes are shown in Table 5.3. Detailed descriptions of the generator configurations may be found in Refs. [45–48]. In all cases a SM Higgs boson mass of 125 GeV is assumed. Generated events are passed through a full GEANT4 [49] simulation of the ATLAS detector.

Production of $t\bar{t}H$, $t\bar{t}W$, $t\bar{t}Z$, and tZ is simulated with a next-to-leading order (NLO) QCD matrix element computed by MadGraph5_aMC@NLO (Powheg for $t\bar{t}H$), matched to the Pythia 8 parton shower. Production VH is simulated at leading order with Pyhtia 8 and EvtGen with the A14 Pythia 8 tune. Production of VV, $VVqq$, $V\gamma$, and VVV are simulated with a NLO QCD matrix element computed by Sherpa and matched to the Sherpa parton shower which uses the NNPDF 3.0 NLO PDF. Production of $t\bar{t}t\bar{t}$, $t\bar{t}t$, $t\bar{t}W^+W^-$ and $tW(Z/\gamma^*)$ are simulated at leading order with MadGraph5_aMC@NLO using NNPDF 2.3 LO and matched to the Pythia 8 parton shower.

All processes which result in a final state formed by two or three or more prompt leptons are considered when evaluating the prompt contributions with Monte-Carlo simulations in the $2\ell^{sc}$, 3ℓ and 4ℓ channels, respectively. The $V\gamma$ processes for photon conversion backgrounds are taken from the Monte-Carlo simulations. The non-prompt lepton background is estimated using data-driven methods, and several cross-checks are done with $t\bar{t}$, single top and V+jets Monte-Carlo simulations.

Process	ME Generator	Parton Shower	PDF	Tune
$t\bar{t}H$	POWHEG [147]	PYTHIA 8 [43]	NNPDF 3.0 NLO [148]	A14 [44]
VH	PYHTIA 8	PYTHIA 8	NNPDF 2.3 LO	A14
$t\bar{t}W$	MG5_AMC	PYTHIA 8	NNPDF 3.0 NLO/2.3 LO	A14
$t\bar{t}(Z/\gamma^*)$	MG5_AMC	PYTHIA 8	MEN 3.0 NLO	A14
$t(Z/\gamma^*)$	MG5_AMC	PYTHIA 8	NNPDF 3.0 NLO	A14
$t\bar{t}$	POWHEG [147]	PYTHIA 8	NNPDF 3.0 NLO/2.3 LO	A14
s-, t-channel, Wt single top	POWHEG [149, 150]	PYTHIA 8	NNPDF 3.0 NLO/2.3 LO	A14
VV, $qqVV$, VVV	SHERPA 2.2.2 [151]	SHERPA	NNPDF 3.0 NNLO	SHERPA default
$Z \to \ell^+\ell^-$	SHERPA 2.2.2	SHERPA	NNPDF 3.0 NNLO	SHERPA default
$W \to \ell\nu$	SHERPA 2.2.2	SHERPA	NNPDF 3.0 NNLO	SHERPA default
$Z\gamma$ / $W\gamma$	SHERPA 2.2.4/2.2.2	SHERPA	NNPDF 3.0 NNLO	SHERPA default
$t\bar{t}t\bar{t}$, $t\bar{t}t$	MG5_AMC	PYTHIA 8	NNPDF 2.3 LO	A14
$t\bar{t}W^+W^-$	MG5_AMC	PYTHIA 8	NNPDF 2.3 LO	A14
$tW(Z/\gamma^*)$	MG5_AMC	PYTHIA 8	NNPDF 3.0 NLO	A14

Table 5.3: Configurations used for event generation of background processes. If only one parton distribution function (PDF) is shown, the same one is used for both the matrix element (ME) and parton shower generators; if two are shown, the first is used for the matrix element calculation and the second for the parton shower. “V” refers to production of an electroweak boson (W or Z/γ^*). “Tune” refers to the underlying-event tune of the parton shower generator. “MG5_AMC” refers to MADGRAPH5_AMC@NLO 2.2.1; “PYTHIA 6” refers to version 6.427; “PYTHIA 8” refers to version 8.2; “HERWIG++” refers to version 2.7. The samples have heavy flavor hadron decays modeled by EVTGEN 1.2.0 [152], except for samples generated with “SHERPA". In Tables A.1, A.2, A.3, A.4, A.5 and A.6 (from appendix A) all Monte-Carlo samples used in the analysis are shown.

5.3.1 Legend name for distribution plots

Table 5.4 includes the details on the group of samples shown in the legend of the data versus background plots presented in this thesis, for the $2\ell^{sc}$, 3ℓ and 4ℓ channels. Note that in the prompt category, the V+γ events are considered even if these are not "events with all prompt leptons" because their estimation are done with Monte-Carlo and not with the data-driven method. Opposite-sign WW processes are removed when the data-driven results are shown in the $2\ell^{sc}$ channel, as it will be double-counted with the electron charge misidentification and light flavor non-prompt leptons background estimation.

Legend Name	Sample included
Wjets	W + jets production with charge mis-identification electron & fake leptons. Details in Table A.6.
Zjets	Z + jets production with charge mis-identification electron & fake leptons. Details in Tables A.4-A.5.
WW,WZ,ZZ	Diboson production. Details in Table A.1.
VVV	Triboson production. Details in Table A.1.
VH	Vector boson + Higgs production. Details in Table A.1.
Top	Charge mis-identification electron & fake lep produced when top quarks ($t\bar{t}$, single top). Details in Tables A.5.
Rare Top	Rare processes with top-quark. Including $t\bar{t}t\bar{t}$, $t\bar{t}t$, $t\bar{t}W^{+}W^{-}$ and tWZ/γ^{*}. Details in Table A.2.
ttX	Prompt leptons with top quarks($t\bar{t}V$, $t\bar{t}H$, tZ and Rare Top. Details in Table A.1.
Vgam/$V\gamma$	V(W,Z)+photon production. Details in Table A.3.
Prompt	WW,WZ,ZZ,VH,VVV,ttX,Vgam. All these processes are estimated with Monte-Carlo.
Non-Prompt/Fake	W + jets, Z + jets, Top. Or (Full/semi)data-driven fake lepton background estimation.
Misid/chargeflip	Data-driven electron charge mis-identification background estimation.

Table 5.4: Details on the group of samples/events mentioned in the legend of plots shown in the thesis, for the $2\ell^{sc}$, 3ℓ and 4ℓ channels.

6 Analysis Overview

Contents

In section 2.2.4, various production modes to bosonic final states in the LHC have been discussed. The pair-production and associate-production are the two most important charged Higgses. Moreover, the $W^{\pm}$ and Z bosons from the charged Higgs will further decay into leptons, neutrinos, or jets. The BRs of the various final states containing or not light leptons (electrons and muons) are shown in Table 6.1. The channels with 0 or 1 leptons have the highest BRs but are dominated by multi-jets (QCD) processes produced in abundance at the LHC. The final states studied in the present analysis include multilepton topologies for which the hadronic background is less severe and includes:

A Same-charge-two-lepton ($2\ell^{sc}$) events with $E_{\mathrm{T}}^{\mathrm{miss}}$ and multi-jets (see Figure. 6.1);

B Three-lepton (3ℓ) events with $E_{\mathrm{T}}^{\mathrm{miss}}$ and multi-jets (see Figure. 6.2);

C Four-lepton (4ℓ) events with $E_{\mathrm{T}}^{\mathrm{miss}}$ (see Figure 6.3).

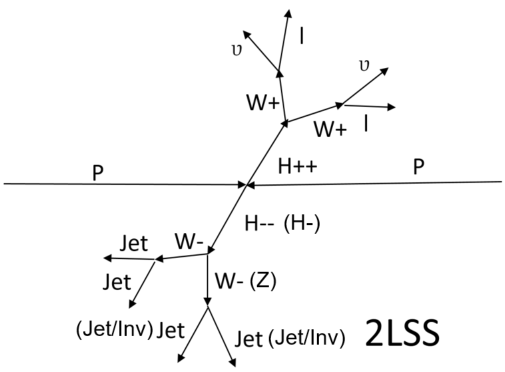

Figure 6.1: Illustration of the features in kinematic of $2\ell^{sc}$ events with $E_{\mathrm{T}}^{\mathrm{miss}}$ and multi-jets for both pair-production and associate-production .

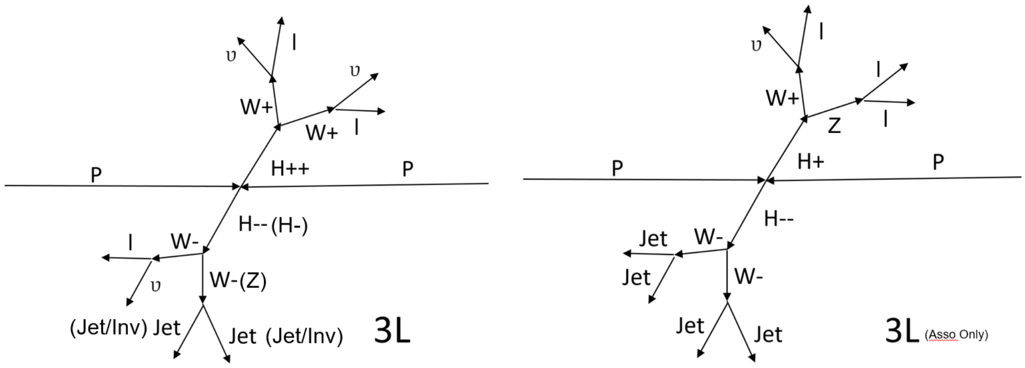

Figure 6.2: Illustration of the features in kinematic of 3ℓ events with $E_{\mathrm{T}}^{\mathrm{miss}}$ and multi-jets for both pair-production and associate-production .

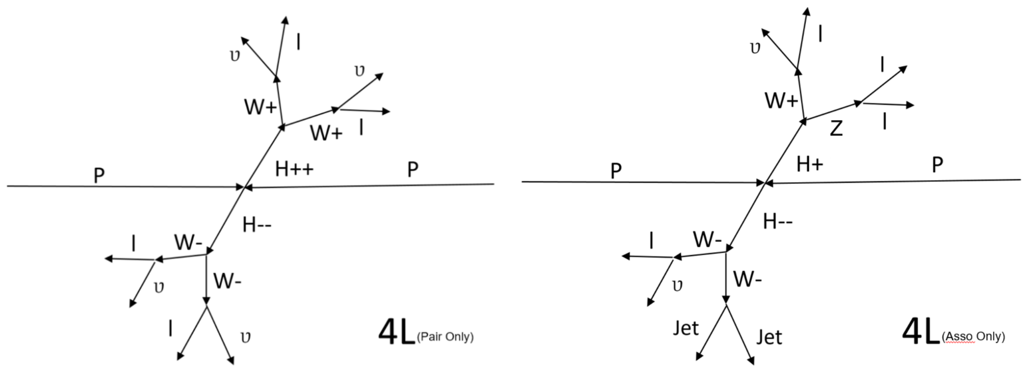

Figure 6.3: Illustration of the features in kinematic of 4ℓ events for both pair-production and associate-production .

In order to suppress the multi-jets background, very hard requirements must be placed on the key kinematic variables, which is not the case for the multilepton *signal* regions. In this analysis, only the multileptonic final states are considered. Despite the lower BRs, these channels are still crucial for searches beyond the SM (BSM) and allow us to probe the (softer) BSM phase space usually not covered by 0 or 1 lepton searches.

The experimental signatures considered in the present analysis for the pair-production mode:

$$H^{\pm\pm}H^{\mp\mp} \longrightarrow 4W \rightarrow \ell^{\pm}\ell^{\pm} + E_{\mathrm{T}}^{\mathrm{miss}} + 4j \qquad (2\ell^{sc}) \tag{6.1}$$

$$\rightarrow \ell^{\pm}\ell^{\mp}\ell^{\mp} + E_{\mathrm{T}}^{\mathrm{miss}} + 2j \qquad (3L) \tag{6.2}$$

$$\rightarrow \ell^{\pm}\ell^{\pm}\ell^{\mp}\ell^{\mp} + E_{\mathrm{T}}^{\mathrm{miss}} \qquad (4L) \tag{6.3}$$

For associate-production, currently we just look at the same final states as for the pair-production :

$$H^{\pm\pm}H^{\mp} \longrightarrow WWWZ \rightarrow \ell^{\pm}\ell^{\pm} + E_{\mathrm{T}}^{\mathrm{miss}} + 4j \qquad (2\ell^{sc}) \tag{6.4}$$

$$\rightarrow \ell^{\pm}\ell^{\mp}\ell^{\mp} + E_{\mathrm{T}}^{\mathrm{miss}} + 2j \qquad (3L) \tag{6.5}$$

$$\rightarrow \ell^{\pm}\ell^{\pm}\ell^{\mp}\ell^{\mp} + E_{\mathrm{T}}^{\mathrm{miss}} \qquad (4L) \tag{6.6}$$

$H^{\pm\pm}H^{\mp\mp} \rightarrow$	$4W \rightarrow$	BR (in %)
$4\ W \rightarrow jj$	0ℓ + 8 jets	20.1
$3\ W \rightarrow jj$, $1\ W \rightarrow \nu\ell$	$1\ell + E_{\mathrm{T}}^{\mathrm{miss}}$ + 6 jets	39.7
$2\ W \rightarrow jj$, $2\ W \rightarrow \nu\ell$	$2\ell + E_{\mathrm{T}}^{\mathrm{miss}}$ + 4 jets	29.3 ($2\ell^{sc}$: 9.8)
$1\ W \rightarrow jj$, $3\ W \rightarrow \nu\ell$	$3\ell + E_{\mathrm{T}}^{\mathrm{miss}}$ + 2 jets	9.6
$4\ W \rightarrow \nu\ell$	$4\ell + E_{\mathrm{T}}^{\mathrm{miss}}$ + no jets	1.2

(a)

$H^{\pm\pm}H^{\mp} \rightarrow$	$WWWZ \rightarrow$	BR (in %)
$3\ W \rightarrow jj$, $Z \rightarrow jj$	0ℓ + 8 jets	22.0
$3\ W \rightarrow jj$, $Z \rightarrow \nu\nu$	$0\ell + E_{\mathrm{T}}^{\mathrm{miss}}$ + 6 jets	6.3
$2\ W \rightarrow jj$, $1\ W \rightarrow \nu\ell$, $Z \rightarrow jj$	$1\ell + E_{\mathrm{T}}^{\mathrm{miss}}$ + 6 jets	31.1
$2\ W \rightarrow jj$, $1\ W \rightarrow \nu\ell$, $Z \rightarrow \nu\nu$	$1\ell + E_{\mathrm{T}}^{\mathrm{miss}}$ + 4 jets	8.9
$3\ W \rightarrow jj$, $Z \rightarrow \ell\ell$	2ℓ + 6 jets	3.1 ($2\ell^{sc}$: 0)
$1\ W \rightarrow jj$, $2\ W \rightarrow \nu\ell$, $Z \rightarrow jj$	$2\ell + E_{\mathrm{T}}^{\mathrm{miss}}$ + 4 jets	14.6 ($2\ell^{sc}$: 4.7)
$1\ W \rightarrow jj$, $2\ W \rightarrow \nu\ell$, $Z \rightarrow \nu\nu$	$2\ell + E_{\mathrm{T}}^{\mathrm{miss}}$ + 2 jets	4.2 ($2\ell^{sc}$: 1.4)
$2\ W \rightarrow jj$, $1\ W \rightarrow \nu\ell$, $Z \rightarrow \ell\ell$	$3\ell + E_{\mathrm{T}}^{\mathrm{miss}}$ + 4 jets	4.4
$3\ W \rightarrow \nu\ell$, $Z \rightarrow jj$	$3\ell + E_{\mathrm{T}}^{\mathrm{miss}}$ + 2 jets	2.3
$3\ W \rightarrow \nu\ell$, $Z \rightarrow \nu\nu$	$3\ell + E_{\mathrm{T}}^{\mathrm{miss}}$	0.7
$1\ W \rightarrow jj$, $2\ W \rightarrow \nu\ell$, $Z \rightarrow \ell\ell$	$4\ell + E_{\mathrm{T}}^{\mathrm{miss}}$ + 2 jets	2.1
$3\ W \rightarrow \nu\ell$, $Z \rightarrow \ell\ell$	$5\ell + E_{\mathrm{T}}^{\mathrm{miss}}$ + no jets	0.3

(b)

Table 6.1: Decay channels and BRs of (a) Pair-production of $H^{\pm\pm}$ and (b) associate-production of $H^{\pm\pm}$ and $H^{\mp}$. For simplification, All tauons are temporary considered as leptonic decay here. In the actual analysis, only leptonic tauon decay (where tauons decay into electrons or muons and neutrinos) will be considered in event selection.

Even if the associate-production can lead to a richer phenomenology when compared to the $H^{\pm\pm}$ pair-production, it was decided to focus on the same experimental signature for both production modes. Few arguments below:

i) When referring to the exclusive same-charge-two-lepton ($2\ell^{sc}$) channel, the additional channel 2ℓ + 2jets + $E_{\mathrm{T}}^{\mathrm{miss}}$ is not dominant compared to the 2ℓ + 4jets + $E_{\mathrm{T}}^{\mathrm{miss}}$ one (BR 4.2% compared to 14.6%). In addition, a lower requirement on the number of jets may introduce much more QCD background.

ii) When referring to the exclusive three-lepton (3ℓ) channel, the additional channel 3ℓ + 0jets + $E_{\mathrm{T}}^{\mathrm{miss}}$ is not dominant when compared to the 3ℓ + 2/4jets + $E_{\mathrm{T}}^{\mathrm{miss}}$ channel (0.7% compared to 6.7%). Similarly to the same-charge lepton channel, relaxing the requirement on the number of jets is expected to increase considerably the SM background.

iii) When referring to the four-lepton (4ℓ) channel, the additional channel 5ℓ + 0jets + $E_{\mathrm{T}}^{\mathrm{miss}}$ is not dominant when compared to the 4ℓ + 0/2jets + $E_{\mathrm{T}}^{\mathrm{miss}}$ channel (0.3% compared to 2.0%). This channel is expected to have low statistics and the improvement brought by a dedicated 5 lepton Signal Region (SR) will be negligible.

Even if the 4ℓ channel will not bring a huge increase in sensitivity it is still preferred to keep an exclusive 3ℓ channel and an exclusive 4ℓ channel. This is because both channels are very clean (only few SM processes can give such final states), and the *signal* regions, which are defined with very loose cuts on key kinematic variables, can be very sensitive to Beyond SM processes. In addition, the detector background is expected (and found) to be very low in these final states, thus less challenging to study. It can be concluded that this approach ensures a more complete scan of the Beyond SM phase space for new physics, in particular $H^{\pm\pm}$ and $H^{\pm}$ *signal*s.

6.1 Physics Object Selection in analysis

The physics object reconstruction has been described in Chapter 4. This section describes the specific object selection criteria that are used for the analysis presented in this thesis.

6.1.1 Trigger

Table 6.2: A summary of the triggers used in the presented analyses. "nod0" for electrons triggers indicates the d_0 requirement is removed (which is originally included in electron identification). More details of trigger description can be found in Ref. [153, 154].

2015	Description
HLT_e26_lhmedium_L1EM20VH	≥1 electron with p_T >26 GeV, MEDIUM identification and L1 p_T >20 GeV
HLT_e60_lhmedium	≥1 electron with p_T >60 GeV, MEDIUM identification
HLT_e120_lhloose	≥1 electron with p_T >120 GeV, LOOSE identification
HLT_mu20_iloose_L1MU15	≥1 CB muon with p_T >20 GeV, Loose isolation and L1 p_T >15 GeV
HLT_mu50	≥1 CB muon with p_T >50 GeV
2016-2018	Description
HLT_e26_lhtight_nod0_ivarloose	≥1 electron with p_T >26 GeV, TIGHT identification and Loose isolation
HLT_e60_lhmedium_nod0	≥1 electron with p_T >60 GeV, MEDIUM identification
HLT_e140_lhloose_nod0	≥1 electron with p_T >140 GeV, LOOSE identification
HLT_mu26_ivarmedium	≥1 CB muon with p_T >26 GeV, Medium isolation
HLT_mu50	≥1 CB muon with p_T >50 GeV

Candidate events are selected for read-out using lepton triggers that require the one electron or muon to satisfy identification criteria similar to those used in the offline reconstruction, isolation criteria, and a transverse momentum requirement of $p_T > 26$ GeV [153, 154]. With increasing p_T the requirements on identification and isolation become less stringent. All events must contain at least one tight lepton with p_T^{ℓ} >30 GeV that triggered the event.

6.1.2 Electron and Muon

This analysis uses four different lepton definitions with different quality requirements that are named "*baseline*", "*candidate*", "*candidate**", and "*signal*" leptons (Table 6.3). Leptons' transverse momentums are required to be higher than 10 GeV for all defined leptons. The longitudinal impact parameter of the lepton, z_0, is required to satisfy $|z_0 \sin\theta| < 0.5$ mm. The transverse impact parameter divided by its uncertainty, $|d_0|/\sigma(d_0)$, is required to be less than 5 for electrons, and 3 for muons (for *baseline* the value is 10). Electrons also need to be within $|\eta| < 2.47$ region and not in crack region ($1.37 < |\eta| < 1.52$), while muons need to be within $|\eta| < 2.5$.

The *baseline* selection is only for $E_{\mathrm{T}}^{\mathrm{miss}}$ reconstruction, with least requirements, as discussed in section 4.8.

In order to study the contributions from non-prompt leptons or photon converted to/misidentified as leptons, the "*candidate*" selection requirements are used, with LOOSE (MEDIUM) identification for electrons (muons) and no isolation requirements. In the 3ℓ channel, the opposite sign lepton (also denoted with "lepton 0" later in this thesis) is required to pass the "*candidate*" requirements.

*candidate** selection is defined by changing only the isolation requirement from no isolation to Loose isolation for both electron and muons. This isolation is used only in 4ℓ channel to select pure lepton *candidate*s but not as strict as prompt lepton BDT isolation.

"*signal*" lepton selection is applied for *signal* search for both leptons in $2\ell^{sc}$ channel and for the two same-charge leptons in the 3ℓ channel. The TIGHT (MEDIUM) identification and prompt lepton BDT isolation criteria are applied for electrons (muons). Electrons also need to satisfy the ECIDS requirements (section 4.4).

For all *signal* electrons, there must be no association with a vertex from a reconstructed photon conversion [155] in the detector material. To further reduce the photon conversion background in the $2\ell^{sc}$ channel, additional requirements are applied to the *signal* electrons [156]: i) the candidate must not have a reconstructed displaced vertex with radius $r > 20$ mm whose reconstruction uses the track associated with the electron, ii) the invariant mass of the system formed by the track associated with the electron and the closest track at the primary or a conversion vertex is required to be larger than 100 MeV; these selections are referred to as the photon conversion veto.

6.1.3 Jet

Jets followed the same requirement defined in section 4.6. Only jets passing the overlap removal (details will be discussed in Section 6.1.4) are further considered in the analysis. Jets containing b-hadrons are identified via b-tagging technique (Section 4.6).

6.1.4 Overlap Removal

After electron, muon, and jet selection, the overlap between reconstructed leptons or jets is resolved. First, one electron is removed if it shares an ID track with another electron which has higher p_T.

Table 6.3: The requirements applied to define the categories of leptons: *Baseline*, *Candidate* and *minimally isolated (Candidate*)*, and *Signal* leptons. The overlap removal procedure is not applied for the leptons. In the $2\ell^{sc}$ channel, the photon conversion veto is required in addition to the *Candidate* and *Signal* criteria.

Lepton	Electrons			
Category	*Baseline*	*Candidate*	*Candidate**	*Signal*
$\lvert z_0 \sin\theta\rvert$	< 0.5 mm			
$\lvert d_0\rvert/\sigma(d_0)$	< 5			
Identification	LOOSE			TIGHT
Isolation	No		Loose	Prompt lepton BDT
Electron charge identification	No	Yes		
Lepton	**Muons**			
Category	*Baseline*	*Candidate*	*Candidate**	*Signal*
$\lvert z_0 \sin\theta\rvert$	< 0.5 mm			
$\lvert d_0\rvert/\sigma(d_0)$	< 10	< 3		
Identification	MEDIUM			
Isolation	No		Loose	Prompt lepton BDT

Reject	**Against**	**Criteria**
electron ($e1$)	electron ($e2$)	share track, p_T ($e1$) < p_T ($e2$)
muon	electron	is calo-muon and share ID track
electron	muon	share ID track
jet	electron	$\Delta R < 0.2$
electron	jet	$\Delta R < 0.4$
jet	muon	$N_{Track} < 3$ and $\Delta R < 0.2$
muon	jet	$\Delta R < 0.4$

Table 6.4: Summary of overlap removal between electrons, muons and jets. Steps performed in the listed order. Only surviving objects participate in subsequent steps.

Secondly, calo-muons are removed if they share ID tracks with an electron. Thirdly, the remaining electrons are removed if they share tracks with muons. Fourthly, ambiguities between electrons and jets are resolved: jets with an identified electron nearby ($\Delta R < 0.2$) are removed; if the ΔR between the electron and jet is in the range of $0.2 < \Delta R < 0.4$, the electron is removed. Finally, if a muon and a jet are closer than $\Delta R = 0.4$, and the jet features less than three tracks, the jet is removed; Otherwise the muon is discarded. *signal*, *candidate* and *candidate** leptons are used in this overlap removal procedure. The illustration of overlap removal steps is shown in Table 6.4.

6.2 Event pre-selection

The event selection proceeds in two steps: the pre-selection and the *signal* regions (SRs) selection. Three channels defined as described in Section 6 and summarized in Table 6.5.

- **Same-charge-two-lepton ($2\ell^{sc}$)**: Only events with exactly two *signal* leptons of same electric charge are entering in this category (any event with a third *candidate* lepton are vetoed). Depending on the flavor of the two *signal* leptons forming a same-charge pair, three channels are defined: ee, $\mu\mu$, $e\mu$.
- **Three-lepton (3ℓ)**: exactly three *candidate* leptons with a total charge of ±1 are requested in each event. A veto is imposed on events for which at least one same-flavor opposite-charge (SFOC) lepton pair has an invariant mass within a ±10 GeV window around the Z-boson mass.
- **Four-lepton (4ℓ)**: exactly four *candidate** leptons with a total charge of 0 or ±2 are requested in each event. A veto is imposed on events which contain at least one same-flavor opposite-sign lepton pair with an invariant mass within a ±10 GeV window around the Z-boson mass (M_Z = 91.2 GeV) [1]. Lastly a cut on the 4ℓ mass is applied ($M_{4\ell}$ >100 GeV).

In all channels ($2\ell^{sc}$, 3ℓ and 4ℓ) at least one lepton must be *signal* lepton, the one used for the trigger matching. i) In the $2\ell^{sc}$ channel both leptons must be *signal* leptons; no other *candidate* leptons must be present in the event. ii) In the 3ℓ channel, the same-charge lepton pair must satisfy the *signal* lepton requirements; the remaining lepton should pass the *candidate* requirements; no other *candidate* lepton must be in the event. iii) In the 4ℓ channel, all leptons must pass the *candidate** requirements; no other *candidate* lepton must be in the event.

For the background-related measurements, the lepton condition might be relaxed from e.g. *signal* to *candidate*. Clear details are later in Chapter 7. The lepton conditions/categories were detailed in section 6.1.2. The *signal* regions selection will be discussed in Chapter 8.

6.3 Discriminating variables

Besides lepton and jet identification and kinematics quantities, several event level variables are defined to exploit the *signal* features described above and summarized in Table 6.6:

- **For same-charge-two-lepton ($2\ell^{sc}$) channel:**

  M_{jets} (or m_{jets}): the invariant mass of all jets in the event. When there are more than 4 jets in the event, only the leading 4 jets are considered for the calculation of the invariant mass.

  $M_{\ell\ell}$ ($M_{2\ell}$): di-lepton invariant mass. While a complete reconstruction of the $H^{\pm\pm}$ bosons is not possible using leptons due to escaping neutrinos, the variable still reflects the mass scale of the boson.

[1] For the associate-production , the Z boson veto will affect all signal events. Due to the large amount of background (e.g. ZZ) and small cross-section of associate-production , in the present analysis this Z boson veto is still applied. If there is a significant possibility of improvement in the future, this veto could be removed for better signal efficiency.

Table 6.5: The pre-selection criteria for the $2\ell^{sc}$, 3ℓ and 4ℓ analysis channels. The leptons are required to pass the *candidate*, *candidate** or *signal* requirements. The leptons are ordered by decreasing p_{T} ($\ell_1, \ell_2, ...$) in the $2\ell^{sc}$ and 4ℓ channels, while for the 3ℓ channel ℓ_1 and ℓ_2 denote the two same-charge leptons and ℓ_0 denotes the lepton with a charge opposite to the total lepton charge. Q_ℓ denotes the charge of each lepton. SFOC refers to same-flavor opposite-charge lepton pairs. The symbol "–" means no requirement is made. The equal sign (=) is used to emphasize that the selection criterion has to be exactly the given number. To ensure enough statistics for analysis, the $2\ell^{sc}$ channel only require >=3 jets.

Selection criteria	$2\ell^{sc}$	3ℓ	4ℓ
At least one offline *signal* lepton with $p_{\mathrm{T}}^{\ell} > 30$ GeVthat triggered the event			
N_ℓ (*candidate*)	=2	=3	=4
N_ℓ (*candidate**)	–	–	=4
N_ℓ (*signal*)	=2	≥2 ($\ell_{1,2}$)	≥1
$\lvert\sum Q_\ell\rvert$	=2	=1	≠4
Lepton p_{T}	$p_{\mathrm{T}}^{\ell_1,\ell_2} > 30, 20$ GeV	$p_{\mathrm{T}}^{\ell_0,\ell_1,\ell_2} > 10, 20, 20$ GeV	$p_{\mathrm{T}}^{\ell_1,\ell_2,\ell_3,\ell_4} > 10$ GeV
$E_{\mathrm{T}}^{\mathrm{miss}}$	> 70 GeV	> 30 GeV	> 30 GeV
N_{jets}	≥ 3	≥ 2	–
$N_{b\text{-jets}}$	=0		
Low SFOC $m_{\ell\ell}$ veto	–	$m_{\ell\ell}^{\mathrm{oc}} > 15$ GeV	
Z boson decay veto	$\lvert m_{ee}^{\mathrm{sc}} - m_Z\rvert > 10$ GeV	$\lvert m_{\ell\ell}^{\mathrm{oc}} - m_Z\rvert > 10$ GeV	
			$m_{4\ell} > 100$ GeV

$\Delta R_{\ell\ell}$ (or $\Delta R_{\ell^\pm\ell^\pm}$): the distance in $\eta - \phi$ between two same-charge leptons. The same sign leptons tend to be close for the *signal*, while some part the background favors a back-to-back topology. The distribution is shown in Figure fig:dRllMCOnly.

$\Delta\phi(\ell\ell, E_{\mathrm{T}}^{\mathrm{miss}})$: difference in azimuth between the di-lepton system and the $E_{\mathrm{T}}^{\mathrm{miss}}$.

$$\Delta\phi(\ell\ell, \mathrm{E}_{\mathrm{T}}^{\mathrm{miss}}) = |\phi(\ell\ell) - \phi(E_{\mathrm{T}}^{\mathrm{miss}})|, \in [0, \pi] \tag{6.7}$$

S: this is a variable used by the $2\ell^{sc}$ channel to describe the "spreads" of the azimuthal angles of leptons, $E_{\mathrm{T}}^{\mathrm{miss}}$, and jets, defined as the Root mean square (R.M.S.) of the ϕ's of the leptons and $E_{\mathrm{T}}^{\mathrm{miss}}$ times that of the jets divided by the RMS of the ϕ's of leptons, $E_{\mathrm{T}}^{\mathrm{miss}}$, and jets:

$$\mathrm{S} = \frac{\mathrm{R.M.S.}(\phi_{\ell_1}, \phi_{\ell_2}, \phi_{E_{\mathrm{T}}^{\mathrm{miss}}}) * \mathrm{R.M.S.}(\phi_{j1}, \phi_{j2}, \cdots)}{\mathrm{R.M.S.}(\phi_{\ell_1,}, \phi_{\ell_2}, \phi_{E_{\mathrm{T}}^{\mathrm{miss}}}, \phi_{j1}, \phi_{j2}, \cdots)}. \tag{6.8}$$

In the $2\ell^{sc}$ channel, the W bosons originating from one Higgs particle should decay to charged leptons and neutrinos, and the W bosons from the other Higgs particle should both decay to hadronic jets. The two charged leptons tend to be close in the azimuthal plane if the original Higgs boson carried relative large momentum. The directions of $E_{\mathrm{T}}^{\mathrm{miss}}$ and leptons should be centered around the direction of the Higgs particle. Thus, smaller spread in the azimuthal angles of leptons in the events are expected. The same correlations are expected for the jets from the other Higgs particle. The ratio of the R.M.S. defined above characterizes the feature of *signal* events.

$E_{\mathrm{T}}^{\mathrm{miss}}$ Missing transverse energy.

- **For three-lepton (3ℓ) channel:**

$\Delta R_{\ell\ell}$ (or $\Delta R_{\ell^\pm\ell^\pm}$): the distance in $\eta - \phi$ between two same-charge leptons. The same sign leptons tend to be close for the *signal*, while some part the background favors a back-to-back topology. In discussion about the 3ℓ channel, $\Delta R_{\ell\ell}$ is always refer to $\Delta R_{\ell^\pm\ell^\pm}$. The distribution is shown in Figure fig:dRll3LMCOnly.

$\Delta R_{\ell-jet}$ (or $\Delta R_{\ell-\mathrm{jet}}$): the minimal distance in $\eta - \phi$ between the opposite-sign lepton and leading jet. In the discussion about 3ℓ channel, $\Delta R_{\ell-jet}$ is always refer to $\Delta R_{\ell^\mp-\mathrm{lead\text{-}jet}}$.

$M_{x\ell}$ ($M_{3\ell}$): the invariant mass of three leptons.

$p_{\mathrm{T}}^{\mathrm{leading\ jet}}$: the leading jet p_{T}.

$\Delta R_{\ell^\mp,\ell^\pm\ell^\pm}$: the distance in $\eta - \phi$ plane between the same-charge lepton pair and the opposite sign lepton in each event.

$E_{\mathrm{T}}^{\mathrm{miss}}$ Missing transverse energy

- **For four-lepton (4ℓ) channel:**

$M_{x\ell}$ ($M_{4\ell}$): The invariant mass of four leptons.

$p_{\mathrm{T}}^{\ell_1}$: The transverse momentum of the highest p_{T} lepton.

$\Delta R_{\ell^\pm\ell^\pm}^{\mathrm{max}}$: The maximal distance in $\eta - \phi$ plane between the same-charge lepton pairs in each event.

$\Delta R_{\ell^\pm\ell^\pm}^{\mathrm{min}}$: The minimal distance in $\eta - \phi$ plane between the same-charge lepton pairs in each event.

$E_{\mathrm{T}}^{\mathrm{miss}}$ Missing transverse energy.

Channel	Related variables
$2\ell^{sc}$	M_{jets}, $M_{x\ell}$, $\Delta R_{\ell\ell}$, $\Delta\phi(\ell\ell, E_{\mathrm{T}}^{\mathrm{miss}})$, S, $E_{\mathrm{T}}^{\mathrm{miss}}$
3ℓ	$\Delta R_{\ell\ell}$, $\Delta R_{\ell-jet}$, $M_{x\ell}$, $p_{\mathrm{T}}^{\mathrm{leading\ jet}}$, $E_{\mathrm{T}}^{\mathrm{miss}}$, $\Delta R_{\ell^\mp,\ell^\pm\ell^\pm}$
4ℓ	$M_{x\ell}$, $p_{\mathrm{T}}^{\ell_1}$, $\Delta R_{\ell^\pm\ell^\pm}^{\mathrm{max}}$, $\Delta R_{\ell^\pm\ell^\pm}^{\mathrm{min}}$, $E_{\mathrm{T}}^{\mathrm{miss}}$

Table 6.6: Event level variables are defined to exploit the *signal* features. Some of all variables will be used as discriminating variable for *signal* region definition. For variable $M_{x\ell}$, x equals to the lepton numbers of the corresponding channel.

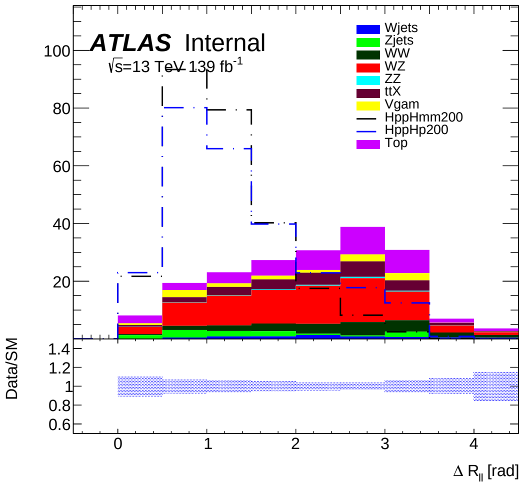

(a) ee channel

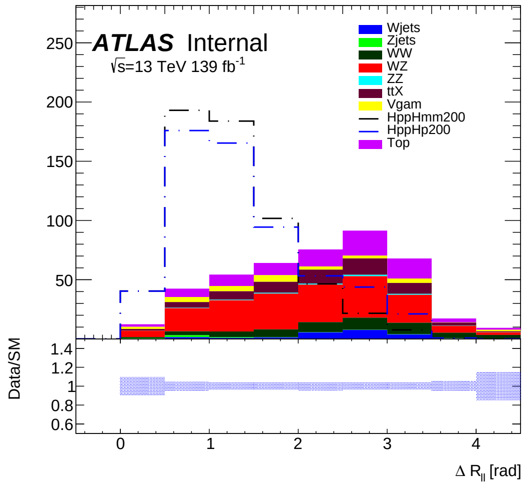

(b) $e\mu$ channel

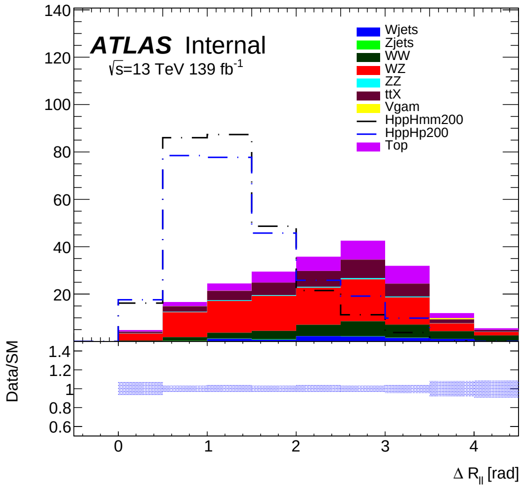

(c) $\mu\mu$ channel

Figure 6.4: $2\ell^{sc}$ channel: $\Delta R_{\ell^{\pm}\ell^{\pm}}$ distribution in the ee, $\mu\mu$ and $e\mu$ channels at the event pre-selection stage (Top left: ee. Top right: $\mu\mu$. Bottom: $e\mu$). Only the statistical uncertainties are shown. The signal is scaled to the same integral as background MC to have better vision.

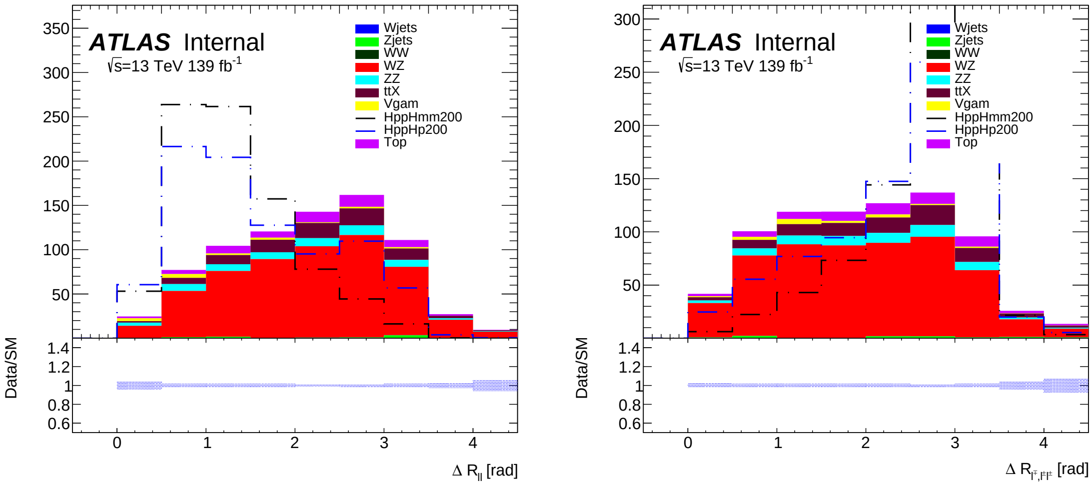

(a) $\Delta R_{\ell^{\pm}\ell^{\pm}}$ (b) $\Delta R_{\ell^{\mp},\ell^{\pm}\ell^{\pm}}$

Figure 6.5: 3ℓ channel, $\Delta R_{\ell^{\pm}\ell^{\pm}}$ and $\Delta R_{\ell^{\pm}\ell^{\pm},\ell^{\mp}}$ at the event pre-selection stage. Left is the same-charge di-leptons distance in $\eta - \phi$ plane; here the signal tends to be smaller than the SM background. Right is the $\eta - \phi$ distance between opposite-charge lepton and same-charge lepton pair; here the signal tends to become larger than the background. Only the statistical uncertainties are shown. The signal is scaled to the same integral as background MC to have better vision.

Sources of background events

The analysis channels ($2\ell^{sc}$, 3ℓ and 4ℓ) are populated by different sources of irreducible (prompt leptons) and reducible (fake leptons and electron charge mis-identification backgrounds). The $2\ell^{sc}$ topology is populated with events containing one prompt lepton (from W, and to some lesser extent from Z bosons) and one non-prompt lepton. The $2\ell^{sc}$ events with electrons can also originate from the opposite sign pairs originating from Drell-Yan and $t\bar{t}$ production, where the charge of one of the electron is mis-identified (the charge mis-identification rate is negligible for muons). In this channel the dominant prompt same-charge sources in the SRs are coming from WZ and $t\bar{t}V$.

For 3ℓ, a significant part of the expected SM contribution originate from di-boson production. In particular, the WZ production, where both bosons decay to leptons, presents also other *signal* features like significant $E_{\mathrm{T}}^{\mathrm{miss}}$ and absence of b-jets for most of the production cross section. It should be noted that the same-flavor opposite charge lepton pairs are predominantly produced in the Z bosons mass window.

In the 4ℓ channel, the main source of prompt SM background is from ZZ events.

In all channels, the $t\bar{t}$ processes are highly suppressed by requiring exactly 0 b-jets in the event. The non-prompt leptons from di-boson processes, e.g. $WZ \rightarrow qq\nu\nu$, were checked and have negligible contribution in all channels.

7 Background Estimations

Contents

The background sources can be divided into two main categories. One category is populated by the SM events which contain only reconstructed prompt leptons. The second category contains non-prompt leptons, charge-flip and photon converted electrons. Lepton candidates reconstructed from these different sources share the properties of being less isolated, having larger impact parameters relative to the primary vertex and being less likely to satisfy the lepton identification criteria.

The backgrounds from SM processes with prompt leptons are estimated with the Monte-Carlo simulations, except for background from WZ production, for which the normalization is corrected using data in a dedicated control region (Section 7.1.1). Background from non-prompt leptons and electron charge-flip are estimated using data-driven methods. Background from $V\gamma$ production can contribute in the SRs if the photon converts to an electron–positron pair, and is estimated using the Monte-Carlo simulations.

Selection criteria	$t\bar{t}$	Z + jets	WZ
At least one offline tight lepton with $p_{\mathrm{T}}^{\ell} > 30$ GeVthat triggered the event			
N_{ℓ} (type T)	=2	=2	=3
$\lvert \sum Q_{\ell} \rvert$	=0	=0	=1
Lepton p_{T}	$p_{\mathrm{T}}^{\ell_1,\ell_2} > 30, 20$ GeV	$p_{\mathrm{T}}^{\ell_1,\ell_2} > 30, 20$ GeV	$p_{\mathrm{T}}^{\ell_0,\ell_1,\ell_2} > 30, 20, 20$ GeV
N_{jets}	≥ 2	≥ 1	–
$N_{b\text{-jets}}$	≥ 2	=0	
same-flavor pairs	–	≥ 1	
Z boson decay veto	$\lvert m_{\ell\ell} - m_Z \rvert > 20$ GeV	$\lvert m_{\ell\ell} - m_Z \rvert < 45$ GeV	$\lvert m_{\ell\ell}^{\text{same-flavor}} - m_Z \rvert < 10$ GeV

Table 7.1: The selection criteria for the $t\bar{t}$, Z + jets and WZ validation regions. The leptons are required to pass the tight (T) requirements. The symbol "–" means no requirement is made. The equal sign (=) is used to emphasize that the selection criterion has to be exactly the given number.

7.1 Validation Regions

Three validations, $t\bar{t}$, Z + jets (Drell-Yan) and WZ regions, are defined for the most important three background process. Selections for validation regions are listed in Table 7.1.

The events selected by the $t\bar{t}$ validation region are divided into ee and $\mu\mu$ channels and are compared with the simulation. Distributions of $E_{\mathrm{T}}^{\mathrm{miss}}$ are shown in Figure 7.1. The comparisons show that the defined region is indeed dominated by $t\bar{t}$ events and this process is reasonably well-modelled by the simulation. The agreement in the tails is not that good, but here the statistics is quite low.

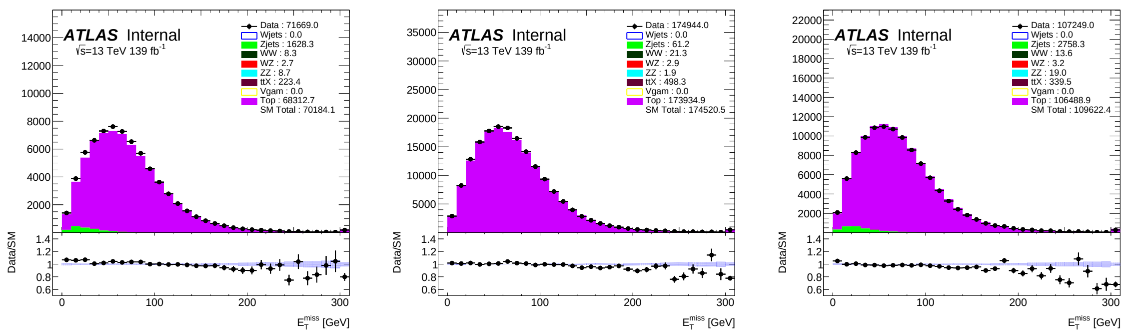

(a) ee channel (b) $e\mu$ channel (c) $\mu\mu$ channel

Figure 7.1: E_{T}^{miss} of $t\bar{t}$ validation region for ee, $e\mu$,and $\mu\mu$ channels from left to right. Uncertainty is stat only. The non-prompt lepton background is taken from the Monte-Carlo simulations.

Distributions of the invariant mass of the di-lepton system for the Z+jets validation region are shown in Figure 7.2. The comparisons show that the events with two leptons of opposite sign are dominated by Drell-Yan and are well modelled by the Monte-Carlo simulation. Justified by the agreement, we use the charge mis-identification rate measured with data to scale the opposite sign events in Drell-Yan Monte-Carlo samples to predict the Drell-Yan contribution in the $2\ell^{sc}$ signal region. This is explained in more details in section 7.2.2.

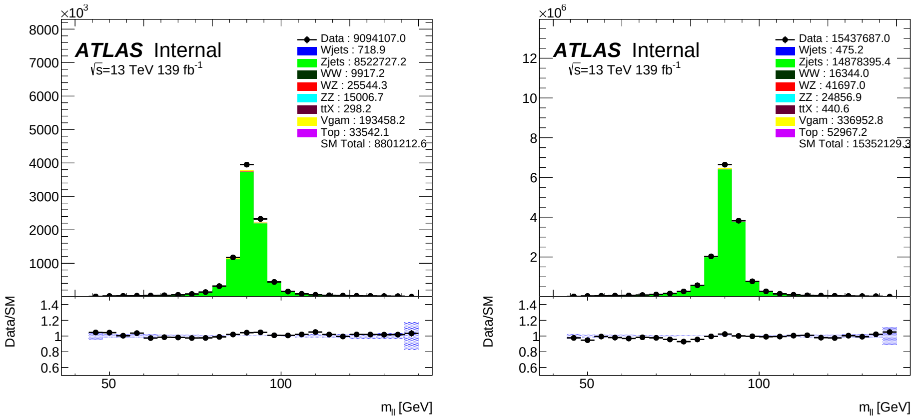

(a) ee channel

(b) $\mu\mu$ channel

Figure 7.2: Invariant mass of the two leptons of $Z+$jets validation region for ee and $\mu\mu$ channels from left to right. Uncertainty is stat only. The non-prompt lepton background is taken from the Monte-Carlo simulations.

The WZ validation region is inclusive. The Z candidate is defined as the pair of leptons with same flavor and opposite charge of which the invariant mass passes the Z window cut. The distributions of $M_{\ell\ell\ell}$ and $E_{\mathrm{T}}^{\mathrm{miss}}$ are shown in Figure 7.3. A good agreement is observed, within statistical uncertainties. Specially for Sherpa WZ Monte-Carlo simulations, it is known that the QCD simulation is not perfect, leading to a discrepancy between data and Monte-Carlo. This discrepancy can be covered by QCD variation uncertainty; the QCD uncertainty is coming from variations of the renormalization factor and factorization factor in the PDF function (in this figure μ_f=1 and μ_r=1 is for the nominal scale in Monte-Carlo while μ_f=0.5 and μ_r=0.5 is for the variation).

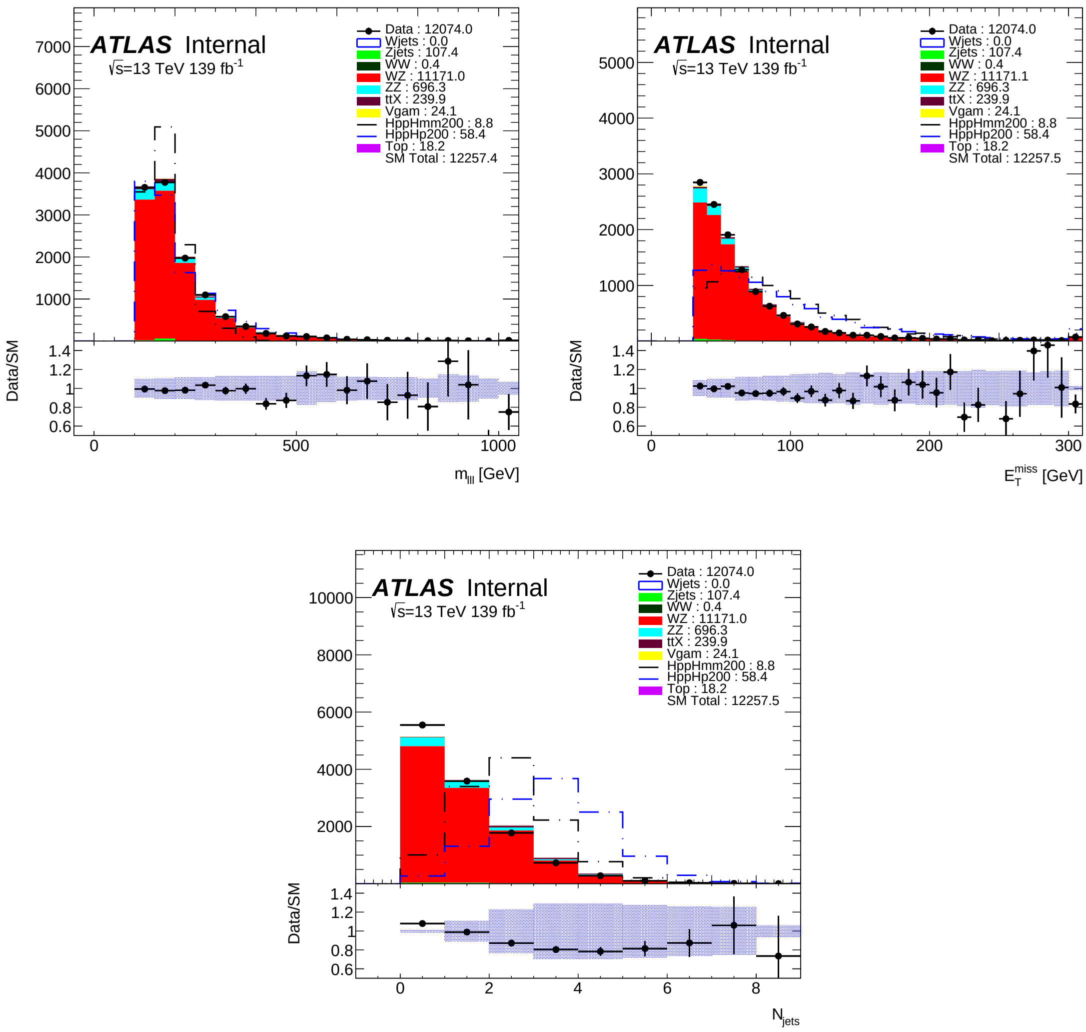

Figure 7.3: $M_{\ell\ell\ell}$, $E_{\mathrm{T}}^{\mathrm{miss}}$ and Jet multiplicity of WZ validation region. Uncertainty contains statistics and QCD variation. The non-prompt lepton background is taken from the Monte-Carlo simulations. Data and Monte-Carlo simulations agree well across $M_{\ell\ell\ell}$, $E_{\mathrm{T}}^{\mathrm{miss}}$, but badly across Jet multiplicity. This implies a correction is needed for number of jets >= 2.

7.1.1 WZ Normalization

WZ process is the most important irreducible background in $2\ell^{sc}$ and 3ℓ channels. However, the jet multiplicity distribution in the WZ validation region (Figure 7.3) shows that the WZ processes are not well modeled in regions with the number of jets >= 2. This was already seen in several analyses in the ATLAS collaboration. Thus a dedicated study was performed to measure a correction (normalization) factor to scale the WZ processes in regions with the number of jets >= 2.

Figure 7.4 shows the results obtained with a constant function fit employed to get the WZ normalization factor (NF); and it is used to fit the jet multiplicity ratio between Data with non-WZ (from the Monte-Carlo) subtracted and WZ Monte-Carlo. The obtained normalization factor for the WZ processes is 0.83±0.02(stat)±0.07(syst).

Several sources are considered for the systematic uncertainties. First is the N_{jets} uncertainty. WZ is the dominant process in both $2\ell^{sc}$ and 3ℓ channels. The requirement on the number of jets in the 3ℓ channel is $\geq$ 2 jets, while in same-charge-two-lepton ($2\ell^{sc}$) is $\geq$ 3 jets. Thus, a linear fit in the WZ control region after requiring $\geq$ 3 jets is performed. The difference (Figure 7.4 left and right) is taken into account as a normalization uncertainty (8.4%).

The second is the shape uncertainty. It is estimated from the scale variations[1], while the same normalization is applied to all distributions. Results are shown in Figure 7.5, in the ≥2 jets WZ control region. This uncertainty is around 5% inclusively. The shape uncertainty is also computed in the WZ control region defined with ≥3 jets and the results are shown in Figure 7.5. It is lower than 2% except in the region with $N_{\text{jets}} \geq 9$. However, this source is partially included in the "N_{jets}" uncertainty. Conservatively, an overall 3% uncertainty is assigned.

The final is the fitting function uncertainty. This check is performed by changing the linear function to a quadratic polynomial when performing the fit in the WZ control region. Quadratic fit model uncertainty is taken as the maximum relative difference between the Linear and Quadratic fit results in each jet multiplicity distribution bin. This uncertainty is set to 0 when the statistical uncertainty of data covers the difference. The results in the ≥2 jets WZ control region are compared in Figure 7.4 and it can be seen that the two functions disagree at most by 9%. The results in the WZ control region, when the cut on the number of jets is tightened to $\geq$ 3, are shown in Figure 7.4; the agreement is very good, the differences are covered by the statistical uncertainty. Because the shape uncertainty already considers the differences in the results obtained in the ≥2 jets and ≥3jets WZ control regions, and the difference between fitting functions in Figure 7.4 is close to the combination of the $N_{\text{jets}}$and Shape uncertainties, no additional "fit function" uncertainty is assigned. Including all the above sources, the final theoretical uncertainty is 9.0% (relative value).

The measurement was done in a dedicated WZ N_{jets} control region [2]; The obtained normalization factor is 0.83±0.07 and it is used in all the analysis steps (but for the signal region optimization), in the $2\ell^{sc}$, 3ℓ and 4ℓ channels. The quoted uncertainty includes the statistical and systematic components. The jet multiplicity distribution in this WZ CR is shown in Figure 7.6(a), after the normalization factor

[1] Parton shower can also cause the shape uncertainty but was checked to be negligible.

[2] At least one pair of same-flavor opposite-sign leptons with $|M_{\ell\ell} - M_Z| < 10$ GeV (Z-selection), B-jet Veto and at least two jets. WZ N_{jets} control region purity: 83.1%, pair-production signal contamination (200 GeV point): 0.16%, associate-production signal contamination (200 GeV point): 1.55%.

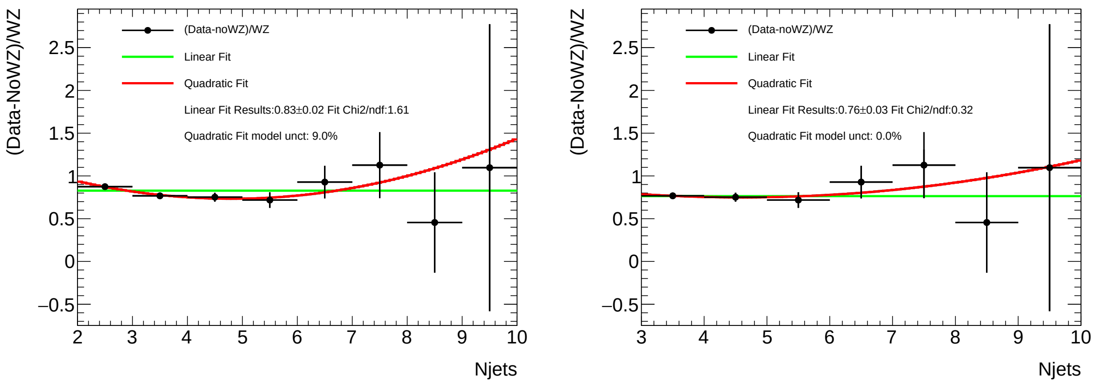

Figure 7.4: Liner and Quadratic Fit results in the WZ control region defined with the number of jets ≥2/3. Error band is statistics only. The Linear fit result 0.82±0.02 is the normalization factor applied to WZ processes in the $2\ell^{sc}$ and 3ℓ channels results (both channels require $N_{\text{jets}} \geq 2$). In the 4l channel, the WZ contribution is negligible.

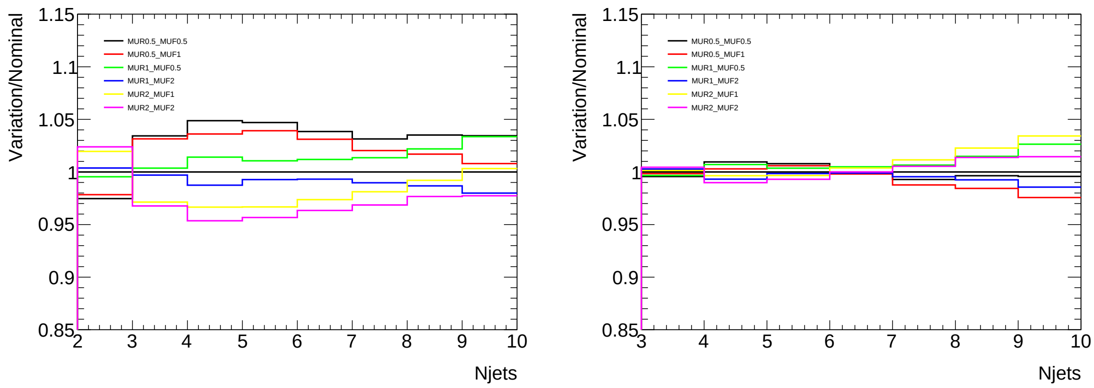

Figure 7.5: Remain shape variation from WZ scale uncertainty ($WZ \geq 2/3$ jets control region). The same normalization is applied to all distributions. The uncertainty from shape variation is around 5% inclusively.

is applied; for illustration the distribution in the 3ℓ pre-selection region is also shown in Figure 7.6(b). Good agreement between the data and estimated background is found, the remaining discrepancies covered by the assigned systematic uncertainties[3].

[3] Non-prompt lepton estimation will be described in details in Chapter 7.

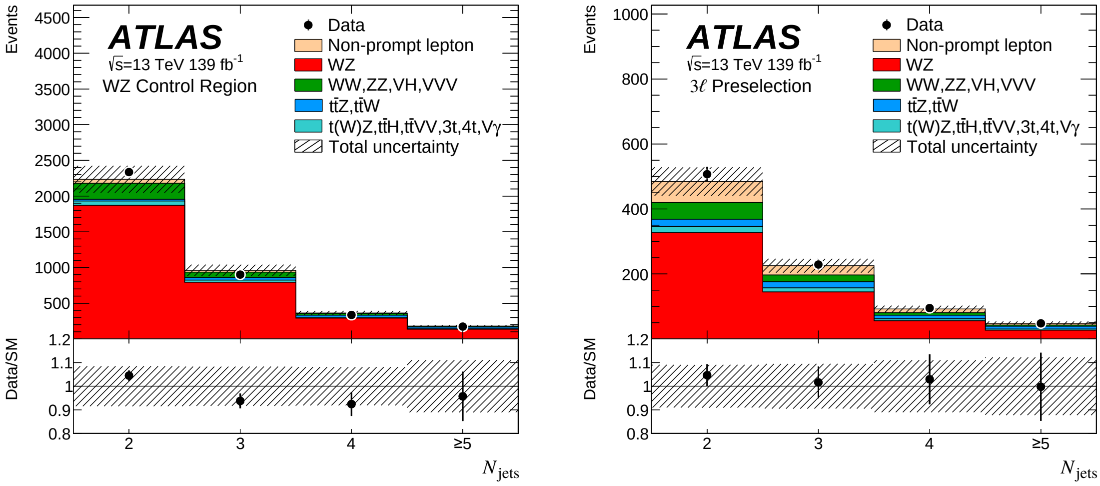

Figure 7.6: Distribution of jet multiplicity in the WZ control region (left) and in the 3ℓ pre-selection region (right). The data (dots) are compared with the expected contributions from relevant SM processes and the reducible background. The WZ normalization factor is applied. The last bin includes overflows, and the uncertainty is stat only. The non-prompt lepton background is estimated with the fake factor method presented later in the document.

7.2 Two lepton same charge channel

7.2.1 Event selection and Prompt background

The di-lepton events are classified into three channels according to the flavors of the two leptons: ee, $\mu\mu$ and $e\mu$. The event selection listed in Table 7.2 is referred to as the event pre-selection. The leading lepton is required to have $p_{\mathrm{T}} > 30$ GeV, so that the triggers are operated at the plateau region of their efficiency curves. A cut on the invariant mass between the electron pair is added to remove the charge flip background in this channel.

At the pre-selection stage, the background in $2\ell^{sc}$ channel is mainly from $t\bar{t}$, $W+$jets, $V\gamma$ (fake/non-prompt sources or leptons) and WZ, $W^{\pm}W^{\pm}$ and $t\bar{t}V$ (prompt sources of leptons), with V standing for W or Z vector bosons. This is illustrated in Figures 7.7 and 7.8, where the distributions of the jet multiplicity and $E_{\mathrm{T}}^{\mathrm{miss}}$ of the events that pass the pre-selections of the three channels are shown. The discrepancy between data and the background taken only from the Monte-Carlo simulations indicates that data-driven estimations are needed for the fake leptons and charge mis-identification of electrons background sources.

To estimate the charge flip background, the probability of an electron to have a wrong charge is needed; it is measured in bins of electron p_{T} and η with $Z \to e^+e^-$ events in data (section 7.2.2). The SM W^+W^- production contributes to the *signal* region due to electron charge flip and is included in the data-driven estimations; the $t\bar{t}$ and single top production process contributes also to this category and are treated by the data-driven estimations. The fake factor method (section 7.2.3) is used to estimate

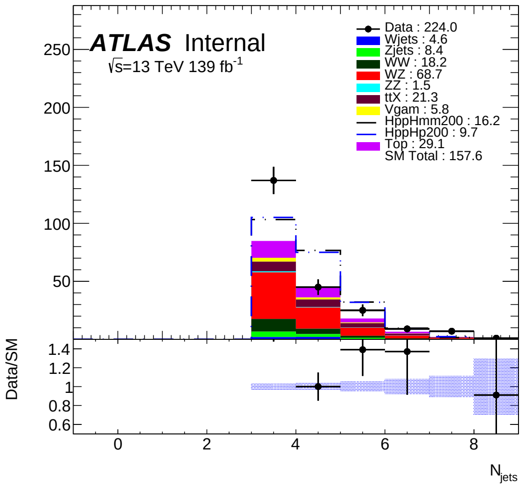

(a) ee channel

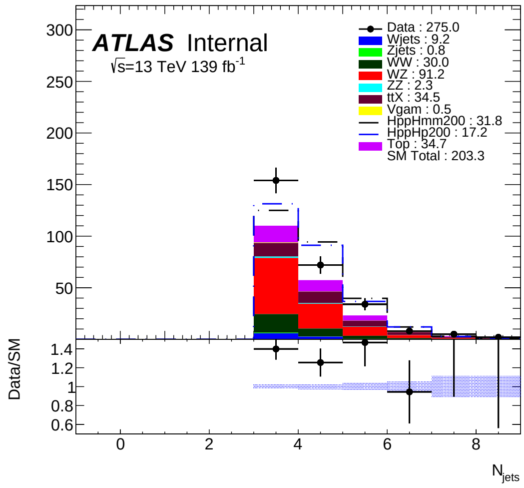

(b) $\mu\mu$ channel

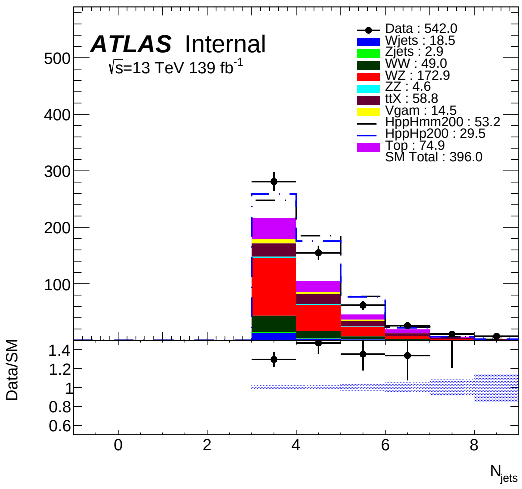

(c) $e\mu$ channel

Figure 7.7: $2\ell^{sc}$ channel, left to right: Jet multiplicities of ee (Top left), $\mu\mu$ (Top right) and $e\mu$ (Bottom) SS channels at the event pre-selection stage. Only the statistical uncertainties are shown. The non-prompt lepton background is taken from the Monte-Carlo simulations. The signal is scaled to the same integral as data and that the prediction is given in the legend.

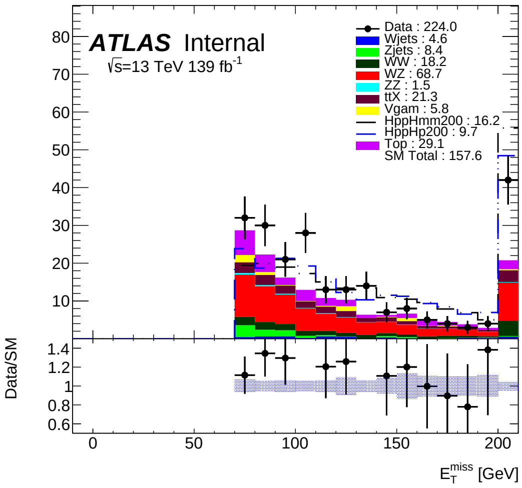

(a) ee channel

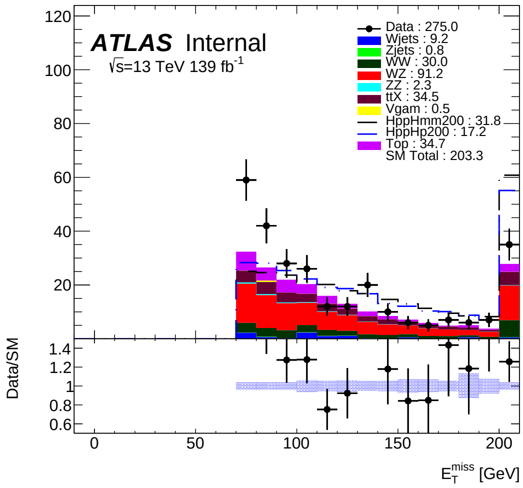

(b) $\mu\mu$ channel

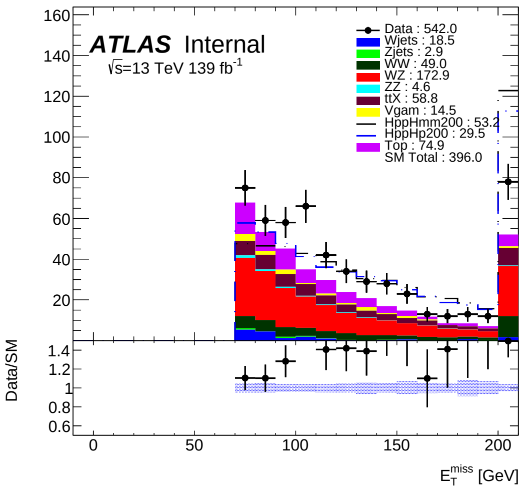

(c) $e\mu$ channel

Figure 7.8: $2\ell^{sc}$ channel, left to right: $E_{\mathrm{T}}^{\mathrm{miss}}$ distribution in the ee (Top left), $\mu\mu$ (Top right) and $e\mu$ (Bottom) SS channels at the event pre-selection stage. Only the statistical uncertainties are shown. The non-prompt lepton background is taken from the Monte-Carlo simulations. The signal is scaled to the same integral as data and that the prediction is given in the legend.

Selection criteria	$2\ell^{sc}$ pre-selection
At least one offline *signal* lepton with $p_{\mathrm{T}}^{\ell} > 30$ GeVthat triggered the event	
N_ℓ (*Candidate*)	=2
N_ℓ (*signal*)	=2
$\lvert \sum Q_\ell \rvert$	=2
Lepton p_{T}	$p_{\mathrm{T}}^{\ell_1,\ell_2} > 30, 20$ GeV
$E_{\mathrm{T}}^{\mathrm{miss}}$	> 70 GeV
N_{jets}	≥ 3
$N_{b\text{-jets}}$	=0
Z boson decay veto	$\lvert m_{ee}^{\mathrm{sc}} - m_Z \rvert > 10$ GeV

Table 7.2: The pre-selection criteria for the $2\ell^{sc}$ analysis channels. The leptons are required to pass the *signal* or *candidate* requirements. The leptons are ordered by decreasing p_{T} ($\ell_1, \ell_2, ...$). The equal sign (=) is used to emphasize that the selection criterion has to be exactly the given number.

the contributions from W+jets, Z+jets, $t\bar{t}$, single top (all processes leading to fake/non-prompt leptons in the final state).

In order to validate the background estimation methods with more statistics, but also to assess the systematics uncertainties, the background estimation was obtained at the pre-selection stage.

7.2.2 Charge mis-identification background

For the $2\ell^{sc}$ channel, events from $Z+$jets and $t\bar{t}$ can enter the *signal* region due to charge flip. This is only relevant for electrons since the charge-flip rate is negligible for muons in the kinematic regions of interest for the presented analysis[4].

The $Z+$jets processes are contributing mostly in the low $E_{\mathrm{T}}^{\mathrm{miss}}$ ($E_{\mathrm{T}}^{\mathrm{miss}} < 70$ GeV) region, which is the region used for the fake factor calculation. The $t\bar{t}$ processes are populating the high $E_{\mathrm{T}}^{\mathrm{miss}}$ ($E_{\mathrm{T}}^{\mathrm{miss}} > 70$ GeV) region, thus the pre-selection region and the defined $2\ell^{sc}$ *signal* regions.

Charge flip rate measurement

The electron charge flip rates are measured in data using a statistical method based on a likelihood. The likelihood method assumes that for $Z \to e^+e^-$ events, the probability to reconstruct a pair of same charge electrons is $(\varepsilon_1 + \varepsilon_2)$, where ε_1 and ε_2 are the probabilities of charge flip for the two electrons, respectively. The charge flip rates are parametrized as a function of η and p_{T} of the electrons. The η dependence is particularly important since the amount of material the electrons traversed before entering the calorimeter is strongly dependent on the region of the detector where the electron is reconstructed. The charge flip rates (η, p_{T}) are measured from the total number of events and the

[4] This has been validated with the $Z \to \mu^+\mu^-$ Powheg sample: out of 18978622 events selected with Z mass window, only 42 events are reconstructed with two muons of the same charge.

	$20 < p_{\mathrm{T}}/\mathrm{GeV} < 60$	$60 < p_{\mathrm{T}}/\mathrm{GeV} < 90$	$90 < p_{\mathrm{T}}/\mathrm{GeV} < 130$	$130 < p_{\mathrm{T}}/\mathrm{GeV} < 1000$
$0.00< \lvert\eta\rvert <0.60$	0.002±0.000	0.010±0.001	0.032±0.005	0.116±0.016
$0.60< \lvert\eta\rvert <1.10$	0.004±0.000	0.022±0.002	0.064±0.009	0.229±0.026
$1.10< \lvert\eta\rvert <1.37$	0.008±0.001	0.053±0.005	0.139±0.020	0.525±0.061
$1.52< \lvert\eta\rvert <1.70$	0.012±0.001	0.069±0.009	0.246±0.038	0.768±0.111
$1.70< \lvert\eta\rvert <2.30$	0.023±0.001	0.087±0.007	0.355±0.032	1.205±0.103
$2.30< \lvert\eta\rvert <2.47$	0.058±0.003	0.378±0.039	1.328±0.166	3.140±0.474

Table 7.3: *Signal* electron's charge flip rates (in %), in data, measured with the likelihood method applied on Z events. The uncertainty is stat-only (absolute values).

number of events with a pair of same charge electrons by maximizing the following likelihood function constructed from Poisson statistics[5]:

$$\ln \mathcal{L}(\varepsilon|N_{tot}, N_{sc}) = \sum_{i,j} \ln \left[N_{tot}^{i,j}(\varepsilon_i(1-\varepsilon_j) + \varepsilon_j(1-\varepsilon_i)) \right] N_{sc}^{i,j} - N_{tot}^{i,j}(\varepsilon_i(1-\varepsilon_j) + \varepsilon_j(1-\varepsilon_i)) \tag{7.1}$$

$$\rightarrow \sum_{i,j} \ln \left[N_{tot}^{i,j}(\varepsilon_i + \varepsilon_j) \right] N_{sc}^{i,j} - N_{tot}^{i,j}(\varepsilon_i + \varepsilon_j) \tag{7.2}$$

where $N_{tot}^{i,j}$ and $N_{sc}^{i,j}$ are the total number of candidate events and the number of events, which have a same-charge electron pair, having the first and second lepton in the i-th and j-th bin, respectively. The bin index i, j denotes each cell in η-p_{T} 2D space.

For *signal* electrons, the intervals of the η bins are [0, 0.6], [0.6, 1.1] , [1.1, 1.37], [1.52, 1.7], [1.7, 2.3], [2.3, 2.47] and the intervals of the p_{T} bins (in GeV) are [20, 60], [60, 90], [90, 130], [130, 1000]. The events are selected with an invariant mass window of [80 GeV, 100 GeV]; in order to study the background composition, the mass window is extended to [60 GeV, 120 GeV] to have wider sidebands.

In order to validate that the charge flip rates can be parameterized as a function of p_{T} and η and that the likelihood is correctly implemented, the method is applied on $Z \rightarrow e^+e^-$ Monte-Carlo samples, and the results are compared with the actual charge flip rates obtained using Monte-Carlo truth information. Both methods use events with two electrons from the Z boson decay that pass the *signal* electron definition (Table 6.3) and are in the aforementioned Z-mass interval. For the likelihood method, these events are then divided into events with the same-charge leptons pair (SC) and events with the opposite-charge leptons pair (OC), and the rates are measured with these events. For the "truth method", the charge flip rate is calculated with a simple equation defined by the numbers of wrong/correct charge (Q) electron:

$$\varepsilon_i = N_{wrongQ}^i / (N_{wrongQ}^i + N_{correctQ}^i), \tag{7.3}$$

where i is the bin index. Generally speaking, a good agreement is observed between the different measurements, as illustrated in figure 7.9.

[5] High order terms were removed.

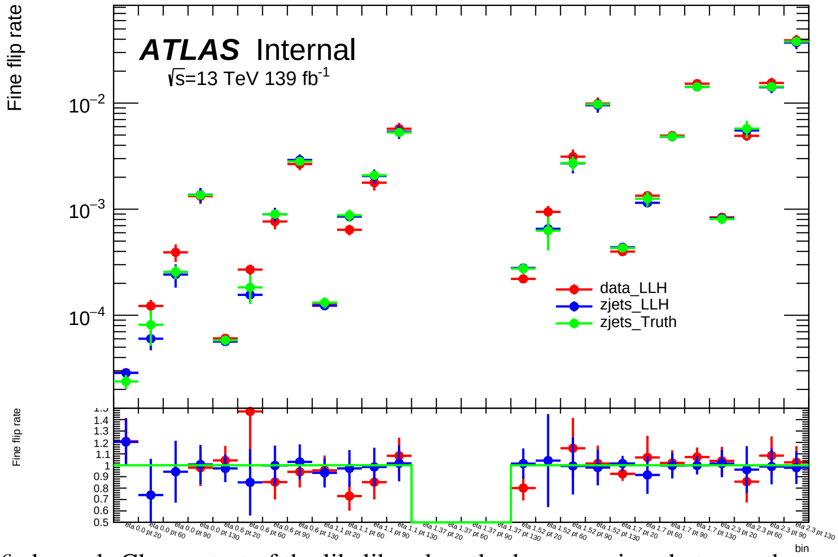

Figure 7.9: $2\ell^{sc}$ channel. Closure test of the likelihood method: comparison between the measured electron charge flip rate with the likelihood method in data (red) and Z Monte-Carlo (blue), and the rates determined with the truth information using the same $Z \to ee$ Monte-Carlo sample. The uncertainty is statistics only. In the lower pad, the ratio between the results with Z_LLH and Data_LLH (red) and Z_truth_MC and Data_LLH (blue). The x axis shows the η bins used in the measurement; note that the bins in the crack region are not used (hence the drop).

As we will need to subtract the contributions due to charge flips from the fake lepton control regions, we need to measure also the charge flip rate for electrons passing the *candidate* requirements but failing the *signal* ones (*CandNotSig*). To measure the charge flip rates for the *CandNotSig* electrons, the same likelihood method is applied to the events that contain one *signal* and one *candidate* but non-*signal* electron candidates, of which the invariant mass is inside the Z mass window [80 GeV, 100 GeV].

For *CandNotSig* electrons, for the measurement in data with the likelihood method (the likelihood written in Eq. (7.4)), coarse bins are used due to limited statistics.

$$\ln \mathcal{L}(\varepsilon^{CandNotSig}|N_{tot}, N_{sc}) = \sum_{i,j} \ln \left[N_{tot}^{i,j}(\varepsilon^{i,j}) \right] N_{sc}^{i,j} - N_{tot}^{i,j}(\varepsilon^{i,j}) \tag{7.4}$$

$$\varepsilon^{i,j} = \varepsilon_i^{CandNotSig} + \varepsilon_j^{signal,\text{fixed}} \tag{7.5}$$

The intervals of the η bins are [0, 1.37] and [1.52, 2.47] and the intervals (in GeV) of the p_{T} bins are [20, 60] and [60, 1000].

To reduce the number of free parameters in the likelihood function and increase statistics for each single likelihood fit, the *signal* electron charge flip rate is fixed to the measured values in data with the likelihood method (the likelihood being shown in Eq. (7.2)). To measure the *CandNotSig* electron charge flip rate in the endcap (barrel), the *signal* electron is required to be located in the barrel (endcap). The rates measured with the likelihood method using $Z \to e^+e^-$ (Powheg) Monte-Carlo

$Z \to e^+e^-$ Monte-Carlo truth method	$0 < \|\eta\| < 1.37$	$1.52 < \|\eta\| < 2.47$
20< p_T/GeV <60	0.022±0.002	0.09 ±0.006
60< p_T/GeV <1000	0.25±0.042	0.402±0.076
$Z \to e^+e^-$ Monte-Carlo likelihood method	$0 < \|\eta\| < 1.37$	$1.52 < \|\eta\| < 2.47$
20< p_T/GeV <60	0.018±0.003	0.093 ±0.002
60< p_T/GeV <1000	0.226±0.06	0.329±0.047

Table 7.4: Closure test of *CandNotSig* electron's charge flip rates (in %) measured using $Z \to e^+e^-$ (Powheg) Monte-Carlo samples. The uncertainty is stat-only (absolute values). Good agreement is observed.

Data-driven	$0 < \|\eta\| < 1.37$	$1.52 < \|\eta\| < 2.47$
20< p_T/GeV <60	0.018±0.003	0.087 ±0.002
60< p_T/GeV <1000	0.262±0.064	0.419±0.052

Table 7.5: *CandNotSig* electron's charge flip rates (in %), measured in data with the likelihood method applied on Z events. The uncertainty is stat-only (absolute values).

samples and the ones using the truth information are compared in Table 7.4; the agreement is very good, validating the method.

The measured charge flip rates in data, using the likelihood method applied on Z events, are presented in Table 7.3 and Table 7.5 for *signal* and *CandNotSig* electrons respectively.

Charge Flip Systematics

Events used to measure the charge flip rates are contaminated by background events. A template fit is performed on the distributions of the invariant mass of the electron pairs to determine the background contributions in N_{tot} and N_{sc} in Eq. (7.2) and are subtracted. The *signal* shape is taken from $Z \to ee$ Monte-Carlo with the same selection as data. The background shape(PDF) is a cubic polynomial function (shown in Eq. (7.6)). The range of function parameters, c0,c1,c2,c3, is [-100.,100.].

$$\text{Background PDF} = c3 * m_{ee}^3 + c2 * m_{ee}^2 + c1 * m_{ee} + c0 \tag{7.6}$$

The global fit for number of events is shown in Figure 7.10 for *signal* pairs and in Figure 7.11 for *signal* and *CandNotSig* electrons pairs. For the inclusive selection (opposite- and same-charge electron pairs combined), only one inclusive fit is performed. The differences in the charge flip rates obtained after subtracting the background estimated with the two fitting ranges [60,120] GeV and [70,110] GeV has been taken into account as a systematic uncertainty, to account for the fit stability and for the variation in the background composition/level. This systematic uncertainty is found to be 3% for the nominal (*signal*) measurement and around 7% for the *CandNotSig* measurement.

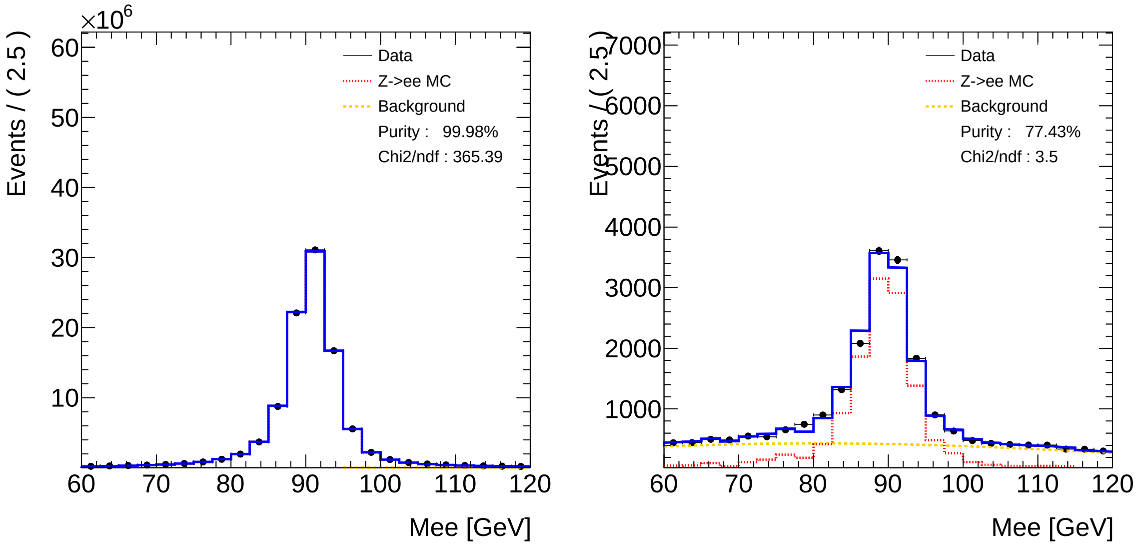

(a) all electron pairs

(b) same-sign electron pairs

Figure 7.10: SS2L channel. Distributions of the invariant mass of the two *signal* electron candidates (inclusive p_{T} and η). Left: all OS+SS events; the *signal* purity obtained from the fit is 99.98% in central region (80-100 GeV). Right: all SS events; the *signal* purity obtained from the fit is 77.43% in central region (80-100 GeV). The black dots show the data, the blue dash line is for the fit and the yellow dash line is for the background template.

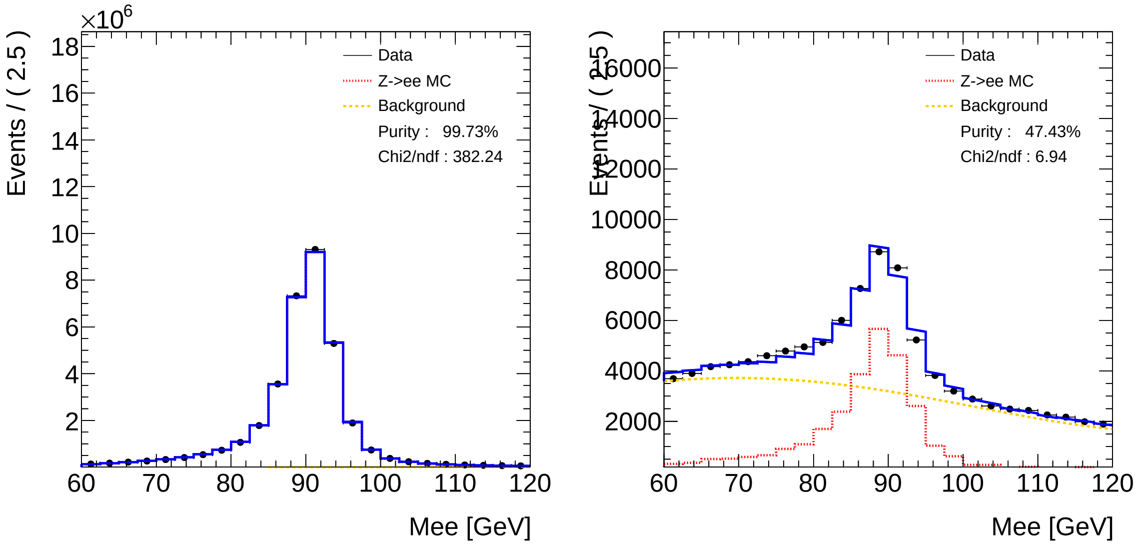

(a) all electron pairs

(b) same-sign electron pairs

Figure 7.11: SS2L channel. Distributions of the invariant mass of the one *CandNotSig* electron and one *signal* electron (inclusive p_{T} and η). Left: all OS+SS events; the *signal* purity obtained from the fit is 99.73%. Right: all SS events; *signal* purity obtained from the fit is 47.73%. The black dots show the data, the blue dash line is for the fit and the yellow dash line is for the background template.

Z+jets	Relative Uncertainty	$N^{sc}_{\text{predicted}}$	N^{sc}_{rawMC}
Signal	1.90%	6767 ± 7	6640 ± 320
CandNotSig	0.69%	9996 ± 18	10100 ± 400
$t\bar{t}$	Relative Uncertainty	$N^{sc}_{\text{predicted}}$	N^{sc}_{rawMC}
Signal	2.98%	247.1 ± 0.4	254 ± 6
CandNotSig	10.45%	173.22 ± 0.30	191 ± 5
$W^{\mp}W^{\pm}$	Relative Uncertainty	$N^{sc}_{\text{predicted}}$	N^{sc}_{rawMC}
Signal	9.39%	47.11 ± 0.20	51.5 ± 2.2
CandNotSig	26.41%	28.85±0.12	36.5 ± 1.9

Table 7.6: The relative difference in percentage between the predicted number of same sign events obtained with the charge flip rates measured with the likelihood method in $Z \to ee$ Monte-Carlo (estimated using Eq. (7.7)) and the raw same-charge contribution taken from the Monte-Carlo simulations. The uncertainty is stat only. The $Z \to ee$ events are required to have a pair of electrons whose invariant mass is within a Z mass window between 80 and 100 GeV. Fake/non-prompt leptons in $Z \to ee$, $t\bar{t}$ and $W^{\mp}W^{\pm}$ events were removed using the truth lepton information.

In the ee channel, given the charge flip rate, the ratio of the number of same charge events to that of opposite sign events should be:

$$r = (\varepsilon_1 + \varepsilon_2)/(1 - \varepsilon_1 - \varepsilon_2) \tag{7.7}$$

In the $e\mu$ channel the ε_i parameter (i being 1 or 2) is 0 for the muon.

One can use this ratio in Eq. (7.7) together with the events in the control region of the opposite charge electrons to estimate the number of events with electrons of the same charge. A Monte-Carlo closure test is performed to test this method. In this test, the Monte-Carlo charge flip rates measured from $Z \to ee$ events with the likelihood method are used to obtain the prediction of the number of the same charge events from Z+jets, $t\bar{t}$ and $W^{\mp}W^{\pm}$ processes. The predictions are compared with the raw number of events taken from the Monte-Carlo simulations using the truth electron information (classification done with the truth match method described in section 4.3). The non-closure results are shown in Table 7.6. The difference is coming from the different shapes of the p_{T} and η distributions of the different processes (see Figure 7.12), and the bin sizes of the measured charge flip rate; it is included as a source of systematic uncertainty.

Given the results from the results of the tests presented in this section, conservative systematic uncertainties (methodical uncertainty, originate from the kinematic differences of the different process) of 10% for *signal* charge flip rates and of 30% for *CandNotSig* charge flip rates are assigned. They are covering the non-closure shown in Table 7.6; are assigned independent of the [η, p_{T}] values.

Summary of all sources of uncertainties:

- Statistical uncertainty from likelihood fit because of the limited stat in the measurement regions. (2%~16%, depend on [η, p_{T}] values.)

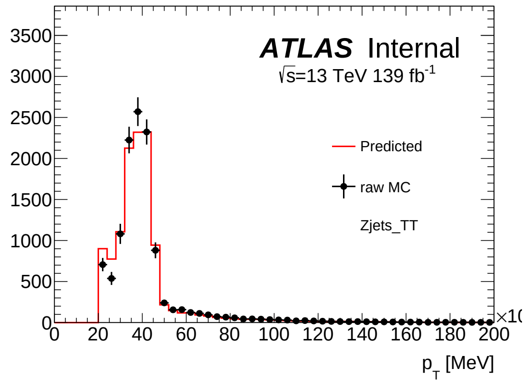

(a) $Z+$jets events

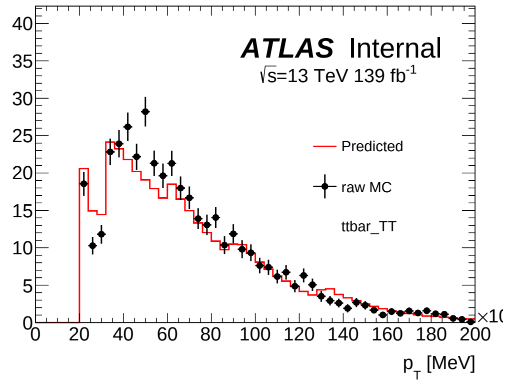

(b) $t\bar{t}$ events

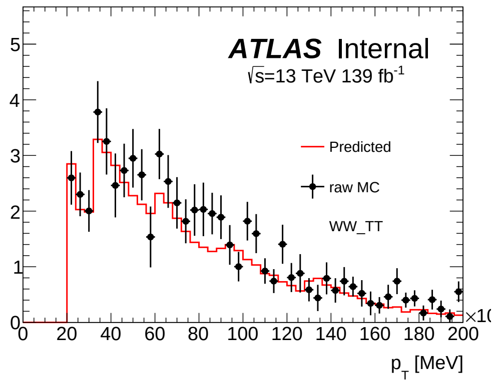

(c) Opposite-sign WW events

Figure 7.12: $2\ell^{sc}$ channel. Distributions of p_{T} between predicted-same-sign and raw Monte-Carlo *signal-signal* electron pairs, in $Z \rightarrow ee$, $t\bar{t}$ and $W^{\mp}W^{\pm}$ Monte-Carlo processes. Uncertainty is statistics only. Note that "TT" indicates two *signal* lepton pair.

- Background subtraction uncertainties by varying the cut on the invariant mass fitting range of the two electrons used in the measurement. (~3% for *signal* and ~7% for *CandNotSig*)
- The uncertainty of method: The kinematic differences of the charge flip rates between the different sources of electron charge flip processes. (~10% for *signal* and ~30% for *CandNotSig*).
- FSR uncertainty: Compare truth rates with/without FSR contribution. (<1%)

Charge flip estimation

The background due to electron charge flip in the $2\ell^{sc}$ channel is estimated with opposite sign di-leptons events in data samples scaled by the ratio r defined in Eq. (7.7). The charge flip rates are taken from data (Tables 7.3 and 7.5).

7.2.3 Non-prompt lepton background

Given the low SM background with prompt and well isolated same-charge leptons in the $2\ell^{sc}$ final state, the fake lepton background is very important in this channel. As it is not well modeled by the Monte-Carlo simulations, data-driven techniques must be considered. In this analysis, the fake factor method described below is used.

Data-driven fake factor method

The method is based on a same-charge control region enriched in fake leptons. The control region consists of events with one lepton passing the *signal* lepton selection and another so-called *CandNotSig* (or "anti-*signal*") lepton that passes the *candidate* lepton selection and fails the *signal* selection (see section 6.1.2 for the lepton definitions). The contribution due to fake leptons is obtained with the number of events in this control region scaled by a projection factor – the contributions from other sources, like charge flip and di-boson process that can produce prompt same-charge leptons, $t\bar{t}V$, etc, are subtracted. The projection factor is further called "fake factor", and it is measured in an independent sample of events that is defined with requirements on $E_{\mathrm{T}}^{\mathrm{miss}}$ (< 70 GeV), di-lepton mass and number of b-jets in the event. The full selection is shown in Table 7.7. The signal contamination in this region is expected to be negligible.

Selection criteria	$2\ell^{sc}$ pre-selection
At least one offline *signal* lepton with $p_{\mathrm{T}}^{\ell} > 30$ GeVthat triggered the event	
N_ℓ (*candidate*)	=2
N_ℓ (*candidate**)	–
N_ℓ (*signal*)	=2
$\lvert \sum Q_\ell \rvert$	=2
Lepton p_{T}	$p_{\mathrm{T}}^{\ell_1,\ell_2} > 30, 20$ GeV
$\boldsymbol{E_{\mathrm{T}}^{\mathrm{miss}}}$	**< 70 GeV**
N_{jets}	≥ 3
$N_{b\text{-jets}}$	=0
Low SFOC $m_{\ell\ell}$ veto	–
Z boson decay veto	$\lvert m_{ee}^{\mathrm{sc}} - m_Z \rvert > 10$ GeV

Table 7.7: The pre-selection criteria for the $2\ell^{sc}$ channel fake factor measurement. The leptons are required to pass the *signal* or *candidate* requirements. The leptons are ordered by decreasing p_{T} ($\ell_1, \ell_2, ...$). The symbol "–" means no requirement is made. The equal sign (=) is used to emphasize that the selection criterion has to be exactly the given number.

The basic fake factor idea is defined as the ratio between the number of events with two *signal* leptons of the same sign and that with one *signal* and one non-*signal* lepton of the same sign,

$$\theta_\ell = \frac{N_{\ell\ell}}{N_{\ell\not\ell}}, \tag{7.8}$$

where ℓ denotes the *signal* e or μ and $\not\ell$ denotes the non-*signal* e or μ.

In the high jet-multiplicity region, the fake factors are assumed to be independent of $E_{\mathrm{T}}^{\mathrm{miss}}$, they are measured with di-lepton event with high jet multiplicity ($N_{jet} \geq 3$) and low $E_{\mathrm{T}}^{\mathrm{miss}}$. The $E_{\mathrm{T}}^{\mathrm{miss}}$ dependency is studied and the results shown in section 7.2.3.

The fake factors are measured with events after the subtraction of prompt same sign events and contamination from charge flip events. The electron fake factor is measured with ee events, and the muon fake factor is measured with $\mu\mu$ events. The fake factors, θ_e and θ_μ are computed as:

$$\theta_e = \frac{N_{ee}}{N_{e\not e}}(E_{\mathrm{T}}^{\mathrm{miss}} < 70\mathrm{GeV}) = \frac{N_{ee}^{\mathrm{Data}} - N_{ee}^{\mathrm{PromptSC}} - N_{ee}^{\mathrm{chargeflip}}}{N_{e\not e}^{\mathrm{Data}} - N_{e\not e}^{\mathrm{PromptSC}} - N_{e\not e}^{\mathrm{chargeflip}}} \tag{7.9}$$

$$\theta_\mu = \frac{N_{\mu\mu}}{N_{\mu\not\mu}}(E_{\mathrm{T}}^{\mathrm{miss}} < 70\mathrm{GeV}) = \frac{N_{\mu\mu}^{\mathrm{Data}} - N_{\mu\mu}^{\mathrm{PromptSC}}}{N_{\mu\not\mu}^{\mathrm{Data}} - N_{\mu\not\mu}^{\mathrm{PromptSC}}} \tag{7.10}$$

N^{PromptSC} is the contribution due to processes with prompt leptons with the same electric charge and is estimated with simulations. For θ_e, $N^{\mathrm{chargeflip}}$ is the contribution from the charge flip and is estimated using the scaled opposite-signed events, i.e. using the same technique explained in section 7.2.2.

Fake factor measurement

The measurement of the electron fake factor is performed in the ee channel. The two *signal* electrons events (i.e., the number of events at the numerator) are contaminated with fake electron events and charge flip electron events, thus the subtraction of charge misidentification electron is necessary. The events with *signal* electron plus *CandNotSig* electron (i.e., the number of events at the denominator) are considered to be enriched in fake electrons.

In the early results, it was observed that a p_{T}-inclusive fake factor is not sufficient to model the shape of the distributions of the p_{T} of leading and subleading leptons. This issue can be seen in Figure 7.13, where the fake factor method is used with inclusive fake factors.

Therefore, a p_{T} binned fake factor measurement is well motivated and hence implemented to obtain the fake factors for the fake factor method in the $2\ell^{sc}$ channel. Three p_{T} binned fake factors for each flavor are now measured; The p_{T} bins are: [20, 40], [40, 60] and [60, inf) GeV. In order to separate the leptons into different p_{T} bins: i) For events with two *signal* leptons (numerator), the sub-leading lepton is assumed to be the fake candidate, and its p_{T} information is used to decide the binning. This approach is checked with a Monte-Carlo closure test: the truth-based test is used to evaluate the probability that the leading lepton is actually a fake lepton. The results are shown in Table 7.10 and discussed in section 7.2.3. ii) For events with one *signal* lepton and one *CandNotSig* lepton (denominator), the *CandNotSig* lepton is chosen to be the fake candidate, and its p_{T} information is used to decide the binning. In each p_{T} bin, the fake factor is calculated independently.

The observed data, the reducible background, and the charge flip predictions obtained in the fake enriched measurement regions are listed in Table 7.8 for electrons and Table 7.9 for muons.

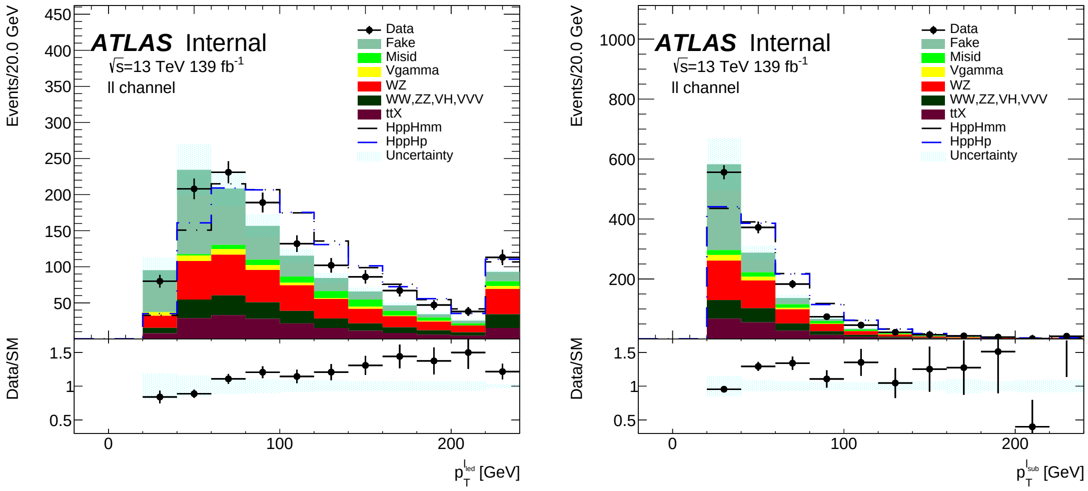

Figure 7.13: $2\ell^{sc}$ channel. Leading lepton p_{T} and sub-leading lepton p_{T} distribution at event pre-selection stage. Data-driven fake results were applied with **inclusive fake factors**. The tension found in these distributions motivates the use of a p_{T} binned fake factor measurement. All uncertainties are included. The non-prompt lepton background is taken from data-driven estimations. Two signals for the $m_{H^{\pm\pm}}$ 200 GeV mass point are shown; their distribution is scaled to the same integral as data.

	Num (TT)	Den (TL)	Num (TT)	Den (TL)	Num (TT)	Den (TL)
	20-40 GeV		40-60 GeV		> 60 GeV	
Data	163	2530	98	475	154	330
charge flip	30.9 ± 0.5	42.5 ± 0.5	24.8 ± 0.4	16.33 ± 0.31	55.6 ± 0.8	28.4 ± 0.4
WZ	36.6 ± 0.5	30.3 ± 0.7	30.9 ± 0.5	14.5 ± 0.4	37.2 ± 0.5	13.3 ± 0.5
ZZ	5.26 ± 0.14	4.90 ± 0.27	2.96 ± 0.11	1.75 ± 0.09	3.40 ± 0.11	1.61 ± 0.14
WW	3.93 ± 0.12	12.4 ± 1.4	3.86 ± 0.10	3.4 ± 0.6	5.37 ± 0.16	7.7 ± 1.1
ttX	4.80 ± 0.20	6.11 ± 0.23	5.03 ± 0.20	2.64 ± 0.15	5.16 ± 0.22	2.66 ± 0.15
Vgam	15.9 ± 3.0	71 ± 7	6.6 ± 2.0	14.7 ± 2.8	6.3 ± 2.1	22.0 ± 3.2
Monte-Carlo	66.7 ± 3.0	125 ± 7	49.6 ± 2.1	37.1 ± 2.9	57.5 ± 2.2	47.3 ± 3.4
Fake factor	0.028 ± 0.006		0.056 ± 0.024		0.160 ± 0.051	

Table 7.8: Electron fake factor: estimation of Prompt SS and Vγ Monte-Carlo, charge flip events and the observed data in the *signal*+*signal* (TT) and *signal*+anti-*signal* (TL) measurement regions; *VVV* processes are taken into account, and their contribution is small. The charge flip is subtracted both at the numerator or denominator. The uncertainties here are stat-only.

	Num (TT)	Den (TL)	Num (TT)	Den (TL)	Num (TT)	Den (TL)
	20-40 GeV		40-60 GeV		> 60 GeV	
Data	138	2770	88	773	80	387
WZ	44.9 ± 0.6	25.2 ± 0.9	33.5 ± 0.5	8.0 ± 0.4	32.0 ± 0.4	5.03 ± 0.31
ZZ	4.07 ± 0.10	3.12 ± 0.21	1.89 ± 0.06	0.61 ± 0.04	1.42 ± 0.05	0.47 ± 0.06
WW	7.31 ± 0.11	10.2 ± 1.2	7.28 ± 0.12	3.0 ± 0.6	7.06 ± 0.11	2.0 ± 0.5
ttX	8.23 ± 0.26	5.92 ± 0.22	8.20 ± 0.26	2.39 ± 0.14	7.26 ± 0.25	1.62 ± 0.12
Vgam	0.29 ± 0.28	16 ± 4	0.04 ± 0.04	3.7 ± 2.3	0.0 ± 0.0	1.6 ± 0.9
Monte-Carlo	65.3 ± 0.7	61 ± 4	51.2 ± 0.6	17.7 ± 2.5	48.1 ± 0.5	10.7 ± 1.1
Fake factor	0.027 ± 0.004		0.049 ± 0.013		0.085 ± 0.024	

Table 7.9: Muon fake factor: estimation for Prompt SS and Vγ Monte-Carlo events and the observed data in the *signal*+*signal* (TT) and *signal*+anti-*signal* (TL) measurement regions; VVV processes are taken into account, and their contribution is small. The uncertainties here are stat-only.

Fake factor application

In the $2\ell^{sc}$ channel, the fake factors mentioned above are further used in the pre-selection region, and later on also in the signal regions to estimate the fake lepton background. The equations used are:

$$N_{ee}^{fakes}(E_{\mathrm{T}}^{\mathrm{miss}} \geq 70\mathrm{GeV}) = (N_{e\not{e}} - N_{e\not{e}}^{\mathrm{PromptSC}} - N_{e\not{e}}^{\mathrm{chargeflip}}) \times \theta_e, \tag{7.11}$$

$$N_{\mu\mu}^{fakes}(E_{\mathrm{T}}^{\mathrm{miss}} \geq 70\mathrm{GeV}) = (N_{\mu\not{\mu}}^{\mathrm{Data}} - N_{\mu\not{\mu}}^{\mathrm{PromptSC}}) \times \theta_\mu, \tag{7.12}$$

$$N_{e\mu}^{fakes}(E_{\mathrm{T}}^{\mathrm{miss}} \geq 70\mathrm{GeV}) = (N_{e\not{\mu}} - N_{e\not{\mu}}^{\mathrm{PromptSC}} - N_{e\not{\mu}}^{\mathrm{chargeflip}}) \times \theta_\mu + (N_{\mu\not{e}} - N_{\mu\not{e}}^{\mathrm{PromptSC}} - N_{\mu\not{e}}^{\mathrm{chargeflip}}) \times \theta_e. \tag{7.13}$$

Fake leptons systematics uncertainties

The following sources of systematic uncertainties are included in the estimation of background from fake leptons: The first is the statistical uncertainty on fake factors. The second is the uncertainty due to the Monte-Carlo modeling of the prompt processes that are used for the fake factor measurement (uncertainties of lepton reconstruction and efficiency measurement, the cross-sections for normalizations, and jet/$E_{\mathrm{T}}^{\mathrm{miss}}$ energy scales). The third is the systematic and statistical uncertainties on the charge flip rates, which are extrapolated to the fake factor measurement.

The fourth is the method uncertainty of choosing the sub-leading lepton as the fake lepton candidate. This uncertainty is estimated by comparing the Monte-Carlo-based fake factor with the truth Monte-Carlo fake factor (details in Table 7.10). Comparison is done in the three p_{T} bins used to compute the fake factors; the uncertainty is increasing from 6-10% in the $p_{\mathrm{T}} < 60$ region to 46% (for electrons)

82% (for muons). Besides the stat uncertainty source, it is the only source measured and further assigned per p_{T} bin.

The last one is the Monte-Carlo-based $E_{\mathrm{T}}^{\mathrm{miss}}$ extrapolation uncertainty. The fake factor is calculated in the low $E_{\mathrm{T}}^{\mathrm{miss}}$ region, but it will be used in the high $E_{\mathrm{T}}^{\mathrm{miss}}$ regions. To account for possible changes in the fake factor, we compare the non-prompt Monte-Carlo yields with the Monte-Carlo-based fake factor estimation in the low and high $E_{\mathrm{T}}^{\mathrm{miss}}$ regions. The difference between the two predictions is taken as a source of systematic uncertainty (results in table 7.11).

Electron	20-40 GeV	40-60 GeV	60-inf GeV
Nominal numerator	26.4 ± 5.7	7.4 ± 1.3	6.3 ± 0.9
Truth numerator	23.8 ± 5.7	6.9 ± 1.3	9.5 ± 1.1
Nominal factor	0.0115 ± 0.0025	0.019 ± 0.0035	0.02 ± 0.0032
Truth factor	0.0104 ± 0.0025	0.0179 ± 0.0036	0.0292 ± 0.0036
Relative uncertainty (%)	9.6	6.0	46.0
Muon	20-40 GeV	40-60 GeV	60-inf GeV
Nominal numerator	47.0 ± 3.5	12.6± 1.4	6.1 ± 0.9
Truth numerator	43.2 ± 3.5	11.3 ± 1.3	11.1 ± 1.3
Nominal factor	0.0176 ± 0.0014	0.0162 ± 0.0019	0.0147 ± 0.0022
Truth factor	0.0162 ± 0.0013	0.0146 ± 0.0018	0.0267 ± 0.0031
Relative uncertainty (%)	8.0	10.9	81.6

Table 7.10: Monte-Carlo-based (using Non-prompt Monte-Carlo samples) fake factor closure test, showing results when the sub-leading lepton is the fake candidate (nominal), and when the fake lepton is selected using the truth lepton information. The uncertainties here are stat-only. The relative uncertainty will be assigned to each fake factor separately; these are the so-called "method uncertainties".

To compute the prompt-Monte-Carlo modeling, charge flip estimation, Monte-Carlo-based $E_{\mathrm{T}}^{\mathrm{miss}}$ extrapolation systematic uncertainties associated with the three fake factors, a simplified method is employed (mainly due to lack of statistics in p_{T} bins). It assumes that the relative systematic uncertainties are the same for all fake factors (independent on the p_{T} bin). Some technical details are discussed below (here, the term 'events' always assumes that the background of the prompt leptons is subtracted). For each systematic source variation, firstly the signal+anti-*signal* events are used to evaluate the expected fake-lepton background in *signal*+*signal* region. Secondly, by comparing the expected fake-lepton background and the varied *signal*+*signal* events, the inclusive relative difference in the event yields is used as uncertainty on the fake factors, no matter the p_{T} bin. The break-down uncertainties sources on the electron and muon fake factors are shown in Table 7.12. The final fake factors and the associated uncertainties are shown in Table 7.13.

A closure test is performed to check the stability of fake factors. It is done by applying the computed fake factors to the entire (low and high) $E_{\mathrm{T}}^{\mathrm{miss}}$ range. The results of the closure test are shown in Figure 7.14, the agreement between data and background estimation is generally well in the entire $E_{\mathrm{T}}^{\mathrm{miss}}$ range, in all channels. The differences are well within the assigned uncertainties. This test gives confidence that the fake factors measured in the designed control region (with $E_{\mathrm{T}}^{\mathrm{miss}}$ <70 GeV) are representative for the *signal* regions (defined with higher cuts on $E_{\mathrm{T}}^{\mathrm{miss}}$).

Flavor	Monte-Carlo-fake calculated	Monte-Carlo-fake counted	Relative uncertainty (%)
Electron	28.01±3.09	22.66±1.78	19.1
Muon	39.51±2.57	42.40±2.62	7.3

Table 7.11: The Monte-Carlo-based $E_{\mathrm{T}}^{\mathrm{miss}}$ extrapolation uncertainty. The "Monte-Carlo-fake calculated" results used the Monte-Carlo-based fake factor to calculate the non-prompt leptons contribution in the pre-selection region. The "Monte-Carlo-fake counted" results were counted in the pre-selection with non-prompt Monte-Carlo. The uncertainties here are stat-only. Relative uncertainty is assigned from central value differences for conservative.

Sources	unct(%) [e]	unct(%) [μ]
charge flip	15.9	-
Monte-Carlo closure	19.1	7.3
Prompt-Monte-Carlo theory uncertainty	17.4	15.8
electron efficiency	7.43	-
electron resolution and scale	0.56	0.02
muon scale/ID/sagitta	0.01	0.54
muon efficiency	-	0.75
Pileup reweighting data-scale-factor	0.3	0.63
JET category reduction/energy scale/energy resolution	12.77	10.06
Flavor tagging	0.31	0.28
MET Variation	1.70	2.07
Total global unct	33.74	22.76

Table 7.12: Summary of the uncertainties assigned to the electron (left) and muon (right) fake factors (in %). The "charge flip" source originates from the charge flip background subtraction (see Eq. (7.11)), and it is treated as correlated in the extraction procedure. In the Prompt-Monte-Carlo, theory uncertainty source enters: i) the uncertainty on the WZ process as quoted in 7.1.1, ii) the uncertainties on the other processes leading to prompt leptons from cross section.

Electron	Fake factor
20-40 GeV	$0.028 \pm 0.006_{\mathrm{stat}} \pm 0.009_{\mathrm{glob\ syst}} \pm 0.003_{\mathrm{method\ syst}}$
40-60 GeV	$0.056 \pm 0.024_{\mathrm{stat}} \pm 0.018_{\mathrm{glob\ syst}} \pm 0.003_{\mathrm{method\ syst}}$
60-inf GeV	$0.160 \pm 0.051_{\mathrm{stat}} \pm 0.053_{\mathrm{glob\ syst}} \pm 0.073_{\mathrm{method\ syst}}$
Muon	Fake factor
20-40 GeV	$0.027 \pm 0.004_{\mathrm{stat}} \pm 0.005_{\mathrm{glob\ syst}} \pm 0.002_{\mathrm{method\ syst}}$
40-60 GeV	$0.049 \pm 0.013_{\mathrm{stat}} \pm 0.010_{\mathrm{glob\ syst}} \pm 0.005_{\mathrm{method\ syst}}$
60-inf GeV	$0.085 \pm 0.024_{\mathrm{stat}} \pm 0.017_{\mathrm{glob\ syst}} \pm 0.069_{\mathrm{method\ syst}}$

Table 7.13: Summary of all fake factors include all sources of uncertainties. Global systematic uncertainty indicates combination of uncertainties used simplified calculation method(In Table 7.12). Method systematic uncertainty indicates method uncertainty(Table 7.10)

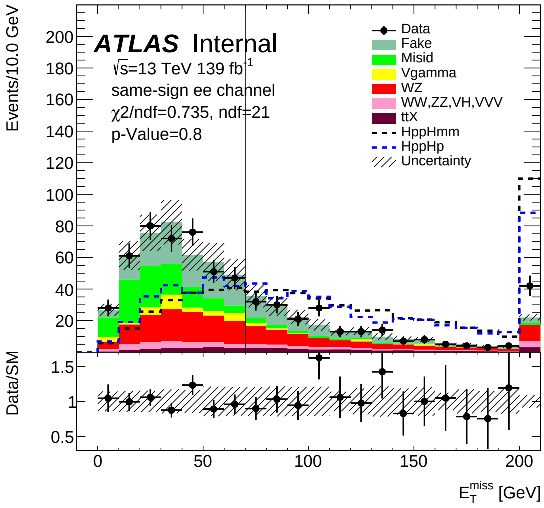

(a) *ee* channel

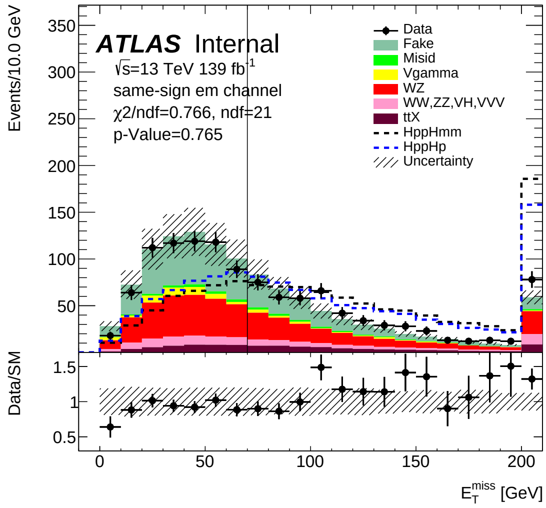

(b) $e\mu$ channel

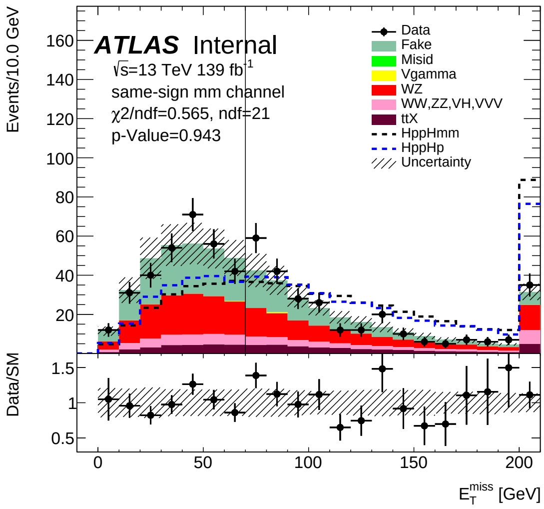

(c) $\mu\mu$ channel

Figure 7.14: $2\ell^{sc}$ channel. Fake estimation validation plots ($E_{\mathrm{T}}^{\mathrm{miss}}$ distribution).
Top Left(ee), Top Right($e\mu$) and Bottom($\mu\mu$) plots show the fake lepton background estimation in the combined fake-calculation and pre-selection region (separated by black line drawn for $E_{\mathrm{T}}^{\mathrm{miss}}$ = 70 GeV). The uncertainty includes the statistic uncertainty and all sources of systematic uncertainties on the background estimation. Two *signal*s points with 200 GeV $m_{H^{++}}$ mass are shown. The signal is scaled to the same integral as data.

7.2.4 Background validation

With data-driven estimations of the contributions from fake and charge-flipped leptons, the total background is compared with the number of observed events in data in Table 7.14. The background from fake leptons is implemented using the events in the "*signal+CandNotSig* di-lepton" region, weighted by the fake factors. As mentioned, the WZ, ZZ, same sign WW, etc., backgrounds are estimated from the Monte-Carlo simulation. The very good agreement between data and prediction validates the data-driven background estimate methods described above. More background validations distributions are shown in Figures 7.15-7.17. Generally, an agreement between data and background is seen, validating the data-driven methods used for the charge flip electron background and fake/non-prompt lepton background estimation.

	Data	Prompt	Fake	charge flip	Total background
ee	224	113.83±18.78	67.22±19.16	14.06±2.71	195.11±26.97
$\mu\mu$	275	160.37±24.46	93.92 ± 21.39	-	254.29±32.49
$e\mu$	542	299.1±44.46	168.62±42.58	15.81±2.88	483.52±61.63

	WZ	WW,ZZ,VH,VVV	ttX	Vγ
ee	68.67±9.34	18.09±3.66	21.27±4.25	5.8±2.56
$\mu\mu$	91.2±11.83	34.13±6.86	34.5 ± 6.89	0.55 ± 0.57
$e\mu$	172.89±22.09	52.9±10.64	58.8±11.75	15.81±2.88

Table 7.14: Data and SM background prediction after the pre-selection requirements mentioned in Table 7.2 are applied. The charge flip and fake lepton background contributions are estimated using the data-driven methods described in this section. Both statistic and systematic uncertainty sources are included. $V\gamma$ samples are included in the prompt category for the electrons from photon conversions. The lower table shows the break-down of the different background sources entering in the "Prompt" category.

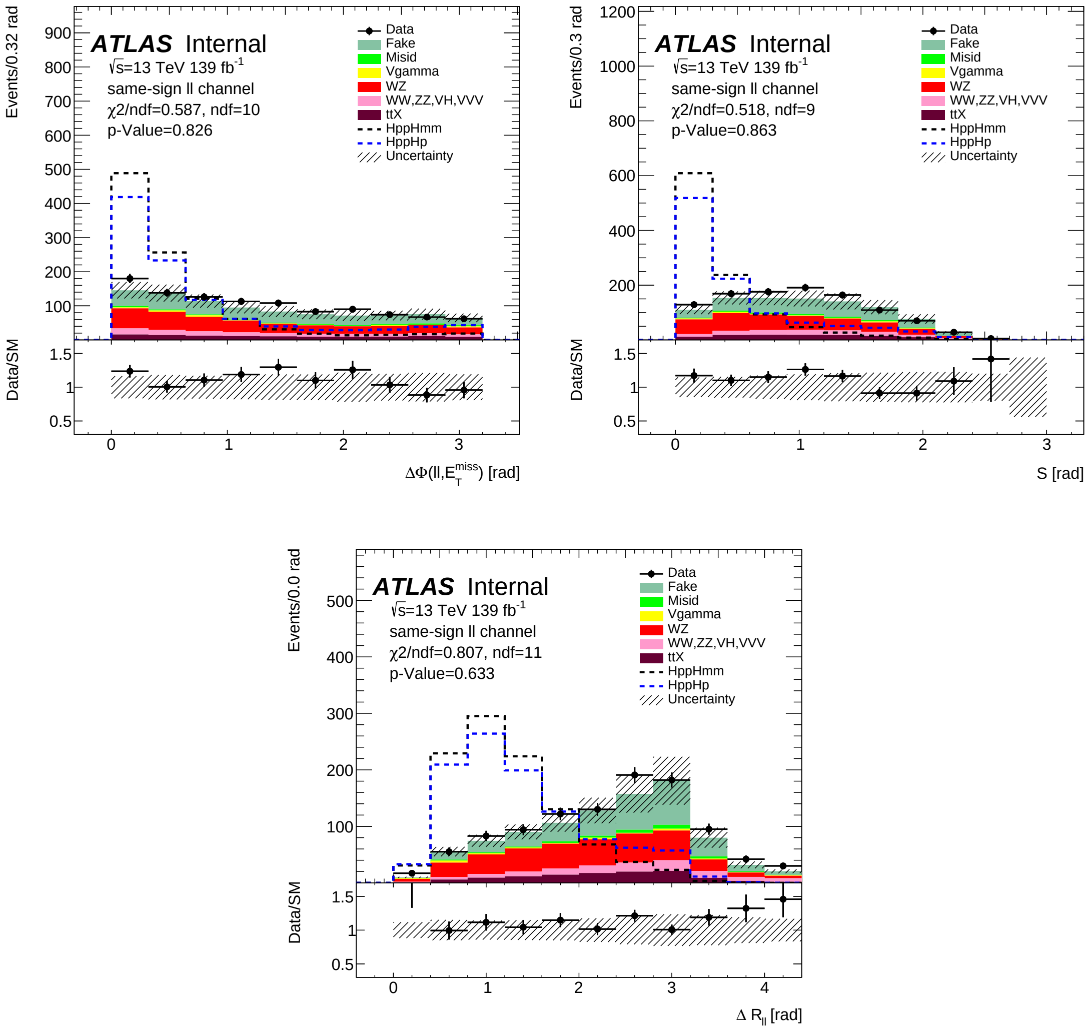

Figure 7.15: $2\ell^{sc}$ channel. Angular-related discriminating distribution at pre-selection stage (Table 7.2). Two *signal*s points with a mass of 200 GeV are shown. All uncertainties included. The non-prompt lepton background is taken from data-driven estimations. the signal is scaled to the same integral as data.

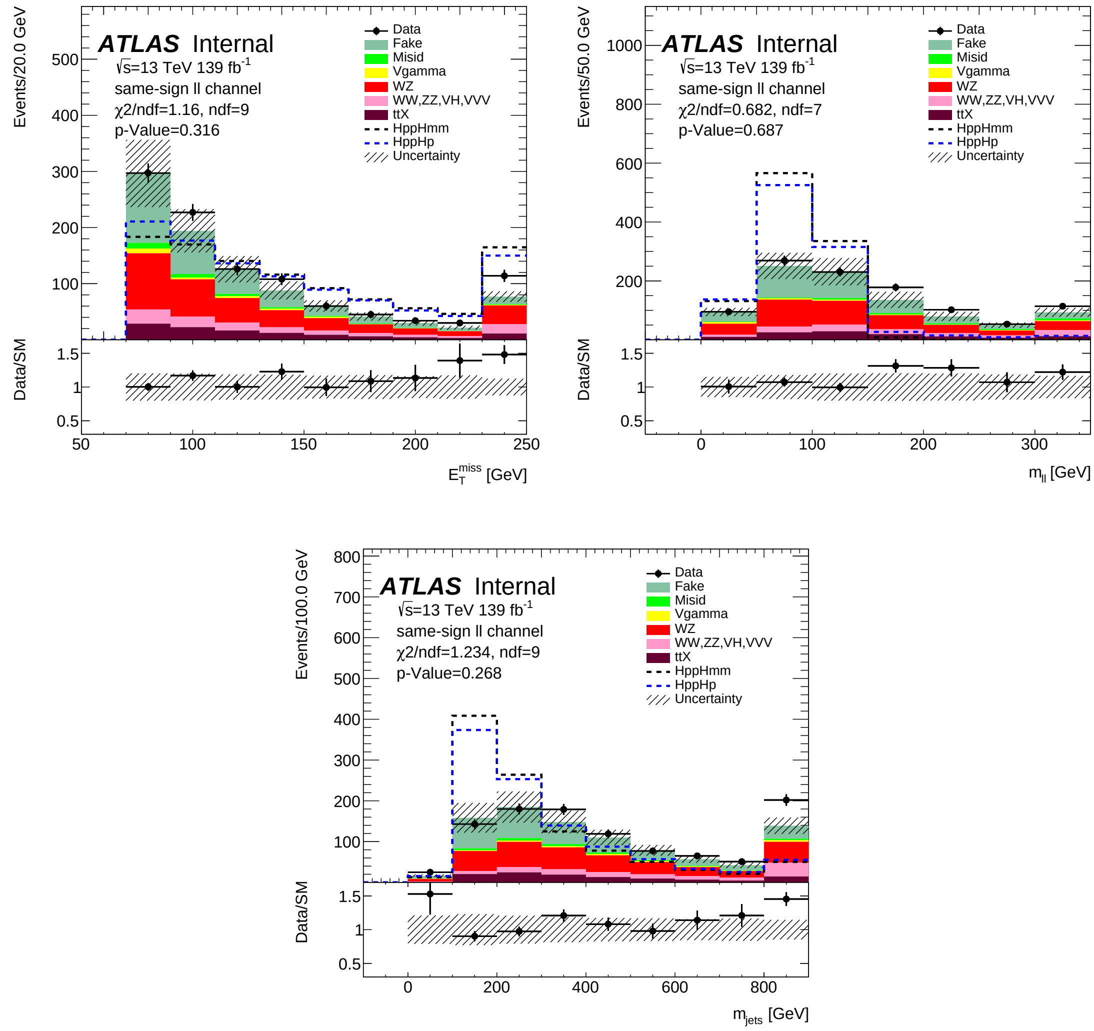

Figure 7.16: $2\ell^{sc}$ channel. Distribution of mass-related discriminating variables at pre-selection stage (Table 7.2). Two *signal*s points with a mass of 200 GeV are shown. All uncertainties are included. The non-prompt lepton background is taken from data-driven estimations. the signal is scaled to the same integral as data.

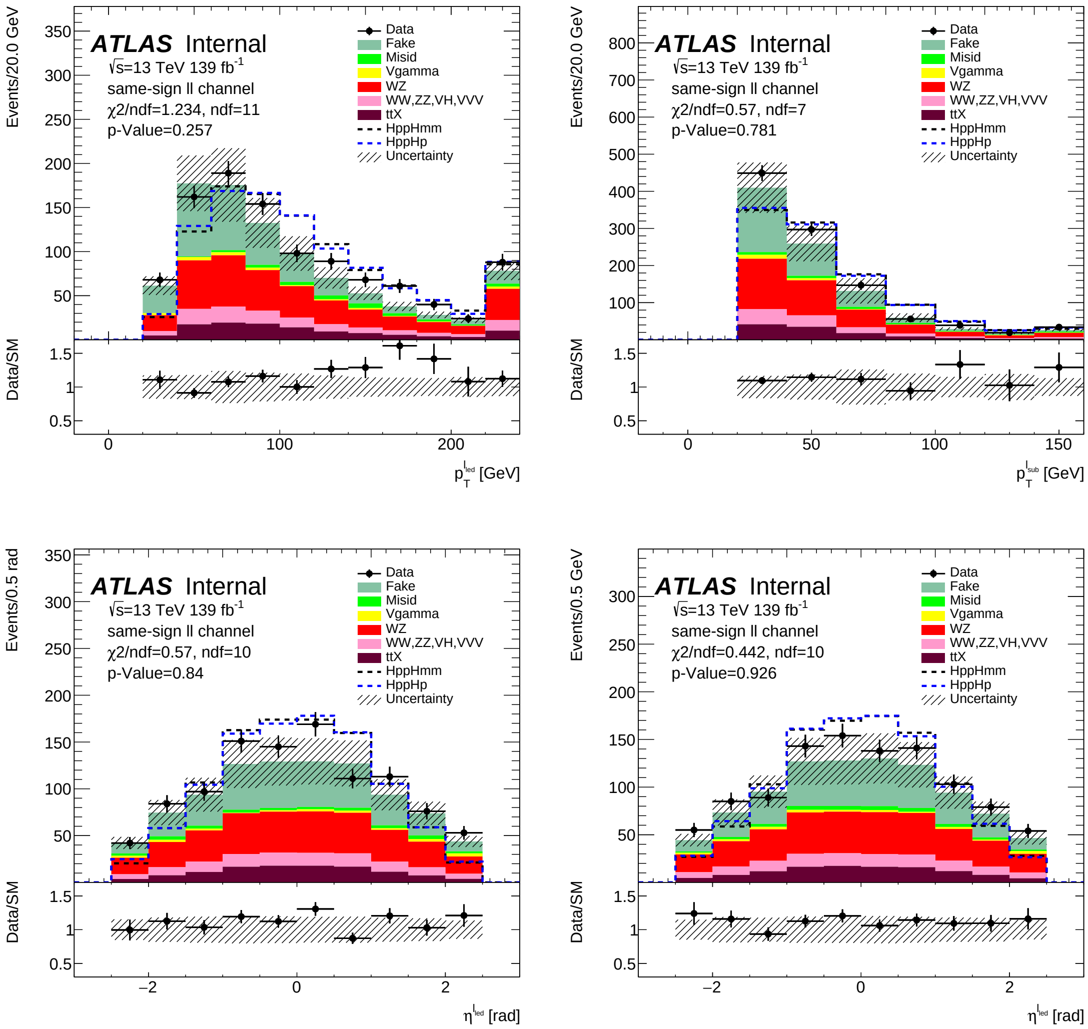

Figure 7.17: $2\ell^{sc}$ channel. Kinematics variable distribution at pre-selection stage. Two *signal*s points with a mass of 200 GeV are shown. All uncertainties are included. The non-prompt lepton background is taken from data-driven estimations. the signal is scaled to the same integral as data.

7.3 Three lepton channel

7.3.1 Event selection and Prompt background

Selection criteria	3ℓ
At least one offline *signal* lepton with p_{T}^{ℓ}>30 GeV that triggered the event	
N_{ℓ} (*candidate*)	=3
N_{ℓ} (*signal*)	≥2 ($\ell_{1,2}$)
$\lvert \sum Q_{\ell} \rvert$	=1
Lepton p_{T}	$p_{\mathrm{T}}^{\ell_0,\ell_1,\ell_2} > 10, 20, 20$ GeV
$E_{\mathrm{T}}^{\mathrm{miss}}$	> 30 GeV
N_{jets}	≥ 2
$N_{b\text{-jets}}$	=0
Low SFOC $m_{\ell\ell}$ veto	$m_{\ell\ell}^{\mathrm{oc}} > 15$ GeV
Z boson decays veto	$\lvert m_{\ell\ell}^{\mathrm{oc}} - m_Z \rvert > 10$ GeV

Table 7.15: The pre-selection criteria for the 3ℓ analysis channels. The leptons are required to pass the *candidate* or *signal* requirements. The lepton 0 is always the opposite charge lepton. The equal sign (=) is used to emphasize that the selection criterion has to be exactly the given number.

The event pre-selection in 3ℓ is illustrated in Table 7.15. Exactly three loose leptons with a total charge(sum of the charge of the three leptons) of ±1 are requested in each event. The lepton matched to the trigger is requested to have a $p_{\mathrm{T}} > 30$ GeV, and pass the *signal* requirements from Tables 6.3. The two leptons forming the same charge pair are also required to satisfy the *signal* lepton definition (as these leptons are more likely to be fake/non-prompt). The lepton not in the same charge pair has a more relaxed definition, and should satisfy the *candidate* lepton definition. Some notation for 3ℓ section:

- The symbols used to refer to the three selected leptons:

  - Leptons are named as lepton 1 (ℓ_0), lepton 2 (ℓ_1) and lepton 3 (ℓ_2).

  1 The lepton 0 (ℓ_0) is always the opposite sign lepton.

  2 The lepton 1 (ℓ_1) and 2 (ℓ_2) are the same sign leptons.

  3 The lepton 1 (ℓ_1) is closer to the lepton 0 (ℓ_0): $\Delta R(\ell_0, \ell_1) < \Delta R(\ell_0, \ell_2)$.

  4 $x\ell\not\ell$ denotes includes both $x\ell\not\ell$ and $x\not\ell\ell$ events. The crossed symbol corresponds to *CandNotSig* leptons. The x stands for the lepton 0 (ℓ_0). This notation convention is mainly used in the fake lepton estimation section 7.3.2.

- Possible final states/sub-channels:

  SFOC0 0 same-flavor-opposite-charge (SFOC) lepton pairs: $e^{\mp}\mu^{\pm}\mu^{\pm}$, $\mu^{\mp}e^{\pm}e^{\pm}$.

SFOC12 1 or 2 same-flavor-opposite-charge (SFOC) lepton pairs: $e^{\mp}e^{\pm}\mu^{\pm}$, $\mu^{\mp}\mu^{\pm}e^{\pm}$, $e^{\mp}e^{\pm}e^{\pm}$, $\mu^{\mp}\mu^{\pm}\mu^{\pm}$.

A veto is imposed by requiring that the events with all SFOC lepton pairs **not** in Z-window ($|M_{\ell\ell}^{os} - M_Z| > 10$ GeV). The low mass Drell-Yann processes are rejected by requiring that the events with all SFOC lepton pairs satisfy $M_{\ell\ell}^{os} > 15$ GeV. vents with significant missing transverse energy $E_{\mathrm{T}}^{\mathrm{miss}} > 30$ GeV are selected (see Figure 7.24). Events with one or more jets tagged as b-jet are rejected to suppress $t\bar{t}$ process. The distributions of the jet and b-jet multiplicities are shown in Figure 7.18 with pre-selection jet or b-jet requirements relaxed. The distributions of the discriminating variables and kinematic variables, with all background estimation from the Monte-Carlo simulation, are shown in Figures 7.19 and 7.20.

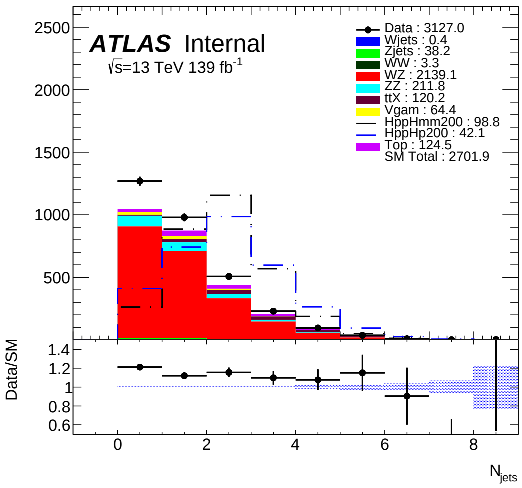

(a) Njets distribution (Linear Scale)

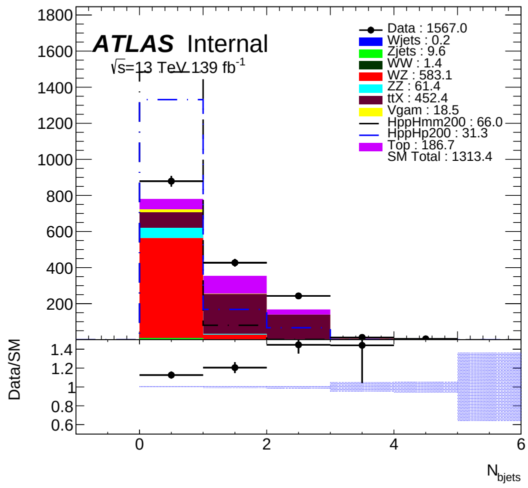

(b) Nbjets distribution (Linear Scale)

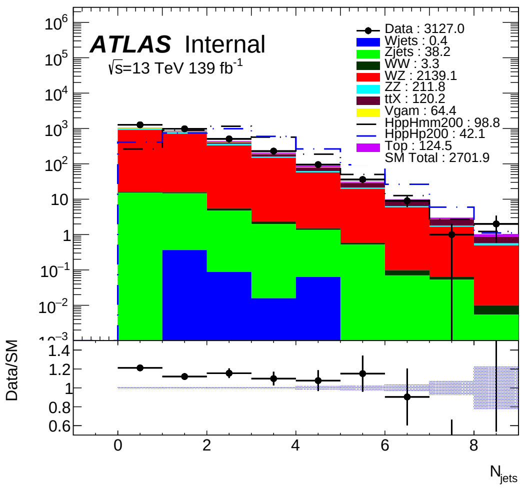

(c) Njets distribution (Log Scale)

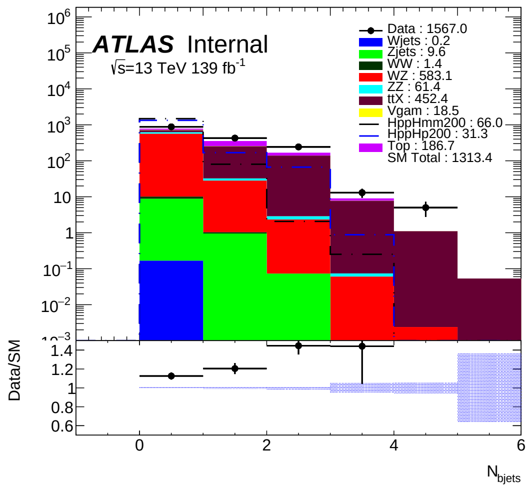

(d) Nbjets distribution (Log Scale)

Figure 7.18: In the 3ℓ channel, the distributions of the jet/b-jet multiplicity before pre-selection region selection. For jet multiplicity distribution, the N_{jets}>=2 cut is removed; for numbers of b-jets distribution, the $N_{b\text{-jets}}$=0 cut is removed. The fake background in taken from the Monte-Carlo simulations. Note that the signal is scaled to data integral, for better visibility. The bottom panels of each figure show the ratio between data and the total SM prediction. The error band includes only the statistical uncertainty. The top two figures are shown in linear scale, while the bottom two figures were shown in log scale.

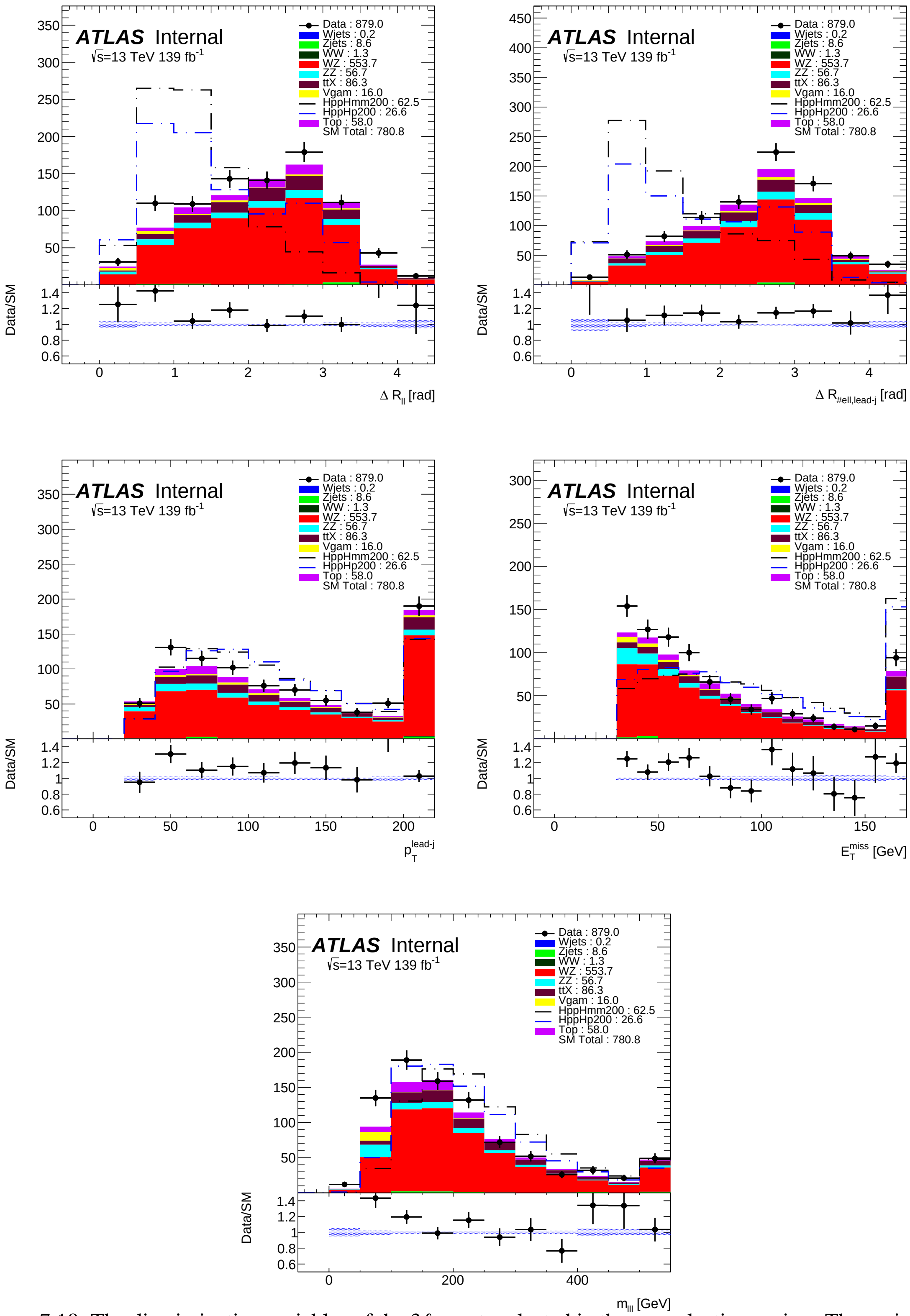

Figure 7.19: The discriminating variables of the 3ℓ events selected in the pre-selection region. The variables shown from the left top are the ΔR between same-sign leptons, ΔR between the lepton-jet, p_{T} of the leading lepton, E_T^{miss} and tri-lepton mass. The non-prompt background is taken from the Monte-Carlo simulations. Note that the signal is scaled to data integral. The error band includes only the statistical uncertainty.

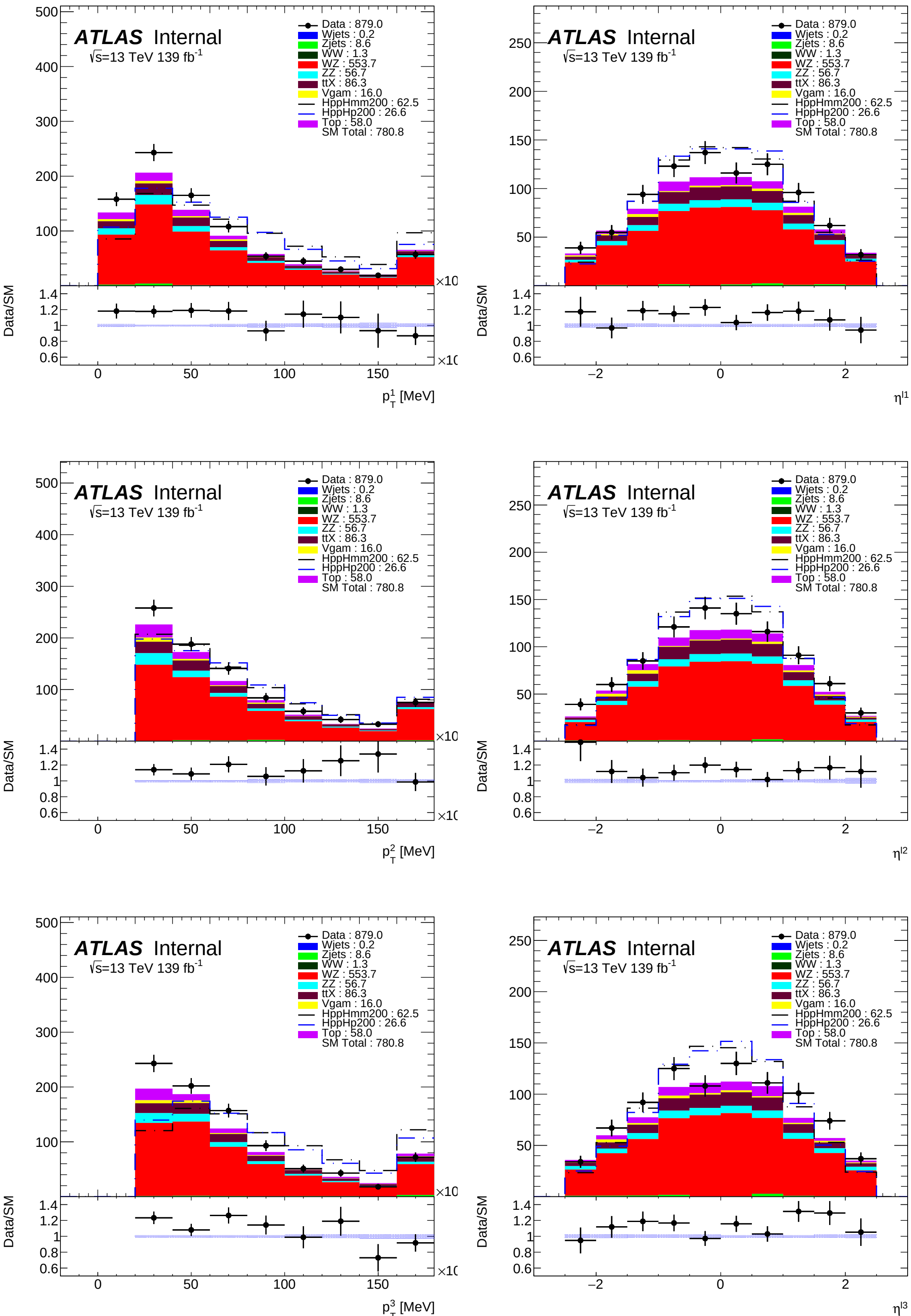

Figure 7.20: The kinematic variables of the 3ℓ events included in the pre-selection region. The non-prompt background is taken from the Monte-Carlo simulations. Note that the signal is scaled to data integral, for better visibility. Only the statistical uncertainty is shown.

7.3.2 Fake/Non-prompt lepton background

Fake enriched control region (CRs)

Selection criteria	3ℓ fake estimation
At least one offline *signal* lepton with $p_T^{\ell} > 30$ GeVthat triggered the event	
N_ℓ (*candidate*)	=3
N_ℓ (*signal*)	≥2 ($\ell_{1,2}$)
$\lvert \sum Q_\ell \rvert$	=1
Lepton p_T	$p_T^{\ell_0,\ell_1,\ell_2} > 10, 20, 20$ GeV
E_T^{miss}	> 30 GeV
N_{jets}	**=1**
$N_{b\text{-jets}}$	**-**
Low SFOC $m_{\ell\ell}$ veto	$m_{\ell\ell}^{oc} > 15$ GeV
Z boson decays veto	$\lvert m_{\ell\ell}^{oc} - m_Z \rvert > 10$ GeV

Table 7.16: The pre-selection criteria for the 3ℓ fake estimation. The leptons are required to pass the *candidate* or *signal* requirements. The lepton 0 is always the opposite charge lepton. The symbol "–" means no requirement is made. The equal sign (=) is used to emphasize that the selection criterion has to be exactly the given number.

In the 3ℓ channel, the fake leptons originate mostly from $t\bar{t}$ and Z+jets processes. To define a region enriched in fake/non-prompt leptons (thus with a low level of prompt lepton contamination), one of the selected leptons from the same-charge pair are required to pass the *candidate* requirements but to fail the *signal* ones. Therefore, in order to study and estimate the fake lepton background, the fake enriched control region is defined (Table 7.16). This region is a low jet multiplicity sample disjoint from the pre-selection region. Only events with the same-charge-same-flavor, for example, xee and $x\mu\mu$, are used for the lepton fake factor calculation. Events with same-sign-different-flavor, for example, $xe\mu$, are used for lepton fake factor systematic uncertainty estimation (to get the "$e\mu$ closure" sources detailed in in section 7.3.2).

Another region enriched by $t\bar{t}$ and $t\bar{t}X$ processes is defined with the pre-selection cuts but with the jets condition change to $N_{\text{b-jets}} = 1$. This region is used to validate mainly the fake lepton background estimation. The main contributions of background in the fake enriched CRs are expected to be the VV and $t\bar{t}X$ ($t\bar{t}H$, $t\bar{t}V$, tZ) processes, as illustrated in the distributions shown in Figure 7.18.

Fake factor measurement

The fake factors are calculated in the fake estimation regions using the formula 7.14:

$$\theta_{e/\mu} = \frac{(Data - N_{prompt})_{xee/x\mu\mu}}{(Data - N_{prompt})_{xe\not{e}/x\mu\not{\mu}}} \tag{7.14}$$

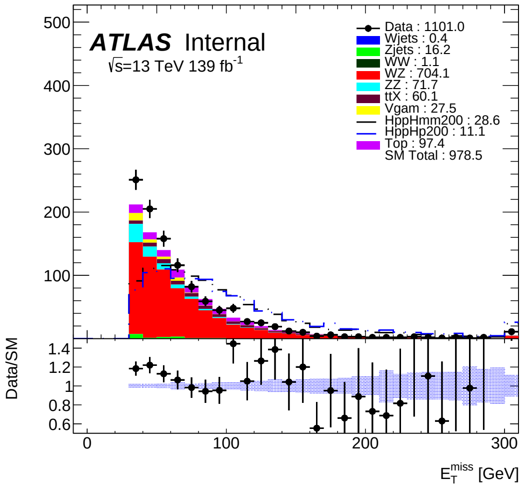

(a) Fake enrich region ($x\ell\ell$)

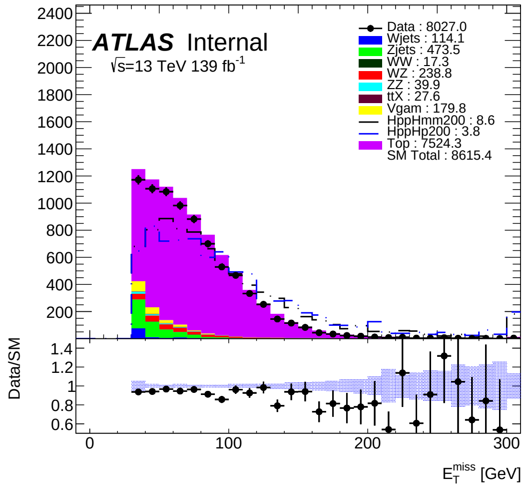

(b) Fake enrich region ($x\ell\not\ell$)

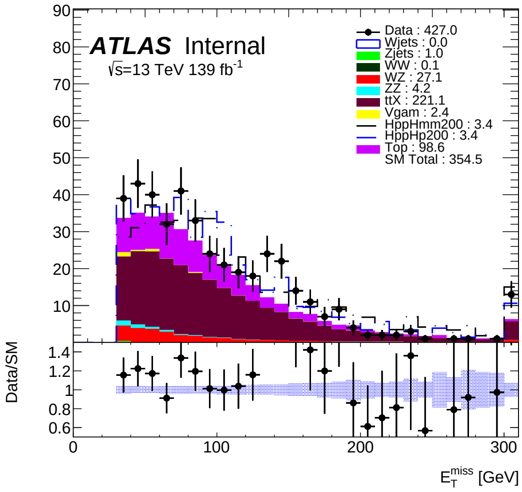

(c) Top validation region ($x\ell\ell$)

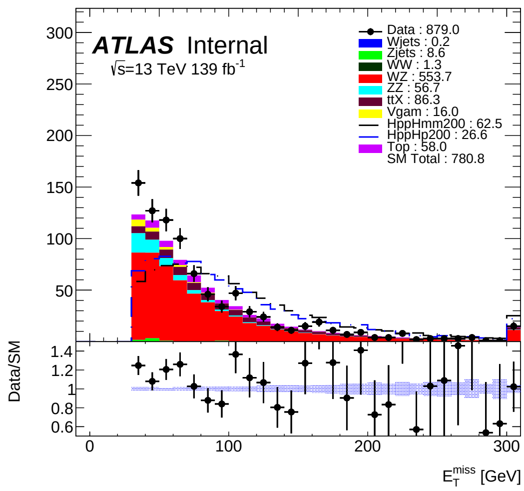

(d) pre-selection region ($x\ell\ell$)

Figure 7.21: 3ℓ Channel. $E_{\mathrm{T}}^{\mathrm{miss}}$ distribution in different regions. The non-prompt lepton background in taken from the Monte-Carlo simulations. Note that the signal is scaled to data integral, for better visibility. The error band includes only the statistical uncertainty.

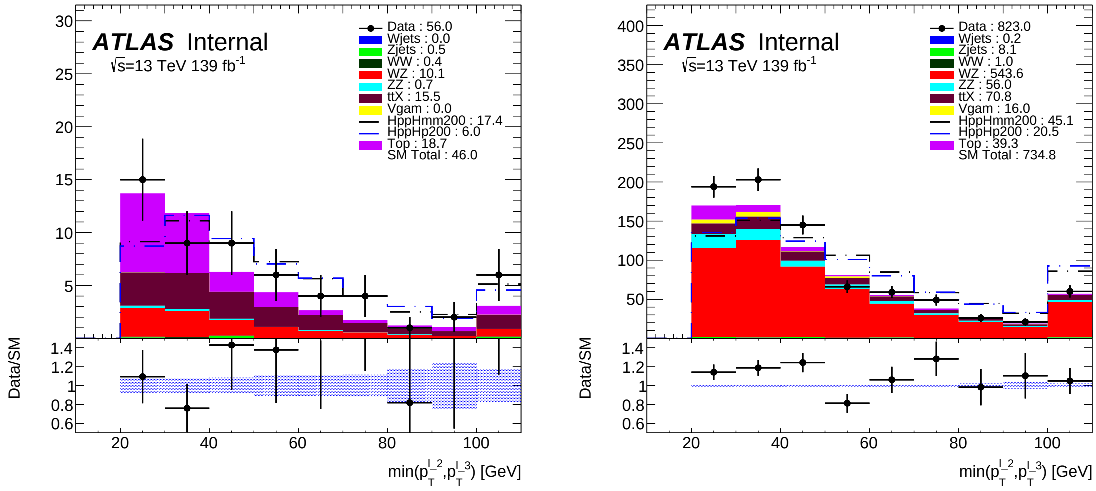

(a) 0 same-flavor-opposite-charge pairs

(b) 1/2 same-flavor-opposite-charge pair

Figure 7.22: The distributions of the 3ℓ events included in the pre-selection region. The non-prompt lepton background in taken from the Monte-Carlo simulations. Note that the signal is scaled to data integral, for better visibility. Only the statistical uncertainty is shown.

Here the index $\not{e}$ and $\not{\mu}$ indicate the *CandNotSig* while e and μ indicate the electrons and muons that pass the *signal* selection. The opposite charge lepton is indicated by "x" (can be an electron or a muon), and it is assumed to be prompt – in the "opposite charge lepton purity" source of systematic uncertainty entry, in section 7.3.2, is a discussion about the possibility that this lepton is actually non-prompt. Due to low statistics, the fake factor is measured inclusively.

The number of events entering at the numerator and denominator, as well as the fake factors, are shown in Table 7.17. The break-down of the different prompt processes is summarized in Table 7.18. The $E_{\mathrm{T}}^{\mathrm{miss}}$ distribution in the fake enriched control region, pre-selection region, and Top validation region is shown in Figure 7.21. To understand better the background composition in these regions, the minimum lepton p_{T} of same-sign leptons pair is shown in Figures 7.22 and 7.23. One can see that the fake enriched control region and pre-selection region are dominated by WZ process; the Top validation region is dominated by $t\bar{t}X$ process. The most dominant non-prompt process in all three regions is the Top pair production. The non-prompt leptons from Z in the fake enriched control region are a sub-dominant contribution (especially in the low $E_{\mathrm{T}}^{\mathrm{miss}}$ (<50 GeV) region), and in the other two regions are negligible.

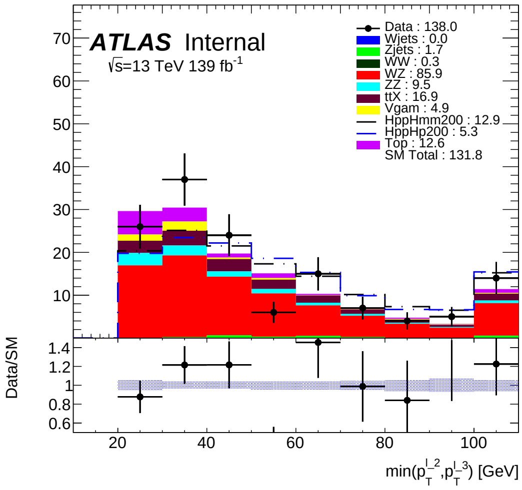

(a) xee channel

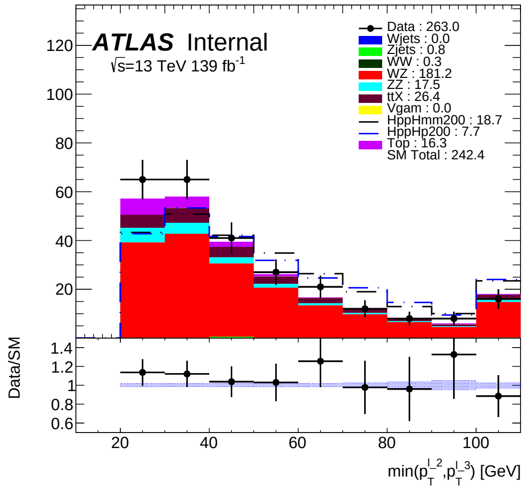

(b) $x\mu\mu$ channel

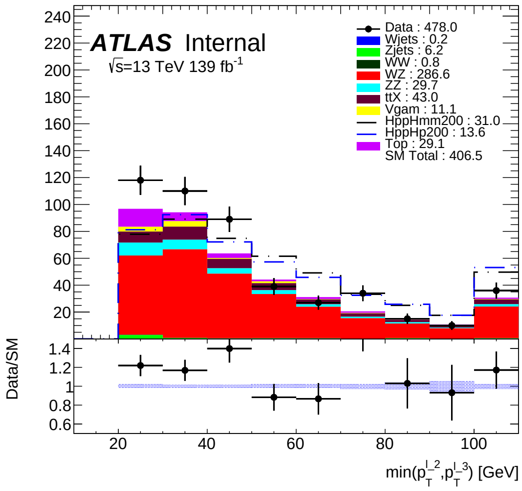

(c) $xe\mu$ channel

Figure 7.23: The distributions of the 3ℓ events included in the pre-selection region. The non-prompt lepton background is taken from the Monte-Carlo simulations. Note that the signal is scaled to data integral, for better visibility. Only the statistical uncertainty is shown.

Fake enriched control region					
Channel	Data	Prompt	Data − Prompt	Non-prompt Monte-Carlo	Data-driven fake ℓ
$xe\not{e}$	1699	118.67 ± 5.3	1580.33 ± 41.56	1667.51 ± 22.81	-
$x\mu\not{\mu}$	2232	89.87 ± 3.93	2142.13 ± 47.4	2164.77 ± 19.96	-
Channel	Data	Prompt	Data − Prompt	Non-prompt Monte-Carlo	Data-driven fake ℓ
xee	178	145.24 ± 2.47	32.76 ± 13.57	21.9 ± 2.43	32.76 ± 13.57
$x\mu\mu$	351	281.79 ± 3.32	69.21 ± 19.02	32.69 ± 3.39	69.21 ± 19.02
'In-situ' results (calculated in this region)					
$\theta_e^{data-driven}$: 0.021 ± 0.009			$\theta_\mu^{data-driven}$: 0.032 ± 0.009		
$\theta_e^{Monte-Carlo-based}$: 0.013 ± 0.001			$\theta_\mu^{Monte-Carlo-based}$: 0.015 ± 0.002		

Table 7.17: Fake factor estimation results (summary). "Data / Prompt / Non-Prompt" entries show the data / prompt leptons from the Monte-Carlo / fake/non-prompt lepton from the Monte-Carlo yield in the dedicated region. "Data − Prompt" shows the area for fake lepton candidates by subtracting the prompt lepton contribution from data. "Data-driven fake ℓ" is estimated by applying the fake factor from Y in each region. The uncertainty is statistical only.

Fake enriched control region					
Denominator					
Channel	Prompt	WZ	WW,ZZ,VH,VVV	ttX	$V\gamma$
$xe\not{e}$	118.67 ± 5.3	55.55 ± 1.5	15.91 ± 0.54	7.11 ± 0.21	40.11 ± 5.05
$x\mu\not{\mu}$	89.87 ± 3.93	50.6 ± 1.36	15.48 ± 0.47	5.85 ± 0.19	17.95 ± 3.65
Numerator					
Channel	Prompt	WZ	WW,ZZ,VH,VVV	ttX	$V\gamma$
xee	145.24 ± 2.47	107.71 ± 2.02	18.72 ± 0.45	11.47 ± 0.26	7.34 ± 1.33
$x\mu\mu$	281.79 ± 3.32	228.5 ± 3.15	33.34 ± 0.71	18.54 ± 0.34	1.41 ± 0.71

Table 7.18: Break-down of the prompt lepton background in the fake factor calculation. In all sub-channels, WZ is the most dominant source of prompt leptons. The uncertainty is statistical only.

Fake factor application

The "fake factors" for electrons θ_e and muons θ_μ can be used to estimate the fake contribution as follows:

$$N_{xe\mu} = \theta_e \times N_{x\mu\not{e}} + \theta_\mu \times N_{xe\not{\mu}}, \tag{7.15}$$
$$N_{xee} = \theta_e \times N_{xe\not{e}}, \tag{7.16}$$
$$N_{x\mu\mu} = \theta_\mu \times N_{x\mu\not{\mu}}, \tag{7.17}$$

where the data yields indicated by N always has the subtraction of the prompt contribution (estimated with Monte-Carlo) performed.

Tables 7.19, 7.20 and 7.21 shows the details of fake factor calculation and its application; these tables contain also some information relevant for the systematic uncertainties computation (the discussion in section 7.3.2).

Fake enriched control region

Channel	Data	Prompt	Data − Prompt	Non-prompt Monte-Carlo	Data-driven fake ℓ
$xe\not{e}$	1699	118.67 ± 5.3	1580.33 ± 41.56	1667.51 ± 22.81	-
$xe\not{\mu}$	1863	75.21 ± 3.53	1787.79 ± 43.3	1821.26 ± 23.65	-
$x\mu\not{e}$	2233	229.61 ± 6.7	2003.39 ± 47.72	1958.98 ± 32.88	-
$x\mu\not{\mu}$	2232	89.87 ± 3.93	2142.13 ± 47.4	2164.77 ± 19.96	-

Channel	Data	Prompt	Data − Prompt	Non-prompt Monte-Carlo	Data-driven fake ℓ
xee	178	145.24 ± 2.47	32.76 ± 13.57	21.9 ± 2.43	32.76 ± 13.57
$xe\mu$	572	470.06 ± 5.02	101.94 ± 24.44	52.84 ± 3.41	99.28 ± 24.17
$x\mu\mu$	351	281.79 ± 3.32	69.21 ± 19.02	32.69 ± 3.39	69.21 ± 19.02

’In-situ’ results (calculated in this region)

$\theta_e^{data-driven}$: 0.021 ± 0.009
$\theta_e^{Monte-Carlo-based}$: 0.013 ± 0.001

$\theta_\mu^{data-driven}$: 0.032 ± 0.009
$\theta_\mu^{Monte-Carlo-based}$: 0.015 ± 0.002

Table 7.19: Fake factor estimation and simple application (counted events) results in the fake enriched control region. "Data / Prompt / Non-Prompt" entries show the data / prompt leptons from the Monte-Carlo / fake/non-prompt lepton from the Monte-Carlo yield in the dedicated region. "Data − Prompt" shows the area for fake lepton candidates by subtracting the prompt lepton contribution from data. "Data-driven fake ℓ" is estimated by applying the fake factor from Y in each region. The uncertainty is the statistical component only.

Fake estimation systematics

Various sources of systematic uncertainties are included in the estimation of background from fake/non-prompt leptons. The uncertainty due to Monte-Carlo modeling (variations of lepton identification efficiencies measurements, cross sections for normalizations and jet/E_{T}^{miss} energy scales) of the prompt processes can affect the fake factor calculation. The total uncertainty in this category is 53.6% for the electron fake factor, and 43.1% for the muon fake factor.

The stability of the fake factor across the fake enriched control region and pre-selection region is considered as a systematic uncertainty attributed to the sample composition dependence (Tables 7.19 and 7.20). The difference between the Monte-Carlo-based and data-driven "in-situ" nominal fake factors (shown in Table 7.19) is taken as a source of (relative) uncertainty. For electrons, 13.3% relative uncertainty is taken, as it covers the difference. For muons, 15.4% relative uncertainty is taken, as it covers the difference.

The fake factors are measured in the xee and $x\mu\mu$ channels for electrons and muons, respectively. The closure quality is verified in $xe\mu$ the channel. This uncertainty is calculated only in the fake enriched control region. The data-driven fake lepton background estimation in the $xe\mu$ sub-channel (99.28) agrees very well with data minus prompt yield (101.94). Given the very good agreement, no source of uncertainty is added.

The fake factor method assumes as well that the "opposite-charge" lepton is prompt (not fake or pre-selection region

Channel	Data	Prompt	Data − Prompt	Non-prompt Monte-Carlo	Data-driven fake ℓ
$xe\not{e}$	1018	108.71 ± 5.2	909.29 ± 32.33	898.95 ± 12.73	-
$xe\not{\mu}$	1044	71.76 ± 2.83	972.24 ± 32.43	1024.88 ± 17.18	-
$x\mu\not{e}$	1280	189.95 ± 5.83	1090.05 ± 36.25	1116.81 ± 22.69	-
$x\mu\not{\mu}$	1254	79.39 ± 2.6	1174.61 ± 35.51	1189.77 ± 14.43	-

Channel	Data	Prompt	Data − Prompt	Non-prompt Monte-Carlo	Data-driven fake ℓ
xee	138	122.52 ± 1.41	15.48 ± 11.83	13.34 ± 1.82	19.1 ± 8.18
$xe\mu$	478	384.03 ± 2.39	93.97 ± 21.99	33.87 ± 2.47	54.0 ± 13.15
$x\mu\mu$	263	233.04 ± 1.37	29.96 ± 16.28	15.54 ± 1.64	37.59 ± 10.57

'In-situ' results (calculated in this region)

$\theta_e^{data-driven}$: -	$\theta_\mu^{data-driven}$: -
$\theta_e^{Monte-Carlo-based}$: 0.015 ± 0.002	$\theta_\mu^{Monte-Carlo-based}$: 0.013 ± 0.001

Table 7.20: Fake factor estimation and simple application (counted events) results in the pre-selection region. "Data / Prompt / Non-Prompt" entries show the data / prompt leptons from the Monte-Carlo / fake/non-prompt lepton from the Monte-Carlo yield in the dedicated region. "Data − Prompt" shows the area for fake lepton candidates by subtracting the prompt lepton contribution from data. "Data-driven fake ℓ" is estimated by applying the fake factor from X in each region. The uncertainty is the statistical component only.

non-prompt). This hypothesis is verified by checking at the main non-prompt background contribution ($t\bar{t}$) in the fake calculation channel from the Monte-Carlo simulation. The lepton with an "opposite-charge" is found to be non-prompt at a rate (compare to all non-prompt background) of around 20%. This 20% is taken as a source of systematic uncertainty. When all sources of systematic uncertainties are combined, we obtain 58.73% for the electron fake factor, 49.9% for the muon fake factor.

To have more validation about fake factors, even the Top validation (=1bjet) region is enriched in quite different types of background compared to the pre-selection region and fake enriched control region. Table 7.21 shows the measurement in Top validation region. The results are consistent with nominal fake factor values.

T: Top validation region					
Channel	Data	Prompt	Data − Prompt	Non-prompt Monte-Carlo	Data-driven fake ℓ
$xe\not{e}$	1233	35.19 ± 1.35	1197.81 ± 35.14	1285.06 ± 13.19	-
$xe\not{\mu}$	1410	26.8 ± 0.93	1383.2 ± 37.56	1427.47 ± 13.88	-
$x\mu\not{e}$	1410	49.87 ± 2.04	1360.13 ± 37.61	1455.93 ± 14.35	-
$x\mu\not{\mu}$	1624	30.55 ± 1.92	1593.45 ± 40.35	1665.57 ± 15.02	-
Channel	Data	Prompt	Data − Prompt	Non-prompt Monte-Carlo	Data-driven fake ℓ
xee	80	46.28 ± 0.62	33.72 ± 8.96	21.43 ± 1.69	25.15 ± 10.78
$xe\mu$	225	130.93 ± 1.19	94.07 ± 15.05	48.45 ± 2.51	72.83 ± 17.46
$x\mu\mu$	122	79.16 ± 0.73	42.84 ± 11.07	24.6 ± 1.82	50.99 ± 14.34

'In-situ' results (calculated in this region)

$\theta_e^{data-driven}$: 0.028 ± 0.008	$\theta_\mu^{data-driven}$: 0.027 ± 0.007
$\theta_e^{Monte-Carlo-based}$: 0.017 ± 0.001	$\theta_\mu^{Monte-Carlo-based}$: 0.015 ± 0.001

Table 7.21: Fake factor estimation and simple application (counted events) results in the Top validation region. "Data / Prompt / Non-Prompt" entries show the data / prompt leptons from the Monte-Carlo / fake/non-prompt lepton from the Monte-Carlo yield in the dedicated region. "Data − Prompt" shows the area for fake lepton candidates by subtracting the prompt lepton contribution from data. "Data-driven fake ℓ" is estimated by applying the fake factor from Top in each region. The uncertainty is the statistical component only.

7.3.3 Background validation

Background validations distributions are shown in Figures 7.24 (3ℓ inclusive), 7.25 (SFOC12 sub-channel), 7.26 (SFOC0 sub-channel), at pre-selection level. Generally, a good agreement between data and background estimation is seen, validating the data-driven methods used for the non-prompt lepton background estimation. Yields after data-driven estimation are shown in Table 7.22. Figures 7.27 give further validation in different sub-channels. Result in SFOC12 shows good agreement. Result in SFOC0 informed that fake estimation is not as good as other sub-channels, but still within assigned uncertainty.

As illustrated in the Figure 7.24 at the pre-selection level, several kinematic variable: ΔR_{ℓ_i-jet}, $\Delta R_{\ell^\pm\ell^\pm}$, $E_{\mathrm{T}}^{\mathrm{miss}}$, $M_{3\ell}$, $p_{\mathrm{T}}^{\text{leading jet}}$ have the potential to further discriminate the signal from the background.

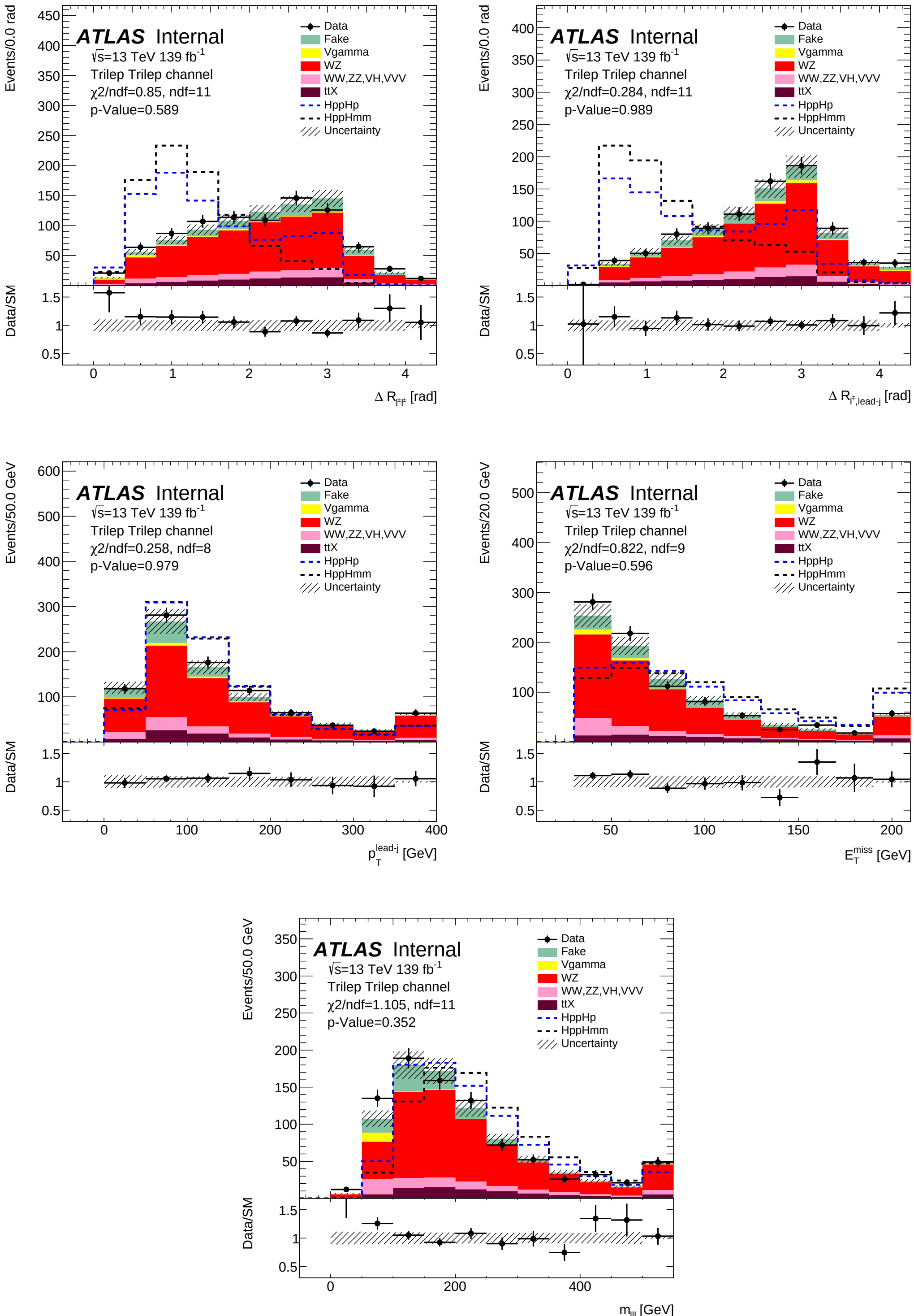

Figure 7.24: In the 3ℓ channel (inclusive, SFOC12 + SFOC0), the distributions of the 3ℓ events included in the pre-selection stage. The variables shown from the left top are the ΔR between same-sign leptons, ΔR between the lepton-jet, p_{T} of the leading lepton, E_T^{miss} and tri-lepton mass. Note that the signal is scaled to data integral. The uncertainty includes the statistic uncertainty and all sources of systematic uncertainties on the background estimation. The non-prompt lepton background is taken from the data-driven method. Two signals points with a mass of 200 GeV are shown.

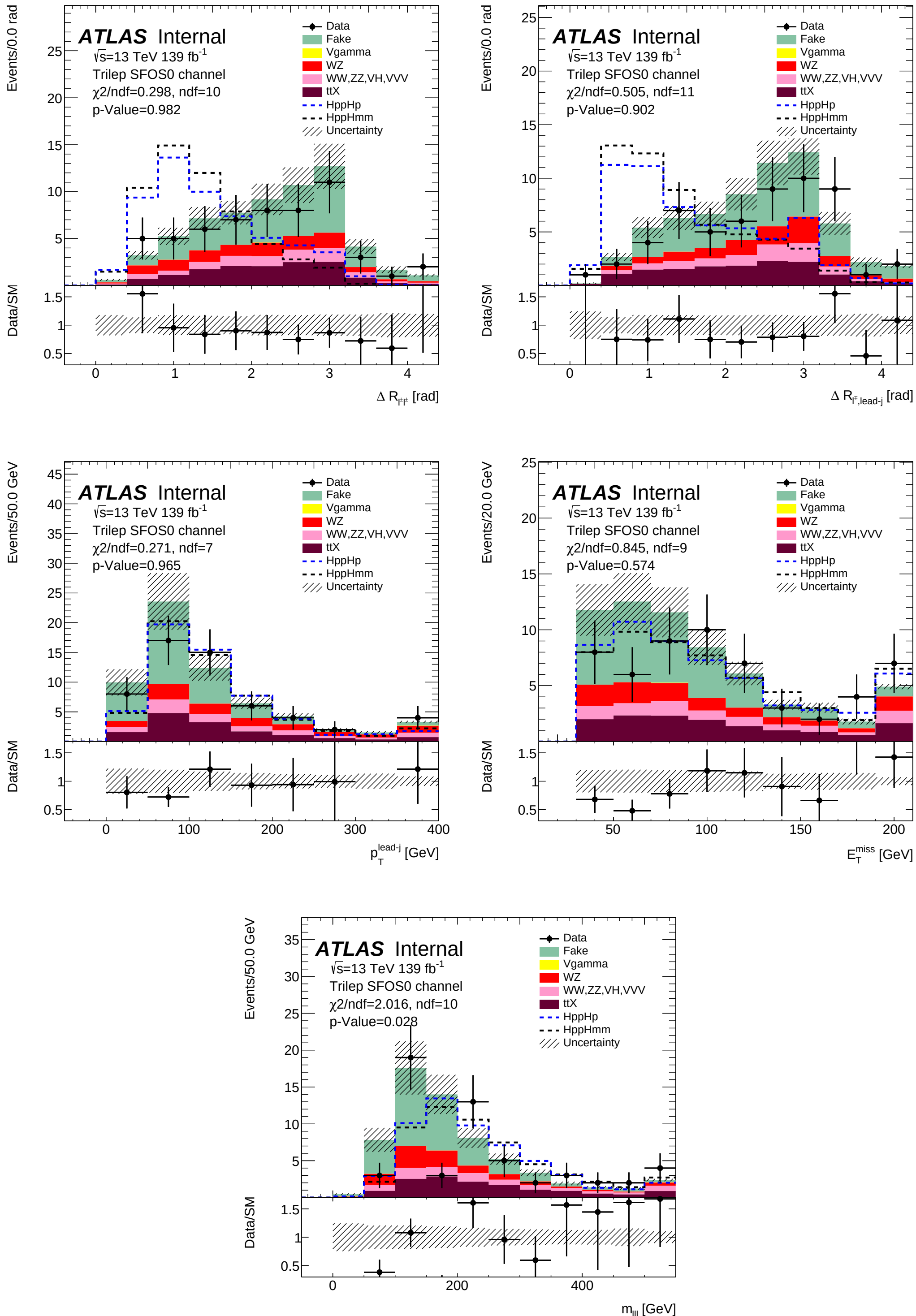

Figure 7.25: In the 3ℓ SFOC0 (SFOS has same meaning as SFOC, same-flavor-opposite-sign) channel, the distributions of the 3ℓ events included in the pre-selection stage. The variables shown from the left top are the ΔR between same-sign leptons, ΔR between the lepton-jet, p_{T} of the leading lepton, E_T^{miss} and tri-lepton mass. Note that the signal is scaled to data integral. The uncertainty includes the statistic uncertainty and all sources of systematic uncertainties on the background estimation. The non-prompt lepton background is taken from the data-driven method. Two signals points with a mass of 200 GeV are shown.

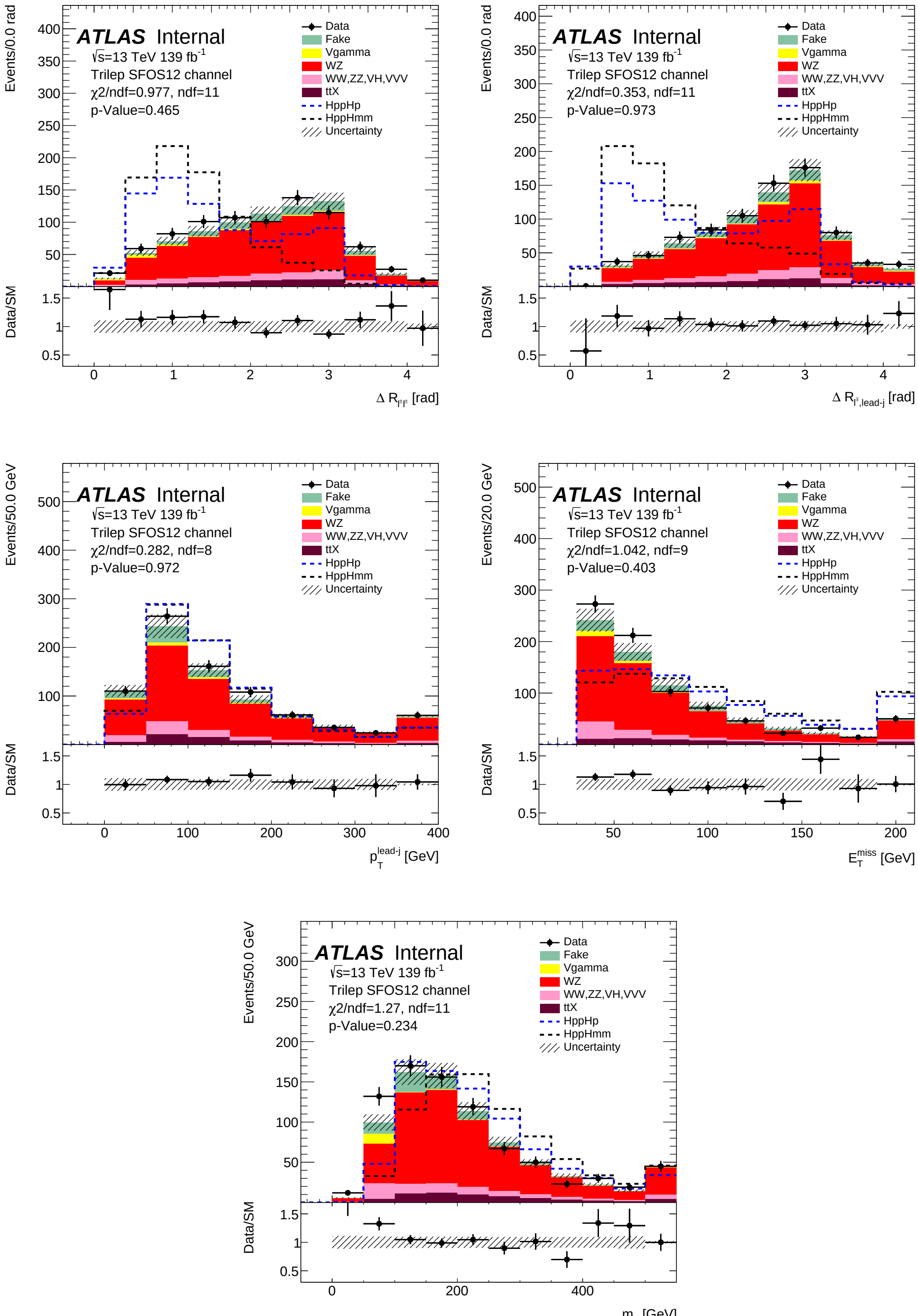

Figure 7.26: In the 3ℓ SFOC12 (SFOS has same meaning as SFOC, same-flavor-opposite-sign) channel the distributions of the 3ℓ events included in the pre-selection stage. The variables shown from the left top are the ΔR between same-sign leptons, ΔR between the lepton-jet, p_{T} of the leading lepton, E_T^{miss} and 3ℓ mass. Note that the signal is scaled to data integral. The uncertainty includes the statistic uncertainty and all sources of systematic uncertainties on the background estimation. The non-prompt lepton background is taken from the data-driven method. Two signals points with a mass of 200 GeV are shown.

	Data	Prompt	Fake	Total background
3ℓ	879	730.91 ± 92.71	109.05 ± 64.15	839.96 ± 112.74
Monte-Carlo Composition	WZ	WW,ZZ,VH,VVV	ttX	$V\gamma$
Yield	553.59 ± 57.13	83.6 ± 17.96	77.7 ± 15.63	16.03 ± 5.94

Table 7.22: Data and SM background prediction after the pre-selection requirements mentioned in Table 7.15 are applied. The fake lepton background contributions are estimated using the data-driven methods described above. Both statistic and systematic uncertainty sources are included. V+gamma samples are included in the prompt category for the electrons from photon conversions. The break-down of the prompt Monte-Carlo contributions is shown in the “Monte-Carlo composition" entry.

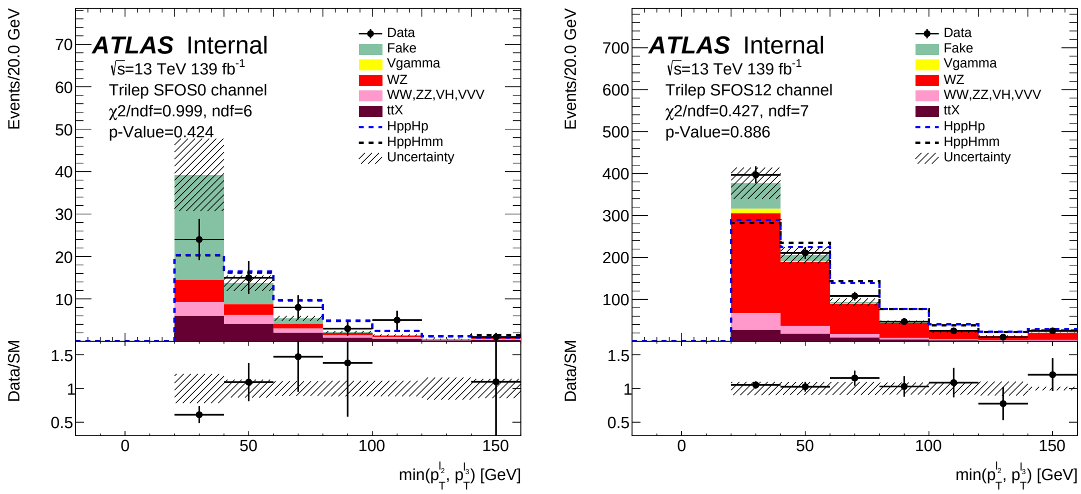

(a) SFOC0 channel

(b) SFOC12 channel

Figure 7.27: In the 3ℓ (SFOS has same meaning as SFOC, same-flavor-opposite-sign) channel, the distributions of the 3ℓ events included in the pre-selection stage, per lepton sub-channel. Note that the signal is scaled to data integral. The uncertainty includes the statistic uncertainty and all sources of systematic uncertainties on the background estimation. The non-prompt lepton background is taken from the data-driven method. Two signals points with a mass of 200 GeV are shown.

Selection criteria	4ℓ pre-selection
At least one offline *signal* lepton with $p_{\mathrm{T}}^{\ell} > 30$ GeVthat triggered the event	
N_ℓ *candidate**)	=4
$\lvert \sum Q_\ell \rvert$	≠4
Lepton p_{T}	$p_{\mathrm{T}}^{\ell_1,\ell_2,\ell_3,\ell_4} > 10$ GeV
$E_{\mathrm{T}}^{\mathrm{miss}}$	> 30 GeV
N_{jets}	–
$N_{b\text{-jets}}$	=0
Low SFOC $m_{\ell\ell}$ veto	$m_{\ell\ell}^{\mathrm{oc}} > 15$ GeV
Z boson decay veto	$\lvert m_{\ell\ell}^{\mathrm{oc}} - m_Z \rvert > 10$ GeV
$m_{4\ell}$	> 100 GeV

Table 7.23: The pre-selection criteria for the 4ℓ analysis channels. The leptons are required to pass the *candidate** or *signal* requirements. The leptons are ordered by decreasing p_{T} ($\ell_1, \ell_2, ...$) in the $2\ell^{sc}$ and 4ℓ channels, The symbol "–" means no requirement is made. The equal sign (=) is used to emphasize that the selection criterion has to be exactly the given number.

7.4 Four lepton channel

The 4ℓ signature is expected to have a signal rate that is five times lower than in the 3ℓ channel. However, the background is expected to be lower as well. The SM contributions are expected to be dominated by the ZZ production, with simultaneous decay in di-leptons of each Z boson. Smaller contributions are expected from rare processes like $t\bar{t}Z$, $t\bar{t}H$, four tops, etc. However, those processes also lead to several prominent hadronic jets in the event. The *signal* four lepton signature is expected to have no extra hard jets, large transverse missing momentum, and a typical topology due to the same-sign W's originating from the same $H^{\pm\pm}$ boson.

7.4.1 Event selection and Prompt background

Similar as for $2\ell^{sc}$ and 3ℓ, for the 4ℓ channel, a pre-selection is defined in order to select events with four leptons. The leptons are ordered with increasing p_T; thus the index 1 is for the lepton with the highest p_T, and index 4 is for the lepton with the lowest p_{T}. The main contributions to the background and the description of various variables that are essential for signal discrimination are investigated.

The flavor composition in the sample is an important feature of the signal. Indeed, the decays of the four W-bosons in the final state are flavor-uncorrelated, therefore the distribution of the number of leptons is expected to follow a binomial distribution. However, for the main prompt backgrounds (containing Z bosons), the production is expected to proceed by same-flavor pairs, and therefore, the events are concentrated in 0, 2, or 4 electron bins. Following the same argument, the background is expected to have quite often two same-flavor opposite-charge lepton pairs, while for the signal the combinatorial association significantly populates the bins with zero and one SFOC as well.

7.4.2 Non-prompt lepton background

Unlike for the $2\ell^{sc}$ and 3ℓ channels, because of very low statistics, the fake lepton background contribution in the 4ℓ channel is estimated using the “Fake Scale Factor" method. This is a semi-data-driven technique since it takes advantage of both data and Monte Carlo simulation, and it has already been validated by other analyses (ttZ→ 4ℓ for instance and more recently ttV→ 4ℓ [157]). The underlying idea of the Fake Scale Factor method is to correct Monte Carlo prediction of fake rates according to the source and flavor of the fake lepton. To compute the correction factors, the statistics are increased by using the three-lepton final states. Two control regions are defined and used for this study based on the flavor composition.

The first is the Z+jets enriched region where the light flavor non-prompt dominated. This region requires exact three *candidate** leptons with $p_{\mathrm{T}} > 10$ GeV. For the lepton used for the trigger matching, the tight lepton requirements must be satisfied, and the p_{T} should be > 30 GeV. Total charge of all three leptons must satisfy $Q_{3\ell} = \pm 1$. Each event must include 1 SFOC lepton pair with an invariant mass $M_{\ell^+\ell^-}$ within the Z-mass window $|M_{\ell^+\ell^-}| < 10$ GeV; the remaining lepton selected to be an electron and to be the non-prompt candidate. To reduce the WZ contribution, $E_{\mathrm{T}}^{\mathrm{miss}} < 50$ GeV and the transverse mass $M_T < 50$ GeV (the transverse mass is calculated here using the transverse momentum vector of $E_{\mathrm{T}}^{\mathrm{miss}}$ and of the ”fake” lepton candidate) are required.

The second is the Top enriched region, where the heavy flavor non-prompt dominated. Same as Z+jets enriched region, events must satisfy exact three *candidate** leptons with $p_{\mathrm{T}} > 10$ GeV, total charge and trigger requirements. No SFOC lepton pair is allowed to avoid Z boson contributions. Either one or two jets pass $p_{\mathrm{T}}^{1,(2)} > 30(25)$ GeV. Subleading lepton of same-sign lepton pair is considered to be the ”Fake” candidate (relevant for later p_{T} variation studies).

Even if these regions are not orthogonal by construction, the overlap between the two was checked using Data and Monte-Carlo samples, and no event was found to enter both.

For muons, since the light flavor contribution is found to be negligible, only the heavy flavor is considered to be controlled (Eq. 7.18, Table 7.24). The muon heavy flavor scale factor is defined as:

$$\lambda_H^{\mu} = (N_{\mathrm{data}} - N_{\mathrm{prompt}} - N_{\mathrm{light}})/N_{\mathrm{heavy}}, \tag{7.18}$$

where the N_{data} and N_{prompt} are yields from data and prompt lepton background. The N_{light} and N_{heavy} stand for the yield of non-prompt lepton background where the non-prompt candidates are found from heavy-flavor and light-flavor hadron decay.

For electrons both control regions (CRs) are considered. Most of the non-prompt leptons are coming from heavy flavor decays and from light flavor sources.

Considering the two non-prompt lepton sources, Heavy (H) and Light (L), we define two different Fake Scale Factors (FSFs), namely the corrections to the Monte Carlo efficiency for a fake lepton to pass the *candidate** requirement:

$$\lambda_L^e,\ \lambda_H^e \tag{7.19}$$

where L and H stands for light and heavy flavor, respectively. These are defined as:

$$N_{Data-Prompt}^{e,Z\text{+jets}} = \lambda_H^e N_{\mathrm{Heavy}}^{e,Z\text{+jets}} + \lambda_L^e N_{\mathrm{Light}}^{e,Z\text{+jets}} \tag{7.20}$$

$$N^{e,t\bar{t}}_{Data-Prompt} = \lambda^e_H N^{e,t\bar{t}}_{\text{Heavy}} + \lambda^e_L N^{e,t\bar{t}}_{\text{Light}} \tag{7.21}$$

By solving Eq. (7.21) and Eq. (7.20), the λ^e_L, λ^e_H factors can be computed as:

$$\lambda^e_H = \frac{N^{e,Z\text{+jets}}_{Data-Prompt} * N^{e,t\bar{t}}_{\text{Light}} - N^{e,t\bar{t}}_{Data-Prompt} * N^{e,Z\text{+jets}}_{\text{Light}}}{Determinant} \tag{7.22}$$

$$\lambda^e_L = \frac{-N^{e,Z\text{+jets}}_{Data-Prompt} * N^{e,t\bar{t}}_{\text{Heavy}} + N^{e,t\bar{t}}_{Data-Prompt} * N^{e,Z\text{+jets}}_{\text{Heavy}}}{Determinant} \tag{7.23}$$

With

$$Determinant = N^{e,Z\text{+jets}}_{\text{Heavy}} * N^{e,t\bar{t}}_{\text{Light}} - N^{e,Z\text{+jets}}_{\text{Light}} * N^{e,t\bar{t}}_{\text{Heavy}} \tag{7.24}$$

The predictions of the different processes entering in the heavy/light fake lepton enriched CRs are shown in Table 7.24. These prediction are used with the equations 7.22, 7.23 and 7.18, to get the λ scaling factors. This is just an event counting exercise (so no shape fit), which leads to the correction factor presented in Table 7.24 and further used to get the fake electron and fake muon background estimation in e.g., the signal regions.

Region	Data	Prompt	Heavy flavor fake ℓ	Light flavor fake ℓ
Electrons, $Z+$jets	3420	781.82±16.41	948.65±39.48	1281.07±135.24
Electrons, $t\bar{t}$	1609	83.38±2.84	1321.5±13.57	176.36±5.62
Muons, $t\bar{t}$	914	74.6±1.15	838.99±11.14	48.8±3.07

fake scale factors:	
λ^e_H = 0.98 ± 0.18 (stat)	λ^e_L = 1.34 ± 0.17 (stat)
λ^μ_H = 0.94 ± 0.04 (stat)	

Table 7.24: The yields in the Z+jets and Top enriched control regions and the λ scaling factors. Only the statistical errors are shown.

7.4.3 Uncertainties

Three sources of uncertainties on the fake scale factors are considered (with details shown in Table 7.25). First is the statistical uncertainty: λ^e_H = 0.98 ± 0.18 (stat), λ^e_L = 1.34 ± 0.17 (stat), λ^μ_H = 0.94 ± 0.04 (stat). The statistical uncertainty on the electron correction factor is larger than the muon one mainly because the *signal* electron definition is much tighter than the muon one. Also, the non-prompt electron sample is divided into HF and LF sources, unlike the one for muon (which is already dominated by a single non-prompt muon source, heavy flavor). Theoretical uncertainty associated with the VV, $t\bar{t}X$ and Vγ background contributions comes mainly from PDF and QCD scale variations. This uncertainty is propagated in the λ factors calculation and found negligible contribution.

The flavor composition uncertainty has been considered by split $t\bar{t}$ samples as a function of the b-jets multiplicity. "Top+B-jet veto" requires $N_{\mathrm{b-jets}} = 0$ for $t\bar{t}$ CR, while "Top+B-jet enrich" requires $N_{\mathrm{b-jets}} > 0$ for $t\bar{t}$ CR. Due to lack of statistics, the results in the "$N_{\mathrm{b-jets}} > 0$ for Z+jets CR" control region are not considered when computing this source of uncertainty. The corrections factors obtained in these regions are consistent with nominal ones. A conservative (relative) uncertainty of 2% is considered for λ^e_H, 1% for λ^e_L and 3% for λ^μ_H.

To account the p_{T} dependence of the scaling factors, Four regions are defined for separated calculation:
i) $p_{\mathrm{T}}^{\ell,\mathrm{fake}} > 18$ GeV for Z+jets CR and $p_{\mathrm{T}}^{\ell,\mathrm{fake}} > 18$ GeV for $t\bar{t}$ CR,
ii) $p_{\mathrm{T}}^{\ell,\mathrm{fake}} > 18$ GeV for Z+jets CR and $p_{\mathrm{T}}^{\ell,\mathrm{fake}} < 18$ GeV for $t\bar{t}$ CR,
iii) $p_{\mathrm{T}}^{\ell,\mathrm{fake}} < 18$ GeV for Z+jets CR and $p_{\mathrm{T}}^{\ell,\mathrm{fake}} > 18$ GeV for $t\bar{t}$ CR,
iv) $p_{\mathrm{T}}^{\ell,\mathrm{fake}} < 18$ GeV for Z+jets CR and $p_{\mathrm{T}}^{\ell,\mathrm{fake}} < 18$ GeV for $t\bar{t}$ CR.
The corrections factors obtained in these regions are consistent with nominal ones. A conservative (relative) uncertainty of 5% is considered for λ^e_H, 4% for λ^e_L and 2% for λ^μ_H.

The Total (relative) systematic uncertainty assigned to the scaling factors are 6.0% for λ^e_H, 15.0% for λ^e_L, 4.0% for λ^μ_L. And the final fake scale factors are $\lambda^e_H = 0.98 \pm 0.18$ (stat) $\pm$ 0.06 (syst), $\lambda^e_L = 1.34 \pm 0.17$ (stat) $\pm$ 0.20 (syst), $\lambda^\mu_H = 0.94 \pm 0.04$ (stat) $\pm$ 0.04 (syst).

Variation Type	λ^e_H	λ^e_L	λ^μ_H
Nominal	0.98 ± 0.18	1.34 ± 0.17	0.94 ± 0.04
Prompt Theory uncertainty(%)	<1	14	<1
Samples stability:			
Top+Bveto	0.96 ± 0.19	1.35 ± 0.18	0.96 ± 0.05
Top+Bselec	1.00 ± 0.19	1.33 ± 0.18	0.92 ± 0.05
Assigned uncertainty(%)	2	1	3
p_{T} stability			
i)	0.94 ± 0.17	1.37 ± 0.19	0.93 ± 0.06
ii)	1.01 ± 0.19	1.34 ± 0.19	0.95 ± 0.05
iii)	0.94 ± 0.24	1.36 ± 0.24	0.93 ± 0.06
iv)	1.01 ± 0.19	1.30 ± 0.24	0.95 ± 0.05
Assigned uncertainty(%)	5	4	2

Table 7.25: Fake scale factors (λ) variations. The theory uncertainty from prompt processes is propagated from the yield variations. Unless otherwise specified, the uncertainties are statistical only.

7.4.4 Background validation

Once the λ corrections factors are known, the fake lepton background estimation can be performed. This is done by applying the correction factors as a function of the nature of the non-prompt leptons and (from all non-prompt Monte-Carlo samples: $t\bar{t}$, single top and V+jet) and the lepton flavor. Events with N expected non-prompt leptons will be reweighted by $\prod_{i=1}^{N} FSF_i$; A sum over i is needed as in the event can be more than one fake lepton, where i is the index of the fake lepton.

The agreement between data and background at the pre-selection level, using the semi-data-driven method described in this section for the fake lepton background estimation, is shown in Figure 7.28 and 7.29. The agreement between the data and the Monte-Carlo is generally good. The observed data and the background yields, at the pre-selection level, are shown in Table 7.26.

	Data	Prompt Monte-Carlo	Non-prompt Leptons	Total background
Pre-Selection	63	41.8 ± 5.38	24.75 ± 4.86	66.55 ± 7.25
Monte-Carlo	WZ	WW,ZZ,VH,VVV	$t\bar{t}X$	$V\gamma$
Yield	2.9 ± 0.47	31.02 ± 3.66	7.23 ± 1.12	0.66 ± 0.39

Table 7.26: Data and SM background prediction after the pre-selection requirements mentioned in table 7.23 are applied. The non-prompt lepton background contributions are estimated using the fake scale factor methods described above. Both statistic and systematic uncertainty sources are included. $V\gamma$ samples are included in the prompt category for the electrons from photon conversions. The break-down of the prompt Monte-Carlo contributions is shown in the “Monte-Carlo composition" entry.

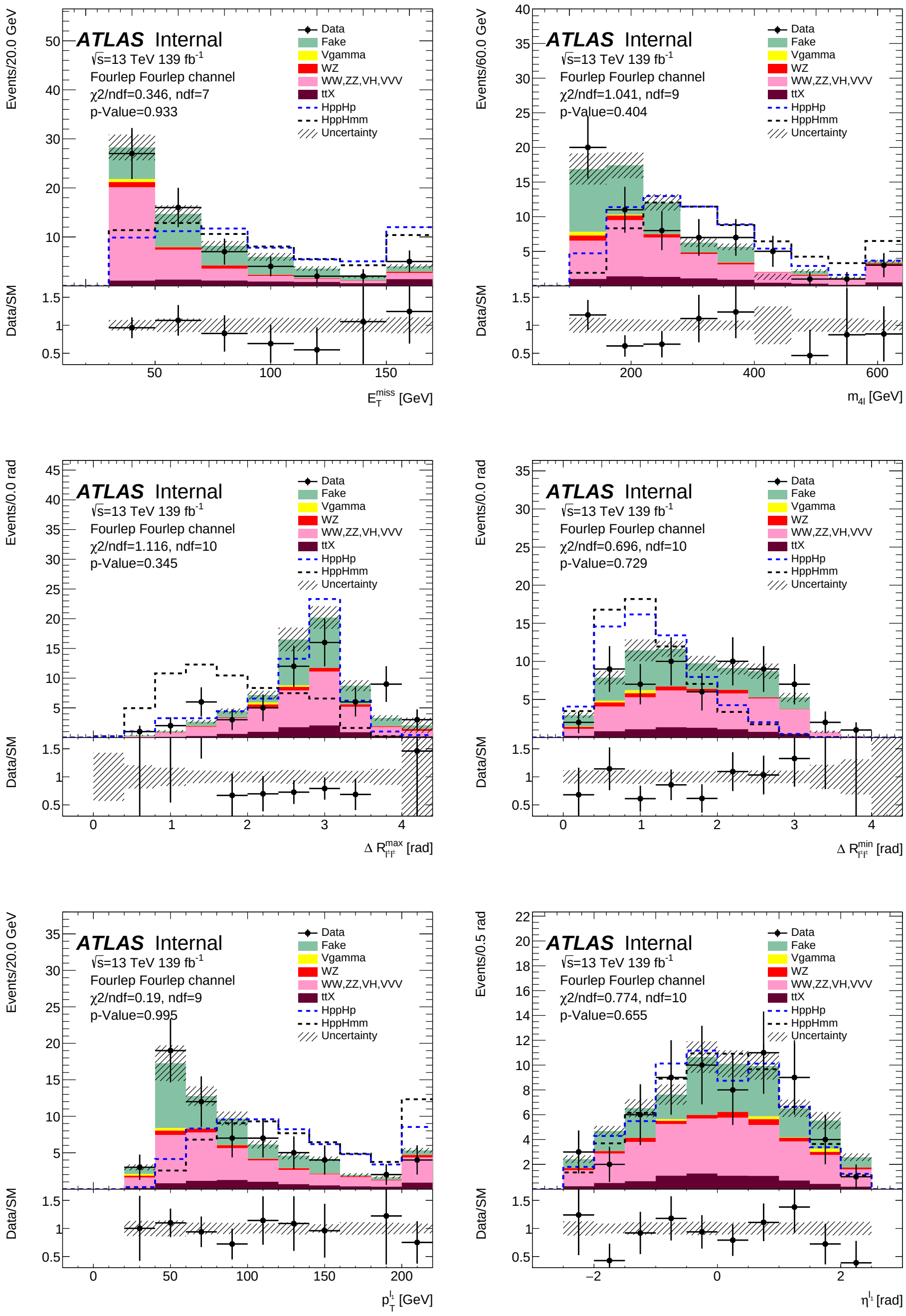

Figure 7.28: In the 4ℓ channel, the distributions of the 4ℓ events at the pre-selection level. Only the statistical uncertainty is shown. The non-prompt lepton background is estimated using the method described in section 7.4.2. Note that the signal is scaled to data integral, for better visibility. The bottom panels of each figure show the ratio between data and the total SM prediction (including prompt Monte Carlo and fake lepton background estimates). The error band includes the uncertainty on fake estimates and the total error obtained by adding in quadrature the Monte Carlo statistics. Two signal points with a mass of 200 GeV are shown.

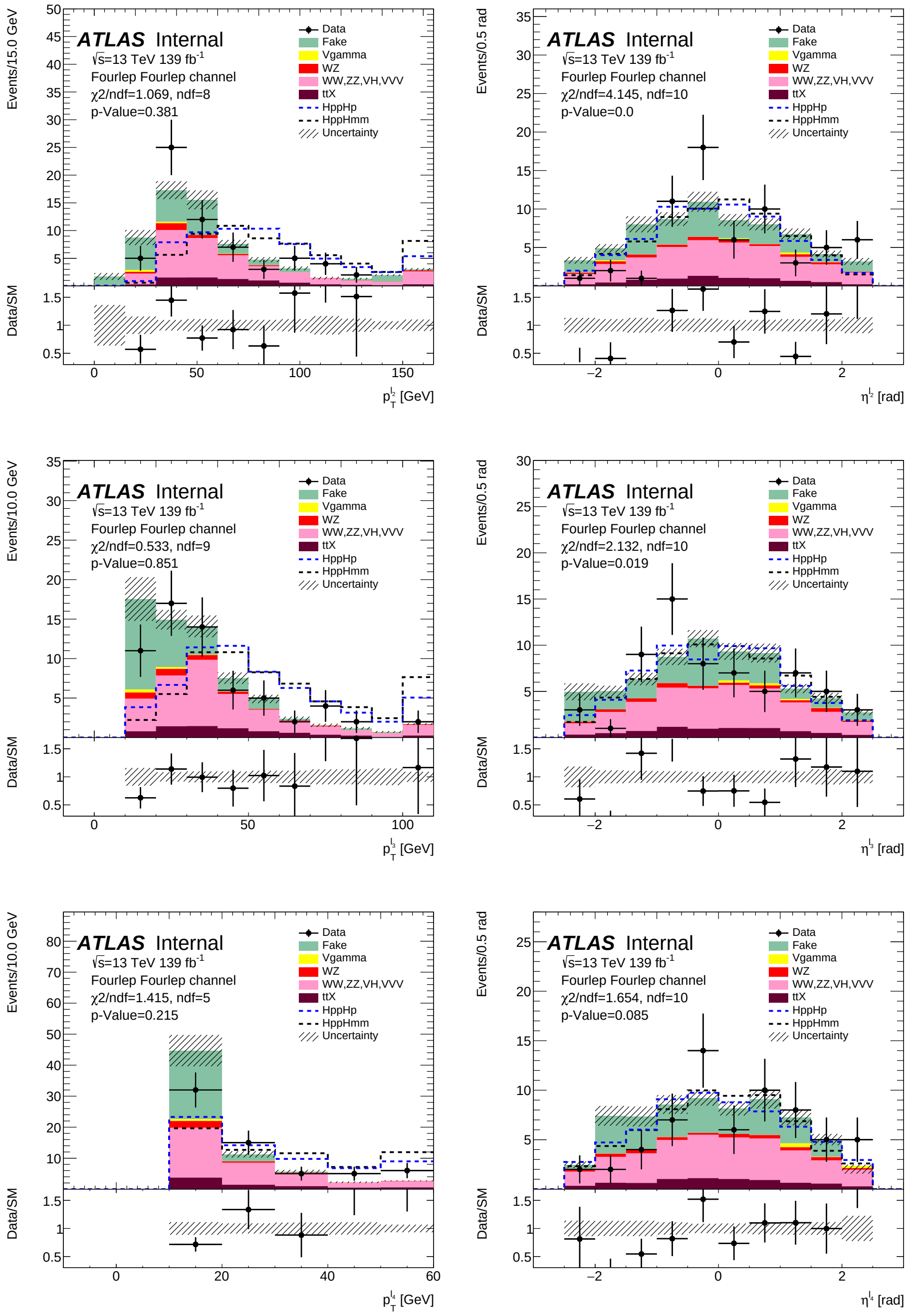

Figure 7.29: The distributions of the 4ℓ events at the pre-selection level. Only the statistical uncertainty is shown. The non-prompt lepton background is estimated using the method described in section 7.4.2. Note that the signal is scaled to data integral, for better visibility. The bottom panels of each figure show the ratio between data and the total SM prediction (including prompt Monte Carlo and fake lepton background estimates). The error band includes the uncertainty on fake estimates and the total error obtained by adding in quadrature the Monte Carlo statistics. Two signal points with a mass of 200 GeV are shown.

8 Signal Region

Contents

Cut optimization is used in the signal area definition. Although machine learning technologies such as BDT have shown greater power in classifying signals and backgrounds, considering transferring the results to other models with similar structures or final states, cutting optimization is more stable and reliable.

8.1 Cut optimization

The method of rectangular cuts (trained with the Simulated Annealing algorithm) implemented in the TMVA tool-kit [50] is adopted to optimize the cut-based definitions of the signal regions. The cuts are optimized independently for each mass point and for each of the leptonic channels.

For the analysis channel, the lists of variables used as input to the tool are:

- $2\ell^{sc}$: S, $m_{\ell\ell}$, $\Delta R_{\ell\ell}$, $\Delta\Phi(\ell\ell, E_{\mathrm{T}}^{miss})$, m_{jets}, E_{T}^{miss};
- 3ℓ: $\Delta R_{\ell\ell}$, $\Delta R_{\ell-jet}$, $M_{3\ell}$, $p_{\mathrm{T}}^{\text{leading jet}}$, $E_{\mathrm{T}}^{\text{miss}}$;
- 4ℓ: $M_{4\ell}$, $p_{\mathrm{T}}^{\ell_1}$, $\Delta R_{\ell^\pm\ell^\pm}^{\max}$, $\Delta R_{\ell^\pm\ell^\pm}^{\min}$, $E_{\mathrm{T}}^{\text{miss}}$;

These variables were found to be the most optimal in the previous version of the analysis [23] and simply re-used in this version. Details on their computation are given in section 6.3. Signal characteristics are similar between pair-production and associate-production signals. And for simplicity, only pair-production signal events were used for signal optimization. Thus the optimized cuts will be used for both pair-production and associate-production signals. This will lead to smaller sensitivity to associate-production signals in some of the analysis channels.

Cuts Optimization

For all analysis channels, the optimization of cuts is performed by TMVA. TMVA Cuts Optimization method maximizes the background rejection at a given signal efficiency[1], and scans over the full range of the signal efficiency (from 1% to 100% with a step size of 1%). A group of cuts with maximum significance will be derived after the cut optimization scan. In each analysis channel, further checks will be performed to have a set of stable cuts.

Simulated Annealing

For one given signal efficiency, the Simulated Annealing algorithm is used to achieve a group of cuts with the best background rejection. The Simulated Annealing algorithm is aiming for solving global minimization problem, inspired by the annealing process in condensed matter physics. Simulated annealing can be used to approximate the global minimum for a function with many variables. In this analysis, the Simulated Annealing algorithm is working with Increasing Adaptive Approach (IncAdaptive) option[2]: the algorithm seeks local minima and explores their neighborhood, while changing the ambient temperature depending on the number of failures in the previous steps. The performance can be improved by increasing the number of iteration steps (MaxCalls), or by adjusting the minimal temperature (MinTemp). Manual adjustments of the speed of the temperature increase (TempScale and AdaptiveSpeed) for individual data sets might also improve the performance.

Working points significance and uncertainties

There will be 100 working points obtained from the TMVA corresponding to a signal efficiency from 1% to 100%. Each analysis channel will scan one-by-one using the Cowan formula to evaluate the expected significances, and perform further check with cuts.

$$Significance = \sqrt{2 * ((sig + bkg) * \log(1 + \frac{sig}{bkg}) - sig)} \tag{8.1}$$

This significance is defined by the formula [158], in order to account for systematics, b is increased by the one sigma error on the background (accounts for the uncertainties from non-prompt lepton and charge flip background, and for the uncertainties on the prompt process).

[1] This efficiency is also called "target efficiency".

[2] The following configuration is used for the cuts optimization:factory->BookMethod(TMVA::Types::kCuts, "CutsSA","!H:!V:FitMethod=SA:EffSel:MaxCalls =150000:KernelTemp=IncAdaptive:InitialTemp=1e+6:MinTemp=1e-6:Eps=1e-10:UseDefaultScale"); For more details, please check the TMVA user guide.

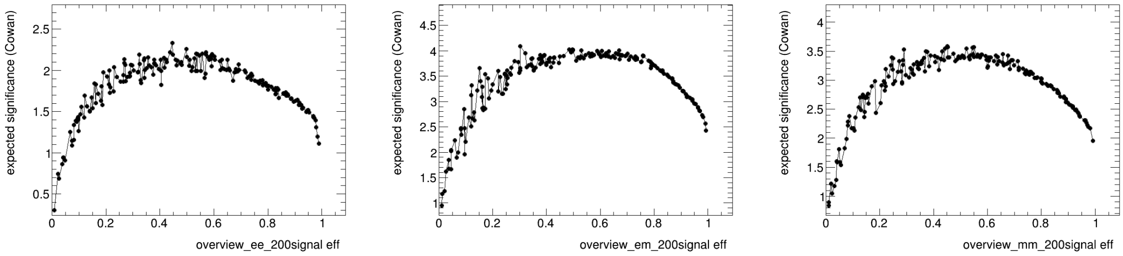

(a) ee channel (b) $e\mu$ channel (c) $\mu\mu$ channel

Figure 8.1: $2\ell^{sc}$ channel. Expected significances (Cowan) for different working points (provided by TMVA CutsSA) of the signal selection for the 200 GeV mass point, Left: ee channel, Middle: $e\mu$ channel Right: $\mu\mu$ channel.

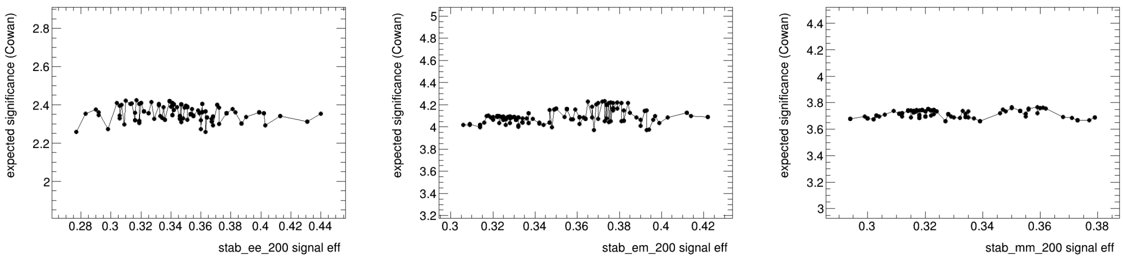

(a) ee channel (b) $e\mu$ channel (c) $\mu\mu$ channel

Figure 8.2: $2\ell^{sc}$ channel. Expected significances (Cowan) for different working points (by varying baseline cut value) of the signal selection for the 200 GeV mass point, Left: ee channel, Middle: $e\mu$ channel Right: $\mu\mu$ channel.

8.2 Signal region: Two same charge leptons

The signal region definition is based based on TMVA Cut optimization (See Section 8.1). Additional checks were performed to have stable cuts. Attention has been paid to the problem of "over-training" due to the statistical fluctuations in the background. As an example, for the $m_{H^{++}} = 200$ GeV mass signal point, the expected significances as a function of the signal efficiency is shown in Figure 8.1.

The working points corresponding to the highest expected significance and most common cuts are taken as the baseline of the definition of the signal regions. The baseline cuts also need to pass a stability check by varying two cuts values each time (shown in Figure 8.2).

- All cuts were rounded with 1 digit.
- For two of six variables:
  - Varying cuts values on both variables in a small range, e.g., 10 GeV for mass-related variables and 0.1 for angular-related variables.
  - Make sure the signal efficiency does not change significantly (within 10%).

mass	ch.	$M_{jets} >$	$M_{jets} <$	S <	$\Delta R_{\ell\ell} <$	$\Delta\phi(\ell\ell, E_{\mathrm{T}}^{\mathrm{miss}}) <$	$M_{\ell\ell} <$	$M_{\ell\ell} >$	$E_{\mathrm{T}}^{\mathrm{miss}} >$
200	ee	100	450	0.3	1.8	0.8	150	40	100
300		100	500	0.6	2.1	0.8	240	90	130
400		300	700	0.6	2.2	0.9	340	130	170
500-600		400	1000	0.9	2.4	1.0	400	130	200
200	$\mu\mu$	100	450	0.3	1.9	0.7	150	40	100
300		100	500	0.6	1.9	1.0	240	90	130
400		300	700	0.9	2.1	1.0	340	130	170
500-600		400	1000	0.9	2.4	1.0	400	130	200
200	$e\mu$	100	450	0.3	1.9	0.7	150	40	100
300		100	500	0.6	2.1	0.9	240	90	130
400		300	700	0.9	2.2	1.0	340	130	170
500-600		400	1000	0.9	2.4	1.0	400	130	200

Table 8.1: Cut values for the definition of the $2\ell^{sc}$ channel signal regions. All numbers for masses and $E_{\mathrm{T}}^{\mathrm{miss}}$ are in unit of GeV.

mass	ch.	$M_{jets} >$	$M_{jets} <$	S <	$\Delta R_{\ell\ell} <$	$\Delta\phi(\ell\ell, E_{\mathrm{T}}^{\mathrm{miss}}) <$	$M_{\ell\ell} <$	$M_{\ell\ell} >$	$E_{\mathrm{T}}^{\mathrm{miss}} >$
200	$\ell\ell$	100	450	0.3	1.9	0.7	150	40	100
300		100	500	0.6	2.1	0.9	240	90	130
400		300	700	0.9	2.2	1.0	340	130	170
500-600		400	1000	0.9	2.4	1.0	400	130	200

Table 8.2: Harmonized cut values for the definition of the $2\ell^{sc}$ channel signal regions. All numbers for masses and E_{T}^{miss} are in unit of GeV.

- Check if the expected significances fluctuate significantly (within 10%).

Some cut values obtained from the training are further refined by re-training a subset of the cuts while fixing some cuts (of which the cut values from the TMVA are reasonable) from the previous iteration, and in reference to the other channels of lepton flavors: in cases when the expected significances fluctuate significantly, the stabler cuts from the other channels of lepton flavors will be tested and adopted. The tuned cut values are presented in Table 8.1. It is found that optimization results for the three sub-channels are quite similar to each other. The three sub-channel signal regions are further harmonized to $e\mu$ selection definition to keep the most sensitive region unchanged (Table 8.2). A summary of the all $2\ell^{sc}$ SRs is shown in Table 8.8.

In the $2\ell^{sc}$ channel, six discriminating variables ($E_{\mathrm{T}}^{\mathrm{miss}}$, $\Delta R_{\ell\ell}$, $\Delta\Phi(\ell\ell, E_{\mathrm{T}}^{\mathrm{miss}})$, S, $M_{\ell\ell}$ and M_{jets}) are selected and used to define the signal region; they were found to be the most optimal in the previous version of the analysis. The cut-flows in the ee, $\mu\mu$ and eμ channels with the 200 GeV mass signal points are listed in Table 8.3.

ee channel	Prompt	Charge-Flip	Non-prompt	Total	HppHmm(eff)	HppHp
Initial	-	-	-	-	134.25	99.65
Pre-Selection	113.83±1.76	14.06±2.71	67.22±19.16	195.11±19.43	18.30±0.23(100.0 %)	11.26±0.22(100.0 %)
M_{jets}	60.55±1.19	8.57±1.65	45.94±12.94	115.07±13.1	14.80±0.20(80.9 %)	8.74±0.20(77.6 %)
S	9.23±0.68	0.78±0.15	5.06±1.37	15.08±1.54	9.46±0.17(51.7 %)	4.77±0.15(42.3 %)
$\Delta R_{\ell\ell}$	6.09±0.19	0.54±0.1	3.86±1.02	10.49±1.05	9.12±0.16(49.8 %)	4.59±0.14(40.8 %)
$\Delta\Phi(\ell\ell, E_{\mathrm{T}}^{\mathrm{miss}})$	4.46±0.16	0.38±0.07	2.63±0.7	7.47±0.73	8.13±0.16(44.4 %)	3.97±0.13(35.3 %)
$M_{\ell\ell}$	2.81±0.13	0.28±0.05	1.91±0.53	5.0±0.54	7.38±0.15(40.3 %)	3.50±0.13(31.1 %)
$E_{\mathrm{T}}^{\mathrm{miss}}$	1.9±0.09	0.13±0.02	1.04±0.3	3.07±0.31	6.18±0.14(33.8 %)	2.75±0.12(24.4 %)
$e\mu$ channel	Prompt	Charge-Flip	Non-prompt	Total	HppHmm(eff)	HppHp
Initial	-	-	-	-	237.75	183.77
Pre-Selection	299.1±2.89	15.81±2.88	168.62±42.58	483.52±42.78	60.10±0.41(100.0 %)	34.28±0.38(100.0 %)
M_{jets}	160.3±2.12	9.63±1.76	115.25±28.75	285.18±28.88	48.24±0.36(80.3 %)	26.82±0.34(78.2 %)
S	24.22±0.747	0.81±0.15	8.62±2.09	33.66±2.22	29.09±0.28(48.4 %)	14.14±0.24(41.2 %)
$\Delta R_{\ell\ell}$	17.56±0.71	0.48±0.09	5.52±1.29	23.56±1.48	27.91±0.28(46.4 %)	13.56±0.24(39.5 %)
$\Delta\Phi(\ell\ell, E_{\mathrm{T}}^{\mathrm{miss}})$	12.81±0.69	0.34±0.06	4.03±0.98	17.18±1.2	24.65±0.26(41.0 %)	11.92±0.22(34.8 %)
$M_{\ell\ell}$	8.48±0.23	0.23±0.04	2.59±0.63	11.31±0.67	22.79±0.25(37.9 %)	11.04±0.22(32.2 %)
$E_{\mathrm{T}}^{\mathrm{miss}}$	5.98±0.2	0.12±0.02	1.47±0.36	7.57±0.41	18.94±0.23(31.5 %)	9.04±0.20(26.3 %)
$\mu\mu$ channel	Prompt	Charge-Flip	Non-prompt	Total	HppHmm(eff)	HppHp
Initial	-	-	-	-	106.49	84.50
Pre-Selection	160.37±1.08	0.0±0.0	93.92±21.39	254.29±21.42	35.95±0.31(100.0 %)	20.07±0.28(100.0 %)
M_{jets}	87.38±0.93	0.0±0.0	63.24±14.25	150.62±14.28	29.20±0.27(81.2 %)	15.90±0.26(79.2 %)
S	12.39±0.26	0.0±0.0	4.05±0.85	16.44±0.89	17.44±0.22(48.5 %)	8.15±0.19 (40.6 %)
$\Delta R_{\ell\ell}$	8.94±0.2	0.0±0.0	2.77±0.6	11.71±0.64	16.77±0.20(46.6 %)	7.75±0.17(38.6 %)
$\Delta\Phi(\ell\ell, E_{\mathrm{T}}^{\mathrm{miss}})$	6.45±0.18	0.0±0.0	1.97±0.43	8.42±0.46	14.82±0.19(41.2 %)	6.82±0.16(34.0 %)
$M_{\ell\ell}$	4.43±0.15	0.0±0.0	1.5±0.34	5.93±0.37	13.81±0.19(38.4 %)	6.31±0.16(31.4 %)
$E_{\mathrm{T}}^{\mathrm{miss}}$	3.12±0.12	0.0±0.0	0.93±0.22	4.05±0.25	11.32±0.17(31.4 %)	5.13±0.14(25.6 %)

Table 8.3: Cutflow of 200 GeV mass signal point. Uncertainty contains statistics and charge-flip/non-prompt systematic sources. Eff stands for signal efficiency.

8.3 Signal region: Three leptons

As illustrated in the figures presented in section 7.3.3 at the pre-selection level, several kinematic variables have the potential to further discriminate the signal from the background. The strategy used to extract the signal is based on rectangular cuts optimization (details in section 8.1).

The optimization is performed as a function of the $H^{\pm\pm}$ mass for $M_{H^{\pm\pm}}$ ranging from 200 to 500 GeV in steps of 100 GeV. For the 600 GeV mass point, the same signal regions for the 500 GeV mass point are used.

The optimization procedure uses five discriminating variables, shown in Table 8.4; these variables were found to be the best discriminants in the previous version of the analysis [159] and reused for this round. The TMVA package (CutsSA option) is used to scan the cuts, starting from the pre-selection level.

The algorithm proceeds as follows:

- Inherited from previous analysis [159], 5 variables are selected: $\Delta R_{\ell\ell}$, $E_{\mathrm{T}}^{\mathrm{miss}}$, $M_{3\ell}$, $\Delta R_{\ell-jet}$, and $p_{\mathrm{T}}^{\text{leading jet}}$. Their separation powers, which are defined by the integral of the overlap between signal and background PDFs, are shown in Table 8.4. The distributions of the variables used as

Rank	Variable	Separation
1	$\Delta R_{\ell-jet}$	2.667e-01
2	$\Delta R_{\ell^\pm\ell^\pm}$	2.155e-01
3	$E_{\mathrm{T}}^{\mathrm{miss}}$	6.170e-02
4	$M_{3\ell}$	5.006e-02
5	$p_{\mathrm{T}}^{\text{leading jet}}$	2.162e-02

Table 8.4: The separation power of the 3ℓ discriminating variables. Separation power is defined by the integral of the overlap between signal and background PDFs.

an input for the signal region optimization are shown in Figure 7.24. No large correlations are observed between the variables chosen for the optimization.

- The TMVA package (CutsSA option) is used to scan the cuts, starting from the pre-selection level. The general strategy of cut optimization presented in section 8.1) is also applied here.
- To choose the best working point, the significance vs. signal efficiency plots were generated and shown in Figure 8.3.
- In order to limit the efficiency loss for the signal and to reduce the sensitivity to statistical fluctuations, only operating points corresponding to efficiency above 40% are included in the optimization. A "temperature for smoothing" is also defined, i.e., the RMS in the previous 5 points, and it is used as an indicator of the significance stability. It also helps to avoid working points where the significance estimate is unstable due to low background statistics (typically at low efficiency).
- The optimization procedure is repeated for each of the four optimization points considered in this analysis and corresponding to $M_{H^{\pm\pm}} = 200, 300, 400, 500$ GeV.
- In order to simplify the cuts and to reduce the fluctuations, the cut values are further rounded. All energy cut values (the unit is GeV) have been applied with a 5 GeV precision (10 GeV for values above 100 GeV). For angular variables, 0.1(radian) precision is applied.
- All signal region definition are listed in Table 8.5. The cut-flows for 3ℓ channels with the 200 GeV mass signal points are listed in Table 8.5.

	Prompt MC	Fake Leptons	Total Background	H++ (Eff)	H+ (Eff)
Initial	-	-	-	245.58	310.06
Pre-selection	730.91±3.06	110.66±37.3	841.57±37.43	70.73±0.44 (100.0 %)	30.96±0.36 (100.0 %)
$\Delta R_{\ell^\pm\ell^\pm}$	236.79±2.01	27.91±9.49	264.7±9.7	52.77±0.38 (74.6 %)	18.95±0.29 (61.2 %)
$E_{\mathrm{T}}^{\mathrm{miss}}$	236.79±2.01	27.91±9.49	264.7±9.7	52.77±0.38 (74.6 %)	18.95±0.29 (61.2 %)
$M_{3\ell}$	89.46±0.83	7.18±2.43	96.64±2.57	43.15±0.35 (61.0 %)	12.83±0.24 (41.4 %)
$\Delta R_{\ell-jet}$	16.58±0.48	2.01±0.68	18.59±0.83	31.95±0.3 (45.2 %)	9.02±0.2 (29.1 %)
$p_{\mathrm{T}}^{\text{leading jet}}$	15.73±0.47	1.87±0.64	17.6±0.79	31.39±0.29 (44.4 %)	8.85±0.2 (28.6 %)

Table 8.5: 3ℓ channel. Cutflow for the 200 GeV mass signal point. The quoted uncertainty contains the statistical component, and all the uncertainties associated to the fake lepton background estimation (when relevant). Eff stands for the signal efficiency.

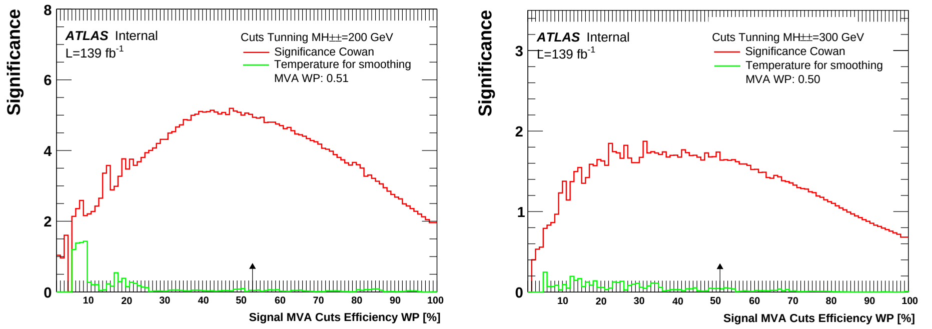

Figure 8.3: In the 3ℓ channel, the significance scan as a function of efficiency (X-axis shows the signal efficiency, from 1% to 100% with a 1% step.) is illustrated for two signal mass points $M_{H^{\pm\pm}}$ = 200 GeV (left) and $M_{H^{\pm\pm}}$ = 300 GeV (right). The arrow indicates the chosen working point.

8.4 Signal region: Four leptons

As for the $2\ell^{sc}$ and 3ℓ channels, the multi-variate cuts optimization algorithm is based on TMVA framework (option CutsSA) and uses a set of variables identified as sensitive to the signal for all considered $H^{\pm\pm}$ masses; the optimization procedure takes into account the systematic uncertainties (see section 8.1 for details). In the 4ℓ channel, the signal optimization procedure is very similar to the one used in the 3ℓ channel (Section 8.3).

Rank	Variable	Separation
1	$\Delta R^{\text{max}}_{\ell^\pm\ell^\pm}$	2.750e-01
2	$\Delta R^{\text{min}}_{\ell^\pm\ell^\pm}$	1.435e-01
3	$M_{4\ell}$	9.250e-02
4	$p_{\text{T}}^{\ell_1}$	8.511e-02
5	$E_{\text{T}}^{\text{miss}}$	6.107e-02

Table 8.6: The separation power of the 4ℓ discriminating variables. Separation power is defined by the integral of the overlap between signal and background PDFs. This ranking was obtained by looking at the pair-production mode.

Five observables are chosen for the optimization procedure: E_T^{miss}, the invariant mass of the four leptons $M_{4\ell}$, the transverse momentum $p_{\text{T}}^{\ell_0}$ of the highest p_{T} lepton, and the minimal $\Delta R^{\text{max}}_{\ell^\pm\ell^\pm}$ and maximal $\Delta R^{\text{min}}_{\ell^\pm\ell^\pm}$ distance in $\eta - \phi$ plane between the same-sign lepton pairs in each event. These variables were found to be the most discriminant between signal and background in the previous version of the analysis and only used now. The distributions of these variables are shown in Figure 7.28 and their separation power is shown in Table 8.6. No lepton flavor information is used in the optimization, as such a separation was found to not be very useful.

The optimization procedure is repeated for each of the four signal points considered in this analysis and corresponding to $M_{H^{\pm\pm}} = 200, 300, 400, 500$ GeV (for the 600 GeV mass signal point, the 500 GeV mass point signal regions is used). The significance scan is illustrated in Figure 8.4.

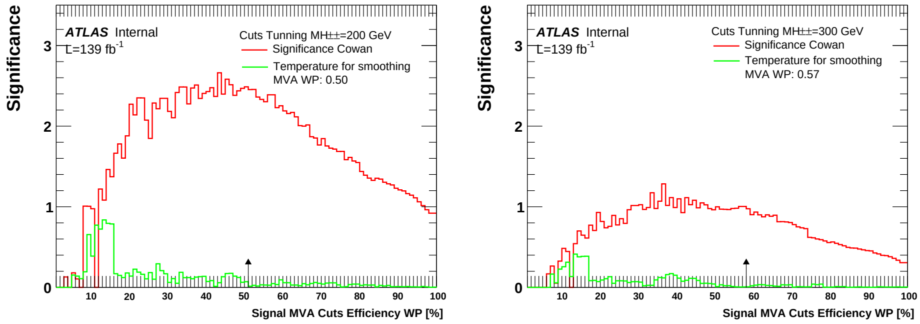

Figure 8.4: In the 4ℓ channel, the significance scan as a function of efficiency (the X-axis is the signal efficiency ,from 1% to 100% with 1% step.), illustrated for two signal mass points $M_{H^{\pm\pm}}$ = 200 GeV (left) and $M_{H^{\pm\pm}}$ = 300 GeV (right). The arrow indicate the chosen working point. The significance is calculated with Cowan formula 8.1. The green curve indicates the "temperature for smoothing" (as defined in section 8.3). The arrow indicates the chosen working point.

	Prompt MC	Fakes Leptons	Total Background	H++ (Eff)	H+ (Eff)
Initial	-	-	-	15.06	46.52
Pre-selection	41.8±0.67	24.75±5.14	66.55±5.18	9.0±0.16 (100.0 %)	4.16±0.13 (100.0 %)
$E_{\mathrm{T}}^{\mathrm{miss}}$	15.3±0.32	14.45±3.08	29.75±3.09	6.49±0.13 (72.1 %)	3.18±0.12 (76.4 %)
$M_{4\ell}$	9.43±0.25	5.74±1.22	15.18±1.25	5.33±0.12 (59.2 %)	2.28±0.1 (54.8 %)
$p_T^{\ell_1}$	9.06±0.24	4.97±1.05	14.03±1.08	4.69±0.11 (59.0 %)	1.93±0.08 (54.1 %)
$\Delta R^{\mathrm{min}}_{\ell^\pm\ell^\pm}$	2.09±0.12	1.63±0.32	3.72±0.34	3.81±0.1 (42.3 %)	1.39±0.08 (33.4 %)
$\Delta R^{\mathrm{max}}_{\ell^\pm\ell^\pm}$	0.36±0.06	0.15±0.0	0.5±0.06	3.29±0.09 (36.1 %)	0.36±0.04 (8.7 %)

Table 8.7: 4ℓ channel. Cutflow for the 200 GeV mass signal point. The quoted uncertainty contains the statistical component. Eff stands for the signal efficiency.

Unlike discriminating variable distribution in $2\ell^{sc}$ and 3ℓ channel, it is found in figure 7.28 that discriminating variable $\Delta R^{\mathrm{max}}_{\ell^\pm\ell^\pm}$ shape are different between pair-production and associate-production . Dedicate test was performed specially for associate-production, and no improvement was found. All signal region definition are listed in Table 8.5. The cut-flows for 4ℓ channels with the 200 GeV mass signal points are listed in Table 8.7.

8.5 Signal region summary

The signal regions defined for the $2\ell^{sc}$, 3ℓ and 4ℓ channels, for each mass point, are illustrated in Table 8.8. These requirements are added on top of the pre-selection defined in Table 6.5. The variables used in this table are detailed in section 6.3.

To better account for the background distribution in the 3ℓ channel, each 3ℓ SR is divided in two, depending on the number same-flavor opposite-charge pairs. One 3ℓ SR is defined when zero such pairs (SFOC 0) exist in the event and another when one or two such pairs (SFOC 1,2) exist, respectively. This approach was found to increase the sensitivity of the 3ℓ channel when performing the statistical interpretation (and placing limits on the charged Higgs boson mass). For the same reason, the $2\ell^{sc}$ channel is split into three sub-channels.

Table 8.8: The signal regions selection applied on top of the pre-selection defined in Table 6.5. The variables used in this table are detailed in section 6.3.

Selection criteria	$2\ell^{sc}$ $e^\pm e^\pm$; $e^\pm\mu^\pm$; $\mu^\pm\mu^\pm$	3ℓ SFOC 0; SFOC 1,2	4ℓ
$m_{H^\pm H^\pm}$ = 200 GeV, $m_{H^\pm}$ = 196 GeV			
m_{jets} [GeV]	[100, 450]		
S [rad.]	<0.3		
$\Delta R_{\ell^\pm\ell^\pm}$ [rad.]	<1.9	[0.2, 1.7]	
$\Delta\phi(\ell\ell, E_{\text{T}}^{\text{miss}})$ [rad.]	<0.7		
$m_{x\ell}$ [GeV]	[40, 150]	>160	>230
$E_{\text{T}}^{\text{miss}}$ [GeV]	>100	>30	>60
$\Delta R_{\ell\text{jet}}$ [rad.]		[0.1, 1.5]	
$p_{\text{T}}^{\text{leading jet}}$ [GeV]		>40	
$p_{\text{T}}^{\ell_1}$ [GeV]			>65
$\Delta R_{\ell^\pm\ell^\pm}^{\text{min}}$ [rad.]			[0.2, 1.2]
$\Delta R_{\ell^\pm\ell^\pm}^{\text{max}}$ [rad.]			[0.3, 2.0]
$m_{H^\pm H^\pm}$ = 300 GeV, $m_{H^\pm}$ = 295 GeV			
m_{jets} [GeV]	[100, 500]		
S [rad.]	<0.6		
$\Delta R_{\ell^\pm\ell^\pm}$ [rad.]	<2.1	[0.0, 2.1]	
$\Delta\phi(\ell\ell, E_{\text{T}}^{\text{miss}})$ [rad.]	<0.9		
$m_{x\ell}$ [GeV]	[90, 240]	>190	>270
$E_{\text{T}}^{\text{miss}}$ [GeV]	>130	>55	>60
$\Delta R_{\ell\text{jet}}$ [rad.]		[0.1, 2.0]	
$p_{\text{T}}^{\text{leading jet}}$ [GeV]		>70	
$p_{\text{T}}^{\ell_1}$ [GeV]			>80
$\Delta R_{\ell^\pm\ell^\pm}^{\text{min}}$ [rad.]			[0.2, 2.0]
$\Delta R_{\ell^\pm\ell^\pm}^{\text{max}}$ [rad.]			[0.5, 2.6]
$m_{H^\pm H^\pm}$ = 400 GeV, $m_{H^\pm}$ = 395 GeV			
m_{jets} [GeV]	[300, 700]		
S [rad.]	<0.6		
$\Delta R_{\ell^\pm\ell^\pm}$ [rad.]	<2.2	[0.2, 2.5]	
$\Delta\phi(\ell\ell, E_{\text{T}}^{\text{miss}})$ [rad.]	<1.0		
$m_{x\ell}$ [GeV]	[130, 340]	>240	>360
$E_{\text{T}}^{\text{miss}}$ [GeV]	>170	>80	>60
$\Delta R_{\ell\text{jet}}$ [rad.]		[0.1,2.3]	
$p_{\text{T}}^{\text{leading jet}}$ [GeV]		>100	
$p_{\text{T}}^{\ell_1}$ [GeV]			>110
$\Delta R_{\ell^\pm\ell^\pm}^{\text{min}}$ [rad.]			[0.5, 2.4]
$\Delta R_{\ell^\pm\ell^\pm}^{\text{max}}$ [rad.]			[0.4, 3.1]
$m_{H^\pm H^\pm}$ = 500 GeV, $m_{H^\pm}$ = 496 GeV, $m_{H^\pm H^\pm}$ = 600 GeV, $m_{H^\pm}$ = 602 GeV			
m_{jets} [GeV]	[400, 1000]		
S [rad.]	<0.9		
$\Delta R_{\ell^\pm\ell^\pm}$ [rad.]	<2.4	[0.3, 2.8]	
$\Delta\phi(\ell\ell, E_{\text{T}}^{\text{miss}})$ [rad.]	<1.0		
$m_{x\ell}$ [GeV]	[130, 400]	>310	>440
$E_{\text{T}}^{\text{miss}}$ [GeV]	>200	>90	>60
$\Delta R_{\ell\text{jet}}$ [rad.]		[0.5, 2.3]	
$p_{\text{T}}^{\text{leading jet}}$ [GeV]		>95	
$p_{\text{T}}^{\ell_1}$ [GeV]			>130
$\Delta R_{\ell^\pm\ell^\pm}^{\text{min}}$ [rad.]			[0.6, 2.4]
$\Delta R_{\ell^\pm\ell^\pm}^{\text{max}}$ [rad.]			[0.6, 3.1]

9 Systematic Uncertainties

Contents

Both the theoretical and experimental uncertainties are considered in this analysis. The signal process and the background with prompt leptons are taken from the Monte-Carlo simulations. The uncertainties related to the normalizations and the acceptances are mostly from the finite precision of the prediction of cross sections and differential kinematics, and are of theoretical nature. Experimental uncertainties arise from the finite accuracy of the detector simulation and the uncertainties associated to the data-driven methods that are used to estimate the instrumental backgrounds.

9.1 Theory uncertainty

The theoretical uncertainties include PDF variations, QCD renormalization and factorization scale, parton shower uncertainty and generation comparison.

9.1.1 pair-production and associate-production uncertainties

The PDF uncertainties of the signal yields are evaluated using the LHAPDF6 library [88]. For the PDF (NNPDF30_nlo_as_0118), the generated events are re-weighted with

$$\omega_i = \frac{x_1 f_{1i}(x_1; Q^2)}{x_1 f_{10}(x_1; Q^2)} \frac{x_2 f_{2i}(x_2; Q^2)}{x_2 f_{20}(x_2; Q^2)}, i = 1, 2, \cdots, 100. \tag{9.1}$$

where the functions f_{10} and f_{20} in the denominators are the nominal PDFs; f_{1i} and f_{2i} in the numerators are the variation PDF members. Q is the QCD factorization scale, and x is the momentum fraction to the whole beam momentum. 1 and 2 stand for the two different beams.

For each variation PDF member, the expected signal yield is estimated by the re-weighted signal samples. The PDF uncertainties are obtained following the prescription in eq. (10) - (13) of Ref. [88] and recommendation from ATLAS PMG group [1]. The study is performed for the inclusive $2\ell^{sc}$, 3ℓ

[1] https://twiki.cern.ch/twiki/bin/view/AtlasProtected/PmgSystematicUncertaintyRecipes

and 4ℓ phase spaces, by applying the corresponding pre-selections to the truth level quantities of the signal samples. The PDF uncertainties are found to be in the range of 2.5% to 4.5%.

The signal cross-section can also vary with the assumed renormalization/factorization scale. The variations due to the factorization scale (taken to be equal to the renormalization scale in this study) range from 1.5 to 8.7%.

The signal events are showered with both PYTHIA (with underlying event tune of "A14") and HERWIG generators (with underlying event tune of "H7-UE-MMHT") to estimate the uncertainty of the acceptance. The difference in the acceptance is found to be 2.4%, 1.8% and 3.8% for $2\ell^{sc}$, 3ℓ and 4ℓ channels respectively. Based on the above studies, as well as on the comparison with the study of SUSY $2\ell^{sc}$ and 3ℓ analysis [160], the overall uncertainty of 11% is assumed for the signal normalization.

9.1.2 Standard model background uncertainties

The WZ production is the most important background source in the 2LSS and 3L channels, and the analysis phase space covers the high jet multiplicity region; For a region with jet multiplicity equal to or higher than 2, a data-driven study was performed (and detailed in Section 7.1.1), and the uncertainty is estimated to be 9.0% for the WZ background. For the WZ background in regions with lower jet multiplicities, the uncertainty treatment is the same as for the other diboson processes. Details are below.

For $t\bar{t}V(t\bar{t}W, t\bar{t}Z)$ processes, conservative uncertainties [161] were assigned: 13%[2] for QCD scale uncertainty, 4% for PDF uncertainty.

For other diboson processes (ZZ, WW, and VVV), Vγ process, other $t\bar{t}X$ processes ($t\bar{t}H$ and tZ) and rare processes, the variation weight is used for the estimation the of systematic on the cross-section:

- 100 PDF variations using evaluated using LHAPDF. Note that for Sherpa samples (ZZ, WW, VVV, and Vγ) NNPDF3.0nnlo PDF variations were applied. For other processes, NNPDF3.0nlo PDF variations were applied.

- 7 variations (relative to the nominal) of the renormalization and factorization scale parameters;

For the rare backgrounds (3Tops, 4Tops, $t\bar{t}WW$, $t\bar{t}WW\ell\ell$ and VH), a conservative uncertainty of 50% is used as total theory uncertainty. Uncertainties are computed in each $2\ell^{sc}$, 3ℓ and 4ℓ set of signal regions. The final uncertainties in the signal regions defined are summarized in Table 9.1.

[2] According to Ref. [162], 13% is not enough for $t\bar{t}W$. Larger uncertainty (50%) was tested in final likelihood fit (Appendix O.2 in Ref. [163]) and the effect is negligible.

Process	Theory uncertainty											
	$2\ell^{sc}$						3ℓ				4ℓ	
	ee		$e\mu$		$\mu\mu$		SFOC0		SFOC12		4ℓ	
	QCD	PDF	QCD	PDF	QCD	PDF	QCD	PDF	QCD	PDF	QCD	PDF
WZ	9.0%										14.8%	0.11%
$t\bar{t}X$	13.0% for QCD, 4.0% for PDF											
ZZ	43.1%	7.7%	27.9%	1.4%	23.6%	1.3%	17.2%	2.1%	26.1%	1.2%	14.9%	2.1%
WW	31.3%	1.0%	24.5%	2.0%	34.1%	1.5%	17.2%	2.6%	41.0%	1.5%	-	-
$V\gamma$	-	-	40.7%	2.5%	-	-	-	-	15.3 %	1.9%	-	-
VVV	7.4%	2.3%	8.4%	2.6%	8.4%	1.3%	10.5%	1.7%	10.5%	1.4%	7.9%	1.4%
Rare process	50%											

Table 9.1: Summary of relative theory uncertainty assigned for the various background processes entering in the $2\ell^{sc}$, 3ℓ and 4ℓ 200 Mass points signal regions. Other mass points have similar theoretical uncertainties. The rare backgrounds are 3Tops, 4Tops, $t\bar{t}WW$, $t\bar{t}WW\ell\ell$, and VH. When a process is not entering the signal region, we use "-". For the WZ and rare processes, the quoted uncertainty includes the QCD scale and PDF variations. In $2\ell^{sc}$ channel, WW only contains same-sign WW.

9.2 Experimental uncertainty

There are two general groups in ATLAS of uncertainties that affect the accuracies of the detector simulations. The first group impacts the acceptance of the signal region selection. The impact on the event yields in the signal region due to this type of uncertainty is estimated by applying the same event selection on the simulated samples with varying by ±1 standard deviation from the nominal. It includes: The uncertainties related to event reconstruction include the lepton [127, 164] and jet [132] energy scales and resolutions, and the uncertainties of the $E_{\mathrm{T}}^{\mathrm{miss}}$ soft term [143]. The overall impact on the background from SM processes with prompt leptons, and the signal yields in the SRs from these systematic uncertainties is found to be lower than 10%. The dominant contribution comes from the jet energy scale component.

The second group impacts the normalization of the yield in the signal region. It includes: The uncertainty in the combined 2015–2018 integrated luminosity is 1.7% [165], obtained using the LUCID-2 detector [166] for the primary luminosity measurements. Uncertainties in the modelling of pile-up interactions are estimated by reweighting the distribution of the average number of pp interactions per bunch crossing in the simulation, such that the average number of interactions changes by ±9%. The impact of these uncertainties on the background event yields estimated from the Monte-Carlo simulation is found to be lower than 2%. The uncertainties in the efficiencies of the electron [125] and muon [127] reconstruction, identification and trigger are also included. Their impact on the estimated yields in the SRs for the signal and the background from SM processes with prompt leptons are lower than 5%. The uncertainties in the b-jet identification are found to be negligible.

There are two more analysis specific uncertainties. The uncertainties in the background yield from electron charge-flip are in the range of 20–30% for the $2\ell^{sc}$ ee and $e\mu$ channels. The uncertainties in the non-prompt-lepton contributions in the SRs are between 25% and 90% and include the uncertainties described in Section 7.2.3, 7.3.2, 7.4.2, and statistical uncertainties in the control regions where the contributions are estimated.

The relative uncertainty in the background yields obtained in a fit of background to the observed data is shown in Figure 9.1 for all SRs. The statistical uncertainties originate from the limited number of preselected and opposite-charge data events used in the fake factor method and the charge-flip electron background estimate, respectively, as well as the effect of the limited number of simulated events for SM processes with prompt leptons. The total uncertainty is computed using all sources of uncertainty, and they are treated as uncorrelated. The uncertainties range from 10% to 30% and are dominated by the statistical uncertainties in the non-prompt-lepton estimate and the theory uncertainties. An exception is the $2\ell^{sc}$ SR defined for $m_{H^{\pm\pm}} = 300$ GeV, where the uncertainties from most sources are of similar size. The uncertainties associated with the charge-flip background are small in all $2\ell^{sc}$ SRs. In the 4ℓ channel, the statistical uncertainty of the non-prompt leptons comes from the limited number of events in the Z+jets, $t\bar{t}$ and tW Monte-Carlo simulation samples.

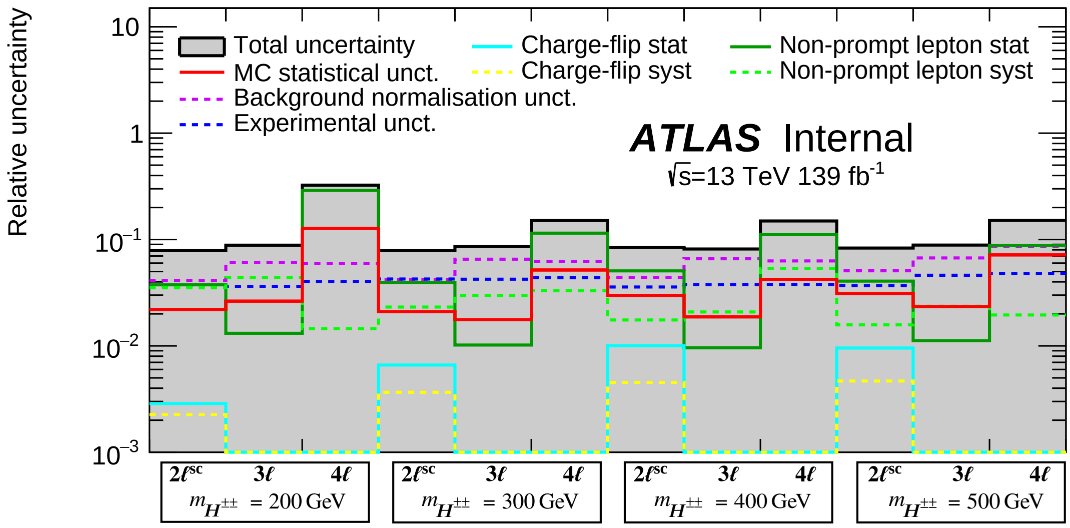

Figure 9.1: Contributions of different categories of uncertainties relative to the expected background yields in the defined SRs. The uncertainties are shown for the combination of the individual channels of the $2\ell^{ss}$, 3ℓ and 4ℓ SRs, respectively.

10 Statistical analysis and results

Contents

10.1 Event Yield

The expected and observed event yields in all the defined signal regions ($2\ell^{sc}$, 3ℓ, and 4ℓ, as defined in section 8.5) of the 200 - 500 GeV mass signal points are shown in Figure 10.1 - 10.4. One can observe a uniform performance in all channels. The ratio between signal and background (S/B) as well as the signal significance ($S/\sqrt{B}$) in the different channels for the $m_{H^{\pm\pm}}$ = 200 GeV signal mass point are shown in Figure 10.5. A combined distribution plot for background processes can be found in Figure 10.6. The yield details can be found in Table 10.2. No significant excess has been found. The data is used to constrain the signal model.

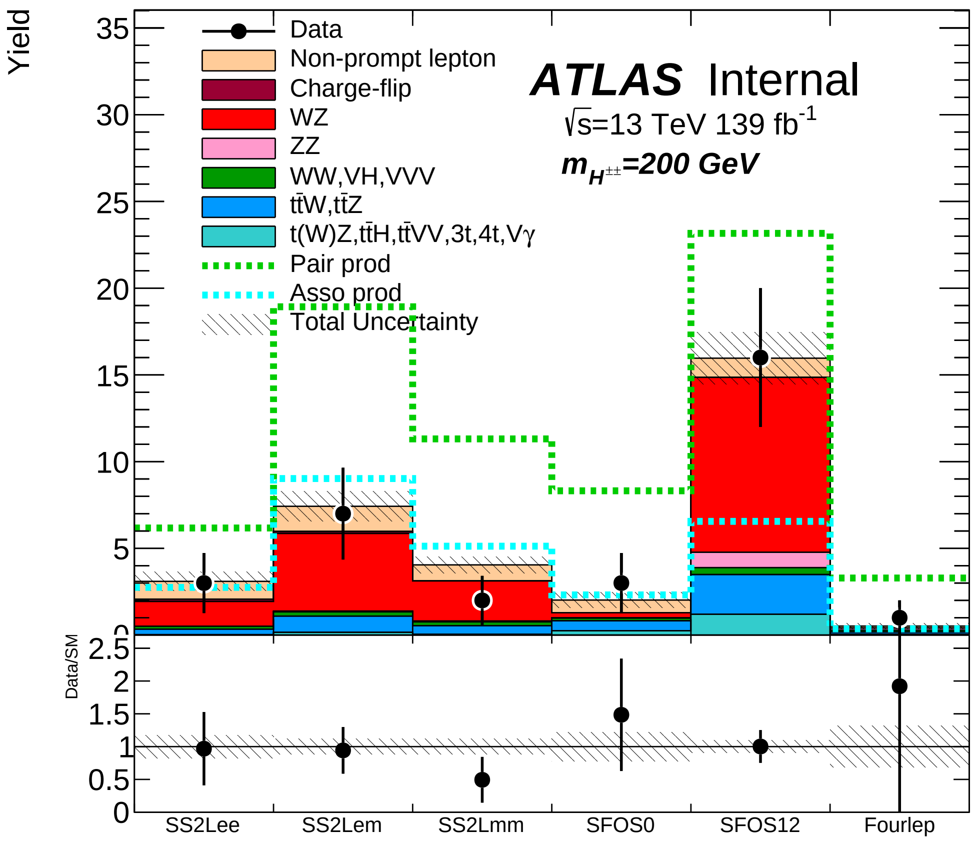

Figure 10.1: 200 GeV mass point: Signal and background (non-prompt(fake) leptons and charge-flip(MisID) from data-driven estimation) yields in all signal regions. The uncertainty includes all stat. and syst. sources. SFOS0 and SFOS12 are the SFOC0 and SFOC12 channels defined for the 3ℓ channel, respectively. P-value is driven from the χ^2 score between data and background estimation.

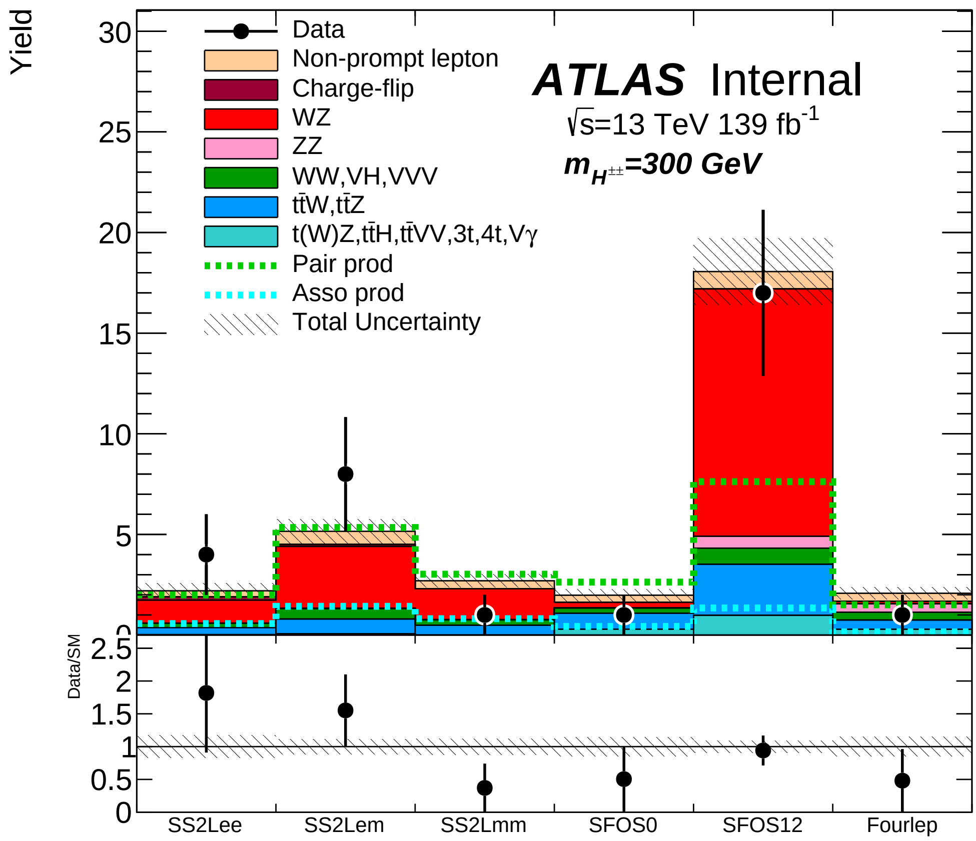

Figure 10.2: 300 GeV mass point: Signal and background (non-prompt(fake) leptons and charge-flip(MisID) from data-driven estimation) yields in all signal regions. The uncertainty includes all stat. and syst. sources. SFOS0 and SFOS12 are the SFOC0 and SFOC12 channels defined for the 3ℓ channel, respectively. P-value is driven from the χ^2 score between data and background estimation.

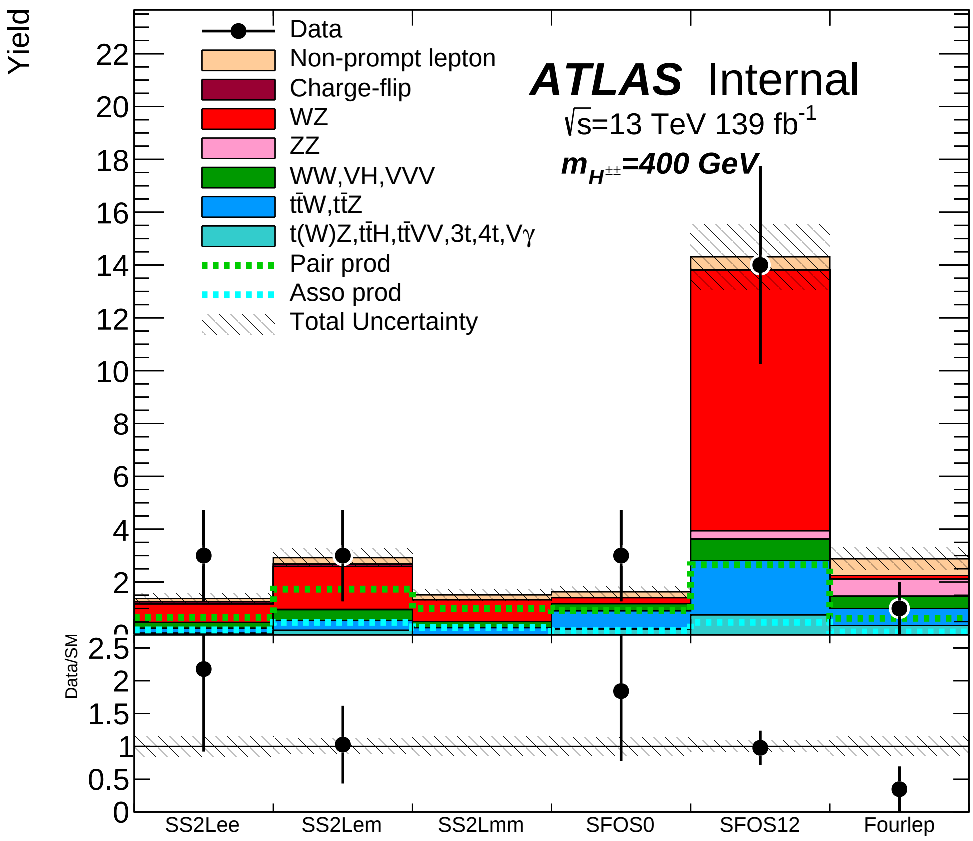

Figure 10.3: 400 GeV mass point: Signal and background (non-prompt(fake) leptons and charge-flip(MisID) from data-driven estimation) yields in all signal regions. The uncertainty includes all stat. and syst. sources. SFOS0 and SFOS12 are the SFOC0 and SFOC12 channels defined for the 3ℓ channel, respectively. P-value is driven from the χ^2 score between data and background estimation.

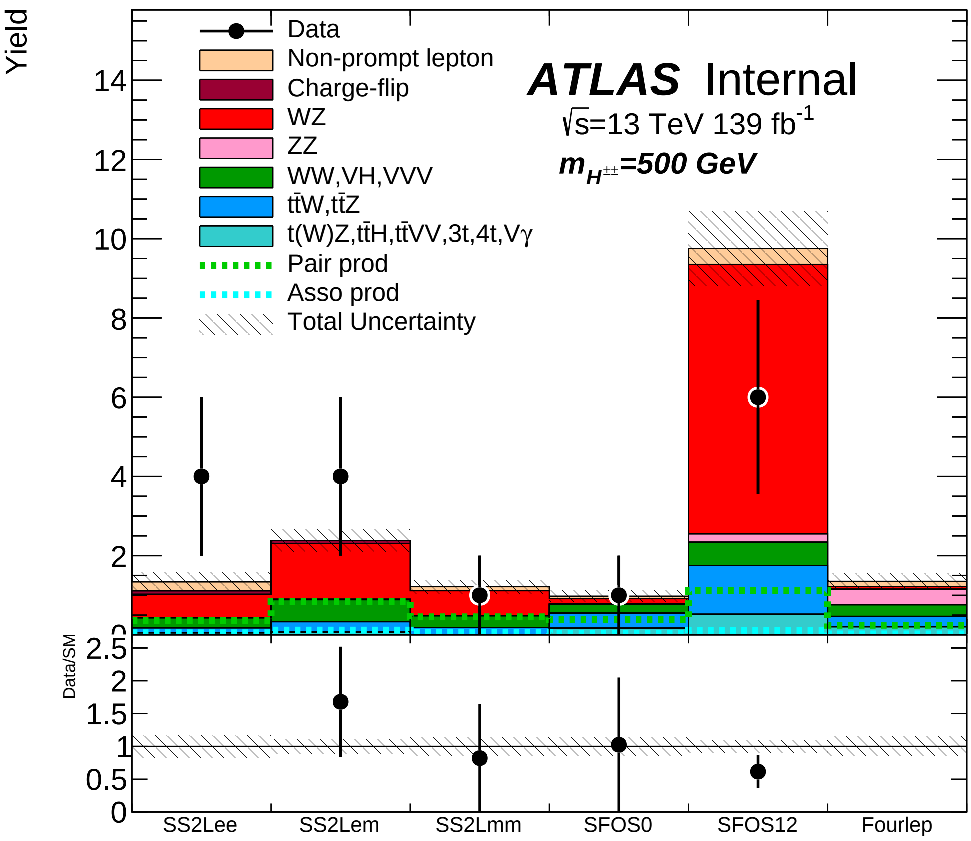

Figure 10.4: 500 GeV mass point: Signal and background (non-prompt(fake) leptons and charge-flip(MisID) from data-driven estimation) yields in all signal regions. The uncertainty includes all stat. and syst. sources. SFOS0 and SFOS12 are the SFOC0 and SFOC12 channels defined for the 3ℓ channel, respectively. P-value is driven from the χ^2 score between data and background estimation.

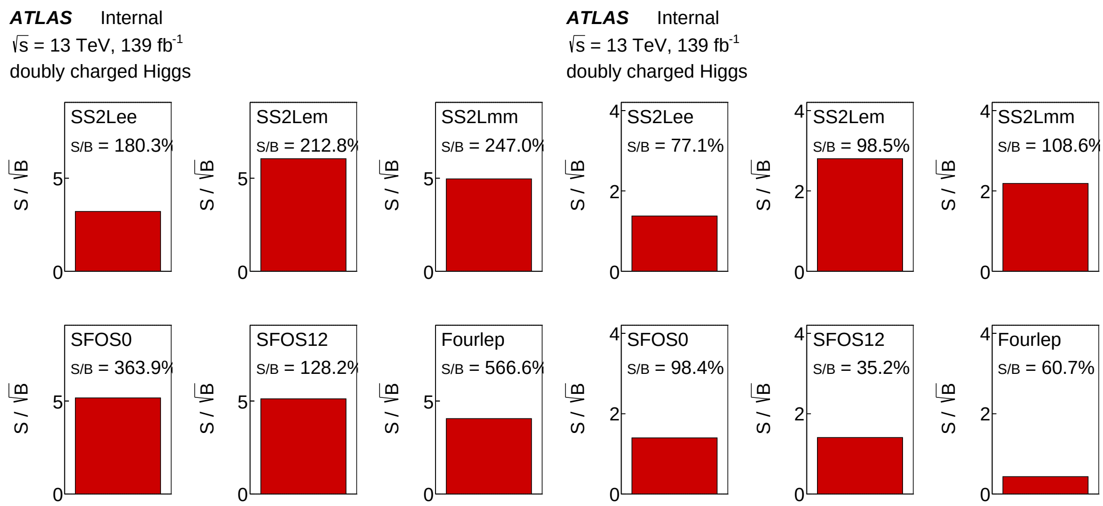

(a) pair-production (b) associate-production

Figure 10.5: $m_{H++} = 200$ GeV signal mass point: The ratio between signal and background (S/B) and the signal significance ($S/\sqrt{B}$). SFOS0 and SFOS12 are the SFOC0 and SFOC12 channels defined for the 3ℓ channel, respectively.

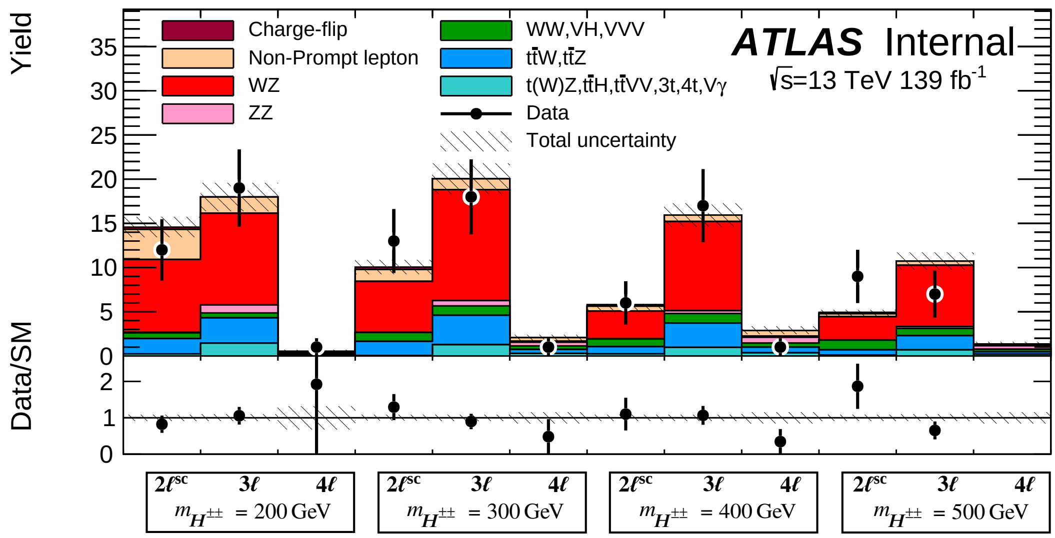

Figure 10.6: Data events yields compared with the expected contributions from relevant background sources, for the combination of the individual channels of the $2\ell^{sc}$, 3ℓ, and 4ℓ SRs, respectively.

10.2 Statistical Analysis

The statistical analysis of the results is done with TtHFitter[1]. The procedure is based on the likelihood ratio test. The parameter of interest (POI) is the signal strength, defined as the cross section of the hypothetical contribution from physics beyond the SM in a unit of the cross section of the benchmark model. The hypothesis tests are performed using one bin per signal region, and there is no control region involved. The likelihood functions are constructed by Poisson statistics of counting experiments in the 6 signal regions: the 3 sub-channels (ee,$e\mu$ and $\mu\mu$) for $2\ell^{sc}$ channel, the two same-flavor-opposite-charge sub-channels (SFOC0, SFOC12) for the 3ℓ, and the signal region for 4ℓ. The systematic uncertainties are treated as nuisance parameters implemented in the likelihood functions. $\mathrm{CL_s}$ method [51] is used to derive the 95% Confidence Level (CL) upper limits on the signal production cross-section.

10.2.1 Likelihood Function

The likelihood function is defined with Poissonian terms to describe the statistical fluctuations of the data, and Gaussian terms to model the systematic uncertainties,

$$\mathcal{L}(\mu,\theta) = \prod_{i}^{\text{bins}} \mathcal{L}_{\text{pois}}(N^i_{\text{data}} \,|\, \mu s^i(\theta) + b^i(\theta)) \times \mathcal{L}_{\text{gaus}}(\theta), \tag{10.1}$$

where μ is the signal strength parameterizing the ratio between the expected signal events from the hypothesis and the median signal events from theory prediction, θ is the nuisance parameter to parametrizes the effect of systematic uncertainties. N^i_{data} is the number of data events in the i-th bin, $s^i(\theta)$ is the expected signal yield in the i-th bin while $b^i(\theta)$ is the expected background yield in the i-th bin. The fit values of nuisance parameters (θ) of $M_{H^{\pm\pm}}$ = 300 GeV signal is shown in Figure 10.7. After fitting, all nuisance parameters are kept within one standard deviation.

10.2.2 Hypothesis Test

To obtain the expected 95% CL limits on the production cross-section of the signal, the null hypothesis is set asthe S+B hypothesis, which means the new physics is needed to understand the data. A test-statistic q_μ is defined as [158]:

$$q_\mu = -2\ln\left(\frac{\mathcal{L}(\mu,\hat{\hat{\theta}}_\mu)}{\mathcal{L}(\hat{\mu},\hat{\theta})}\right), \tag{10.2}$$

[1] https://twiki.cern.ch/twiki/bin/viewauth/AtlasProtected/TtHFitter

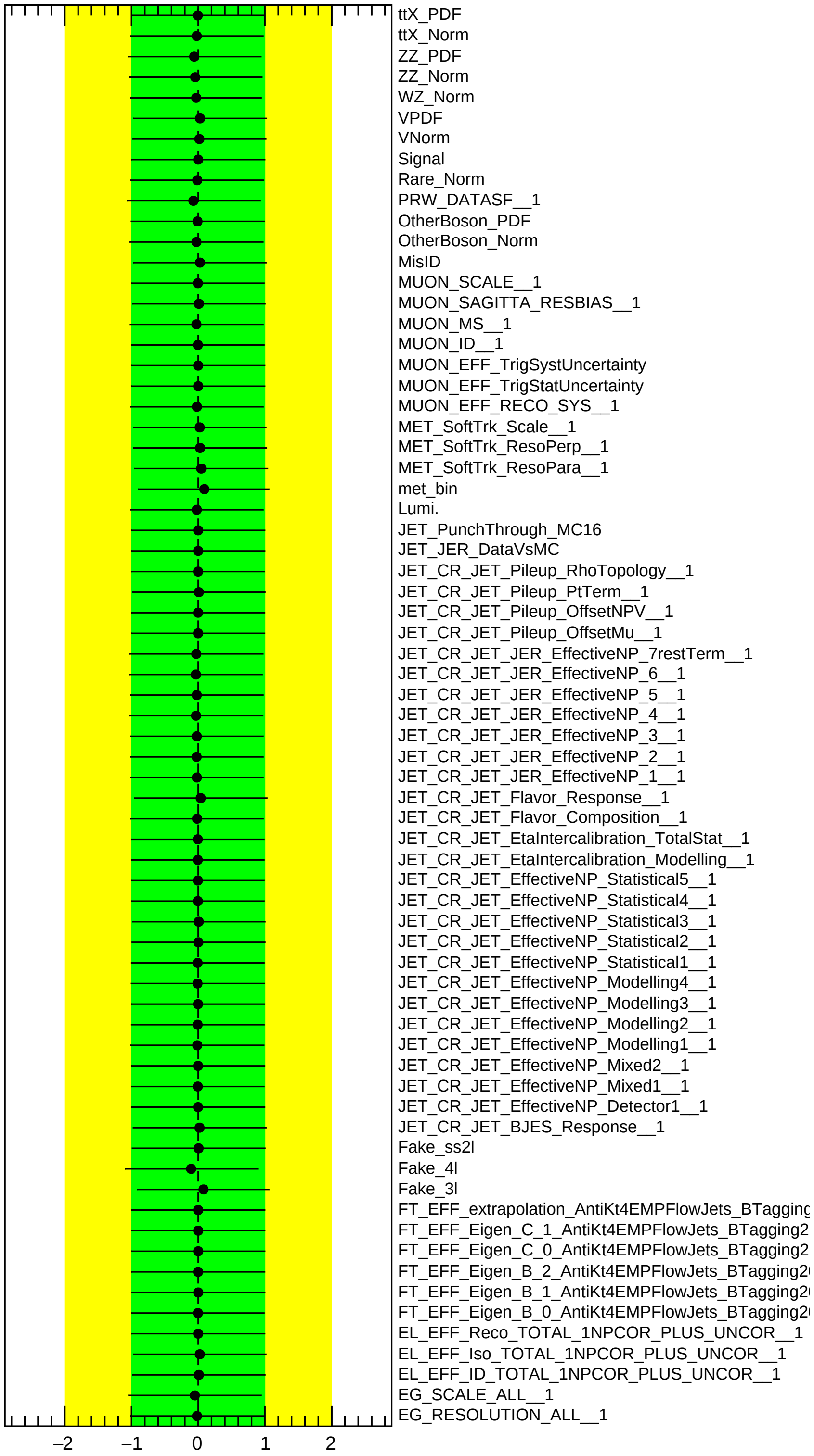

Figure 10.7: The fit values of nuisance parameters. After fitting, all nuisance parameters are kept within one standard deviation.

where $\mathcal{L}(\hat{\mu}, \hat{\theta})$ is the unconditional maximum likelihood with floating μ and θ parameters, while $\mathcal{L}(\mu, \hat{\hat{\theta}}_{\mu})$ is the conditional maximum likelihood with fixed μ. The test-statistic by definition non-negative. Higer value of q_{μ} indicates the increasing incompat-ibility between the data and the null hypothesis.

The probability density function of the test-statistic ($f(q_{\mu}\,|\,\text{hypo})$) need to be determined in order to derive the 95% CL limits. They are estimated using asymptotic formulae [158] instead of generating a large amount of pseudo experiments[2] Once the probability density functions are known, the probability $p_{\text{S+B}}$ can be defined that an S+B hypothesis gives a test-statistic above a reference value q_{μ}^{ref},

$$p_{\text{S+B}} = P(q_{\mu} > q_{\mu}^{\text{ref}}\,|\,\text{S}+\text{B}) = \int_{q_{\mu}^{\text{ref}}}^{\infty} f(q_{\mu}\,|\,\text{S}+\text{B})\,\mathrm{d}q_{\mu}. \tag{10.3}$$

Likewise, the probability p_{B} is defined that a background-only hypothesis exhibits a test-statistic lower than the reference value:

$$p_{\text{B}} = P(q_{\mu} < q_{\mu}^{\text{ref}}\,|\,\text{B}) = \int_{-\infty}^{q_{\mu}^{\text{ref}}} f(q_{\mu}\,|\,\text{B})\,\mathrm{d}q_{\mu}. \tag{10.4}$$

For a given set of signal mass or branching ratios, the S+B hypothesis is tested for several values of μ. For expected limits, the $p_{\text{S+B}}$ value is then computed using the median of the B hypothesis test-statistic distribution as a reference value. To obtain the median of the B hypothesis, *Asimov data set* [158] is used. This is a pseudo-data set that represents the predicted SM background and follows Poissonian distribution in each bin. For the observed limits, the reference value is determined from the fit to observed data. The excluded μ at 95% CL is defined to fulfill the following requirement:

$$\text{CL}_{\text{s}} \equiv \frac{p_{\text{S+B}}}{1 - p_{\text{B}}} < 5\% \tag{10.5}$$

The fraction in Eq. (10.5) accounts for the probability that the S+B hypothesis gives.

10.3 Results and Interpretation

The upper limits on the signal strength of both pair-production and associate-production are shown in Table 10.1. The expected and observed limits obtained after combining the $2\ell^{sc}$, 3ℓ and 4ℓ channels are shown in Figure 10.8 (versus $H^{\pm\pm}$ mass) for pair production, and for associate production, with all uncertainties included and only with the stat uncertainty included. Combining all channels, the benchmark model is expected to be excluded at $m_{H^{\pm\pm}} < 352$ GeV (358 GeV for expected results) for the charged Higgs pair-production and $m_{H^{\pm\pm}} < 228$ GeV (225 GeV for expected results) for the charged Higgs associate-production.

To have conservative choice of final limit, $m_{H^{\pm\pm}} > 350$ GeV is set for the pair-production, while $m_{H^{\pm\pm}} > 220$ GeV is set for the associate-production. To validate the interpolation, these two mass

[2] Also named toy experiments, which are more time-consuming but more precise.

Pair-production (36.1 fb^{-1})	200	300	400	500	600
All combined	0.89(0.69)	3.09(3.34)	11.32(8.05)	23.34(16.32)	43.93(30.37)
Pair-production (139.0 fb^{-1})	**200**	**300**	**400**	**500**	**600**
All combined	0.19(0.19)	0.59(0.58)	1.52(1.39)	3.20(2.67)	6.72(5.64)
$2\ell^{sc}$ ee	0.80(0.81)	3.38(2.23)	9.48(5.42)	20.63(10.26)	45.14(22.28)
$2\ell^{sc}$ $e\mu$	0.33(0.49)	1.07(1.57)	2.48(3.95)	7.59(8.15)	15.73(16.89)
$2\ell^{sc}$ $\mu\mu$	0.35(0.37)	1.72(1.13)	2.91(2.82)	7.70(5.35)	16.45(11.43)
3ℓ SFOC0	0.65(0.52)	1.24(1.62)	6.30(4.41)	9.12(9.01)	19.47(19.21)
3ℓ SFOC12	0.42(0.42)	1.25(1.36)	3.42(3.51)	4.58(6.96)	9.57(14.56)
4ℓ	1.12(0.90)	2.20(2.94)	5.29(8.04)	10.28(16.06)	22.31(34.89)
Associate-production (139.0 fb^{-1})	**200**	**300**	**400**	**500**	**600**
All combined	0.45(0.49)	2.86(2.51)	6.44(5.83)	28.41(21.71)	49.33(37.93)
$2\ell^{sc}$ ee	1.83(1.85)	11.96(7.85)	34.56(19.50)	>1000(73.36)	>1000(>1000)
$2\ell^{sc}$ $e\mu$	0.74(1.07)	4.00(5.88)	9.26(14.76)	54.80(58.86)	>1000(222.51)
$2\ell^{sc}$ $\mu\mu$	0.74(0.78)	6.49(4.24)	10.65(10.32)	54.89(38.14)	104.38(67.07)
3ℓ SFOC0	2.35(1.86)	7.72(10.06)	37.24(26.01)	>1000(232.36)	>1000(>1000)
3ℓ SFOC12	1.49(1.49)	7.09(7.71)	18.95(19.46)	74.92(71.34)	>1000(>1000)
4ℓ	10.82(8.53)	21.84(29.27)	31.62(48.17)	>1000(>1000)	>1000(>1000)

Table 10.1: The observed (expected) upper limits on production cross-section. The 36.1 fb^{-1} results are taken from the previous version of the analysis [23]. The 139.0 fb^{-1} results are obtained using the signal regions optimized for this version of the analysis and summarized in section 8.5. The improvement is coming from two sources: a) pure statistical, around a factor of 2, and b) analytical, around a factor of 2 to 3, including improved object selection, finer background estimation, more stable and harmonized signal regions, and constraint of WZ processes.

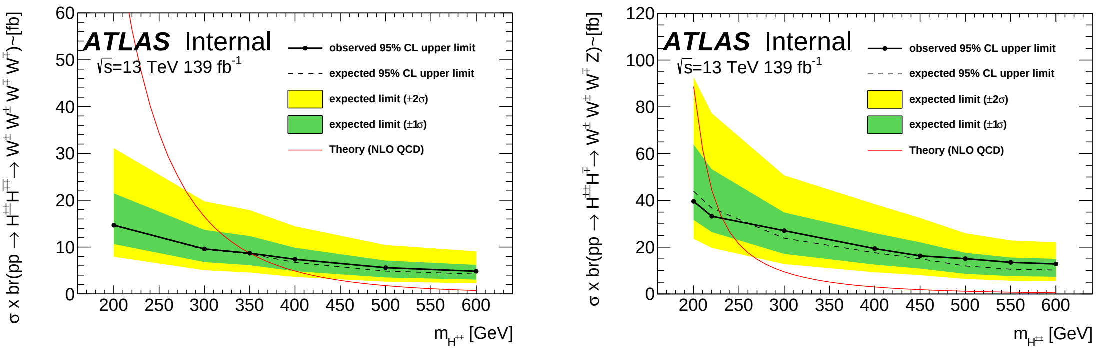

(a) pair-production

(b) associate-production

Figure 10.8: Expected and observed limits for the combination of $2\ell^{sc}$, 3ℓ and 4ℓ channels. The benchmark model is observed to be excluded at $m_{H^{\pm\pm}} < 350$ GeV for pair-production and 220 GeV for associate-production .

points are simulated and tested with the signal regions of the 300 GeV and 200 GeV mass points. Two other mass points, the 450 and 550 GeV, are also simulated to check the interpolation at the higher range for the associate-production.

Table 10.2: The expected background and the observed data event yields in the *signal* regions. The *signal* yield is for the corresponding mass point and is normalized to the luminosity of 139 fb^{-1}. The displayed numbers include all sources of statistical and systematic uncertainties. The overall *signal* acceptances A_{PP} and A_{AP} and the observed upper limit on extra contributions to each *signal* region at 95% confidence level, n_{95}, are also presented. The data and background yields obtained for $m_{H^{\pm\pm}}$ = 200 GeV, 300 GeV and 400 GeV are also valid for $m_{H^{\pm\pm}}$ = 220 GeV, 350 GeV and 450 GeV, respectively. The data and background yields obtained for $m_{H^{\pm\pm}}$ = 500 GeV *signal* regions are also valid for $m_{H^{\pm\pm}}$ = 550 GeV and $m_{H^{\pm\pm}}$ = 600 GeV. Selections with $\mu\mu$, three or four leptons are not affected by the electron charge-flip background, so these contributions are denoted by "–".

SR	$2\ell^{sc}$			3ℓ		4ℓ
	ee	$e\mu$	$\mu\mu$	Number of same-flavour opposite-charge pairs 0	> 0	
$m_{H^{\pm\pm}}$ = 200 GeV						
Prompt lepton	1.90±0.31	5.8±0.7	3.12±0.36	1.29±0.17	14.9±1.4	0.36±0.07
Charge-flip	0.13±0.04	0.118±0.035	–	–	–	–
Non-prompt lepton	1.0±0.5	1.45±0.5	0.93±0.31	0.7±0.4	1.11±0.71	0.15±0.15
Total background	3.1±0.5	7.3±0.9	4.0±0.5	2.0±0.4	15.97±1.48	0.51±0.17
Data	3	7	2	3	16	1
n_{95}	4.95	6.68	3.78	5.43	9.78	3.68
$H^{\pm\pm}H^{\mp\mp}$	6.2±0.8	18.9±2.2	11.3±1.3	8.3±1.0	23.16±2.68	3.29±0.38
A_{PP} [%]	0.055	0.168	0.100	0.074	0.206	0.029
$H^{\pm\pm}H^{\mp}$	2.8±0.4	9.0±1.1	5.1±0.6	2.32±0.29	6.56±0.76	0.36±0.06
A_{AP} [%]	0.022	0.073	0.042	0.019	0.053	0.003
$m_{H^{\pm\pm}}$ = 220 GeV						
$H^{\pm\pm}H^{\mp}$	1.74±0.21	5.1±0.6	3.1±0.4	1.45±0.18	4.1±0.5	0.23±0.04
A_{AP} [%]	0.028	0.082	0.050	0.023	0.066	0.004
$m_{H^{\pm\pm}}$ = 300 GeV						
Prompt lepton	1.66±0.28	4.3±0.5	2.30±0.26	1.62±0.20	17.2±1.6	1.69±0.19
Charge-flip	0.17±0.07	0.102±0.034	–	–	–	–
Non-prompt lepton	0.3±0.25	0.65±0.33	0.39±0.19	0.36±0.23	0.9±0.6	0.41±0.25
Total background	2.1±0.4	5.1±0.6	2.69±0.32	1.98±0.29	18.1±1.6	2.10±0.30
Data	4	8	1	1	17	1
n_{95}	6.72	9.21	3.24	3.27	9.52	3.31
$H^{\pm\pm}H^{\mp\mp}$	1.99±0.24	5.3±0.6	3.03±0.35	2.63±0.30	7.6±0.9	1.50±0.17
A_{PP} [%]	0.087	0.233	0.132	0.115	0.333	0.065
$H^{\pm\pm}H^{\mp}$	0.57±0.07	1.43±0.16	0.81±0.09	0.43±0.05	1.35±0.16	0.156±0.020
A_{AP} [%]	0.043	0.109	0.062	0.033	0.103	0.012
$m_{H^{\pm\pm}}$ = 350 GeV						
$H^{\pm\pm}H^{\mp\mp}$	1.20±0.14	3.11±0.35	1.74±0.20	1.57±0.18	4.5±0.5	0.89±0.10
A_{PP} [%]	0.099	0.257	0.144	0.130	0.372	0.074
$m_{H^{\pm\pm}}$ = 400 GeV						
Prompt lepton	0.87±0.12	2.52±0.29	1.33±0.16	1.41±0.18	13.8±1.2	2.26±0.25
Charge-flip	0.09±0.04	0.10±0.04	–	–	–	–
Non-prompt lepton	0.12±0.17	0.24±0.20	0.19±0.13	0.22±0.15	0.5±0.33	0.6±0.4
Total background	1.08±0.21	2.86±0.35	1.52±0.21	1.63±0.22	14.3±1.2	2.9±0.4
Data	3	3	0	3	14	1
n_{95}	6.25	5.03	2.48	5.73	9.05	3.33
$H^{\pm\pm}H^{\mp\mp}$	0.66±0.08	1.73±0.19	1.0±0.11	0.91±0.11	2.65±0.30	0.63±0.07
A_{PP} [%]	0.097	0.255	0.147	0.134	0.391	0.093
$H^{\pm\pm}H^{\mp}$	0.186±0.023	0.48±0.06	0.271±0.032	0.156±0.019	0.48±0.06	0.107±0.013
A_{AP} [%]	0.046	0.115	0.065	0.038	0.115	0.026
$m_{H^{\pm\pm}}$ = 450 GeV						
$H^{\pm\pm}H^{\mp}$	0.126±0.016	0.34±0.04	0.200±0.023	0.119±0.015	0.36±0.04	0.074±0.010
A_{AP} [%]	0.048	0.129	0.076	0.045	0.136	0.028
$m_{H^{\pm\pm}}$ = 500 GeV						
Prompt lepton	0.97±0.14	2.25±0.27	1.12±0.15	0.92±0.14	9.4±0.9	1.23±0.17
Charge-flip	0.089±0.032	0.08±0.04	–	–	–	–
Non-prompt lepton	0.23±0.19	< 0.1	0.10±0.09	0.06±0.06	0.4±0.27	0.13±0.12
Total background	1.29±0.23	2.33±0.27	1.22±0.17	0.98±0.14	9.8±0.9	1.36±0.20
Data	4	4	1	1	6	0
n_{95}	7.63	6.54	3.46	3.56	5.13	2.47
$H^{\pm\pm}H^{\mp\mp}$	0.37±0.04	0.85±0.1	0.45±0.05	0.39±0.04	1.12±0.13	0.243±0.028
A_{PP} [%]	0.150	0.346	0.183	0.159	0.455	0.098
$H^{\pm\pm}H^{\mp}$	0.114±0.014	0.263±0.030	0.140±0.017	0.074±0.009	0.242±0.028	0.051±0.006
A_{AP} [%]	0.068	0.158	0.084	0.044	0.145	0.031
$m_{H^{\pm\pm}}$ = 550 GeV						
$H^{\pm\pm}H^{\mp}$	0.089±0.011	0.195±0.023	0.105±0.012	0.053±0.006	0.174±0.020	0.039±0.005
A_{AP} [%]	0.08	0.175	0.094	0.048	0.156	0.035
$m_{H^{\pm\pm}}$ = 600 GeV						
$H^{\pm\pm}H^{\mp\mp}$	0.170±0.020	0.40±0.05	0.220±0.025	0.182±0.021	0.54±0.06	0.112±0.013
A_{PP} [%]	0.167	0.394	0.217	0.177	0.532	0.108
$H^{\pm\pm}H^{\mp}$	0.058±0.007	0.133±0.015	0.070±0.008	0.038±0.005	0.125±0.015	0.0277±0.0034
A_{AP} [%]	0.083	0.191	0.101	0.055	0.180	0.040

11 Conclusion and Prospects

Conclusion

This thesis presents a search for the pair- and associate-production of doubly charged Higgs with 139 fb^{-1} of proton-proton collision data at a center-of-mass energy of 13 TeV collected by the ATLAS collaboration during the year 2015 to 2018. The search is carried out through the selection of multilepton events ($2\ell^{sc}$, 3ℓ and 4ℓ) with missing transverse energy and several jets. A multi-variate cut-based search strategy is adopted in order to discriminate the signal from the Standard Model background. A significant fraction of this background, in particular for dilepton and trilepton topologies, originates from non-prompt leptons and from charge flip. These contributions are determined using data-driven methods. Several signal regions are defined depending on then flavor structure of the multilepton events, in order to exploit the different signal features and background conditions as a function of the flavor composition.

Dedicated signal regions in the ($2\ell^{sc}$, 3ℓ and 4ℓ channels are defined as the function of different mass hypotheses within the model to look for evidence of $H^{\pm\pm}$ and $H^{\pm}$ bosons. The data sample corresponds to an integrated luminosity of 139 fb^{-1}. The increase in the total integrated luminosity allowed significant improvements in the lepton fake factors measurement and the estimation of the associated uncertainties. The data are found to be in good agreement with the estimated background for all channels investigated. Combining those channels, the model considered is excluded at 95% confidence level for $H^{\pm\pm}$ boson masses below 350 GeV for the pair production of $H^{\pm\pm}$ bosons, and below 230 GeV for the associated production of $H^{\pm\pm}$ and $H^{\pm}$ bosons. Upper limits on the pair (associated) production cross section times branching fraction range from 15 fb to 5 fb (40 fb to 10 fb) when the assumed $H^{\pm\pm}$ mass varies from 200 GeV to 600 GeV. The results obtained for the $H^{\pm\pm}$ pair production scenario increase the exclusion limits beyond those from a previous, similar search by ATLAS using a smaller 13 TeV data set by approximately 130 GeV. In addition, the associated production of $H^{\pm\pm}$ and $H^{\pm}$ bosons is also explored, extending the previous search.

Prospects

The most dominant limitation for the presented analysis is the low statistics. Statistical uncertainties not only affect the final fitting directly but also affect the non-prompt leptons background estimation. The High-Luminosity Large Hadron Collider (HL-LHC) project aims to crank up the performance of the LHC in order to increase the potential for discoveries after 2027. The objective is to increase luminosity by a factor of 10, up to $10^{35}\mathrm{cm}^{-2}\,\mathrm{s}^{-1}$. More statistics also allow the analysis to estimate the non-prompt leptons more precisely. The uncertainties from the SM processes cross-section, especially WZ and $t\bar{t}V$ are also important for the results. With HL-LHC, it is foreseen to have a much better measurement of the SM processes cross-section.

Machine learning has shown its strength in this analysis by generating signal region cuts, rejecting non-prompt leptons (prompt lepton BDT), vetoing b-jets and suppressing charge flip electrons. 0 and 1 leptons channels were not considered in the presented analysis due to the complex and abundant multi-jets processes background. However, these two channels could play important roles in the rapid development of machine learning techniques. The large branch ratio of these two channels provides a great possibility for the next iteration.

Appendix

A Full Sample Lists

DatasetID	Xsection[pb]	K-factor	Filtering Efficiency	Generator and ProcessInfo
WZ				
363357	6.7975	1.0	1.0000E+00	Sherpa_221_NNPDF30NNLO_WqqZvv
363358	3.4328	1.0	1.0000E+00	Sherpa_221_NNPDF30NNLO_WqqZll
363489	11.42	1.0	1.0000E+00	Sherpa_221_NNPDF30NNLO_WlvZqq
364253	4.579	1.0	1.0000E+00	Sherpa_222_NNPDF30NNLO_lllv
364255	3.2344	1.0	1.0	Sherpa_222_NNPDF30NNLO_lvvv
364284	0.047066	1.0	1.0000E+00	Sherpa_222_NNPDF30NNLO_lllvjj_EW6
WW				
363359	24.708	1.0	1.0000E+00	Sherpa_221_NNPDF30NNLO_WpqqWmlv
363360	24.724	1.0	1.0000E+00	Sherpa_221_NNPDF30NNLO_WplvWmqq
364254	12.501	1.0	1.0	Sherpa_222_NNPDF30NNLO_llvv
364285	0.11629	1.0	1.0000E+00	Sherpa_222_NNPDF30NNLO_llvvjj_EW6
364286	0.02521	1.0	1.0000E+00	Sherpa_222_NNPDF30NNLO_llvvjj_ss_EW4
366088	0.018961	1.0	1.0000E+00	Sh_222_NN30NNLO_llvvjj_ss_Min_N_TChannel
ZZ				
364250	1.2523	1.0	1.0000E+00	Sherpa_222_NNPDF30NNLO_llll
364283	0.010545	1.0	1.0000E+00	Sherpa_222_NNPDF30NNLO_lllljj_EW6
363355	15.561	1.0	2.7687E-01	Sherpa_221_NNPDF30NNLO_ZqqZvv
363356	15.564	1.0	1.4158E-01	Sherpa_221_NNPDF30NNLO_ZqqZll
345706	0.010163	1.0	1.0000E+00	Sherpa_222_NNPDF30NNLO_ggllll_130M4l
345707	0.011055	1.0	1.0000E+00	Sherpa_222_NNPDF30NNLO_ggllll_130M4l_5gamma
NLO+ttW				
410155	0.54822	1.096	1.0000E+00	aMcAtNloPythia8EvtGen_MEN30NLO_A14N23LO_ttW
NLO+ttZ				
410218	0.036865	1.12	1.0000E+00	aMcAtNloPythia8EvtGen_MEN30NLO_A14N23LO_ttee
410219	0.036868	1.12	1.0000E+00	aMcAtNloPythia8EvtGen_MEN30NLO_A14N23LO_ttmumu
410220	0.036555	1.12	1.0000E+00	aMcAtNloPythia8EvtGen_MEN30NLO_A14N23LO_tttautau
VH				
342284	1.1021	1.0	1.0	Pythia8EvtGen_A14NNPDF23LO_WH125_inc
342285	0.60072	1.0	1.0	Pythia8EvtGen_A14NNPDF23LO_ZH125_inc
VVV				
364243	0.0017966	1.0	1.0000E+00	Sherpa_222_NNPDF30NNLO_WWZ_4l2v_EW6
364244	0.0035467	1.0	1.0000E+00	Sherpa_222_NNPDF30NNLO_WWZ_2l4v_EW6
364245	0.00018807	1.0	1.0000E+00	Sherpa_222_NNPDF30NNLO_WZZ_5l1v_EW6
364246	0.001668	1.0	4.4626E-01	Sherpa_222_NNPDF30NNLO_WZZ_3l3v_EW6
364247	1.4508e-05	1.0	1.0000E+00	Sherpa_222_NNPDF30NNLO_ZZZ_6l0v_EW6
364248	0.00038533	1.0	2.2453E-01	Sherpa_222_NNPDF30NNLO_ZZZ_4l2v_EW6
364249	0.00038545	1.0	4.4467E-01	Sherpa_222_NNPDF30NNLO_ZZZ_2l4v_EW6
tZ, Wt DS				
410560	0.24041	1.0	1.0000E+00	MadGraphPythia8EvtGen_A14_tZ_4fl_tchan_noAllHad
410656	3.8902	0.9704	1.0000E+00	PowhegPythia8EvtGen_A14_Wt_DS_dilepton_top
410657	3.9665	0.9493	1.0000E+00	PowhegPythia8EvtGen_A14_Wt_DS_dilepton_antitop
ttH				
346344	0.52458	1.0	4.3844E-01	PhPy8EG_A14NNPDF23_NNPDF30ME_ttH125_semilep
346345	0.054667	1.0	1.0000E+00	PhPy8EG_A14NNPDF23_NNPDF30ME_ttH125_dilep

Table A.1: Simulated event samples used as background in the $2\ell^{ss}$, 3ℓ and 4ℓ and final states.

DatasetID	Xsection[pb]	K-factor	Filtering Efficiency	Generator and ProcessInfo
3Tops				
304014	0.0016396	1.0	1.0000E+00	MadGraphPythia8EvtGen_A14NNPDF23_3top_SM
4Tops				
410080	0.0091626	1.00413615479	1.0000E+00	MadGraphPythia8EvtGen_A14NNPDF23_4topSM
WtZ				
410408	0.016071	1.0	1.0000E+00	aMcAtNloPythia8EvtGen_tWZ_Ztoll_minDR1
ttWW				
410081	0.0080952	1.22342593851	1.0000E+00	MadGraphPythia8EvtGen_A14NNPDF23_ttbarWW
ttWll				
407321	0.00026641	1.0	1.0000E+00	MadGraphPythia8EvtGen_A14NNPDF23LO_ttbarWll

Table A.2: Simulated prompt event samples with small contributions the $2\ell^{ss}$, 3ℓ and 4ℓ and final states.

DatasetID	Xsection[pb]	K-factor	Filtering Efficiency	Generator and ProcessInfo
$Z\gamma$				
366140	46.293	1.0	1.0000E+00	Sh_224_NN30NNLO_eegamma_LO_pty_7_15
366141	29.281	1.0	1.0000E+00	Sh_224_NN30NNLO_eegamma_LO_pty_15_35
366142	5.1577	1.0	1.0000E+00	Sh_224_NN30NNLO_eegamma_LO_pty_35_70
366143	0.40363	1.0	1.0000E+00	Sh_224_NN30NNLO_eegamma_LO_pty_70_140
366144	0.053018	1.0	1.0000E+00	Sh_224_NN30NNLO_eegamma_LO_pty_140_E_CMS
366145	46.276	1.0	1.0000E+00	Sh_224_NN30NNLO_mumugamma_LO_pty_7_15
366146	29.28	1.0	1.0000E+00	Sh_224_NN30NNLO_mumugamma_LO_pty_15_35
366147	5.1566	1.0	1.0000E+00	Sh_224_NN30NNLO_mumugamma_LO_pty_35_70
366148	0.40322	1.0	1.0000E+00	Sh_224_NN30NNLO_mumugamma_LO_pty_70_140
366149	0.05289	1.0	1.0000E+00	Sh_224_NN30NNLO_mumugamma_LO_pty_140_E_CMS
366150	46.253	1.0	1.0000E+00	Sh_224_NN30NNLO_tautaugamma_LO_pty_7_15
366151	29.282	1.0	1.0000E+00	Sh_224_NN30NNLO_tautaugamma_LO_pty_15_35
366152	5.1536	1.0	1.0000E+00	Sh_224_NN30NNLO_tautaugamma_LO_pty_35_70
366153	0.40358	1.0	1.0000E+00	Sh_224_NN30NNLO_tautaugamma_LO_pty_70_140
366154	0.052981	1.0	1.0000E+00	Sh_224_NN30NNLO_tautaugamma_LO_pty_140_E_CMS
$W\gamma$				
364522	134.38	1.0	1.0000E+00	Sherpa_222_NNPDF30NNLO_enugamma_pty_15_35
364523	19.074	1.0	1.0000E+00	Sherpa_222_NNPDF30NNLO_enugamma_pty_35_70
364524	1.9215	1.0	1.0000E+00	Sherpa_222_NNPDF30NNLO_enugamma_pty_70_140
364525	0.29803	1.0	1.0000E+00	Sherpa_222_NNPDF30NNLO_enugamma_pty_140_E_CMS
364527	134.45	1.0	1.0000E+00	Sherpa_222_NNPDF30NNLO_munugamma_pty_15_35
364528	19.108	1.0	1.0000E+00	Sherpa_222_NNPDF30NNLO_munugamma_pty_35_70
364529	1.9249	1.0	1.0000E+00	Sherpa_222_NNPDF30NNLO_munugamma_pty_70_140
364530	0.2987	1.0	1.0000E+00	Sherpa_222_NNPDF30NNLO_munugamma_pty_140_E_CMS
364532	134.43	1.0	1.0000E+00	Sherpa_222_NNPDF30NNLO_taunugamma_pty_15_35
364533	19.115	1.0	1.0000E+00	Sherpa_222_NNPDF30NNLO_taunugamma_pty_35_70
364534	1.9288	1.0	1.0000E+00	Sherpa_222_NNPDF30NNLO_taunugamma_pty_70_140
364535	0.29827	1.0	1.0000E+00	Sherpa_222_NNPDF30NNLO_taunugamma_pty_140_E_CMS

Table A.3: Simulation background event sets including prompt photons in the $2\ell^{ss}$, 3ℓ and 4ℓ and final states.

DatasetID	Xsection[pb]	K-factor	Filtering Efficiency	Generator and ProcessInfo
ZJets				
364100	1982.5	0.9751	8.2172E-01	Sherpa_221_NNPDF30NNLO_Zmumu_MAXHTPTV0_70_CVetoBVeto
364101	1982.2	0.9751	1.1355E-01	Sherpa_221_NNPDF30NNLO_Zmumu_MAXHTPTV0_70_CFilterBVeto
364102	1981.5	0.9751	6.5890E-02	Sherpa_221_NNPDF30NNLO_Zmumu_MAXHTPTV0_70_BFilter
364103	109.14	0.9751	6.8992E-01	Sherpa_221_NNPDF30NNLO_Zmumu_MAXHTPTV70_140_CVetoBVeto
364104	108.98	0.9751	1.9665E-01	Sherpa_221_NNPDF30NNLO_Zmumu_MAXHTPTV70_140_CFilterBVeto
364105	109.03	0.9751	1.1556E-01	Sherpa_221_NNPDF30NNLO_Zmumu_MAXHTPTV70_140_BFilter
364106	39.87	0.9751	5.9942E-01	Sherpa_221_NNPDF30NNLO_Zmumu_MAXHTPTV140_280_CVetoBVeto
364107	39.857	0.9751	2.3527E-01	Sherpa_221_NNPDF30NNLO_Zmumu_MAXHTPTV140_280_CFilterBVeto
364108	39.888	0.9751	1.5570E-01	Sherpa_221_NNPDF30NNLO_Zmumu_MAXHTPTV140_280_BFilter
364109	8.5251	0.9751	5.6023E-01	Sherpa_221_NNPDF30NNLO_Zmumu_MAXHTPTV280_500_CVetoBVeto
364110	8.5259	0.9751	2.6641E-01	Sherpa_221_NNPDF30NNLO_Zmumu_MAXHTPTV280_500_CFilterBVeto
364111	8.5292	0.9751	1.7673E-01	Sherpa_221_NNPDF30NNLO_Zmumu_MAXHTPTV280_500_BFilter
364112	1.787	0.9751	1.0000E+00	Sherpa_221_NNPDF30NNLO_Zmumu_MAXHTPTV500_1000
364113	0.14761	0.9751	1.0000E+00	Sherpa_221_NNPDF30NNLO_Zmumu_MAXHTPTV1000_E_CMS
364114	1981.6	0.9751	8.2133E-01	Sherpa_221_NNPDF30NNLO_Zee_MAXHTPTV0_70_CVetoBVeto
364115	1981.7	0.9751	1.1387E-01	Sherpa_221_NNPDF30NNLO_Zee_MAXHTPTV0_70_CFilterBVeto
364116	1982.0	0.9751	6.5756E-02	Sherpa_221_NNPDF30NNLO_Zee_MAXHTPTV0_70_BFilter
364117	110.64	0.9751	6.9426E-01	Sherpa_221_NNPDF30NNLO_Zee_MAXHTPTV70_140_CVetoBVeto
364118	110.5	0.9751	1.9068E-01	Sherpa_221_NNPDF30NNLO_Zee_MAXHTPTV70_140_CFilterBVeto
364119	110.46	0.9751	1.1826E-01	Sherpa_221_NNPDF30NNLO_Zee_MAXHTPTV70_140_BFilter
364120	40.645	0.9751	6.1615E-01	Sherpa_221_NNPDF30NNLO_Zee_MAXHTPTV140_280_CVetoBVeto
364121	40.671	0.9751	2.3291E-01	Sherpa_221_NNPDF30NNLO_Zee_MAXHTPTV140_280_CFilterBVeto
364122	40.675	0.9751	1.5332E-01	Sherpa_221_NNPDF30NNLO_Zee_MAXHTPTV140_280_BFilter
364123	8.6703	0.9751	5.6739E-01	Sherpa_221_NNPDF30NNLO_Zee_MAXHTPTV280_500_CVetoBVeto
364124	8.6668	0.9751	2.6620E-01	Sherpa_221_NNPDF30NNLO_Zee_MAXHTPTV280_500_CFilterBVeto
364125	8.6799	0.9751	1.7647E-01	Sherpa_221_NNPDF30NNLO_Zee_MAXHTPTV280_500_BFilter
364126	1.8092	0.9751	1.0000E+00	Sherpa_221_NNPDF30NNLO_Zee_MAXHTPTV500_1000
364127	0.14875	0.9751	1.0000E+00	Sherpa_221_NNPDF30NNLO_Zee_MAXHTPTV1000_E_CMS
364128	1982.0	0.9751	8.3444E-01	Sherpa_221_NNPDF30NNLO_Ztautau_MAXHTPTV0_70_CVetoBVeto
364129	1981.9	0.9751	1.1365E-01	Sherpa_221_NNPDF30NNLO_Ztautau_MAXHTPTV0_70_CFilterBVeto
364130	1982.1	0.9751	6.5763E-02	Sherpa_221_NNPDF30NNLO_Ztautau_MAXHTPTV0_70_BFilter
364131	110.66	0.9751	6.9264E-01	Sherpa_221_NNPDF30NNLO_Ztautau_MAXHTPTV70_140_CVetoBVeto
364132	110.46	0.9751	1.9060E-01	Sherpa_221_NNPDF30NNLO_Ztautau_MAXHTPTV70_140_CFilterBVeto
364133	110.67	0.9751	1.1851E-01	Sherpa_221_NNPDF30NNLO_Ztautau_MAXHTPTV70_140_BFilter
364134	40.756	0.9751	6.1880E-01	Sherpa_221_NNPDF30NNLO_Ztautau_MAXHTPTV140_280_CVetoBVeto
364135	40.716	0.9751	2.3432E-01	Sherpa_221_NNPDF30NNLO_Ztautau_MAXHTPTV140_280_CFilterBVeto
364136	40.746	0.9751	1.5532E-01	Sherpa_221_NNPDF30NNLO_Ztautau_MAXHTPTV140_280_BFilter
364137	8.6726	0.9751	5.6384E-01	Sherpa_221_NNPDF30NNLO_Ztautau_MAXHTPTV280_500_CVetoBVeto
364138	8.6757	0.9751	2.6432E-01	Sherpa_221_NNPDF30NNLO_Ztautau_MAXHTPTV280_500_CFilterBVeto
364139	8.6755	0.9751	1.7628E-01	Sherpa_221_NNPDF30NNLO_Ztautau_MAXHTPTV280_500_BFilter
364140	1.8078	0.9751	1.0000E+00	Sherpa_221_NNPDF30NNLO_Ztautau_MAXHTPTV500_1000
364141	0.14826	0.9751	1.0000E+00	Sherpa_221_NNPDF30NNLO_Ztautau_MAXHTPTV1000_E_CMS

Table A.4: Simulation event sets used for Z+jets background.

DatasetID	Xsection[pb]	K-factor	Filtering Efficiency	Generator and ProcessInfo
DY				
364198	2414.3	0.9751	9.6536E-01	Sherpa_221_NN30NNLO_Zmm_Mll10_40_MAXHTPTV0_70_BVeto
364199	2414.2	0.9751	3.4445E-02	Sherpa_221_NN30NNLO_Zmm_Mll10_40_MAXHTPTV0_70_BFilter
364200	50.33	0.9751	8.9306E-01	Sherpa_221_NN30NNLO_Zmm_Mll10_40_MAXHTPTV70_280_BVeto
364201	50.29	0.9751	1.1212E-01	Sherpa_221_NN30NNLO_Zmm_Mll10_40_MAXHTPTV70_280_BFilter
364202	3.2398	0.9751	8.5373E-01	Sherpa_221_NN30NNLO_Zmm_Mll10_40_MAXHTPTV280_E_CMS_BVeto
364203	3.2813	0.9751	1.6027E-01	Sherpa_221_NN30NNLO_Zmm_Mll10_40_MAXHTPTV280_E_CMS_BFilter
364204	2415.3	0.9751	9.6520E-01	Sherpa_221_NN30NNLO_Zee_Mll10_40_MAXHTPTV0_70_BVeto
364205	2415.5	0.9751	3.4696E-02	Sherpa_221_NN30NNLO_Zee_Mll10_40_MAXHTPTV0_70_BFilter
364206	50.354	0.9751	8.9320E-01	Sherpa_221_NN30NNLO_Zee_Mll10_40_MAXHTPTV70_280_BVeto
364207	50.487	0.9751	0.1087	Sherpa_221_NN30NNLO_Zee_Mll10_40_MAXHTPTV70_280_BFilter
364208	3.2539	0.9751	8.5485E-01	Sherpa_221_NN30NNLO_Zee_Mll10_40_MAXHTPTV280_E_CMS_BVeto
364209	3.2526	0.9751	1.5351E-01	Sherpa_221_NN30NNLO_Zee_Mll10_40_MAXHTPTV280_E_CMS_BFilter
364210	2416.0	0.9751	9.6534E-01	Sherpa_221_NN30NNLO_Ztt_Mll10_40_MAXHTPTV0_70_BVeto
364211	2414.4	0.9751	3.4676E-02	Sherpa_221_NN30NNLO_Ztt_Mll10_40_MAXHTPTV0_70_BFilter
364212	50.376	0.9751	8.9310E-01	Sherpa_221_NN30NNLO_Ztt_Mll10_40_MAXHTPTV70_280_BVeto
364213	50.468	0.9751	0.10985	Sherpa_221_NN30NNLO_Ztt_Mll10_40_MAXHTPTV70_280_BFilter
364214	3.2852	0.9751	8.5552E-01	Sherpa_221_NN30NNLO_Ztt_Mll10_40_MAXHTPTV280_E_CMS_BVeto
364215	3.2813	0.9751	1.5581E-01	Sherpa_221_NN30NNLO_Ztt_Mll10_40_MAXHTPTV280_E_CMS_BFilter
$t\bar{t}$				
410470	729.76	1.13975636159	5.4385E-01	PhPy8EG_A14_ttbar_hdamp258p75_nonallhad
Single Top				
410644	2.027	1.0170	1.0000E+00	PowhegPythia8EvtGen_A14_singletop_schan_lept_top
410645	1.2674	1.0167	1.0000E+00	PowhegPythia8EvtGen_A14_singletop_schan_lept_antitop
410658	36.996	1.1935	1.0000E+00	PhPy8EG_A14_tchan_BW50_lept_top
410659	22.173	1.1849	1.0000E+00	PhPy8EG_A14_tchan_BW50_lept_antitop

Table A.5: Simulation event sets used for Drell-Yan, $t\bar{t}$ and single top backgrounds.

DatasetID	Xsection[pb]	K-factor	Filtering Efficiency	Generator and ProcessInfo
Wjets				
364156	19151.0	0.9702	8.2465E-01	Sherpa_221_NNPDF30NNLO_Wmunu_MAXHTPTV0_70_CVetoBVeto
364157	19143.0	0.9702	1.0000E+00	Sherpa_221_NNPDF30NNLO_Wmunu_MAXHTPTV0_70_CFilterBVeto
364158	19143.0	0.9702	1.0000E+00	Sherpa_221_NNPDF30NNLO_Wmunu_MAXHTPTV0_70_BFilter
364159	945.89	0.9702	6.7430E-01	Sherpa_221_NNPDF30NNLO_Wmunu_MAXHTPTV70_140_CVetoBVeto
364160	946.12	0.9702	2.4357E-01	Sherpa_221_NNPDF30NNLO_Wmunu_MAXHTPTV70_140_CFilterBVeto
364161	944.8	0.9702	8.4525E-02	Sherpa_221_NNPDF30NNLO_Wmunu_MAXHTPTV70_140_BFilter
364162	339.73	0.9702	6.0009E-01	Sherpa_221_NNPDF30NNLO_Wmunu_MAXHTPTV140_280_CVetoBVeto
364163	339.8	0.9702	2.9256E-01	Sherpa_221_NNPDF30NNLO_Wmunu_MAXHTPTV140_280_CFilterBVeto
364164	339.68	0.9702	1.1080E-01	Sherpa_221_NNPDF30NNLO_Wmunu_MAXHTPTV140_280_BFilter
364165	72.084	0.9702	5.4766E-01	Sherpa_221_NNPDF30NNLO_Wmunu_MAXHTPTV280_500_CVetoBVeto
364166	72.103	0.9702	3.2016E-01	Sherpa_221_NNPDF30NNLO_Wmunu_MAXHTPTV280_500_CFilterBVeto
364167	72.063	0.9702	1.3137E-01	Sherpa_221_NNPDF30NNLO_Wmunu_MAXHTPTV280_500_BFilter
364168	15.008	0.9702	1.0000E+00	Sherpa_221_NNPDF30NNLO_Wmunu_MAXHTPTV500_1000
364169	1.2349	0.9702	1.0000E+00	Sherpa_221_NNPDF30NNLO_Wmunu_MAXHTPTV1000_E_CMS
364170	19153.0	0.9702	8.2467E-01	Sherpa_221_NNPDF30NNLO_Wenu_MAXHTPTV0_70_CVetoBVeto
364171	19146.0	0.9702	1.0000E+00	Sherpa_221_NNPDF30NNLO_Wenu_MAXHTPTV0_70_CFilterBVeto
364172	19143.0	0.9702	1.0000E+00	Sherpa_221_NNPDF30NNLO_Wenu_MAXHTPTV0_70_BFilter
364173	944.98	0.9702	6.7483E-01	Sherpa_221_NNPDF30NNLO_Wenu_MAXHTPTV70_140_CVetoBVeto
364174	946.37	0.9702	2.4414E-01	Sherpa_221_NNPDF30NNLO_Wenu_MAXHTPTV70_140_CFilterBVeto
364175	945.63	0.9702	8.5116E-02	Sherpa_221_NNPDF30NNLO_Wenu_MAXHTPTV70_140_BFilter
364176	339.75	0.9702	5.9858E-01	Sherpa_221_NNPDF30NNLO_Wenu_MAXHTPTV140_280_CVetoBVeto
364177	339.8	0.9702	2.8805E-01	Sherpa_221_NNPDF30NNLO_Wenu_MAXHTPTV140_280_CFilterBVeto
364178	339.7	0.9702	1.1088E-01	Sherpa_221_NNPDF30NNLO_Wenu_MAXHTPTV140_280_BFilter
364179	72.077	0.9702	5.4829E-01	Sherpa_221_NNPDF30NNLO_Wenu_MAXHTPTV280_500_CVetoBVeto
364180	72.105	0.9702	3.1969E-01	Sherpa_221_NNPDF30NNLO_Wenu_MAXHTPTV280_500_CFilterBVeto
364181	72.077	0.9702	1.3865E-01	Sherpa_221_NNPDF30NNLO_Wenu_MAXHTPTV280_500_BFilter
364182	15.05	0.9702	1.0000E+00	Sherpa_221_NNPDF30NNLO_Wenu_MAXHTPTV500_1000
364183	1.2344	0.9702	1.0000E+00	Sherpa_221_NNPDF30NNLO_Wenu_MAXHTPTV1000_E_CMS
364184	19155.0	0.9702	8.2462E-01	Sherpa_221_NNPDF30NNLO_Wtaunu_MAXHTPTV0_70_CVetoBVeto
364185	19153.0	0.9702	1.3167E-01	Sherpa_221_NNPDF30NNLO_Wtaunu_MAXHTPTV0_70_CFilterBVeto
364186	19152.0	0.9702	4.5128E-02	Sherpa_221_NNPDF30NNLO_Wtaunu_MAXHTPTV0_70_BFilter
364187	945.58	0.9702	6.7560E-01	Sherpa_221_NNPDF30NNLO_Wtaunu_MAXHTPTV70_140_CVetoBVeto
364188	946.49	0.9702	2.4245E-01	Sherpa_221_NNPDF30NNLO_Wtaunu_MAXHTPTV70_140_CFilterBVeto
364189	945.87	0.9702	8.3903E-02	Sherpa_221_NNPDF30NNLO_Wtaunu_MAXHTPTV70_140_BFilter
364190	339.69	0.9702	5.9884E-01	Sherpa_221_NNPDF30NNLO_Wtaunu_MAXHTPTV140_280_CVetoBVeto
364191	339.84	0.9702	2.8478E-01	Sherpa_221_NNPDF30NNLO_Wtaunu_MAXHTPTV140_280_CFilterBVeto
364192	339.68	0.9702	1.0575E-01	Sherpa_221_NNPDF30NNLO_Wtaunu_MAXHTPTV140_280_BFilter
364193	72.078	0.9702	5.6172E-01	Sherpa_221_NNPDF30NNLO_Wtaunu_MAXHTPTV280_500_CVetoBVeto
364194	71.99	0.9702	3.1863E-01	Sherpa_221_NNPDF30NNLO_Wtaunu_MAXHTPTV280_500_CFilterBVeto
364195	71.944	0.9702	1.3597E-01	Sherpa_221_NNPDF30NNLO_Wtaunu_MAXHTPTV280_500_BFilter
364196	15.052	0.9702	1.0000E+00	Sherpa_221_NNPDF30NNLO_Wtaunu_MAXHTPTV500_1000
364197	1.2342	0.9702	1.0000E+00	Sherpa_221_NNPDF30NNLO_Wtaunu_MAXHTPTV1000_E_CMS

Table A.6: Datasets used for the W + jets background.

List of Figures

List of Tables

Acronyms and notations

E_T Transverse Energy.

p_T Transverse Momentum.

E_T^{miss} Missing Transverse Energy.

pp proton-proton.

$2\ell^{sc}$ same-charge-two-lepton.

3ℓ three-lepton.

4ℓ four-lepton.

ATLAS A Toroidal LHC Aparatus.

BDT Boosted Decision Tree.

BEH Brout–Englert–Higgs.

BR Branch Ratios.

BSM Beyond Standard Model.

CERN *Conseil Européen Pour la Recherche Nucléaire*
European Organization for Nuclear Research.

CKM Cabibbo–Kobayashi–Maskawa.

DTHM Doublet Triplet Higgs Model.

EM Electromagnetic.

GSF GaussianSum Filter.

HF heavy-flavor decay.

IBL Insertable B-Layer.

ID Inner Detector.

IP interaction points.

JES Jet Energy Scale.

JVT Jet Vertex Tagging.

LAr Liquid Argon.

LF light-flavor decay.

LH Likelihood.

LHC Large Hadron Collider.

MDT Monitored Drift Tubes.

MS Muon Spectrometer.

PDF Parton Distribution Function.

PDFs probability density functions.

prompt Prompt produced.

PV Primary Vertex.

QCD quantum chromodynamics.

QED quantum electrodynamics.

QFT quantum field theory.

R.M.S. Root mean square.

RNN Recurrent Neural Network.

SCT Semiconductor Tracker.

SM Standard Model.

SR Signal Region.

TRT Transition Radiation Tracker.

Bibliography

[1] CMS Collaboration, *Observation of a new boson at a mass of 125 GeV with the CMS experiment at the LHC*, Phys. Lett. B **716** (2012) 30, arXiv: 1207.7235 [hep-ex] (cit. on pp. 15, 16, 29, 31).

[2] ATLAS Collaboration, *Observation of a new particle in the search for the Standard Model Higgs boson with the ATLAS detector at the LHC*, Phys. Lett. B **716** (2012) 1, arXiv: 1207.7214 [hep-ex] (cit. on pp. 15, 16, 29, 31).

[3] R. N. Mohapatra and A. Y. Smirnov, *Neutrino Mass and New Physics*, Ann. Rev. Nucl. Part. Sci. **56** (2006) 569, ed. by K. Anagnostopoulos et al., arXiv: hep-ph/0603118 (cit. on pp. 15, 29).

[4] A. Strumia and F. Vissani, *Neutrino masses and mixings and...*, (2006), arXiv: hep-ph/0606054 (cit. on pp. 15, 29).

[5] V. Barger, D. Marfatia and K. Whisnant, *Progress in the physics of massive neutrinos*, Int. J. Mod. Phys. E **12** (2003) 569, arXiv: hep-ph/0308123 (cit. on pp. 15, 29).

[6] W. Konetschny and W. Kummer, *Nonconservation of Total Lepton Number with Scalar Bosons*, Phys. Lett. B **70** (1977) 433 (cit. on pp. 15, 17, 29, 43).

[7] T. P. Cheng and L.-F. Li, *Neutrino masses, mixings, and oscillations in SU(2)×U(1) models of electroweak interactions*, Phys. Rev. D **22** (11 1980) 2860, URL: https://link.aps.org/doi/10.1103/PhysRevD.22.2860 (cit. on pp. 15, 17, 29, 43).

[8] J. Schechter and J. W. F. Valle, *Neutrino Masses in SU(2) x U(1) Theories*, Phys. Rev. D **22** (1980) 2227 (cit. on pp. 15, 17, 29, 43).

[9] G. Lazarides, Q. Shafi and C. Wetterich, *Proton Lifetime and Fermion Masses in an SO(10) Model*, Nucl. Phys. B **181** (1981) 287 (cit. on pp. 15, 17, 29, 43).

[10] P. Fileviez Perez, T. Han, G.-y. Huang, T. Li and K. Wang, *Neutrino Masses and the CERN LHC: Testing Type II Seesaw*, Phys. Rev. **D78** (2008) 015018, arXiv: 0805.3536 [hep-ph] (cit. on pp. 15, 17, 29, 45, 46).

[11] A. Arhrib et al., *The Higgs Potential in the Type II Seesaw Model*, Phys. Rev. **D84** (2011) 095005, arXiv: 1105.1925 [hep-ph] (cit. on pp. 15, 17, 29, 43, 45).

[12] S. Kanemura, M. Kikuchi, K. Yagyu and H. Yokoya, *Bounds on the mass of doubly-charged Higgs bosons in the same-sign diboson decay scenario*, Phys. Rev. **D90** (2014) 115018, arXiv: 1407.6547 [hep-ph] (cit. on pp. 15, 29).

[13] Z. Kang, J. Li, T. Li, Y. Liu and G.-Z. Ning, *Light Doubly Charged Higgs Boson via the WW^* Channel at LHC*, Eur. Phys. J. **C75** (2015) 574, arXiv: 1404.5207 [hep-ph] (cit. on pp. 15, 29).

[14] OPAL Collaboration, *Search for doubly charged Higgs bosons with the OPAL detector at LEP*, Phys. Lett. B **526** (2002) 221, arXiv: hep-ex/0111059 (cit. on pp. 15, 29, 46).

[15] H1 Collaboration, *Search for doubly-charged Higgs boson production at HERA*, Phys. Lett. B **638** (2006) 432, arXiv: hep-ex/0604027 (cit. on pp. 15, 29, 46).

[16] CDF Collaboration, *Search for New Physics in High p_T Like-Sign Dilepton Events at CDF II*, Phys. Rev. Lett. **107** (2011) 181801, arXiv: 1108.0101 [hep-ex] (cit. on pp. 15, 29, 46).

[17] ATLAS Collaboration, *Search for doubly-charged Higgs bosons in like-sign dilepton final states at $\sqrt{s}$ = 7 TeV with the ATLAS detector*, Eur. Phys. J. C **72** (2012) 2244, arXiv: 1210.5070 [hep-ex] (cit. on pp. 15, 29, 46).

[18] CMS Collaboration, *A search for a doubly-charged Higgs boson in pp collisions at $\sqrt{s}$ = 7 TeV*, Eur. Phys. J. C **72** (2012) 2189, arXiv: 1207.2666 [hep-ex] (cit. on pp. 15, 29, 46).

[19] ATLAS Collaboration, *Search for doubly charged Higgs boson production in multilepton final states with the ATLAS detector using proton–proton collisions at $\sqrt{s}$ = 13 TeV*, Eur. Phys. J. C **78** (2018) 199, arXiv: 1710.09748 [hep-ex] (cit. on pp. 15, 29, 46).

[20] CMS Collaboration, *Study of Vector Boson Scattering and Search for New Physics in Events with Two Same-Sign Leptons and Two Jets*, Phys. Rev. Lett. **114** (2015) 051801, arXiv: 1410.6315 [hep-ex] (cit. on pp. 15, 29).

[21] CMS Collaboration, *Observation of Electroweak Production of Same-Sign W Boson Pairs in the Two Jet and Two Same-Sign Lepton Final State in Proton-Proton Collisions at $\sqrt{s}$ = 13 TeV*, Phys. Rev. Lett. **120** (2018) 081801, arXiv: 1709.05822 [hep-ex] (cit. on pp. 15, 29).

[22] H. Georgi and M. Machacek, *Doubly charged Higgs bosons*, Nuclear Physics B **262** (1985) 463, ISSN: 0550-3213 (cit. on pp. 15, 29).

[23] ATLAS Collaboration, *Search for doubly charged scalar bosons decaying into same-sign W boson pairs with the ATLAS detector*, Eur. Phys. J. C **79** (2019) 58, arXiv: 1808.01899 [hep-ex] (cit. on pp. 16, 29, 46, 151, 174).

[24] S. L. Glashow, *Partial Symmetries of Weak Interactions*, Nucl. Phys. **22** (1961) 579 (cit. on pp. 16, 31).

[25] S. Weinberg, *A Model of Leptons*, Phys. Rev. Lett. **19** (1967) 1264 (cit. on pp. 16, 31, 38).

[26] A. Salam, *Weak and Electromagnetic Interactions*, Conf. Proc. C **680519** (1968) 367 (cit. on pp. 16, 31).

[27] S. L. Glashow, J. Iliopoulos and L. Maiani, *Weak Interactions with Lepton-Hadron Symmetry*, Phys. Rev. D **2** (1970) 1285 (cit. on pp. 16, 31).

[28] C. Collaboration, *Observation of top quark production in $\bar{p}p$ collisions*, Phys. Rev. Lett. **74** (1995) 2626, arXiv: hep-ex/9503002 (cit. on pp. 16, 31).

[29] D. Collaboration, *Observation of tau neutrino interactions*, Phys. Lett. B **504** (2001) 218, arXiv: hep-ex/0012035 (cit. on pp. 16, 31).

[30] P. A. M. Dirac, *Quantum theory of emission and absorption of radiation*, Proc. Roy. Soc. Lond. A **114** (1927) 243 (cit. on pp. 16, 31, 34).

[31] W. Pauli, *Relativistic Field Theories of Elementary Particles*, Rev. Mod. Phys. **13** (1941) 203 (cit. on pp. 16, 31).

[32] C.-N. Yang and R. L. Mills, *Conservation of Isotopic Spin and Isotopic Gauge Invariance*, Phys. Rev. **96** (1954) 191, [,150(1954)] (cit. on pp. 16, 31, 35).

[33] S. L. Glashow, *Partial-symmetries of weak interactions*, Nuclear Physics **22** (1961) 579, ISSN: 0029-5582, URL: http://www.sciencedirect.com/science/article/pii/0029558261904692 (cit. on pp. 16, 31).

[34] F. Englert and R. Brout, *Broken Symmetry and the Mass of Gauge Vector Mesons*, Phys. Rev. Lett. **13** (9 1964) 321, URL: https://link.aps.org/doi/10.1103/PhysRevLett.13.321 (cit. on pp. 16, 31).

[35] P. W. Higgs, *Broken Symmetries and the Masses of Gauge Bosons*, Phys. Rev. Lett. **13** (16 1964) 508, URL: https://link.aps.org/doi/10.1103/PhysRevLett.13.508 (cit. on pp. 16, 31).

[36] G. S. Guralnik, C. R. Hagen and T. W. B. Kibble, *Global Conservation Laws and Massless Particles*, Phys. Rev. Lett. **13** (20 1964) 585, URL: https://link.aps.org/doi/10.1103/PhysRevLett.13.585 (cit. on pp. 16, 31).

[37] A. O. Sushkov, W. J. Kim, D. A. R. Dalvit and S. K. Lamoreaux, *New Experimental Limits on Non-Newtonian Forces in the Micrometer Range*, Phys. Rev. Lett. **107** (2011) 171101, arXiv: 1108.2547 [quant-ph] (cit. on pp. 16, 42).

[38] S. Weinberg, *Baryon- and Lepton-Nonconserving Processes*, Phys. Rev. Lett. **43** (21 1979) 1566, URL: https://link.aps.org/doi/10.1103/PhysRevLett.43.1566 (cit. on pp. 17, 43).

[39] L. Evans and P. Bryant, *LHC Machine*, JINST **3** (2008) S08001 (cit. on pp. 17, 47).

[40] ATLAS Collaboration, *The ATLAS Experiment at the CERN Large Hadron Collider*, JINST **3** (2008) S08003 (cit. on pp. 17, 48, 50, 51, 55–58).

[41] ATLAS Collaboration, *2020 ATLAS Good Run Lists For Analysis Run2*, (2020), URL: https://twiki.cern.ch/twiki/bin/viewauth/AtlasProtected/GoodRunListsForAnalysisRun2 (visited on 05/08/2020) (cit. on pp. 18, 83).

[42] J. Alwall et al., *The automated computation of tree-level and next-to-leading order differential cross sections, and their matching to parton shower simulations*, JHEP **07** (2014) 079, arXiv: 1405.0301 [hep-ph] (cit. on pp. 18, 83).

[43] T. Sjostrand, S. Mrenna and P. Z. Skands, *A brief introduction to PYTHIA 8.1*, Comput. Phys. Commun. **178** (2008) 852, arXiv: 0710.3820 [hep-ph] (cit. on pp. 18, 83, 85).

[44] ATLAS Collaboration, *ATLAS Run 1 Pythia8 tunes*, (2014), http://cds.cern.ch/record/1966419 (cit. on pp. 18, 83, 85).

[45] ATLAS Collaboration, *Monte Carlo Generators for the Production of a W or Z/γ^* Boson in Association with Jets at ATLAS in Run 2*, (2015), ATL-PHYS-PUB-2016-003, URL: https://cds.cern.ch/record/2120133 (cit. on pp. 19, 84).

[46] ATLAS Collaboration, *Multi-Boson Simulation for 13 TeV ATLAS Analyses*, (2015), ATL-PHYS-PUB-2016-002, URL: https://cds.cern.ch/record/2119986 (cit. on pp. 19, 84).

[47] ATLAS Collaboration, *Simulation of top quark production for the ATLAS experiment at $\sqrt{s} = 13$ TeV*, (2015), ATL-PHYS-PUB-2016-004, URL: https://cds.cern.ch/record/2120417 (cit. on pp. 19, 84).

[48] ATLAS Collaboration, *Modelling of the $t\bar{t}H$ and $t\bar{t}V$ ($V = W, Z$) processes for $\sqrt{s} = 13$ TeV ATLAS analyses*, (2015), ATL-PHYS-PUB-2016-005, URL: https://cds.cern.ch/record/2120826 (cit. on pp. 19, 84).

[49] S. Agostinelli et al., *Geant4: a simulation toolkit*, Nucl. Instrum. Meth. Phys. Res. A **506** (2003) 250, ISSN: 0168-9002 (cit. on pp. 19, 84).

[50] A. Hoecker et al., *TMVA: Toolkit for Multivariate Data Analysis*, PoS **ACAT** (2007) 040, arXiv: physics/0703039 (cit. on pp. 20, 151).

[51] A. L. Read, *Presentation of search results: the CL_S technique*, J. Phys. G **28** (2002) 2693 (cit. on pp. 22, 171).

[52] H. Georgi and M. Machacek, *DOUBLY CHARGED HIGGS BOSONS*, Nucl. Phys. B **262** (1985) 463 (cit. on p. 29).

[53] UA1 Collaboration, *Experimental Observation of Isolated Large Transverse Energy Electrons with Associated Missing Energy at $\sqrt{s} = 540$ GeV*, Phys. Lett. B **122** (1983) 103, [,611(1983)] (cit. on pp. 31, 38).

[54] J. F. Donoghue, E. Golowich and B. R. Holstein, *Dynamics of the standard model*, Camb. Monogr. Part. Phys. Nucl. Phys. Cosmol. **2** (1992) 1, [Camb. Monogr. Part. Phys. Nucl. Phys. Cosmol.35(2014)] (cit. on p. 32).

[55] M. Kobayashi and T. Maskawa, *CP Violation in the Renormalizable Theory of Weak Interaction*, Prog. Theor. Phys. **49** (1973) 652 (cit. on p. 32).

[56] C. Burgard, *Example: Standard model of physics*, 2016, URL: https://texample.net/tikz/examples/model-physics/ (cit. on p. 33).

[57] P. A. M. Dirac, *The quantum theory of the electron*, Proc. Roy. Soc. Lond. A **117** (1928) 610 (cit. on p. 34).

[58] W. Heisenberg and W. Pauli, *Zur Quantendynamik der Wellenfelder*, Zeitschrift für Physik **56** (1929) 1, ISSN: 0044-3328, URL: https://doi.org/10.1007/BF01340129 (cit. on p. 34).

[59] W. Heisenberg and W. Pauli, *Zur Quantentheorie der Wellenfelder. II*, Zeitschrift für Physik **59** (1930) 168, ISSN: 0044-3328, URL: https://doi.org/10.1007/BF01341423 (cit. on p. 34).

[60] Wikipedia contributors, *Gamma matrices — Wikipedia, The Free Encyclopedia*, https://en.wikipedia.org/w/index.php?title=Gamma_matrices&oldid=1010234032, [Online; accessed 29-March-2021], 2021 (cit. on pp. 34, 36).

[61] Wikipedia contributors, *Quantum electrodynamics — Wikipedia, The Free Encyclopedia*, [Online; accessed 22-February-2021], 2021, URL: https://en.wikipedia.org/w/index.php?title=Quantum_electrodynamics&oldid=1006962799 (cit. on p. 35).

[62] R. Utiyama, *Invariant theoretical interpretation of interaction*, Phys. Rev. **101** (1956) 1597, [,157(1956)] (cit. on p. 35).

[63] Wikipedia contributors, *Pauli matrices — Wikipedia, The Free Encyclopedia*, [Online; accessed 22-February-2021], 2021, URL: https://en.wikipedia.org/w/index.php?title=Pauli_matrices&oldid=1006695199 (cit. on pp. 36, 37).

[64] M. Gell-Mann, *The Eightfold Way: A Theory of strong interaction symmetry*, (1961) (cit. on pp. 36, 41).

[65] C. S. Wu, E. Ambler, R. W. Hayward, D. D. Hoppes and R. P. Hudson, *Experimental Test of Parity Conservation in Beta Decay*, Phys. Rev. **105** (1957) 1413 (cit. on p. 37).

[66] K. Nishijima, *Charge Independence Theory of V Particles*, Prog. Theor. Phys. **13** (1955) 285 (cit. on p. 37).

[67] M. Gell-Mann, *The interpretation of the new particles as displaced charge multiplets*, Nuovo Cim. **4** (1956) 848 (cit. on pp. 37, 41).

[68] UA2 Collaboration, *Observation of Single Isolated Electrons of High Transverse Momentum in Events with Missing Transverse Energy at the CERN anti-p p Collider*, Phys. Lett. B **122** (1983) 476, [,7.45(1983)] (cit. on p. 38).

[69] ALEPH Collaboration, *Measurement of the W boson mass and width in e^+e^- collisions at LEP*, Eur. Phys. J. C **47** (2006) 309, arXiv: hep-ex/0605011 [hep-ex] (cit. on p. 38).

[70] DELPHI Collaboration, *Measurement of the Mass and Width of the W Boson in e^+e^- Collisions at $\sqrt{s}$ = 161-GeV - 209-GeV*, Eur. Phys. J. C **55** (2008) 1, arXiv: 0803.2534 [hep-ex] (cit. on p. 38).

[71] L3 Collaboration, *Measurement of mass and width of the W boson at LEP*, Phys. Lett. B **454** (1999) 386, arXiv: hep-ex/9909010 [hep-ex] (cit. on p. 38).

[72] OPAL Collaboration, *Measurement of the mass and width of the W boson*, Eur. Phys. J. C **45** (2006) 307, arXiv: hep-ex/0508060 [hep-ex] (cit. on p. 38).

[73] CDF Collaboration, *Precise measurement of the W-boson mass with the CDF II detector*, Phys. Rev. Lett. **108** (2012) 151803, arXiv: 1203.0275 [hep-ex] (cit. on p. 38).

[74] D0 Collaboration, *Measurement of the W boson mass with the D0 detector*, Phys. Rev. D **89** (2014) 012005, arXiv: 1310.8628 [hep-ex] (cit. on p. 38).

[75] ALEPH, DELPHI, L3, OPAL, and SLD Collaborations, LEP Electroweak Working Group, SLD Electroweak Group, and SLD Heavy Flavour Group, *Precision electroweak measurements on the Z resonance*, Phys. Rept. **427** (2006) 257, arXiv: hep-ex/0509008 [hep-ex] (cit. on p. 38).

[76] M. Aaboud et al., *Measurement of the W-boson mass in pp collisions at $\sqrt{s}$ = 7 TeV with the ATLAS detector*, Eur. Phys. J. C **78** (2018) 110, [Erratum: Eur.Phys.J.C 78, 898 (2018)], arXiv: 1701.07240 [hep-ex] (cit. on p. 38).

[77] P. D. Group et al., *Review of Particle Physics*, Progress of Theoretical and Experimental Physics **2020** (2020), 083C01, ISSN: 2050-3911, eprint: https://academic.oup.com/ptep/article-pdf/2020/8/083C01/34673722/ptaa104.pdf, URL: https://doi.org/10.1093/ptep/ptaa104 (cit. on pp. 38–40).

[78] Z. Maki, M. Nakagawa and S. Sakata, *Remarks on the Unified Model of Elementary Particles*, Progress of Theoretical Physics **28** (1962) 870 (cit. on p. 39).

[79] U.-G. Meissner, *Chiral QCD: baryon dynamics*, (2000), ed. by M. Shifman and B. Ioffe, arXiv: hep-ph/0007092 (cit. on p. 40).

[80] ATLAS and CMS Collaborations, *Combined Measurement of the Higgs Boson Mass in pp Collisions at $\sqrt{s} = 7$ and 8 TeV with the ATLAS and CMS Experiments*, Phys. Rev. Lett. **114** (2015) 191803, arXiv: 1503.07589 [hep-ex] (cit. on p. 41).

[81] M. Y. Han and Y. Nambu, *Three Triplet Model with Double SU(3) Symmetry*, Phys. Rev. **139** (1965) B1006, [,187(1965)] (cit. on p. 41).

[82] O. W. Greenberg, *Spin and Unitary Spin Independence in a Paraquark Model of Baryons and Mesons*, Phys. Rev. Lett. **13** (1964) 598 (cit. on p. 41).

[83] H. Fritzsch, M. Gell-Mann and H. Leutwyler, *Advantages of the Color Octet Gluon Picture*, Phys. Lett. B **47** (1973) 365 (cit. on p. 41).

[84] H. D. Politzer, *Reliable Perturbative Results for Strong Interactions?*, Phys. Rev. Lett. **30** (1973) 1346 (cit. on p. 42).

[85] D. J. Gross and F. Wilczek, *Ultraviolet Behavior of Nonabelian Gauge Theories*, Phys. Rev. Lett. **30** (1973) 1343 (cit. on p. 42).

[86] J. D. Bjorken and E. A. Paschos, *Inelastic Electron-Proton and γ-Proton Scattering and the Structure of the Nucleon*, Phys. Rev. **185** (5 1969) 1975, URL: https://link.aps.org/doi/10.1103/PhysRev.185.1975 (cit. on p. 42).

[87] S. Catani, F. Krauss, R. Kuhn and B. R. Webber, *QCD Matrix Elements + Parton Showers*, JHEP **11** (2001) 063, arXiv: hep-ph/0109231 (cit. on p. 42).

[88] A. Buckley et al., *LHAPDF6: parton density access in the LHC precision era*, The European Physical Journal C **75** (2015) 132, ISSN: 1434-6052, URL: http://dx.doi.org/10.1140/epjc/s10052-015-3318-8 (cit. on pp. 42, 161).

[89] Y. Fukuda et al., *Evidence for oscillation of atmospheric neutrinos*, Phys. Rev. Lett. **81** (1998) 1562, arXiv: hep-ex/9807003 [hep-ex] (cit. on p. 42).

[90] Q. R. Ahmad et al., *Direct evidence for neutrino flavor transformation from neutral current interactions in the Sudbury Neutrino Observatory*, Phys. Rev. Lett. **89** (2002) 011301, arXiv: nucl-ex/0204008 [nucl-ex] (cit. on p. 42).

[91] E. Majorana, *Teoria simmetrica dell'elettrone e del positrone*, Nuovo Cim. **14** (1937) 171 (cit. on p. 43).

[92] P. Sikivie, L. Susskind, M. Voloshin and V. Zakharov, *Isospin breaking in technicolor models*, Nuclear Physics B **173** (1980) 189, ISSN: 0550-3213, URL: https://www.sciencedirect.com/science/article/pii/055032138090214X (cit. on p. 45).

[93] K. A. Olive et al., *Review of Particle Physics*, Chin. Phys. **C38** (2014) 090001 (cit. on p. 45).

[94] The ATLAS Collaboration, *ATLAS Experiment Public Results*, Accessed: 2019-01-10, URL: https://twiki.cern.ch/twiki/bin/view/AtlasPublic/LuminosityPublicResultsRun2 (cit. on p. 48).

[95] R. Bruce et al., *LHC Run 2: Results and challenges*, (2016) MOAM5P50. 7 p, URL: http://cds.cern.ch/record/2201447 (cit. on p. 48).

[96] E. Mobs, *The CERN accelerator complex. Complexe des accélérateurs du CERN*, (2016), General Photo, URL: https://cds.cern.ch/record/2197559 (cit. on p. 49).

[97] W. Herr and B. Muratori, *Concept of luminosity*, (2006), URL: https://cds.cern.ch/record/941318 (cit. on p. 48).

[98] *ATLAS magnet system: Technical Design Report, 1*, Technical design report. ATLAS, CERN, 1997, URL: https://cds.cern.ch/record/338080 (cit. on pp. 49, 51).

[99] *ATLAS inner detector: Technical Design Report, 1*, Technical Design Report ATLAS, CERN, 1997, URL: https://cds.cern.ch/record/331063 (cit. on p. 50).

[100] G. Aad et al., *Alignment of the ATLAS Inner Detector in Run-2*, Eur. Phys. J. C **80** (2020) 1194, arXiv: 2007.07624 [hep-ex] (cit. on p. 52).

[101] ATLAS Collaboration, *Study of the material of the ATLAS inner detector for Run 2 of the LHC*, JINST **12** (2017) P12009, arXiv: 1707.02826 [hep-ex] (cit. on p. 53).

[102] ATLAS Collaboration, *ATLAS Insertable B-Layer Technical Design Report*, CERN-LHCC-2010-013, 2010, URL: https://cds.cern.ch/record/1291633 (cit. on p. 51).

[103] V. L. Ginzburg and I. M. Frank, *Radiation of a uniformly moving electron due to its transition from one medium into another*, J. Phys. (USSR) **9** (1945) 353 (cit. on p. 54).

[104] *ATLAS liquid-argon calorimeter: Technical Design Report*, Technical Design Report ATLAS, CERN, 1996, URL: https://cds.cern.ch/record/331061 (cit. on pp. 54, 55).

[105] *ATLAS tile calorimeter: Technical Design Report*, Technical Design Report ATLAS, CERN, 1996, URL: https://cds.cern.ch/record/331062 (cit. on pp. 54, 55).

[106] ATLAS Collaboration, *ATLAS Muon Spectrometer: Technical Design Report*, ATLAS-TDR-10; CERN-LHCC-97-022, CERN, 1997, URL: https://cds.cern.ch/record/331068 (cit. on p. 58).

[107] ATLAS Collaboration, *Performance of the ATLAS trigger system in 2015*, Eur. Phys. J. C **77** (2017) 317, arXiv: 1611.09661 [hep-ex] (cit. on pp. 59, 60).

[108] ATLAS Collaboration, *The LUCID detector ATLAS luminosity monitor and its electronic system*, Nucl. Instrum. Meth. A **824** (2016) 311 (cit. on p. 60).

[109] D. Noel, *tikz-track*, https://github.com/ndawe/tikz-track, 2016 (cit. on p. 64).

[110] T. Cornelissen et al., *Concepts, Design and Implementation of the ATLAS New Tracking (NEWT)*, tech. rep. ATL-SOFT-PUB-2007-007. ATL-COM-SOFT-2007-002, CERN, 2007, URL: https://cds.cern.ch/record/1020106 (cit. on p. 63).

[111] ATLAS Collaboration, *Performance of the ATLAS track reconstruction algorithms in dense environments in LHC Run 2*, Eur. Phys. J. C **77** (2017) 673, arXiv: 1704.07983 [hep-ex] (cit. on pp. 63, 64).

[112] R. Fruhwirth, *Application of Kalman filtering to track and vertex fitting*, Nucl. Instrum. Meth. A **262** (1987) 444 (cit. on pp. 64, 67).

[113] ATLAS Collaboration, *A neural network clustering algorithm for the ATLAS silicon pixel detector*, JINST **9** (2014) P09009, arXiv: 1406.7690 [hep-ex] (cit. on p. 64).

[114] ATLAS Collaboration, *dE/dx measurement in the ATLAS Pixel Detector and its use for particle identification*, ATLAS-CONF-2011-016, 2011, URL: https://cds.cern.ch/record/1336519 (cit. on p. 64).

[115] ATLAS Collaboration, *Reconstruction of primary vertices at the ATLAS experiment in Run 1 proton–proton collisions at the LHC*, Eur. Phys. J. C **77** (2017) 332, arXiv: 1611.10235 [hep-ex] (cit. on p. 64).

[116] ATLAS Collaboration, *MCTruthClassifier*, 2019, URL: https://twiki.cern.ch/twiki/bin/view/AtlasProtected/MCTruthClassifier (cit. on p. 65).

[117] ATLAS Collaboration, *Electron efficiency measurements with the ATLAS detector using 2012 LHC proton–proton collision data*, Eur. Phys. J. C **77** (2017) 195, arXiv: 1612.01456 [hep-ex] (cit. on p. 66).

[118] ATLAS Collaboration, *Electron efficiency measurements with the ATLAS detector using the 2015 LHC proton–proton collision data*, ATLAS-CONF-2016-024, 2016, URL: https://cds.cern.ch/record/2157687 (cit. on pp. 66, 69).

[119] ATLAS Collaboration, *Electron and photon reconstruction and performance in ATLAS using a dynamical, topological cell clustering-based approach*, ATL-PHYS-PUB-2017-022, 2017, URL: https://cds.cern.ch/record/2298955 (cit. on pp. 66, 67).

[120] ATLAS Collaboration, *Electron and photon performance measurements with the ATLAS detector using the 2015–2017 LHC proton-proton collision data*, JINST **14** (2019) P12006, arXiv: 1908.00005 [hep-ex] (cit. on pp. 66, 68, 69, 78).

[121] T. G. Cornelissen et al., *The global χ^2 track fitter in ATLAS*, J. Phys. Conf. Ser. **119** (2008) 032013 (cit. on p. 67).

[122] ATLAS Collaboration, *Improved electron reconstruction in ATLAS using the Gaussian Sum Filter-based model for bremsstrahlung*, ATLAS-CONF-2012-047, 2012, URL: https://cds.cern.ch/record/1449796 (cit. on p. 67).

[123] ATLAS Collaboration, *Electron and photon energy calibration with the ATLAS detector using 2015–2016 LHC proton-proton collision data*, JINST **14** (2019) P03017, arXiv: 1812.03848 [hep-ex] (cit. on pp. 67, 68).

[124] C. Anastopoulos et al., *Support Note for Electron ID: electron reconstruction and identification*, tech. rep., CERN, 2017, URL: https://cds.cern.ch/record/2273328 (cit. on p. 70).

[125] ATLAS Collaboration, *Electron reconstruction and identification in the ATLAS experiment using the 2015 and 2016 LHC proton–proton collision data at $\sqrt{s} = 13$ TeV*, Eur. Phys. J. C **79** (2019) 639, arXiv: 1902.04655 [hep-ex] (cit. on pp. 69, 71, 163).

[126] J. Illingworth and J. Kittler, *A survey of the hough transform*, Computer Vision, Graphics, and Image Processing **44** (1988) 87, ISSN: 0734-189X, URL: http://www.sciencedirect.com/science/article/pii/S0734189X88800331 (cit. on p. 71).

[127] ATLAS Collaboration, *Muon reconstruction performance of the ATLAS detector in proton–proton collision data at $\sqrt{s} = 13$ TeV*, Eur. Phys. J. C **76** (2016) 292, arXiv: 1603.05598 [hep-ex] (cit. on pp. 71, 73, 163).

[128] M. Cacciari, G. P. Salam and G. Soyez, *The anti-k_t jet clustering algorithm*, JHEP **04** (2008) 063, arXiv: 0802.1189 [hep-ph] (cit. on p. 74).

[129] M. Cacciari, G. P. Salam and G. Soyez, *FastJet user manual*, Eur. Phys. J. C **72** (2012) 1896, arXiv: 1111.6097 [hep-ph] (cit. on p. 74).

[130] ATLAS Collaboration, *Jet reconstruction and performance using particle flow with the ATLAS Detector*, Eur. Phys. J. C **77** (2017) 466, arXiv: 1703.10485 [hep-ex] (cit. on p. 74).

[131] ATLAS Collaboration, *Topological cell clustering in the ATLAS calorimeters and its performance in LHC Run 1*, Eur. Phys. J. C **77** (2017) 490, arXiv: 1603.02934 [hep-ex] (cit. on p. 74).

[132] ATLAS Collaboration, *Jet energy scale and resolution measured in proton–proton collisions at $\sqrt{s}$ = 13 TeV with the ATLAS detector*, (2020), arXiv: 2007.02645 [hep-ex] (cit. on pp. 74, 163).

[133] ATLAS Collaboration, *Performance of pile-up mitigation techniques for jets in pp collisions at $\sqrt{s}$ = 8 TeV using the ATLAS detector*, Eur. Phys. J. C **76** (2016) 581, arXiv: 1510.03823 [hep-ex] (cit. on pp. 75, 78).

[134] ATLAS Collaboration, *ATLAS b-jet identification performance and efficiency measurement with $t\bar{t}$ events in pp collisions at $\sqrt{s}$ = 13 TeV*, Eur. Phys. J. C **79** (2019) 970, arXiv: 1907.05120 [hep-ex] (cit. on p. 75).

[135] ATLAS Collaboration, *Optimisation and performance studies of the ATLAS b-tagging algorithms for the 2017-18 LHC run*, ATL-PHYS-PUB-2017-013, 2017, URL: https://cds.cern.ch/record/2273281 (cit. on p. 75).

[136] ATLAS Collaboration, *Identification of Jets Containing b-Hadrons with Recurrent Neural Networks at the ATLAS Experiment*, ATL-PHYS-PUB-2017-003, 2017, URL: https://cds.cern.ch/record/2255226 (cit. on pp. 75, 76).

[137] ATLAS Collaboration, *Monte Carlo to Monte Carlo scale factors for flavour tagging efficiency calibration*, ATL-PHYS-PUB-2020-009, 2020, URL: https://cds.cern.ch/record/2718610 (cit. on p. 76).

[138] J. M. Campbell et al., *Report of the Snowmass 2013 energy frontier QCD working group*, arXiv e-prints, arXiv:1310.5189 (2013) arXiv:1310.5189, arXiv: 1310.5189 [hep-ph] (cit. on p. 77).

[139] ATLAS Collaboration, *Muon reconstruction and identification efficiency in ATLAS using the full Run 2 pp collision data set at $\sqrt{s}$ = 13 TeV*, (2020), arXiv: 2012.00578 [hep-ex] (cit. on p. 78).

[140] M. Cacciari and G. P. Salam, *Pileup subtraction using jet areas*, Phys. Lett. B **659** (2008) 119, arXiv: 0707.1378 [hep-ph] (cit. on p. 78).

[141] ATLAS Collaboration, *Evidence for the associated production of the Higgs boson and a top quark pair with the ATLAS detector*, Phys. Rev. D **97** (2018) 072003, arXiv: 1712.08891 [hep-ex] (cit. on pp. 78, 79).

[142] ATLAS Collaboration, *Isolation WPs performance: all plots, different IDs, OR, samples, etc*, 2019, URL: https://indico.cern.ch/event/854783/contributions/3641582/attachments/1944964/3228483/booklet_isoEff.pdf (cit. on p. 78).

[143] ATLAS Collaboration, *Performance of missing transverse momentum reconstruction with the ATLAS detector using proton–proton collisions at $\sqrt{s} = 13$ TeV*, Eur. Phys. J. C **78** (2018) 903, arXiv: 1802.08168 [hep-ex] (cit. on pp. 79, 163).

[144] ATLAS Collaboration, *Performance of algorithms that reconstruct missing transverse momentum in $\sqrt{s} = 8$ TeV proton–proton collisions in the ATLAS detector*, Eur. Phys. J. C **77** (2017) 241, arXiv: 1609.09324 [hep-ex] (cit. on p. 79).

[145] ATLAS Collaboration, *E_T^{miss} performance in the ATLAS detector using 2015–2016 LHC pp collisions*, ATLAS-CONF-2018-023, 2018, URL: https://cds.cern.ch/record/2625233 (cit. on pp. 79, 80).

[146] M. Muhlleitner and M. Spira, *A Note on doubly charged Higgs pair production at hadron colliders*, Phys. Rev. D **68** (2003) 117701, arXiv: hep-ph/0305288 [hep-ph] (cit. on p. 84).

[147] S. Frixione, G. Ridolfi and P. Nason, *A positive-weight next-to-leading-order Monte Carlo for heavy flavour hadroproduction*, JHEP **09** (2007) 126, arXiv: 0707.3088 [hep-ph] (cit. on p. 85).

[148] R. D. Ball et al., *Parton distributions for the LHC run II*, JHEP **04** (2015) 040, arXiv: 1410.8849 [hep-ph] (cit. on p. 85).

[149] E. Re, *Single-top Wt-channel production matched with parton showers using the POWHEG method*, Eur. Phys. J. C **71** (2011) 1547, arXiv: 1009.2450 [hep-ph] (cit. on p. 85).

[150] S. Alioli, P. Nason, C. Oleari and E. Re, *NLO single-top production matched with shower in POWHEG: $s-$ and $t-$channel contributions*, JHEP **09** (2009) 111, arXiv: 0907.4076 [hep-ph] (cit. on p. 85).

[151] T. Gleisberg et al., *Event generation with SHERPA 1.1*, JHEP **02** (2009) 007, arXiv: 0811.4622 [hep-ph] (cit. on p. 85).

[152] D. J. Lange, *The EvtGen particle decay simulation package*, Nucl. Instrum. Meth. A **462** (2001) 152 (cit. on p. 85).

[153] G. Aad et al., *Performance of electron and photon triggers in ATLAS during LHC Run 2*, Eur. Phys. J. C **80** (2020) 47, arXiv: 1909.00761 [hep-ex] (cit. on p. 90).

[154] G. Aad et al., *Performance of the ATLAS muon triggers in Run 2*, JINST **15** (2020) P09015, arXiv: 2004.13447 [physics.ins-det] (cit. on p. 90).

[155] ATLAS Collaboration, *Electron and photon performance measurements with the ATLAS detector using the 2015–2017 LHC proton–proton collision data*, JINST **14** (2019) P12006, arXiv: 1908.00005 [hep-ex] (cit. on p. 91).

[156] ATLAS Collaboration, *Evidence for $t\bar{t}t\bar{t}$ production in the multilepton final state in proton-proton collisions at $\sqrt{s} = 13$ TeV with the ATLAS detector*, Eur. Phys. J. C **80** (2020) 1085, arXiv: 2007.14858 [hep-ex] (cit. on p. 91).

[157] A. M. Sirunyan et al., *Search for physics beyond the standard model in multilepton final states in proton-proton collisions at $\sqrt{s} = 13$ TeV*, JHEP **03** (2020) 051, arXiv: 1911.04968 [hep-ex] (cit. on p. 144).

[158] G. Cowan, K. Cranmer, E. Gross and O. Vitells, *Asymptotic formulae for likelihood-based tests of new physics*, Eur. Phys. J. C **71** (2011) 1554, arXiv: 1007.1727 [physics.data-an] (cit. on pp. 152, 171, 173), Erratum: Eur. Phys. J. C **73** (2013) 2501.

[159] The ATLAS Collaboration, *Search for doubly charged Higgs boson production in multilepton final states with the ATLAS detector using proton–proton collisions at $\sqrt{s} = 13$ TeV*, Eur. Phys. J. **C78** (2017) 52, arXiv: 1710.09748 [hep-ex] (cit. on p. 155).

[160] ATLAS Collaboration, *Search for supersymmetry in final states with two same-sign or three leptons and jets using 36 fb^{-1} of $\sqrt{s} = 13$ TeV pp collision data with the ATLAS detector*, ATLAS-CONF-2017-030, 2017, URL: https://cds.cern.ch/record/2262920 (cit. on p. 162).

[161] D. de Florian et al., *Handbook of LHC Higgs Cross Sections: 4. Deciphering the Nature of the Higgs Sector*, CERN Yellow Reports: Monographs, 869 pages, 295 figures, 248 tables and 1645 citations. Working Group web page: https://twiki.cern.ch/twiki/bin/view/LHCPhysics/LHCHXSWG, 2016, URL: https://cds.cern.ch/record/2227475 (cit. on p. 162).

[162] M. Aaboud et al., *Measurement of the $t\bar{t}Z$ and $t\bar{t}W$ cross sections in proton-proton collisions at $\sqrt{s} = 13$ TeV with the ATLAS detector*, Phys. Rev. D **99** (2019) 072009, arXiv: 1901.03584 [hep-ex] (cit. on p. 162).

[163] H. Xu et al., *Supporting Note: Search for doubly charged scalar bosons decaying to $W^{\pm}W^{\pm}$ at LHC*, tech. rep., CERN, 2019, URL: https://cds.cern.ch/record/2703331 (cit. on p. 162).

[164] ATLAS Collaboration, *Electron and photon energy calibration with the ATLAS detector using 2015–2016 LHC proton–proton collision data*, JINST **14** (2019) P03017, arXiv: 1812.03848 [hep-ex] (cit. on p. 163).

[165] ATLAS Collaboration, *Luminosity determination in pp collisions at $\sqrt{s} = 13$ TeV using the ATLAS detector at the LHC*, ATLAS-CONF-2019-021, 2019, URL: https://cds.cern.ch/record/2677054 (cit. on p. 163).

[166] G. Avoni et al., *The new LUCID-2 detector for luminosity measurement and monitoring in ATLAS*, JINST **13** (2018) P07017 (cit. on p. 163).

B Publications

Published

1. ATLAS Collaboration, *Search for doubly charged scalar bosons decaying into same-sign W boson pairs with the ATLAS detector*, Eur. Phys. J. C 79 (2019) 58, arXiv:1808.01899 [hep-ex].
2. ATLAS Collaboration, *Electron and photon performance measurements with the ATLAS detector using the 2015–2017 LHC proton-proton collision data*, JINST14(2019) P12006, arXiv:1908.00005 [hep-ex].
3. ATLAS Collaboration, *Analysis of $t\bar{t}H$ and $t\bar{t}W$ production in multilepton final states with the ATLAS detector*, ATLAS-CONF-2019-045, 2019, url:http://cds.cern.ch/record/2693930
4. ATLAS Collaboration, *Search for doubly- and singly-charged Higgs bosons decaying into vector bosons in multileptons final states with the ATLAS detector using proton-proton collisions at $\sqrt{s}$ = 13 TeV*, ATLAS-CONF-2020-056, 2020, url:http://cds.cern.ch/record/2743626

Accepted

1. ATLAS Collaboration, *Search for charged Higgs bosons decaying to vector bosons in multilepton final states with the ATLAS detector using proton-proton collisions at 13 TeV*, arXiv:2101.11961 [hep-ex].